3D Topological Photonic Crystals: Theoretical Methods and Applications

Candidate:

Chiara Devescovi

Supervisors:

Aitzol García-Etxarri

Maia G. Vergniory

University of the Basque Country

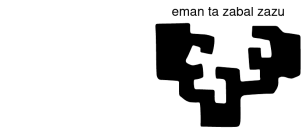

Department of Electricity and Electronics

(cc) 2023 Chiara Devescovi (cc by 4.0)

Resumen

Los cristales fotónicos topológicos representan la convergencia de dos importantes áreas de investigación: la fotónica y los materiales topológicos. Los cristales fotónicos surgieron a finales de la década de 1980, cuando los investigadores comenzaron a explorar estructuras dieléctricas periódicas que podían manipular la propagación de ondas electromagnéticas. Los cristales fotónicos fueron propuestos inicialmente por *S. John* y *E. Yablonovitch*, que posteriormente condujo a la conceptualización de la banda prohibida fotónica, un rango de frecuencia específico en el que está prohibida la propagación de ondas electromagnéticas. La integración de conceptos topológicos en sistemas fotónicos comenzó a ganar fuerza con el descubrimiento de propiedades topológicas en sistemas electrónicos. Aunque el efecto Hall cuántico de la década de 1980 ya había mostrado un gas de electrones 2D con una conductancia Hall cuantizada basada en invariantes topológicas como el número de Chern, fue la observación reveladora de *S. Raghu y F.D.M. Haldane* para resaltar el potencial de replicar estos efectos en estructuras fotónicas. En particular, sus estudios aclararon cómo la cuantización topológica podría surgir de las propiedades globales de la función de onda en la zona de Brillouin y que las fases topológicas son un fenómeno común de las ondas en materiales periódicos, incluso en ausencia de cuantización de la carga eléctrica. Su investigación planteó la hipótesis de la existencia de estados de borde electromagnético topológicamente protegidos dentro de estructuras dieléctricas periódicas 2D compuestas de elementos magnetoópticos que rompen la simetría de inversión del tiempo. Este concepto fue confirmado experimentalmente en 2009 con la observación de un cristal fotónico girotrópico que admite estados de luz quirales topológicamente protegidos. Esto ha abierto vías para estudiar análogos fotónicos de otras fases topológicas. Si bien los resultados se limitaron inicialmente a 2D, la comunidad investigadora ha comenzado a extender los conceptos topológicos a sistemas fotónicos 3D. Esta transición presentó nuevas oportunidades, que llevaron en 2015 a la primera observación experimental de puntos de Weyl, que representan monopolos topológicos en el espacio de

los momentos 3D. Esta fue la primera demostración experimental de los puntos de Weyl, aunque los estudios se remontan a *H. Weyl* en 1929. Estos resultados han sentado las bases para seguir avanzando en la exploración de fases topológicas con gap en 3D. Como mostraremos en esta tesis, los puntos de Weyl pueden verse como una fase intermedia sin gap, en la separación de dos fases distintas con bandas prohibidas topológicamente diferentes. Si bien el estudio de las fases topológicas magnéticas se limitó inicialmente a 2D, estos resultados sugirieron la posibilidad de extender su protección topológica a sistemas 3D con ruptura de simetría por inversión de tiempo.

Uno de los principales objetivos de esta tesis es introducir diseños de cristales fotónicos capaces de realizar fases topológicas de la luz, con un enfoque específico en la tridimensionalidad. Los cristales fotónicos tridimensionales son conceptualmente ricos y desafiantes porque ponen de manifiesto todas las propiedades vectoriales de la luz, lo que lleva a estimulantes desafíos físicos y matemáticos que surgen de la restricción de transversalidad de las ecuaciones de Maxwell. Propondremos el diseño de tres cristales fotónicos distintos que soportan tres fases topológicas distintas: el aislante fotónico 3D Chern; el aislante fotónico axion; y el semimetal fotónico con puntos Weyl desacoplados. Estas fases exhiben características únicas, como correspondencia bulk-boundary vectorial, loops cerrados de Fermi y estados de bisagra quirales, que no se habían propuesto previamente en cristales fotónicos 3D. Para abordar la topología en el electromagnetismo 3D, proponemos métodos de caracterización específicos tridimensionales, incluidos loops fotónicos vectoriales de Wilson y modelos de tight-binding transversales. Estos métodos nos permiten superar los desafíos teóricos asociados con la naturaleza vectorial de la luz y nos permiten modelar y caracterizar en detalle las propiedades topológicas de los sistemas fotónicos 3D. En esta tesis, también sugerimos posibles implementaciones para realizar estas fases topológicas, que incluyen paredes de dominio de cristales fotónicos, estructuras girotrópicas y emisores cuánticos acoplados a los cristales fotónicos. Nuestro objetivo es demostrar su potencial para aplicaciones en propagación de luz, detección de partículas de axiones, magneto-fotónica y simulaciones cuánticas. Estas contribuciones se dividen en tres capítulos principales, como sigue.

El capítulo "Fundamentals" proporciona una base concisa para comprender los cristales fotónicos, con un enfoque específico en tres dimensiones. Al describir los cristales fotónicos, adoptamos un enfoque basado en operadores para las ecuaciones de Maxwell, elegido porque permite una clasificación de las simetrías de los cristales fotónicos de una manera sencilla, al tiempo que resalta los aspectos vectoriales únicos

del espacio 3D. Comenzamos introduciendo relaciones constitutivas para materiales dieléctricos y exploramos las aproximaciones materiales esenciales que gobiernan la respuesta en cristales fotónicos. Estas relaciones son fundamentales para comprender todos los cristales fotónicos dieléctricos, que son el foco principal de esta tesis. Estas aproximaciones incluyen conceptos como linealidad, dispersión insignificante, aproximación hermitiana, ausencia de fuentes y el requisito de positividad del índice de refracción. Para hacer estos conceptos más tangibles, proporcionamos ejemplos del mundo real de materiales comúnmente utilizados en cristales fotónicos. Estos materiales ejemplifican materiales dieléctricos realistas que se adhieren a estas aproximaciones dentro de rangos de frecuencia específicos. Luego, introducimos la formulación del operador de las ecuaciones de Maxwell. Este enfoque nos permite describir ondas clásicas en cristales fotónicos utilizando el formalismo de la mecánica cuántica. Si bien destacamos similitudes y diferencias importantes entre estas dos descripciones, abordamos conceptos como la invariancia de escala, la naturaleza de valor real, vectorial y transversal de los campos electromagnéticos. Finalmente, exploramos la simetría y la topología en el contexto de los cristales fotónicos. Examinamos cómo la periodicidad de la red afecta las ondas electromagnéticas, dando lugar a bandas fotónicas, números de Chern electromagnéticos y un vórtice de polarización en 3D. Esto último está directamente relacionado con la restricción de transversalidad de las ecuaciones de Maxwell. Clasificamos cristales fotónicos topológicos en función de las simetrías de los materiales, en relación con las simetrías internas del tensor dieléctrico. Distinguimos dos simetrías de inversión temporal: una para materiales de tipo silicio y otra para materiales magnetoeléctricos. Introducimos la simetría de la dualidad electromagnética y su papel en esta clasificación. A partir de los principios fundamentales de la tabla periódica de aisladores topológicos, identificamos clases topológicas potenciales para bandas prohibidas fotónicas. Finalmente, incorporamos simetrías de grupos espaciales y analizamos los desafíos que surgen al caracterizar las propiedades de simetría de modos electromagnéticos en un cristal fotónico 3D en el límite de onda larga.

En el capítulo "Methods", presentamos técnicas de modelado y caracterización diseñadas para explorar la topología en cristales fotónicos tridimensionales. La naturaleza vectorial y transversal de la luz hace que determinar invariantes topológicas y desarrollar modelos analíticos 3D sea un desafío. Si bien muchos métodos topológicos se diseñaron para ondas escalares, requieren modificaciones para extenderlos a campos vectoriales en cristales fotónicos. Las condiciones de transversalidad impuestas por

las ecuaciones de Maxwell en materiales dieléctricos periódicos añaden complejidad al problema de Maxwell, a diferencia de otras ondas 3D clásicas. Una razón principal es el comportamiento no analítico de los estados fotónicos en toda la zona de Brillouin en el límite de energía cero, atribuido al obstáculo del punto Γ. Esta característica dificulta la construcción de modelos de tight-binding válidos en toda la zona de Brillouin y dificulta la evaluación de invariantes topológicos, que se definen de forma no local en el espacio de los momentos 3D. Para diseñar y analizar eficazmente las fases topológicas 3D de la luz, pretendemos desarrollar métodos de caracterización adecuados para abordar y resolver estos desafíos específicos. El contenido de este capítulo se divide en dos secciones.

En la sección titulada “Electromagnetic vectorial Wilson loops”, describimos la utilidad de los loops vectoriales electromagnéticos de Wilson y los centros de energía híbridos de Wannier para el análisis topológico en cristales fotónicos. Se pone énfasis en los cristales fotónicos 3D, destacando la naturaleza vectorial y transversal de la luz. La sección extrae metodologías del "Tutorial: Computación de invariantes topológicas en cristales fotónicos 2D" ([1]), y las adapta al contexto 3D. La complejidad de las ondas electromagnéticas 3D, distintas de sus análogos escalares 2D, requiere ajustes específicos para la caracterización topológica. Proporcionamos orientación práctica para calcular invariantes topológicas exclusivas de los cristales fotónicos 3D, como la carga puntual de Weyl, el vector de Chern, el ángulo del axión magnetoeléctrico y la carga monopolo de pared nodal de Weyl. Estas invariantes se aclaran a través de ejemplos de cristales fotónicos 3D. Establecemos los loops electromagnéticos de Wilson como una herramienta poderosa para discernir varios invariantes topológicos 3D, destacando su adaptabilidad a múltiples estructuras fotónicas. La sección culmina con un tutorial para estos cálculos, exponiendo el potencial expansivo del método. Por ejemplo, es potencialmente aplicable para discernir el brading de links nodales fotónicos de multigap y para detectar una topología frágil dentro del gap fundamental de un cristal fotónico 3D, lo que indica su solidez para los cálculos avanzados de topología cuántica y la exploración de nuevas fases fotónicas.

En la sección titulada "Transversality enforced tight binding models", presentamos una extensión innovadora del enfoque de tight-binding a cristales fotónicos tridimensionales, un método tradicionalmente empleado en física del estado sólido para describir la estructura de bandas y las características topológicas de un cristal con un conjunto mínimo de parámetros. Este método de tight-binding, que llamamos tight-binding transversal, está diseñado para superar los desafíos asociados con la simetría

irregular de los estados de frecuencia cero y la naturaleza vectorial y transversal de las ecuaciones de Maxwell que han dificultado la construcción de funciones de base de tight-binding localizadas al máximo en cristales fotónicos 3D. El modelo resultante no solo aborda la obstrucción electromagnética del punto Γ, que surge de la restricción de transversalidad de Maxwell, sino que también reproduce con precisión la simetría, topología y dispersión de energía de las bandas transversales a lo largo de la zona de Brillouin. Demostramos las ventajas computacionales de este método, que permite la simulación de sistemas complejos más allá de la capacidad de los actuales clústeres informáticos de alto rendimiento. La eficacia del modelo se ejemplifica en la simulación de respuestas de topología de orden superior en aisladores fotónicos de axiones y en la extracción del número de capas de Chern en losas de cristales fotónicos. Además, una extensión magnética de nuestro modelo ilustra su utilidad en el modelado de girotropía mediante un acoplamiento no mínimo, mostrando una reducción significativa en los recursos computacionales en comparación con los métodos de resolución exacta de las ecuaciones cristalinas de Maxwell. Las implicaciones prácticas de este progreso son profundas y ofrecen un marco teórico para sondear las respuestas límite de las fases topológicas fotónicas 3D emergentes. Además de su eficiencia computacional, la capacidad de disponer de una expresión matemática simplificada para un modelo eficaz del cristal puede mejorar los estudios analíticos en la comprensión del cristal, entendido como entorno, en el estudio de la dinámica entre emisores cuánticos acoplados a cristales fotónicos. Hasta donde sabemos, esto representa el primer método capaz de proporcionar una representación tight-binding confiable de estructuras periódicas dieléctricas 3D, en toda la zona de Brillouin 3D, lo que marca un paso fundamental en el estudio de la fotónica topológica. Esperamos que el método contribuya significativamente a la exploración de estados límite en futuras fases topológicas fotónicas 3D.

En el capítulo "Results", diseñamos tres cristales fotónicos tridimensionales diferentes, cada uno de los cuales manifiesta una fase topológica específica: un aislante fotónico Chern tridimensional, un aislante fotónico axión y un semimetal Weyl de pared nodal caracterizado por puntos fotónicos Weyl aislados. Estas fases se distinguen por sus características de bulk-boundary, que incluyen correspondencia vectorial de bulk-boundary, loops cerrados de Fermi y estados de bisagra quirales. Describimos las características topológicas de estos cristales fotónicos 3D empleando las metodologías descritas en el capítulo anterior. Esto incluye la aplicación de loops electromagnéticos de Wilson y el modelo transversal de tight-binding, ambos diseñados

específicamente para abordar los desafíos que presentan los sistemas de ondas electromagnéticas dentro de cristales fotónicos 3D. Estas fases topológicas tridimensionales están concebidas dentro de estructuras dieléctricas periódicas. Para estudiar fases invariantes con simetría de inversión del tiempo, consideramos materiales isotrópicos con alta constante dieléctrica. En el contexto de los fenómenos magnéticos, utilizamos medios girotrópicos, cuyos parámetros están en línea con implementaciones tecnológicas realistas de microondas.

En esta sección "3D Chern photonic insulator", presentamos el diseño y la base teórica de una fase topológica tridimensional conocida como aislante fotónico de Chern tridimensional, que se distingue por un vector de Chern compuesto por un triplete de números de Chern. A través de la aniquilación de puntos de Weyl, podemos determinar el valor, la orientación y el signo del vector de Chern, lo que lleva a fases con números de Chern altos, protección topológica en condiciones magnéticas bajas y orientabilidad del vector de Chern. Estas características se manifiestan en la presencia de un número finito de loops de Fermi cerrados en el toro de la zona de Brillouin de la superficie, que actúan como indicadores de la correspondencia bulk-boundary del aislante 3D Chern. La evolución de estos loops desde los arcos abiertos de Fermi de la fase semimetálica de Weyl, durante la transición a un estado con gap, revela una correspondencia bulk-boundary vectorial única que está influenciada por la orientación del vector Chern a través de paredes de dominio con diferentes Chern. Nuestro enfoque permite aisladores Chern 3D con nuevos atributos: números elevados de Chern que facilitan la propagación multimodal de estados topológicos de la superficie, requisitos magnéticos reducidos y la capacidad de dirigir el vector Chern cambiando la dirección de magnetización. Esto proporciona un marco versátil para interconectar diferentes aisladores de Chern 3D, lo que lleva a una variedad de estados de superficie dependiendo de la orientación del vector de Chern. En particular, describimos la relación entre el vector de Chern y el winding de los loops de Fermi en la superficie, estableciendo una correspondencia completa entre el vector y el límite para estos sistemas fotónicos. Además, discutimos las implicaciones de nuestros resultados para el diseño de láseres topológicos y el potencial para manipular modos de superficie unidireccionales en aplicaciones fotónicas. También destacamos la menor necesidad de respuestas magnéticas fuertes, lo que amplía el alcance de los materiales que pueden usarse para fabricaciones experimentales de aisladores topológicos fotónicos 3D. Este trabajo sienta las bases para una mayor exploración y desarrollo en el campo de la fotónica topológica. El potencial fotónico equivalente de un acoplador magnetoeléctrico, que utiliza un setup

3D con vectores Chern que apuntan hacia adentro, presenta un diseño intrigante aún por realizar, que dejamos abierto para investigaciones posteriores.

La sección "Photonic axion insulator" presenta un nuevo enfoque para crear una topología similar a un axión dentro de cristales fotónicos de Weyl en 3D. Al integrar obstrucciones de fase en la modulación de la supercélula de los elementos dieléctricos de los cristales fotónicos con simetría de inversión, unimos estados quirales de propagación de luz en bisagras que están correlacionadas con inversión, lo que conduce a la formación de un canal de luz de axión quiral. Estos canales están integrados dentro de una estructura dieléctrica 3D, lo que los hace resistentes a la radiación en el continuo electromagnético. La clave de nuestro método es la cuantización del ángulo de axión, que se logra mediante la creación de paredes de dominio entre estos cristales fotónicos. También demostramos que al aplicar un campo magnético externo débil, podemos manipular las propiedades girotrópicas del cristal fotónico, manipulando efectivamente los diferentes modos de las fibras fotónicas quirales unidimensionales. Este proceso allana el camino para el control dinámico de los modos de axión y sienta las bases para dispositivos fotónicos controlables magnéticamente. Nuestro diseño representa un aislante topológico de orden superior, con estados de bisagra quirales, con aplicaciones prácticas en tecnología fotónica, mejorando potencialmente la eficiencia y versatilidad del control de la propagación de la luz en comunicaciones y dispositivos ópticos. La siguiente fase de la investigación se centrará en introducir respuestas dinámicas dentro del cristal fotónico del axión. La obtención de un axión dinámico en un cristal fotónico podría ayudar a unificar diferentes enfoques para la detección de materia oscura y contribuir a una mejor comprensión del acoplamiento axión-fotón.

La sección “Unpaired Weyl 3D PhC” propone un nuevo diseño para un cristal fotónico con una característica distintiva: un punto Weyl aislado con una alta carga monopolo ubicado en el punto Γ. Este punto está estabilizado por una pared nodal absorbente en el límite de la zona cúbica de Brillouin. El diseño se diferencia de los sistemas Weyl tradicionales con configuraciones dipolares, sin la correspondiente carga opuesta. El sistema se diseña seleccionando grupos espaciales con simetrías rotacionales capaces de estabilizar una pared nodal en el límite de la zona de Brillouin. El aislamiento y la naturaleza topológica del punto Weyl aislado lo convierten en una plataforma prometedora para el acoplamiento con emisores cuánticos, mejorando potencialmente las interacciones entre ellos debido al entorno del cristal, un notable paso adelante con respecto a lo que se puede lograr con los emisores cuánticos acoplado a los sistemas Weyl dipolares tradicionales. Los resultados iniciales sugieren que es-

tos cristales fotónicos podrían redefinir la comprensión actual de la correspondencia bulk-boundary y las superficies de Fermi, ya que las paredes nodales pueden impedir la existencia de secciones con gap de la zona de Brillouin.

En conclusión, esta tesis examina la teoría de bandas topológicas para ondas electromagnéticas en cristales fotónicos, proporcionando conocimientos y metodologías adaptadas al 3D. A través del desarrollo de técnicas de caracterización, hemos abordado los retos que presenta el carácter vectorial y transversal de la luz. Propusimos diseños realistas para implementar fases topológicas de luz 3D en cristales fotónicos, estableciendo una conexión entre formulaciones teóricas y aplicaciones potenciales. Este trabajo quiere abordar algunas preguntas abiertas y áreas aún por explorar. La búsqueda de bandas planas 3D, la interacción de topologías frágiles con la singularidad Γ y las implicaciones de la dualidad electromagnética para la protección topológica 3D son áreas notables para una mayor investigación. Esperamos que esta tesis pueda proporcionar una comprensión más profunda del electromagnetismo 3D y ofrecer las herramientas que conduzcan a mayores avances en la exploración de los cristales fotónicos topológicos.

Abstract

The concept of topology has revolutionized our understanding of condensed matter physics, leading to the discovery of novel electronic phases and the emergence of topological materials. In recent years, this concept has been extended to the field of photonics, where it has led to the design of a new class of materials known as topological photonic crystals. These materials possess nontrivial topological properties that can lead to unique and robust light propagation phenomena. This thesis presents a comprehensive study of 3D topological photonic crystals, with a focus on the discovery of novel topological phases and the development of new methods for their characterization and design. The main contributions of this work are the proposal and investigation of 3D topological photonic phases, which include: the 3D Chern photonic insulator; the axion photonic insulator; and the 3D Weyl semimetal with unpaired photonic Weyl points. These phases exhibit unique features, such as vectorial bulk-boundary correspondence, closed Fermi loops, chiral hinge channels, and forbidden surface Fermi arcs, which have not been proposed before in 3D photonic crystals. To approach topology in 3D electromagnetism, we propose dimension-specific characterization methods, including vectorial photonic Wilson loops and transversality-enforced tight-binding models. These methods allow us to overcome the theoretical challenges associated with the vectorial nature of light, and permit us to model and characterize the topological properties of 3D photonic systems in detail. Throughout this thesis, we also suggest possible implementations to realize these topological phases, which include PhC domain walls, gyrotropic structures, and quantum emitters coupled to PhCs. Our goal is to demonstrate their potential for applications in guided-light communication, optical switching, particle detection, magneto-photonics, and quantum simulations. Overall, this work aims to contribute to a deeper understanding of topological phenomena in 3D electromagnetism and proposes novel investigation methods and possible applications. We hope that the tools and designs developed in this thesis can be used as a starting point to realize these topological phases in real-world photonic devices.

Contents

Resumen **1**

Abstract **9**

List of abbreviations **16**

Publications **17**

1 Introduction **19**

1.1 Integration of Topological Concepts into Photonics 19
1.2 Photonic Crystals in a Nutshell 20
1.3 Periodic Table of Topological PhCs 21
1.4 Realizing Elusive Topological Phases via PhCs 22
1.5 Aim of This Thesis: Targeting Topological Phases of 3D PhCs 23
1.6 General Outline 24

2 Fundamentals **26**

2.1 Constitutive Relations and Material Approximations 27
2.1.1 Linear approximation 28
2.1.2 Non-dispersive approximation 29
2.1.3 Hermitian approximation 30
2.1.4 Positive index approximation 30
2.1.5 Media satisfying previous assumptions 31
2.1.6 Source-free approximation 32
2.2 Operator-Form of Maxwell Equations 32
2.2.0.1 Dynamical equations 33
2.2.0.2 Divergence-free conditions 34
2.2.1 Electromagnetic observables 34

2.2.2 Frequency domain . . . 35
2.2.3 Energy scalar product . . . 36
2.2.4 Scale invariance of Maxwell equations . . . 37
2.2.5 Complex waves . . . 38
2.2.6 Non-negative frequency waves . . . 39
2.2.7 Photonic particle-hole redundancy . . . 39
2.2.8 Longitudinal and transversal waves . . . 40
2.2.9 Quadratic/linear Maxwell formulation . . . 41
2.3 Symmetry and Topology in PhCs . . . 42
2.3.1 Discrete translational symmetry . . . 43
2.3.1.1 Bloch theory of photonic bands . . . 44
2.3.1.2 Electromagnetic Chern numbers . . . 45
2.3.1.3 Gamma singularity . . . 46
2.3.1.4 TM and TE polarizations . . . 48
2.3.2 Symmetry Classification of Topological PhCs . . . 50
2.3.2.1 Dielectric or material symmetries . . . 51
2.3.2.2 Admissible symmetries in PhCs . . . 53
2.3.2.3 Even time reversal symmetry . . . 53
2.3.2.4 T_3 for real-valued media . . . 54
2.3.2.5 T_1 for magneto-electric coupling . . . 55
2.3.2.6 Electromagnetic duality . . . 56
2.3.2.7 Reduced periodic table of PhCs . . . 57
2.3.2.8 Bulk-boundary correspondence . . . 59
2.3.3 Space-Group Symmetries . . . 59
2.3.3.1 Irrep characterization of photonic modes . . . 60
2.3.3.2 Ill-defined symmetry content at zero-energy . . . 61

3 Methods **62**
3.1 Computing Topological Invariants in *3D* PhC . . . 63
3.1.1 Electromagnetic Wilson Loops . . . 64
3.1.1.1 Discrete Limit . . . 64
3.1.1.2 Gauge Invariance and Band Projectors . . . 65
3.1.1.3 Spectral Properties . . . 65
3.1.1.4 Hybrid Wannier Centers . . . 66
3.1.1.5 Chern Number: Flow of hybrid Wannier centers . . . 67
3.1.2 Numerical Implementation . . . 68

3.1.2.1 Overlap Matrices for Vector Fields 68
3.1.2.2 Componentwise Gauge Fixing 69
3.1.2.3 Polarization Vortex and Wilson Loops 70
3.1.3 Γ-Avoiding Section Chern Number 71
3.1.3.1 Discontinuities at Weyl Nodes 72
3.1.4 Γ-Encircling Wilson Loops 74
3.1.5 Layer Chern Numbers via 3D Effective Models 76
3.1.6 Discussion and outlook 77
3.2 Transversality-Enforced Tight-Binding Models 77
3.2.1 Obstructions to 3D Photonic TB Models 78
3.2.2 Selecting Pseudo-Orbitals Candidates 80
3.2.2.1 Transverse symmetry vector 80
3.2.2.2 Infinite Pseudo Orbital Solutions 81
3.2.2.3 Minimization of the TB Basis 82
3.2.2.4 Negative EBR Coefficients 83
3.2.3 Constructing a Photonic TETB 84
3.2.3.1 Quadratic Mapping and Spectral Filtering 84
3.2.3.2 Enforcing Transversality 84
3.2.3.3 Introduction of a magnetic field perturbation 85
3.2.4 Discussion and outlook 86

4 Results **88**
4.1 3D Chern Photonic Insulator 90
4.1.1 Introduction 90
4.1.2 Initial setup 92
4.1.2.1 Weyl points formation 92
4.1.2.2 Topological charge of photonic Weyl points 93
4.1.2.3 Weyl points annihilation 95
4.1.3 Engineering of the 3D CI gap and its Chern vector 96
4.1.3.1 Three-step procedure 96
4.1.3.2 Cubic 3D CI 97
4.1.3.3 Topological characterization 98
4.1.3.4 Magnetic bias reduction 99
4.1.3.5 Arbitrarily large Chern vectors 101
4.1.4 Surface characterization 102
4.1.4.1 Trivial/Topological domain wall 102

4.1.4.2 Anomalous Hall surface states . . . 103
4.1.4.3 Evolution of FAs into loops . . . 105
4.1.5 Vectorial bulk boundary correspondence . . . 107
4.1.5.1 Orientable Chern vectors . . . 108
4.1.5.2 Domain-wall planar interfaces . . . 108
4.1.5.3 Case C_zI/C_zI . . . 109
4.1.5.4 Case C_xI/C_zI . . . 110
4.1.5.5 Case C_yI/C_zI . . . 112
4.1.5.6 Topology of Fermi loops and vBBC . . . 113
4.1.6 Discussion and outlook . . . 116
4.2 Photonic Axion Insulator . . . 118
4.2.1 Inversion-symmetry pinning . . . 120
4.2.2 Transversality-enforced TB for the *r*AXI . . . 121
4.2.2.1 Gyrotropy . . . 126
4.2.2.2 Supercell modulation . . . 127
4.2.2.3 Magnetic symmetry-indicators . . . 129
4.2.3 Topological characterization . . . 130
4.2.4 Relative AXI domain walls . . . 131
4.2.5 Chiral hinge states . . . 133
4.2.6 Discussion and outlook . . . 135
4.3 Unpaired Photonic Weyl Semimetal . . . 137
4.3.1 Introduction . . . 137
4.3.2 Design strategy: triply periodic structures . . . 138
4.3.3 Nodal wall and unpaired photonic Weyl . . . 140
4.3.4 Topological characterization . . . 141
4.3.5 Discussion and outlook . . . 142

5 Conclusions **144**
5.1 Modeling and Characterization of 3D PhCs . . . 144
5.2 Design and Applications of 3D Topological PhCs . . . 145
5.3 3D Phases of Light Beyond This Thesis . . . 147

Appendix **149**

A Method of Invariants for coupled Weyl points **150**
A.1 Weyl Dipole Formation . . . 150

A.2 Coupling of Weyl points 154
A.2.1 Gap opening by supercell modulations 157
A.2.2 Case $N = N_W > 2$ 159

B Transversality Enforced Tight Binding Model 160
B.1 Transverse Symmetry Vector 160
B.1.1 Transverse bundling: Example in SG No. 224 161
B.2 Non-Minimal Pseudo-Orbital Choice 161
B.2.1 Non-minimal orbital choice: example in SG No. 224 162
B.3 Minimizing the Number of Longitudinal Modes 162
B.3.1 Γ-reduction 163
B.3.2 Multiple solutions 164
B.3.3 Physicality constraint 164
B.3.4 Unphysical orbital choice: example in SG No. 224 165
B.3.5 Minimal orbital choice: example in SG No. 224 166

C Photonic 3D CIs: Generalizations 167
C.1 Bulk Topological Properties 167
C.1.1 Robustness of the topological gap 167
C.1.2 Minimizing the magnetic bias 168
C.1.3 Higher Chern numbers on multi-fold supercells N>2 170
C.1.4 Uniaxial vs cubic supercell modulation 170
C.1.5 Weyl dipole tilted from the Cartesian directions 172
C.2 Surface Topological Properties 172
C.2.1 Winding and symmetries of the Fermi Loops 172
C.2.2 Diagonal Chern vector orientation 173

D Magnetic Properties of the Photonic Axion Insulator 175
D.1 Bulk Symmetry Properties 175
D.1.1 TETB Hamiltonian for the magnetic Weyl phase 175
D.1.2 Magnetic space group analysis 176
D.1.2.1 Case with $|h| = 0$ 179
D.1.2.2 Case with $0 < |h| << |H_z|$ 181
D.2 Domain-Wall and Rod Configurations 182
D.2.1 Gapless Dirac cone on the $x = 0$ plane 182
D.2.2 Magnetic control of the surface gap 183

D.2.3 Topological transition between hinge states 183
D.2.4 Relative phase difference 185

List of abbreviations

AXI	Axion Insulator
BZ	Brillouin Zone
CDW	Charge Density Wave
CI	Chern Insulator
FA	Fermi Arc
FL	Fermi Loop
HWEC	Hybrid Wannier Energy Centers
HOTI	Higher Order Topological Insulator
MLWF	Maximally Localized Wannier Function
PhC	Photonic Crystal
QE	Quantum Emitter
RSI	Real Space Invariants
sBBC	Scalar Bulk Boundary Correspondence
SI	Symmetry Indicators
TB	Tight Binding
TETB	Transversality Enforced Tight Binding
TI	Topological Insulator
TPS	Triply Periodic Surface
TRS	Time Reversal Symmetry
TQC	Topological Quantum Chemistry
UPhW	Unpaired Photonic Weyl
vBBC	Vectorial Bulk Boundary Correspondence
WL	Wilson Loop
WNW	Weyl Nodal Wall
WS	Weyl Semimetal

List of related publications

3D Chern Insulators and Weyl Semimetals in PhCs

1. Devescovi C, García-Díez M, Robredo I, Blanco de Paz M, Lasa-Alonso J, Bradlyn B, Mañes JL, G. Vergniory M, García-Etxarri A. “Cubic 3D Chern photonic insulators with orientable large Chern vectors". *Nature communications*. 2021 Dec 17;12(1):7330.

2. Devescovi C, García-Díez M, Bradlyn B, Mañes JL, Vergniory MG, García-Etxarri A. “Vectorial Bulk-Boundary Correspondence for 3D Photonic Chern Insulators." *Advanced Optical Materials*. 2022 Oct;10(20):2200475.

3. Nguyen DH, Devescovi C, Nguyen DX, Nguyen HS, Bercioux D. “Fermi arc reconstruction in synthetic photonic lattice." *Physical Review Letters*. 2023 Aug 3;131(5):053602.

Axion Topology in PhCs

4. Devescovi C*,Morales-Pérez A*, Hwang Y, García-Díez M, Robredo I, Mañes JL, Bradlyn B, García-Etxarri A, Vergniory MG. “Axion Topology in Photonic Crystal Domain Walls". *preprint arXiv:2305.19805*. 2023 May 31.

Modeling/Characterization Methods for Topological PhCs:

5. Morales-Pérez A*, Devescovi C*, Hwang Y, García-Díez M, Bradlyn B, Mañes JL, Vergniory MG, García-Etxarri A. “Transversality-Enforced Tight-Binding Model for 3D Photonic Crystals aided by Topological Quantum Chemistry". *preprint arXiv:2305.18257*. 2023 May 29.

6. Blanco de Paz M, Devescovi C, Giedke G, Saenz JJ, Vergniory MG, Bradlyn B, Bercioux D, García-Etxarri A. “Tutorial: computing topological invariants in 2D photonic crystals". *Advanced Quantum Technologies*. 2020 Feb;3(2):1900117.

Electromagnetic Duality

7. Lasa-Alonso J, Olmos-Trigo J, Devescovi C, Hernández P, García-Etxarri A, Molina-Terriza G. “Resonant helicity mixing of electromagnetic waves propagating through matter". *Physical Review Research*. 2023 May 24;5(2):023116.

8. Lasa-Alonso J, Devescovi C, Maciel-Escudero C, García-Etxarri A, Molina-Terriza G. “On the origin of the Kerker phenomena". *preprint arXiv:2306.12762*. 2023 Jun 22.

Chapter 1

Introduction

1.1 Integration of Topological Concepts into Photonics

Topological Photonic Crystals (PhCs) represent a convergence of two significant areas of research: photonics and topological materials. PhCs emerged in the late 1980s as researchers began to explore periodic dielectric structures that could manipulate the propagation of electromagnetic waves. PhCs were initially proposed by *S. John [2]* and *E. Yablonovitch [3]*, which later led to the conceptualization of the photonic bandgap [4, 5]—a specific frequency range where electromagnetic wave propagation is forbidden. The integration of topological concepts into photonic systems began in earnest with the discovery of topological properties in electronic systems. While the integer quantum Hall effect of the 1980s had already showcased a 2D electron gas with quantized Hall conductance [6] rooted in topological invariants like the Chern number [7,8], it was *S. Raghu and F.D.M. Haldane*'s insightful observation [9,10] spotlighted the potential of replicating these effects in photonic structures. Specifically, they elucidated how topological quantization could arise from the global properties of wave functions across the Brillouin zone, and that topological phases are a common phenomenon of waves in periodic media, even in the absence of an electric charge quantum. Their research posited the existence of topologically protected electromagnetic edge states within 2D periodic dielectric structures composed of magneto-optical elements breaking time-reversal symmetry (TRS). This concept was experimentally corroborated in 2009 [11] with the observation of a gyrotropic PhC supporting topologically protected chiral edge states of light. This realization opened up avenues for the study of photonic analogs of other topological phases. While these results were initially limited to 2D, the research community began to extend topological concepts to 3D photonic

systems. This transition presented new opportunities, leading in 2015 to the first experimental observation of Weyl points, which represent topological monopoles in the 3D momentum space [12, 13]. This was the first experimental demonstration of Weyl points, despite the studies dating back to *H. Weyl* in 1929 [14]. Such demonstrations were remarkable results as they laid the groundwork for further advances in the exploration of topological gapped phases in 3D. As we will show in this thesis, Weyl points can be viewed as an intermediate topological gapless phase between topologically distinct bandgaps [15]. While the study of strongly gapped magnetic topological phases was initially limited to 2D, these results suggested the possibility of extending their topological protection to 3D systems with broken TRS. One of the main objectives of this thesis is to introduce realistic PhC designs capable of realizing gapped strong-topological phases for light, with a focus on 3D. As well, we aim to develop dimension-specific characterization methods tailored to address the challenges arising from the vectorial and transversal nature of light.

1.2 Photonic Crystals in a Nutshell

PhCs are a specific class of optical materials that consist of a periodic arrangement of dielectric elements, alternating between regions of higher and lower refractive indices. Specifically, in a PhC, the dielectric (susceptibility) tensor $\mathcal{K}(\mathbf{r})$ displays spatial periodicity:

$$\mathcal{K}(\mathbf{r}) = \mathcal{K}(\mathbf{r} + \mathbf{R}),$$

with $\mathbf{R}$ being a lattice vector. The periodicity in the PhC's structure results in the Bragg interference of electromagnetic waves, which in turn, alters the dispersion properties of photonic modes [16, 17]. To comprehend the optical properties of PhCs, a perspective from momentum-space is frequently adopted. As we will detail in the following chapter, in this representation, the two dynamic Maxwell equations (comprising Faraday's and Ampere's laws) can be recast in a Bloch-like form using the Maxwell operator ($\mathcal{M}(\mathbf{k})$), thereby enabling the formulation of a Bloch eigenproblem:

$$\mathcal{M}(\mathbf{k})u_{n,\mathbf{k}}(\mathbf{s}) = \omega_n(\mathbf{k})u_{n,\mathbf{k}}(\mathbf{s}),$$

where $\omega_n(\mathbf{k})$ are electromagnetic bands and $u_{n,\mathbf{k}}(\mathbf{s})$ are Bloch periodic electromagnetic modes. In such a description, concepts from Bloch and topological band theories, commonly applied in condensed matter physics, find direct application in the field of

PhCs [18–21]. Nevertheless, it is important to note that the other pair of Maxwell equations —source-free magnetic and electric Gauss's laws— impose further geometrical constraints on the polarization of Bloch modes. In momentum-space representation, these conditions can be compactly written as:

$$\mathrm{Div}(\mathbf{k})\left[\mathcal{K}(\mathbf{s})u_{n,\mathbf{k}}(\mathbf{s})\right] = 0$$

where $\mathrm{Div}(\mathbf{k})$ is a divergence operator in momentum-space representation. As we will see in **Chapter 3** this constraint leads to a distinct, vortex-like, singularity at the zero-energy limit within the Brillouin zone's origin for the electromagnetic modes present in all-dielectric periodic media in 3D [22]. This singularity necessitates specialized treatment for the application of conventional topological band theory. Intriguingly, this singularity can also give rise to unique 3D electromagnetic topologies, exemplified by the Γ-enforced topology underlying the recent discovery of topological "non-gaps" in 3D PhCs [23]. Accompanying this is the non-analyticity of the Bloch basis in 3D momentum space and the challenge of forming a basis of exponentially localized states, thus making 3D PhCs a conceptually challenging but stimulating field of study.

1.3 Periodic Table of Topological PhCs

As we have mentioned, the spatial variation of the dielectric function in PhCs can lead to photonic bandgaps, which are specific frequency intervals where light propagation is inhibited. The topology of these bandgaps can be systematically classified using the Cartan-Altland-Zirnbauer (CAZ) scheme [24, 25] into distinct topological classes, each characterized by specific topological invariants. The nature and number of these topological invariants depend on both the symmetries of the Maxwell operator ($\mathcal{M}(\mathbf{k})$) and the spatial dimension of the PhC (d). As we will detail in **Chapter 2**, in PhCs, the Maxwell operator recognizes two types of even (bosonic) TRS of the CAZ type, T_1 and T_3. Magneto-electric media are characterized by T_1, while real-valued dielectric materials of the silicon type pertain to T_3. The combination of these two symmetries results in the electro-magnetic duality symmetry (U_2), a natural symmetry of the vacuum [26, 27]. Based on the symmetries of the gapped Maxwell operator, the classification outlines four distinct topological classes, summarized in **Table 1.1**.

Media	Symmetries	Class	$d=1$	$d=2$	$d=3$	$d=4$
Gyrotropic	None	A	0	(1st) $\mathbb{Z}$	(1st) $\mathbb{Z}^3$	(1st) $\mathbb{Z}^6 \oplus$ (2nd) $\mathbb{Z}$
Silicon-type	T_3	AI	0	0	0	(2nd) $\mathbb{Z}$
Magneto-electric	T_1	AI	0	0	0	(2nd) $\mathbb{Z}$
EM Dual	T_3, T_1, U_2	AI $\oplus$ AI	0	0	0	(2nd) $\mathbb{Z}^2$

Table 1.1: Topological classification of dielectric media in the CAZ scheme [28, 29]. Topologically trivial is indicated by zero. 1st and 2nd labels stand for first and second Chern number, respectively. The notation $\mathbb{Z}^n$ indicates the existence of n independent Chern numbers, each for each lower dimensional manifold of the d dimensional space. T_1 and T_3 are bosonic time-reversal symmetry operations. Their product is associated the electromagnetic duality $U_2 = -iT_1T_3$. In the absence of additional symmetries beyond those of the CAZ scheme, strong topology is only achievable in $d \leq 3$.

As shown, for spatial dimensions $d \leq 3$, strong topology in PhC is limited to class A with broken TRS. Incorporating spatial symmetries into topological classification permits the definition of crystalline topological invariants that go beyond the predictions of the CAZ scheme. This facilitates the realization of other symmetry-protected topological phases, even in the presence of TRS [30–35], laying the foundation for silicon-based topological PhCs. Topological PhCs have found widespread applications across various optical devices [18–21], enabling robust and controllable manipulation of light. These applications encompass topological waveguides, lasers, and components for optical communication, ultimately enhancing the performance of photonic technologies.

1.4 Realizing Elusive Topological Phases via PhCs

Beyond their applicative interest, topological PhCs also present a valuable platform for the theoretical exploration of numerous topological phases, often challenging to replicate in electronic counterparts. This is attributed to several pivotal reasons:

- **Tailored Design** - Unlike electronic systems that depend on natural crystal structures, PhCs represent a very versatile platform offering precise custom design capabilities and thus control on their symmetry properties [18, 19]. This allows the investigation and realization of topological phases that are not naturally occurring in electronic materials [36].

- **Extended Symmetries** - While PhCs may lack specific symmetries found in electronic systems (e.g., charge-conjugation [37]), they introduce unique electromagnetic symmetries, such as duality, broadening the spectrum for classifying topological phases [38, 39].

- **3D and Vectorial Properties** - Photonics enable vectorial topological effects, either stemming from light polarization [40] or from 3D spatial variation of the dielectric tensor [41]. The intrinsic 3D nature of electromagnetic fields structures further enriches the scope of topological physics, leading, as we will see, to vectorial bulk-boundary correspondence [42], a largely unexplored concept in (layered) condensed matter systems.

- **Bosonic Nature of Photons**: Unlike electrons, photons are bosonic in nature, which can simplify the realization of certain phases tough to observe in electronic systems. In the context of multi-gap topologies, the lack of a concept of band filling renders the entire photon spectrum accessible, unlike in fermions where only nodes near the Fermi level are probed, facilitating topological band-nodes braiding. Furthermore, the absence of intrinsic spin-orbit interactions in PhCs facilitates the manifestation of nodal phases, which can be fragile in electronic context [43, 44] (Sec. 4.3).

These unique features establish PhCs as a versatile playground for the implementation and study of several elusive topological phases.

1.5 Aim of This Thesis: Targeting Topological Phases of 3D PhCs

One of the main objectives of this thesis is to introduce PhC designs capable of realizing topological phases for light, with a specific focus on 3D. In 3D PhCs, the existence of a bandgap ensures light confinement along all spatial dimensions, in contrast to 2D PhCs which only prevent light propagation within the crystal's plane. 3D PhCs are conceptually rich and stimulating because the full vectorial properties of light are rendered manifest, leading to stimulating physical and mathematical challenges arising from the transversality constraint of Maxwell equations. We will explore design possibilities both within and beyond the CAZ framework. Within the CAZ scheme, we will propose a possible implementation of the photonic 3D Chern insulating state **Section 4.1**, a topological phase characterized by three first Chern invariants - or a Chern vector $\mathbf{C} = (C_x, C_y, C_z)$ - [45–50] in class A, and study its vectorial bulk-boundary correspondence. Beyond the CAZ framework, we will investigate the inversion-symmetric photonic axion insulator **Section 4.2**, also in class A, but featuring a bulk-hinge correspondence distinct from the CAZ counterparts [48, 51–57, 57–59, 59–68]. Finally, we

will outline the design of a nodal 3D PhC where the entire boundary of the Brillouin zone is an absorbing topological nodal wall **Section 4.3**. This 3D phase is situated in class AI, but strictly falls outside the CAZ scheme, due to the absence of a spectral gap and the inclusion of crystalline symmetries.

To effectively design and analyze 3D topological phases of light, we intend to develop dimension-specific characterization methods tailored to address the challenges arising from the vectorial nature of light in 3D.

1.6 General Outline

The content of this thesis is divided as follows:

- **Fundamentals** (**Chapter 2**): We review fundamental ideas in topological photonics, with a focus on 3D, including the concept of transverse photonic bands, electromagnetic Chern numbers, and the Γ-point obstruction in 3D. In the same chapter, we state essential material approximations governing the electromagnetic response in all-dielectric PhCs, which are the primary focus of this text.

- **Methods** (**Chapter 3**). We develop dimension-specific modeling and topological characterization methods tailored to address the challenges arising from the vectorial nature of light in 3D. These include transversality-enforced tight-binding models and electromagnetic Wilson loops in 3D. In the same chapter, we provide a tutorial for computing various topological invariants of 3D PhC. These include the axion angle, the Chern vector, and the Weyl charge of topological nodal walls.

- **Results** (**Chapter 4**). We propose the design of three distinct 3D PhC topological phases: the 3D Chern photonic insulator, the photonic axion insulator, and the nodal-wall Weyl semimetal featuring unpaired photonic Weyl points. These phases exhibit unique bulk-boundary properties, including vectorial bulk-boundary correspondence, closed Fermi loops, chiral hinge channels, and forbidden surface Fermi arcs.

- **Conclusions** (**Chapter 5**). We offer an outlook on potential research avenues based on the designs presented. For each topological phase, we touch upon potential applications. These applications range from magnetic switching of light, unidirectional light propagation, manipulation of quantum emitter interactions,

and particle detection. Furthermore, we highlight how to use the developed modeling and characterization methods for crafting novel PhC designs, leveraging on symmetry and topological properties not discussed in this thesis.

- **Appendix**. We discuss electromagnetic boundary conditions, transversality, and physicality constraints, as well as providing a perturbative expansion of the Maxwell operator suited for photonic Weyl points.

Chapter 2

Fundamentals

This chapter provides a concise foundation for comprehending PhCs, with a specific focus on three dimensions (3D). In the description of PhCs, we will adapt an operator-based approach to Maxwell's equations, first introduced in Ref. [69, 70]. This formulation is slightly different from, though equivalent, those traditionally adopted in foundational works on PhCs such as Refs. [16, 17]. It is chosen here since it allows a straightforward symmetry classification of PhCs, while simultaneously highlighting the unique vectorial aspects of 3D space. The chapter is divided into three sections:

- **Material Approximations** (**Section 2.1**). We introduce constitutive relations for dielectric media and explore the essential material approximations that govern the response in PhCs. These relations are critical for understanding all-dielectric PhCs, which are the primary focus of this text. These approximations encompass concepts like linearity, negligible dispersion, loss or gain, absence of sources, and the requirement of index-positivity. To make these concepts more tangible, we will provide real-world examples of materials commonly used in photonics. These materials exemplify realistic dielectric media that adhere to these approximations within specific frequency ranges.

- **Operator-Form of Maxwell Equations** (**Section 2.2**) In this section, we introduce the operator formulation of Maxwell's equations. This approach allows us to describe classical waves in PhCs using the formalism of quantum mechanics. We will highlight the important similarities and differences between these two descriptions, enabling us to address concepts such like scale-invariance, real-valuedness, and the vectorial and transversal nature of electromagnetic fields. This foundation will be crucial as we explore the symmetries and topological characteristics of photonic structures in the next section.

- **Symmetry and Topology in PhCs** (**Section 2.3**) In this section, we explore symmetry and topology in the context of PhCs. We examine how lattice periodicity affects electromagnetic waves, leading to photonic bands, electromagnetic Chern numbers, and a polarization vortex in 3D. We classify topological PhCs based on material symmetries, pertaining to the dielectric tensor's internal symmetries. We distinguish two time-reversal symmetries: one for real-valued materials and one for magneto-electric media. We introduce electromagnetic duality symmetry and its role in this classification. Drawing from the foundational principles of the periodic table of topological insulators [24, 25], we identify potential topological classes for photonic bandgaps. Finally, we incorporate space-group symmetries and explore methods to characterize electromagnetic modes in 3D PhCs, emphasizing vectorial aspects.

This chapter draws upon seminal works in electromagnetism and topological physics. References such as [71–75] elaborate on classical electromagnetism concepts, while [16, 17, 26, 28, 29, 39, 70, 76–81] integrate these principles into the context of topological PhCs.

2.1 Constitutive Relations and Material Approximations

In this section, we establish the approximations fulfilled by the dielectric materials composing the PhCs examined in this thesis. First, we will introduce the constitutive relations for dielectric materials. These relations elucidate how light's electric and magnetic fields interact with the crystal's structure and its constituent materials, primarily through the dielectric tensor, establishing a link between induced and applied electromagnetic fields. Then, we will explore the range of validity for several critical approximations. These include linearity, negligible dispersion, as well as negligible loss or gain, the absence of sources, and the necessity of index-positivity. To emphasize practical implications, we will provide some examples of frequency ranges in which certain dielectric materials, used to fabricate topological PhCs, conform to these assumptions under their standard operating conditions. The starting point of our discussion is the Maxwell equations for media in the time domain:

$$\begin{aligned} \nabla \cdot \mathbf{D}(\mathbf{r}, t) &= \rho(\mathbf{r}, t) \qquad \text{(Magnetic Gauss's Law)} \\ \nabla \cdot \mathbf{B}(\mathbf{r}, t) &= 0 \qquad\qquad\qquad\quad \text{(Gauss's Law)} \end{aligned} \tag{2.2}$$

$$\begin{aligned} \nabla \times \mathbf{E}(\mathbf{r}, t) &= -\partial_t \mathbf{B}(\mathbf{r}, t) && \text{(Faraday's Law)} \\ \nabla \times \mathbf{H}(\mathbf{r}, t) &= \partial_t \mathbf{D}(\mathbf{r}, t) + \mathbf{J}(\mathbf{r}, t) && \text{(Ampère's Law)} \end{aligned} \tag{2.3}$$

where we incorporate the conventional vacuum constants (ϵ_0 , μ_0 , and c^{-1}) into the definitions of the fields and the dielectric tensors. Here $(\mathbf{E}, \mathbf{H})$ are the applied electric and magnetic fields and $(\mathbf{D}, \mathbf{B})$ are the induced displacement and the magnetic flux density.

2.1.1 Linear approximation

In the linear response regime, the induced polarization and magnetization are linearly related to the applied electric and magnetic fields $(\mathbf{E}, \mathbf{H})$, and the medium's response remains independent of the field strength as long as the fields are weak. Under this assumption, we can establish constitutive relations as expressed below:

$$\begin{pmatrix} \mathbf{D}(t, \mathbf{r}) \\ \mathbf{B}(t, \mathbf{r}) \end{pmatrix} = (\mathcal{K} * (\mathbf{E}, \mathbf{H}))(t) = \int_{-\infty}^{t} dt' \mathcal{K}(t - t', \mathbf{r}) \begin{pmatrix} \mathbf{E}(t, \mathbf{r}) \\ \mathbf{H}(t, \mathbf{r}) \end{pmatrix}, \tag{2.4}$$

where the induced fields, i.e. the displacement $(\mathbf{D})$ and magnetic $(\mathbf{B})$ field, depend on the past field configuration through a convolution via a constitutive 6×6 tensor:

$$\mathcal{K}(t, \mathbf{r}) = \begin{pmatrix} \varepsilon(t, \mathbf{r}) & \xi(t, \mathbf{r}) \\ \zeta(t, \mathbf{r}) & \mu(t, \mathbf{r}) \end{pmatrix}, \tag{2.5}$$

which can be split into 3×3 blocks, representing the electric permittivity (ε), magnetic permeability (μ), and magneto-electric coupling responses (ξ and ζ). The tensor structure of ε and μ becomes relevant in the case of optically birefringent, piezoelectric or gyrotropic crystals, since it captures the non-diagonal or anisotropic properties commonly found in these media. On the other side, the off-diagonal terms ξ and ζ in the 6×6 tensor describe the so-called bianisotropy [74, 75], signifying the presence of magneto-electric effects. The linear response approximation remains valid under the condition that the applied fields are considerably smaller than the material's breakdown strength.

Nonlinear Topological PhCs In this thesis, we concentrate exclusively on investigating topology within linear materials, omitting dis-

cussions on nonlinearities. Nonetheless, it's worth noting that topology has found applications in nonlinear materials, leading to intriguing phenomena like topological edge solitons [82], interacting many-body quantum topological phases of light [83], and backscattering immune parametric amplification [84].

2.1.2 Non-dispersive approximation

The non-dispersive approximation assumes that the susceptibility of the material is independent of frequency, i.e. the response of the medium is instantaneous and uniform across all frequencies. In **Equation 2.4**, the susceptibility can be split into a dispersive part that depends on the past history and a non-dispersive part that refers to the instantaneous response:

$$\mathcal{K}(t, \mathbf{r}) = \mathcal{K}_{ND}(\mathbf{r})\delta(t) + \mathcal{K}_{DIS}(t, \mathbf{r}). \tag{2.6}$$

Whenever dispersion is negliglible, substituting **Equation 2.6** in the integral of **Equation 2.4**, returns:

$$\begin{pmatrix} \mathbf{D}(t, \mathbf{r}) \\ \mathbf{B}(t, \mathbf{r}) \end{pmatrix} = \mathcal{K}(\mathbf{r}) \begin{pmatrix} \mathbf{E}(t, \mathbf{r}) \\ \mathbf{H}(t, \mathbf{r}) \end{pmatrix} \tag{2.7}$$

where $\mathcal{K}(\mathbf{r})$ has no time-dependence. This condition is valid for many practical operating conditions in dielectric PhC crystals and for certain specific frequency regimes. However, it fails for materials with resonant behavior, such as metals, and certain dielectric media with strong absorption or emission characteristics.

Dispersive Topological PhCs In media where dispersion cannot be neglected, more complex models, such as the Lorentz model or the Drude model, are necessary to accurately describe the electromagnetic response. In this thesis, we will exclude metallic and plasma-based PhCs from our analysis, and focus on all-dielectric structures within the non-dispersive approximation. Incorporating dispersion in the PhC discussion has recently led to the concept of "ill-defined" topologies [85] for plasma PhCs and the emergence of phenomena such as the topological energy sinks studied in Ref. [26].

2.1.3 Hermitian approximation

The Hermitian approximation assumes that the PhC does not either absorb or amplify the light passing through it. This means that $\mathcal{K}(\mathbf{r})$ is an Hermitian tensor:

$$\mathcal{K}(\mathbf{r}) = \mathcal{K}^{\dagger}(\mathbf{r}). \tag{2.8}$$

For this approximation to hold, the materials used in the PhC structure should have negligible absorption at the wavelengths of interest. As well, the materials should not exhibit any gain, such as through stimulated emission. This Hermitian constraint translates into:

$$\varepsilon(\mathbf{r}) = \varepsilon^{\dagger}(\mathbf{r}), \tag{2.9}$$

$$\mu(\mathbf{r}) = \mu^{\dagger}(\mathbf{r}), \tag{2.10}$$

and, it implies, for the magnetoelectric coupling:

$$\xi(\mathbf{r}) = \zeta^{\dagger}(\mathbf{r}). \tag{2.11}$$

The Hermitian property of dielectric materials largely simplifies the solving of electromagnetic problems and the design of optical components in PhCs and waveguides, since it enables the application of powerful mathematical techniques such as mode expansion, eigenvalue, and transfer matrix methods.

Beyond the Hermitian approximation Photonics provides an ideal playground to study non-Hermitian topology due to its flexibility to incorporate gain through active media, as well as losses, absorption, and non-reciprocities. This has led to the demonstration of phenomena such as light-funneling via skin-effect [86, 87] and topological lasing [88], both in photonic lattices and PhCs.

2.1.4 Positive index approximation

The positive index approximation assumes that the eigenvalues ($\kappa_i(\mathbf{r})$) of the constitutive tensor $\mathcal{K}(\mathbf{r})$ are strictly positive and bounded away from ∞, uniformly in $\mathbf{r}$. In other words, the medium is a positive index material whenever there exist positive constants $C, c > 0$, which satisfy [17, 89]:

$$0 < c \leq \kappa_i(\mathbf{r}) \leq C < \infty \tag{2.12}$$

$\forall \kappa_i(\mathbf{r}) \in \mathrm{Spec}\{\mathcal{K}(\mathbf{r})\}$, for every $\mathbf{r}$. This constraint will become relevant for the definition of a Maxwell operator in **Section 2.2** via the inverse operator $\mathcal{K}^{-1}(\mathbf{r})$. In practice, this condition is strictly related to the positivity of the principal refractive indices (n_i) of the medium, i.e. the refractive indices along principal axes ($i = 1, 2, 3$). For materials with negligible magneto-electric coupling, the refractive index along i are defined from the eigenvalues of the ϵ and μ sub-tensors as follows:

$$n_i^2 = \varepsilon_i \mu_i. \tag{2.13}$$

Double Positive Materials (DPS) [89], i.e. those where both the principal ε_i permittivities and μ_i permeabilities are strictly positive ($\varepsilon_i > 0$ and $\mu_i > 0$) will be the main focus of this thesis, as they comprise most of the well-known dielectrics.

> **Exploring Further** Negative Index Materials (NIM) [90, 91] and Near Zero-Index (NZI) materials [92,93] explicitly violate the positive-index condition. It is noteworthy that, to the best of our current knowledge, the application of topological principles to the NZIs media and NIMs remains largely unexplored [94, 95].

2.1.5 Media satisfying previous assumptions

In **Table 2.1**, we recapitulate all the previous assumptions done for dielectric media of the type of PhCs studied in this thesis.

Material Approximation	Condition On Dielectric Tensor $\mathcal{K}(t, \mathbf{r})$
Linear Response	$\begin{pmatrix} \mathbf{D}(t,\mathbf{r}) \\ \mathbf{B}(t,\mathbf{r}) \end{pmatrix} = \int_{-\infty}^{t} dt' \mathcal{K}(t-t', \mathbf{r}) \begin{pmatrix} \mathbf{E}(t,\mathbf{r}) \\ \mathbf{H}(t,\mathbf{r}) \end{pmatrix}$
Dispersionless	$\mathcal{K}(t, \mathbf{r}) = \mathcal{K}_{ND}(\mathbf{r})\delta(t)$
Hermitian	$\mathcal{K}(\mathbf{r}) = \mathcal{K}^{\dagger}(\mathbf{r})$
Positive Index	$0 < c \leq \kappa_i(\mathbf{r}) \leq C < \infty, \quad \forall \kappa_i(\mathbf{r}) \in \mathrm{spec}\{\mathcal{K}(\mathbf{r})\}$

Table 2.1: Assumptions on the dielectric media which constitute the PhC.

It is pertinent to question whether the aforementioned assumptions can be physically realized in any realistic dielectric media. In practice, there exists a subset of materials that can be simultaneously approximated as positive index, lossless, non-dispersive, and linear within specific operating frequency ranges. Here are few examples of such materials utilized in the design and fabrication of topological PhCs, as well as topological waveguides, fibers, metamaterials, and ring resonators.

- **Microwave Range**: Alumina (Al_2O_3) [96,97] and (ferrimagnetic) Yittrium Garnet (YIG) [11, 98]

- **Infrared Range**: Gallium Arsenide (GaAs) [99] and Silicon (Si) [100, 101]

- **Visible Range**: Boron Nitride (BN) or Silicon Nitride (SiN_x) [102, 103]

These materials are widely used in photonics and approximately conform to the stated approximations across particular frequency regimes.

2.1.6 Source-free approximation

Another approximation we employ is the source-free approximation, which assumes the absence of free electric charges (charge density ρ) or free electric currents (current density $\mathbf{J}$) within the PhC or the surrounding medium:

$$\rho(\mathbf{r}, t) = 0 = \mathbf{J}(\mathbf{r}, t). \tag{2.14}$$

This simplification helps isolate the crystal's structure and material interactions as the primary factors affecting electromagnetic wave behavior inside it, considering contributions from external sources like antennas, current-carrying wires, or free charges, as perturbations.

2.2 Operator-Form of Maxwell Equations

In this section, we compactly express the Maxwell equations in an operator form [69, 70, 104]. This formulation allows us to apply quantum mechanics methods to classical waves, treating electromagnetic fields akin to a wave function and introducing a Maxwell operator analogous to a Hamiltonian. We separately address the dynamical Maxwell equations (Faraday and Ampère's laws) as a linear Maxwell operator equation acting on electromagnetic fields, while treating the Gauss' laws as geometric constraints for the solutions of this equation. To do so, let us consider the source-free Maxwell equations for dielectric media, setting $\rho = 0 = \mathbf{J}$ in **Equation 2.3**.

2.2.0.1 Dynamical equations

We firstly focus on the two Faraday and Ampere equations, which govern the dynamical evolution. Employing the constitutive relations:

$$\begin{pmatrix} \mathbf{D}(\mathbf{r},t) \\ \mathbf{B}(\mathbf{r},t) \end{pmatrix} = \mathcal{K}(\mathbf{r}) \begin{pmatrix} \mathbf{E}(\mathbf{r},t) \\ \mathbf{H}(\mathbf{r},t) \end{pmatrix}, \tag{2.15}$$

with the assumptions done in the previous section for $\mathcal{K}(\mathbf{r})$:

$$\mathcal{K}(\mathbf{r}) = \begin{pmatrix} \varepsilon(\mathbf{r}) & \xi(\mathbf{r}) \\ \xi^{\dagger}(\mathbf{r}) & \mu(\mathbf{r}) \end{pmatrix}, \tag{2.16}$$

the Faraday and Ampere' equations can be compactified as:

$$\begin{pmatrix} 0 & \boldsymbol{\nabla}\times \\ -\boldsymbol{\nabla}\times & 0 \end{pmatrix} \begin{pmatrix} \mathbf{E}(\mathbf{r},t) \\ \mathbf{H}(\mathbf{r},t) \end{pmatrix} = \partial_t \left(\mathcal{K}(\mathbf{r}) \begin{pmatrix} \mathbf{E}(\mathbf{r},t) \\ \mathbf{H}(\mathbf{r},t) \end{pmatrix} \right). \tag{2.17}$$

Since $\mathcal{K}(\mathbf{r})$ is invertible from the assumptions made in the previous section, these two equations can be written in an operator form, which we will address to as the Schrödinger representation of Maxwell's equations:

$$\mathcal{M}(\mathbf{r}) \begin{pmatrix} \mathbf{E}(\mathbf{r},t) \\ \mathbf{H}(\mathbf{r},t) \end{pmatrix} = i\partial_t \begin{pmatrix} \mathbf{E}(\mathbf{r},t) \\ \mathbf{H}(\mathbf{r},t) \end{pmatrix} \tag{2.18}$$

defining a generalized Maxwell operator:

$$\mathcal{M}(\mathbf{r}) = \mathcal{K}(\mathbf{r})^{-1}\mathrm{Rot}(\mathbf{r}) = \mathcal{K}(\mathbf{r})^{-1} \begin{pmatrix} 0 & +i\boldsymbol{\nabla}\times \\ -i\boldsymbol{\nabla}\times & 0 \end{pmatrix} \tag{2.19}$$

in terms of the free Maxwell operator:

$$\mathcal{M}_{\mathrm{free}}(\mathbf{r}) = \mathrm{Rot} = \begin{pmatrix} 0 & +i\boldsymbol{\nabla}\times \\ -i\boldsymbol{\nabla}\times & 0 \end{pmatrix}. \tag{2.20}$$

The generalized Maxwell operator $\mathcal{M}(\mathbf{r})$ holds similarity to a Schrödinger-like operator, acting on the $\begin{pmatrix} \mathbf{E}(\mathbf{r},t) \\ \mathbf{H}(\mathbf{r},t) \end{pmatrix}$-fields, with the fields playing a role akin to that of a wave function. A more in-depth analysis of the analogies and distinctions between Maxwell and Schrödinger operators is presented in **Table 2.2**.

2.2.0.2 Divergence-free conditions

The remaining two Maxwell equations, the Gauss' laws, can be similarly expressed in terms of the $\mathcal{K}(\mathbf{r},t)$ tensor, as a single equation for the $\begin{pmatrix}\mathbf{E}(\mathbf{r},t)\\ \mathbf{H}(\mathbf{r},t)\end{pmatrix}$-fields:

$$\mathrm{Div}\left(\mathcal{K}(\mathbf{r})\begin{pmatrix}\mathbf{E}(\mathbf{r},t)\\ \mathbf{H}(\mathbf{r},t)\end{pmatrix}\right)=0, \tag{2.21}$$

where the divergence operator is simply $\mathrm{Div}\begin{pmatrix}\ \\ \ \end{pmatrix}=\begin{pmatrix}\boldsymbol{\nabla}\cdot\\ \boldsymbol{\nabla}\cdot\end{pmatrix}$. As we will show in **Section2.3.1.3**, this relation provides a geometrical constraint to electromagnetic solutions of **Equation 2.18**, enforcing transversal propagating of waves with respect to their wavevector.

2.2.1 Electromagnetic observables

In the Schrödinger representation of the Maxwell equations (**Equation 2.18**), the generalized Maxwell operator $\mathcal{M}(\mathbf{r})$ acts on electromagnetic fields similarly to how a Schrödinger operator acts on a wave function. However, a significant departure from quantum mechanics is evident in that physical electromagnetic fields in the time domain are real-valued vector fields. More specifically, electromagnetic fields constitute elements of a Banach space denoted as [17, 105]:

$$\begin{aligned}\mathcal{H}_{\mathrm{real}}=\mathcal{L}^2_{\mathcal{K}}(\mathbb{R}^3,\mathbb{R}^6)=\Bigg\{(\mathbf{E},\mathbf{H}):\mathbb{R}^3\to\mathbb{R}^6\Big|\int d^3\mathbf{r}\big(\mathbf{E},\mathbf{H}\big)\cdot\left(\mathcal{K}\begin{pmatrix}\mathbf{E}\\ \mathbf{H}\end{pmatrix}\right)\\ =\int d\mathbf{r}\,(\mathbf{E}\cdot\mathbf{D}+\mathbf{H}\cdot\mathbf{B})<\infty\Bigg\},\end{aligned} \tag{2.22}$$

whose elements are functions mapping from a three-dimensional real space ($\mathbb{R}^3$) to the six-dimensional space of the electromagnetic Cartesian components ($\mathbb{R}^6$). This mathematical space consists only of square-integrable fields $\mathcal{L}^2_{\mathcal{W}}$, associated to a $\mathcal{W}$-weighted energy norm, a relevant condition for media where finite field energy waves are considered. In contrast to quantum mechanics, the components of the $(\mathbf{E},\mathbf{H})$ fields are directly accessible via experimental observations. More in general, electromagnetic

observables can be represented as functionals of these fields [106]:

$$F_{\text{obs}} : \mathcal{L}^2_{\mathcal{K}}(\mathbb{R}^3, \mathbb{R}^6) \to \mathbb{R}^n. \tag{2.23}$$

Electromagnetic observables do not need to be linear or quadratic in the fields: however, many of the most well known observables, such as the energy density, the Poynting vector, or the Zilch for dual-symmetric media [26, 107], are quadratic in the fields.

2.2.2 Frequency domain

In order to relate the fields to the light's frequency, we make use of the inverse Fourier transform in time:

$$\begin{pmatrix} \mathbf{E}(\omega) \\ \mathbf{H}(\omega) \end{pmatrix} = \frac{1}{\sqrt{2\pi}} \int_{\mathbb{R}} \mathrm{d}t e^{it\omega} \begin{pmatrix} \mathbf{E}(t) \\ \mathbf{H}(t) \end{pmatrix}, \tag{2.24}$$

and write the Maxwell equations in the frequency domain:

$$\begin{pmatrix} 0 & +i\boldsymbol{\nabla}\times \\ -i\boldsymbol{\nabla}\times & 0 \end{pmatrix} \begin{pmatrix} \mathbf{E}(\omega) \\ \mathbf{H}(\omega) \end{pmatrix} = \omega \mathcal{K}(\omega) \begin{pmatrix} \mathbf{E}(\omega) \\ \mathbf{H}(\omega) \end{pmatrix}, \tag{2.25}$$

which constitutes a generalized eigenvalue problem [108] since, in general, $\mathcal{K}(\omega) \neq \mathbb{1}$.

High and zero frequency limits In many physical situations the following limits become relevant:

- In the limit of large frequencies, the medium behaves like the vacuum:

$$\lim_{\omega \to \pm\infty} \mathcal{K}(\omega) = \mathbb{1} \tag{2.26}$$

- In the zero frequency limit, the medium has neither gyrotropy nor bianisotropy:

$$\lim_{\omega \to 0} \mathcal{K}(\omega) = \mathrm{diag}[\varepsilon(0), \mu(0)] = \mathrm{diag}[\overline{\varepsilon(0)}, \overline{\mu(0)}] \tag{2.27}$$

  In the context of topological PhCs, **Equation 2.26**, allows to provide a bound on the topological invariants of PhC bands [85].

Under the dispersionless approximation, it is assumed that:

$$\frac{d}{d\omega} \mathcal{K}(\omega)\Big|_{\omega_L} \approx 0 \tag{2.28}$$

where ω_L represents a specific frequency around which the photonic crystal (PhC) operates. Furthermore, within a certain energy regime where ($\omega \approx \omega_L$), it is considered that:

$$\mathcal{K}(\omega) = \mathcal{K}(\omega_L) = \mathcal{K} \tag{2.29}$$

and hence, in this thesis, we will take $\mathcal{K}$ as independent of frequency.

2.2.3 Energy scalar product

Inner products play a pivotal role in the computation of many topological invariants and symmetry eigenvalues, **Section 2.3.1.2** and **2.3.3**. In the operator-form of Maxwell equations, the fields are equipped with a $\mathcal{K}(\mathbf{r})$-weighted inner product ($\langle\cdot|\cdot\rangle_{\mathcal{K}}$) defined as [16, 17, 108]:

$$\langle\begin{pmatrix}\mathbf{E}\\ \mathbf{H}\end{pmatrix}|\begin{pmatrix}\mathbf{E}'\\ \mathbf{H}'\end{pmatrix}\rangle_{\mathcal{K}} = \int d^3\mathbf{r}\big(\mathbf{E}(\mathbf{r}),\mathbf{H}(\mathbf{r})\big)\cdot\left(\mathcal{K}(\mathbf{r})\begin{pmatrix}\mathbf{E}'(\mathbf{r})\\ \mathbf{H}'(\mathbf{r})\end{pmatrix}\right) = \langle\mathbf{E}|\mathbf{D'}\rangle + \langle\mathbf{H}|\mathbf{B'}\rangle, \tag{2.30}$$

that differs from the usual Euclidean inner product, because of the form of the eigenproblem in **Equation 2.25**. More specifically, eigensolutions of **2.25** with $\mathcal{K}$-frequency independent, $\{\begin{pmatrix}\mathbf{E}\\ \mathbf{H}\end{pmatrix}_j\}$ constitute a biorthogonal basis together with $\{\mathcal{K}\begin{pmatrix}\mathbf{E}\\ \mathbf{H}\end{pmatrix}_{j'}\}$, and not with $\{\begin{pmatrix}\mathbf{E}\\ \mathbf{H}\end{pmatrix}_{j'}\}$, differently from standard eigenvalue problems. Throughout this thesis, the $\mathcal{K}(\mathbf{r})$-weighted product will be referred to as the "energy" scalar product. The reason for this is that the associated $\mathcal{K}$-weighted norm ($||\cdot||^2_{\mathcal{K}}$), defined as:

$$||\begin{pmatrix}\mathbf{E}\\ \mathbf{H}\end{pmatrix}||^2_{\mathcal{K}} = \langle\begin{pmatrix}\mathbf{E}\\ \mathbf{H}\end{pmatrix}|\begin{pmatrix}\mathbf{E}\\ \mathbf{H}\end{pmatrix}\rangle_{\mathcal{K}}, \tag{2.31}$$

simplifies to the conventional expression for electromagnetic energy stored in the fields:

$$\mathcal{E}(\mathbf{E},\mathbf{H}) = \frac{1}{2}||(\mathbf{E},\mathbf{H})||^2_{\mathcal{K}}. \tag{2.32}$$

Note that, even though we have been considering the frequency domain, the definitions for $\langle\cdot|\cdot\rangle_{\mathcal{K}}$ and $||\cdot||$ are valid also in time domain, in virtue of the Parseval's theorem [109].

2.2.4 Scale invariance of Maxwell equations

In the frequency domain and under the dispersionless approximation, the scale-invariance [110, 111] of the Maxwell equations in free space is clearly evident. The free operator ($\mathcal{M}_{\text{free}}(\mathbf{r}) = \text{Rot}$) is a purely kinetic term, so that a rescaling of the real-space coordinates:

$$\mathbf{r}' = s\mathbf{r}, \tag{2.33}$$

$$\boldsymbol{\nabla}' = \boldsymbol{\nabla}'/s, \tag{2.34}$$

leads to a corresponding rescaling of the electromagnetic frequencies:

$$\omega' = \omega/s. \tag{2.35}$$

While the Schrödinger equation for electrons in crystals, which has a *sum* structure, with Hamiltonian:

$$H(\mathbf{r}) = \frac{1}{2m}(-i\hbar\boldsymbol{\nabla})^2 + V(\mathbf{r}), \tag{2.36}$$

the Maxwell operator preserves a *product* structure, even in the presence of a dielectric medium:

$$\mathcal{M}(\mathbf{r}) = \mathcal{K}(\mathbf{r})^{-1}\text{Rot}. \tag{2.37}$$

	Classical Electromagnetism	Quantum Mechanics
Wave Function	$\psi = (\mathbf{E}, \mathbf{H}) \in \mathbb{R}^6$	$\psi \in \mathbb{C}^n$
Hamiltonian Operator	$\mathcal{K}(\mathbf{r})^{-1}\text{Rot}$ (*product* form)	e.g. $H = \frac{1}{2m}(-i\hbar\boldsymbol{\nabla})^2 + V$ (*sum* form)
Hilbert Space	$\mathcal{L}^2_{\mathcal{K}}(\mathbb{R}^3, \mathbb{R}^6)$	$\mathcal{L}^2(\mathbb{R}^3, \mathbb{C}^n)$
Amplitudes	electromagnetic field energy density	probability
Observables	functionals of the fields	Hermitian operators

Table 2.2: Comparison between quantum mechanics and operator-form of classical EM waves, adapted from [17, 29, 106].

Because of this, in the PhC community, it's common practice to define a dimensionless reference quantity [16, 17]:

$$\frac{fc}{|a|} = \frac{\omega c}{2\pi|a|} \tag{2.38}$$

where c represents the speed of light, normalizing the electromagnetic frequencies using a chosen characteristic real-space length scale $|a|$ (e.g. the lattice constant of the PhC).

2.2.5 Complex waves

Working with complex (as opposed to real) Hilbert spaces becomes convenient in order to adapt methods from quantum mechanics to classical electromagnetism. For this purpose, we will split the physical real fields into two complex fields $\psi_{\pm}(t)$:

$$\psi(t) = \begin{pmatrix} \mathbf{E}(t) \\ \mathbf{H}(t) \end{pmatrix} = \psi_{+}(t) + \psi_{-}(t) \tag{2.39}$$

that are defined, in terms of the frequency Fourier transformed fields, where $\psi_{+}(t)$ is defined only in terms of positive frequencies:

$$\psi_{+}(t) = \frac{1}{\sqrt{2\pi}} \int_{0}^{\infty} d\omega e^{i\omega t} \begin{pmatrix} \mathbf{E}(\omega) \\ \mathbf{H}(\omega) \end{pmatrix} \tag{2.40}$$

where $\psi_{-}(t)$ is defined only in terms of negative ones:

$$\psi_{-}(t) = \frac{1}{\sqrt{2\pi}} \int_{0}^{\infty} d\omega e^{-i\omega t} \begin{pmatrix} \mathbf{E}(-\omega) \\ \mathbf{H}(-\omega) \end{pmatrix}. \tag{2.41}$$

Interestingly, $\psi_{+}(t)$ and $\psi_{-}(t)$ evolve according to different source-free Maxwell equations [104, 106]. More specifically, $\omega \geq 0$ solutions evolve with $\mathcal{K}$, via the positive frequency Maxwell operator $\mathcal{M}_{+} = \mathcal{K}^{-1}\mathcal{M}_{\text{free}}$:

$$\mathcal{M}_{+}\psi_{+}(t) = i\partial_{t}\psi_{+}(t) \tag{2.42}$$

while $\omega \leq 0$ states evolve with complex conjugate $\overline{\mathcal{K}}$, via the negative frequency Maxwell operator $\mathcal{M}_{-} = \overline{\mathcal{K}}^{-1}\mathcal{M}_{\text{free}}$:

$$\mathcal{M}_{-}\psi_{-}(t) = i\partial_{t}\psi_{-}(t). \tag{2.43}$$

This allows the fields $(\mathbf{E}(t), \mathbf{H}(t))$ to remain real-valued during time evolution. Importantly, the real-valuedness of the physical waves implies:

$$\begin{pmatrix} \mathbf{E}(\omega) \\ \mathbf{H}(\omega) \end{pmatrix} = \begin{pmatrix} \overline{\mathbf{E}(-\omega)} \\ \overline{\mathbf{H}(-\omega)} \end{pmatrix}. \tag{2.44}$$

Taking the Fourier transform of **Equation 2.44**, shows that the complex waves have their frequency locked:

$$\psi_-(t) = \overline{\psi_+(t)}. \tag{2.45}$$

In other terms, positive and negative frequency contributions of a wave are not independent: knowing one ($\psi_+(t)$) allows the reconstruction of the other ($\psi_-(t)$).

2.2.6 Non-negative frequency waves

As shown in the previous section, real electromagnetic fields in the time domain can be uniquely represented as complex waves with solely non-negative frequencies:

$$\begin{pmatrix} \mathbf{E}(t) \\ \mathbf{H}(t) \end{pmatrix} = \psi_+(t) + \overline{\psi_+(t)} = 2Re[\psi_+(t)] = 2Re[\psi_-(t)]. \tag{2.46}$$

This allows to establish a systematic link between the space of physical solutions and an auxiliary complex Hilbert space:

$$\begin{pmatrix} \mathbf{E}(\mathbf{r},t) \\ \mathbf{H}(\mathbf{r},t) \end{pmatrix} \in L^2_{\mathcal{K}}(\mathbb{R}^3,\mathbb{R}^6) \qquad \leftrightarrow \qquad \psi_+ \in \mathcal{H}_+ = Q_+[L^2_{\mathcal{K}}(\mathbb{R}^3,\mathbb{C}^6)] \tag{2.47}$$

where $\mathcal{L}^2_{\mathcal{K}}$ is a complex Hilbert space equipped with the $\mathcal{K}(\mathbf{r})$-product:

$$\mathcal{L}^2_{\mathcal{K}}(\mathbb{R}^3,\mathbb{C}^6) = \left\{ \psi \,:\, \mathbb{R}^3 \to \mathbb{R}^6 \middle| \int d\mathbf{r}\,(\psi \cdot (\mathcal{K}\psi)) < \infty \right\}, \tag{2.48}$$

and where the spectral projector Q_+ [69, 70, 105], filters non-negative energy solutions with $\omega \leq 0$.

2.2.7 Photonic particle-hole redundancy

From the above definitions, it is easy to check that complex conjugation K maps incoming waves to outgoing waves:

$$K\psi_+ = \overline{\psi}_- \tag{2.49}$$

relating negative to positive frequencies via:

$$KQ_+K = Q_-, \tag{2.50}$$

therefore defining a symmetry between positive and negative frequency operators [28, 105, 106]:

$$K\mathcal{M}_{+}K = -\mathcal{M}_{-}. \tag{2.51}$$

Since K is anti-unitary, anti-commuting, and squares to identity, it acts similarly to an even particle-hole transformation (PH) [24, 25] in quantum mechanics terminology.

However, different from electronic systems, this photonic PH is not a symmetry in the traditional sense. It is rather a constraint of the complex-domain formulation, telling us that the physical, electromagnetic fields need to be real. More specifically, K represents an anti-unitary map between $L^2_{\mathcal{K}}(\mathbb{R}^3, \mathbb{C}^6)$ and the Hilbert space $L^2_{\overline{\mathcal{K}}}(\mathbb{R}^3, \mathbb{C}^6)$ with conjugate weight. As so, it constitutes an unavoidable constraint, related to the real-valued nature of physical fields.

PH constraints In this context, it is worth mentioning the implications of PH on the photonic bands and their topological invariants. In electromagnetism, it is possible to have an infinite number of bands above a band gap, as the number of available modes with positive frequency is typically infinite, in strong contrast with condensed matter systems which have a well-defined ground-state. PH maps these positive and negative bands into each other. In the theory of PhCs, the topological role of negative frequency bands is often overlooked, assuming a vanishing of their Chern number. However, PH symmetry only implies that the total topological Chern number of negative frequency bands has the opposite sign of the Chern number of positive frequency bands, not their vanishing. While negative frequency bands are often neglected for electromagnetic Chern number calculations, examples where they become relevant exist, both in continua (see Refs. [81, 112]) and in PhCs (see Ref. [85]).

2.2.8 Longitudinal and transversal waves

The Hilbert space in which electromagnetic fields live can be geometrically decomposed as a direct sum [69, 70, 105, 106, 113]:

$$L^2_{\mathcal{K}}(\mathbb{R}^3, \mathbb{C}^6) = \mathcal{T} \oplus \mathcal{L} \tag{2.52}$$

where $\mathcal{L}$ are longitudinal gradient fields:

$$\mathcal{L} = \left\{ \psi = \begin{pmatrix} \boldsymbol{\nabla}\chi^E \\ \boldsymbol{\nabla}\chi^H \end{pmatrix} \in L^2_{\mathcal{K}}(\mathbb{R}^3, \mathbb{C}^6) \middle| \begin{pmatrix} \chi^E \\ \chi^H \end{pmatrix} \in L^2(\mathbb{R}^3, \mathbb{C}^2) \right\} = \text{ran}(\boldsymbol{\nabla}, \boldsymbol{\nabla}) = \ker \text{Rot} = \ker \mathcal{M}_+. \tag{2.53}$$

and $\mathcal{T}$ are transversal fields:

$$\mathcal{T} = \mathcal{L}^{\perp_{\mathcal{K}}} = \ker(\text{Div}\mathcal{K}) = \text{ran}\mathcal{M}_+ \tag{2.54}$$

and with "ker" and "ran" referring to the kernel (null space) and range (image) of the linear operator. The $\mathcal{L}$ and $\mathcal{T}$ spaces are, by definition, $\langle\cdot|\cdot\rangle_{\mathcal{K}}$-orthogonal. Only the elements of $\mathcal{T}$ satisfy the divergence-free constraint of Maxwell equations, as it can be verified by taking the scalar product of $\chi = \begin{pmatrix} \boldsymbol{\nabla}\chi^E \\ \boldsymbol{\nabla}\chi^h \end{pmatrix}$ and $\psi \in \mathcal{T}$ and performing partial integration. Therefore, in the absence of sources, only transversal fields satisfy the physicality constraint imposed by Maxwell equations.

2.2.9 Quadratic/linear Maxwell formulation

Please note that from now on we will drop the $\pm$ signs in both the fields and the operators, and focus on complex waves with solely non-negative frequencies ($\omega > 0$). Across this thesis, we will often consider non-bianisotropic media, where the magneto-electric coupling is absent ($\xi = 0$) and the dielectric tensor simplifies to a diagonal form:

$$\mathcal{K} = \begin{pmatrix} \varepsilon & 0 \\ 0 & \mu \end{pmatrix}. \tag{2.55}$$

In that scenario, the auxiliary Maxwell operator is block-off diagonal and squares to [16, 17]:

$$\mathcal{M}^2 = \begin{pmatrix} \mathcal{M}^2_{(EE)} & 0 \\ 0 & \mathcal{M}^2_{(HH)} \end{pmatrix} = \begin{pmatrix} \varepsilon^{-1}\boldsymbol{\nabla}\times\mu^{-1}\boldsymbol{\nabla}\times & 0 \\ 0 & \mu^{-1}\boldsymbol{\nabla}\times\varepsilon^{-1}\boldsymbol{\nabla}\times \end{pmatrix}. \tag{2.56}$$

When this happens, the linear Maxwell eigenproblem,

$$\mathcal{M}\psi = \omega\psi \tag{2.57}$$

splits into two separate quadratic wave equations:

$$\mathcal{M}^2_{EE}\psi^{(E)} = \left(\omega^{(E)}\right)^2 \psi^{(E)} \tag{2.58}$$

$$\mathcal{M}^2_{HH}\psi^{(H)} = \left(\omega^{(H)}\right)^2 \psi^{(H)}, \tag{2.59}$$

where $\omega^{(E)} = \omega^{(H)} = \omega \geq 0$, and for each components of: $\psi = \begin{pmatrix} \psi^{(E)} \\ \psi^{(H)} \end{pmatrix}$. Both the linear and the quadratic formulations are equivalent: while the linear one is convenient when analytically applying quantum mechanics methods to the classical waves, the quadratic one is often employed in numerical solvers. In fact, it is often enough to focus on a single electromagnetic component, either the electric or the magnetic field, and reconstruct the latter via the derivative map [106, 114]. Starting from the electric field only, one can reconstruct the entire electromagnetic field as follows:

$$r^{(E)} : \psi^{(E)} \to \psi = \begin{pmatrix} \psi^{(E)} \\ -i\mu^{-1}\boldsymbol{\nabla} \times (\mathcal{M}^2_{\mathrm{EE}})^{-1/2}\psi^{(E)} \end{pmatrix}, \tag{2.60}$$

and analogously, starting from the magnetic field only:

$$r^{(H)} : \psi^{(H)} \to \psi = \begin{pmatrix} -i\varepsilon^{-1}\boldsymbol{\nabla} \times (\mathcal{M}^2_{\mathrm{HH}})^{-1/2}\psi^{(H)} \\ \psi^{(H)} \end{pmatrix}. \tag{2.61}$$

This equivalence largely simplifies the analysis of electromagnetic problems when dealing with non-bianisotropic media.

	Linear	Quadratic (Electric)	Quadratic (Magnetic)
Operator $\mathcal{M}$	$\begin{pmatrix} 0 & +i\varepsilon^{-1}\boldsymbol{\nabla}\times \\ -i\mu^{-1}\boldsymbol{\nabla}\times & 0 \end{pmatrix}$	$\mathcal{M}^2_{(EE)} = (\varepsilon^{-1}\boldsymbol{\nabla} \times \mu^{-1}\boldsymbol{\nabla}\times)$	$\mathcal{M}^2_{(HH)} = (\mu^{-1}\boldsymbol{\nabla} \times \varepsilon^{-1}\boldsymbol{\nabla}\times)$
Eigenproblem	$\mathcal{M}\psi = \omega\psi$	$\mathcal{M}^2_{EE}\psi^{(E)} = \omega^2\psi^{(E)}$	$\mathcal{M}^2_{HH}\psi^{(H)} = \omega^2\psi^{(H)}$

Table 2.3: Comparison of the linear and quadratic Maxwell formulation for media with negligible magneto-electric coupling ($\xi = 0$.)

2.3 Symmetry and Topology in PhCs

In this section, we will discuss notions of symmetry and topology in the context of PhCs -dielectric materials with discrete translational symmetry.

In order to apply topological-band theory concepts to electromagnetic waves, we aim to express the Maxwell operator for periodic media in a Bloch momentum space representation. We will start by looking at how the lattice periodicity affects electromagnetic waves. This includes concepts like photonic bands, electromagnetic Chern numbers, and the gamma-point obstruction in 3D.

Next, we will dive into classifying topological PhCs based on material symmetries -internal symmetries of the dielectric tensor. We will uncover two types of time-reversal symmetries: one preserved by real-valued materials and another preserved by magneto-electric media. Additionally, we will introduce the concept of electromagnetic duality symmetry, and helicity-preserving systems.

Finally, we will incorporate space-group symmetries, and analyze the challenges arising in characterizing the symmetry eigenvalues of the electromagnetic modes in a 3D PhC in the long-wavelength limit.

2.3.1 Discrete translational symmetry

A PhC is defined by the periodicity of its dielectric tensor $\mathcal{K}(\mathbf{r})$ [16, 17]:

$$\mathcal{K}(\mathbf{r}) = \mathcal{K}(\mathbf{r} + \mathbf{R}) \tag{2.62}$$

where $\mathbf{R} \in \mathcal{R}$ is a vector belonging to a lattice $\mathcal{R}$ defined by the span of three primitive vectors:

$$\mathcal{R} = \mathrm{span}_{\mathbb{Z}}\{\mathbf{a}_1, \mathbf{a}_2, \mathbf{a}_3\} \cong \mathbb{Z}^3. \tag{2.63}$$

Similarly to what it is done in solid-state physics [115, 116], we can decompose coordinate vectors $\mathbf{r}$ in real space $\mathbb{R}^3 \cong \mathbb{W} \times \mathcal{R}$ as $\mathbf{r} = \mathbf{s} + \mathbf{R}$ where $\mathbf{R} \in \mathcal{R}$ and where $\mathbf{s} \in \mathbb{W}$ lives in the (Wigner-Seitz) unit cell. The momentum space can also be decomposed as $\mathbb{R}^3 \cong \mathbb{B} \times \mathcal{G}$ where $\mathcal{G} = \mathrm{span}_{\mathbb{Z}}\{\mathbf{b}_1, \mathbf{b}_2, \mathbf{b}_3\}$ is the dual lattice generated via the following relation:

$$\mathbf{a}_m \cdot \mathbf{b}_n = 2\pi\delta_{m,n}. \tag{2.64}$$

and where $\mathbb{B}$ is first Brillouin zone (BZ), defined as the minimal fundamental cell in momentum space [115, 116]:

$$\mathbb{B} = \left\{ \sum_{m=1}^{3} \beta_m \mathbf{b}_m \in \mathbb{R}^3 \middle| \beta_1, \beta_2, \beta_3 \in [-\frac{1}{2}, \frac{1}{2}) \right\}, \tag{2.65}$$

with its elements referred to as crystal momenta $\mathbf{k} \in \mathbb{B}$. Because of the lattice periodicity, we have that:

$$\mathbf{k} = \mathbf{k} + \mathbf{G} \tag{2.66}$$

with $\mathbf{G} \in \mathcal{G}$. Therefore, the BZ exhibits the topological properties of a torus, denoted as $\mathbb{B} \cong \mathbb{T}^3$, which creates a natural framework for defining topological invariants within this manifold.

2.3.1.1 Bloch theory of photonic bands

Exploiting the periodicity of the Maxwell operator with respect to the lattice, we can represent the electromagnetic fields in momentum space via the Zak-Bloch-Floquet transform [29, 70, 106, 115, 117]:

$$\mathcal{Z}[\psi](\mathbf{k}, \mathbf{s}) = \sum_{\mathbf{R} \in \mathcal{R}} e^{-i\mathbf{k}\cdot(\mathbf{s}+\mathbf{R})} \psi(\mathbf{s} + \mathbf{R}) \tag{2.67}$$

which maps onto the space-periodic part of the Bloch functions, with $\mathbf{k}$ in the BZ $\mathbb{B}$ and for $\mathbf{s}$ in the unit cell $\mathbb{W}$. The $\mathcal{Z}$-transformed fields are periodic in real space, as can be checked from the definition:

$$\mathcal{Z}[\psi](\mathbf{k}, \mathbf{s}) = \mathcal{Z}[\psi](\mathbf{k}, \mathbf{s} - \mathbf{R}), \tag{2.68}$$

and they acquire a phase when translated in momentum space:

$$\mathcal{Z}[\psi](\mathbf{k} - \mathbf{G}, \mathbf{s}) = e^{i\mathbf{G}\cdot\mathbf{s}} \mathcal{Z}[\psi](\mathbf{k}, \mathbf{s}). \tag{2.69}$$

In order to derive the momentum-space formulation of the Maxwell eigenproblem, we apply the $\mathcal{Z}$-transform on the position and momentum operators:

$$\mathcal{Z}\hat{\mathbf{r}}\mathcal{Z}^{-1} = i\boldsymbol{\nabla}_{\mathbf{k}}, \tag{2.70}$$

$$\mathcal{Z}(-i\boldsymbol{\nabla}_{\mathbf{r}})\mathcal{Z}^{-1} = -i\boldsymbol{\nabla}_{\mathbf{s}} + \hat{\mathbf{k}}, \tag{2.71}$$

which translates to the following collection of Maxwell operators:

$$\mathcal{M}(\mathbf{k}) = \mathcal{K}^{-1}\mathrm{Rot}(\mathbf{k}) = \mathcal{K}^{-1} \begin{pmatrix} 0 & +(i\boldsymbol{\nabla}_{\mathbf{s}} - \mathbf{k})\times \\ -(i\boldsymbol{\nabla}_{\mathbf{s}} - \mathbf{k})\times & 0 \end{pmatrix}, \tag{2.72}$$

and their corresponding eigenproblem:

$$\mathcal{M}(\mathbf{k})u_{n,\mathbf{k}}(\mathbf{s}) = \omega_n(\mathbf{k})u_{n,\mathbf{k}}(\mathbf{s}) \tag{2.73}$$

where $\omega_n(\mathbf{k})$ is the n-th photonic band frequency and where $u_{n,\mathbf{k}}(\mathbf{s}) = \begin{pmatrix} u^{(E)}_{n,\mathbf{k}}(\mathbf{s}) \\ u^{(H)}_{n,\mathbf{k}}(\mathbf{s}) \end{pmatrix}$ are the space-periodic part of the Bloch function. These are directly obtained from the $\mathcal{Z}$-transformation, and related to the Bloch functions ($\varphi_{n,\mathbf{k}}(\mathbf{s})$) as:

$$\varphi_{n,\mathbf{k}}(\mathbf{s}) = e^{i\mathbf{k}\cdot\mathbf{s}}u_{n,\mathbf{k}}(\mathbf{s}). \tag{2.74}$$

The space-periodic eigenstates $u_{n,\mathbf{k}}(\mathbf{s})$ are complex-valued electromagnetic vector fields equipped with the usual $\mathcal{K}$-weighted scalar product, with the integrals running over the coordinates in a single unit cell:

$$\langle u|v\rangle_{\mathcal{K}} = \int_{\mathbb{W}} d^3\mathbf{s}u^{\dagger}\begin{pmatrix} \varepsilon & \xi \\ \xi^{\dagger} & \mu \end{pmatrix}v. \tag{2.75}$$

2.3.1.2 Electromagnetic Chern numbers

The momentum-space Bloch formulation of the Maxwell eigenproblem provides the basis for the application of the topological band theory methods to PhCs. In the study of topological PhC, a fundamental concept is that of the electromagnetic Berry connection, which is defined as follows [118–120]:

$$\mathbf{A}_{m,n}(\mathbf{k}) = \langle u_{m,\mathbf{k}}|i\boldsymbol{\nabla}_{\mathbf{k}}u_{n,\mathbf{k}}\rangle_{\mathcal{K}} \tag{2.76}$$

where we consider Bloch-periodic electromagnetic vector fields $u_{n,\mathbf{k}} = \begin{pmatrix} u^{(E)}_{n,\mathbf{k}} \\ u^{(H)}_{n,\mathbf{k}} \end{pmatrix}$, we employ the usual $\mathcal{K}(\mathbf{k})$-weighted scalar product, and where the indices n and m range over the bands below the photonic bandgap of interest. Even though in photonics we do not have the concept of a Fermi level or a ground state, we will often address the N_{band} bands below the bandgap of interest as occupied bands. The Berry phase, a key player in the calculation of numerous topological invariants, is defined as a line integral of the Berry connection along a closed path in momentum space:

$$\phi(\ell) = \oint_{\ell} \mathrm{Tr}\mathbf{A}_{m,n}(\mathbf{k}) \cdot d\boldsymbol{\ell} \quad \mathrm{mod}2\pi, \tag{2.77}$$

and tracing over the occupied bands. Exploiting the Stokes's theorem, one can transform the line integral into a surface integral:

$$\phi(\ell) = \int \mathrm{Tr}\mathbf{F}_{m,n}(\mathbf{k}) \cdot d^2\mathbf{S} \tag{2.78}$$

where $d^2\mathbf{S}$ is the surface differential for the S area defined by the closed loop $\ell = \partial S$ and $\mathbf{F}_{m,n}(\mathbf{k})$ is the Berry curvature:

$$\mathbf{F}_{m,n}(\mathbf{k}) = \boldsymbol{\nabla}_{\mathbf{k}} \times \mathbf{A}_{m,n}(\mathbf{k}). \tag{2.79}$$

When the integration of the Berry curvature is done over the first BZ, the result is quantized in multiples of 2π. This quantization leads to the concept of the Chern number:

$$2\pi C = \int_{\mathrm{BZ}} \mathrm{Tr}\mathbf{F}_{m,n}(\mathbf{k}) \cdot d^2\mathbf{S}. \tag{2.80}$$

When bianisotropy is negligible ($\xi(\mathbf{r}) = 0$), the electromagnetic Chern number (C)-the Chern number defined in terms of the electromagnetic Berry connection of **Equation 2.76**- can be equivalently computed solely from the electric or the magnetic Chern components:

$$\mathbf{A}_{m,n}(\mathbf{k}) = \langle u_{m,\mathbf{k}} | i\boldsymbol{\nabla}_{\mathbf{k}} u_{n,\mathbf{k}} \rangle_{\mathcal{K}} = \langle u^{(E)}_{m,\mathbf{k}} | i\boldsymbol{\nabla}_{\mathbf{k}} u^{(E)}_{n,\mathbf{k}} \rangle_{\varepsilon} + \langle u^{(H)}_{m,\mathbf{k}} | i\boldsymbol{\nabla}_{\mathbf{k}} u^{(H)}_{n,\mathbf{k}} \rangle_{\mu}. \tag{2.81}$$

This results in the equivalence between the electric ($C^{(E)}$), magnetic ($C^{(H)}$) and electromagnetic Chern numbers (C), according to the relation [120]:

$$C = C^{(E)} = C^{(H)} = \frac{C^{(E)} + C^{(H)}}{2}. \tag{2.82}$$

2.3.1.3 Gamma singularity

In 3D PhC, the vectorial nature of the electromagnetic fields gives rise to a vortex-like polarization singularity in momentum-space at the Γ point ($\mathbf{k} = 0$) in the limit of zero-frequency states. This singularity arises from the divergence-free (Gauss) condition of the Maxwell equations in source-free media:

$$\mathrm{Div}\,(\mathcal{K}\psi) = 0, \tag{2.83}$$

which discards longitudinal modes from physical solutions, imposing a transversality constraint for electromagnetic waves. As we will show now, this transversal constraint

has important consequences on the symmetry and topology properties of 3D PhCs [23,121–123]. For simplicity, we will provide a guiding example in a non-bianisotropic ($\xi = 0$), non-magnetic ($\mu = \mathbb{1}$) medium where the Gauss laws is reduced to:

$$\boldsymbol{\nabla} \cdot \left(\varepsilon \boldsymbol{\psi}^{(E)}\right) = 0 = \boldsymbol{\nabla} \cdot \left(\boldsymbol{\psi}^{(H)}\right), \tag{2.84}$$

but the argument holds for the general case [121]. Focusing on the magnetic field component, and applying the Bloch transformation to momentum space, the divergence-free condition translates into:

$$(\mathbf{k} + \mathbf{G}_n) \cdot \boldsymbol{\varphi}^{(H)}_{\mathbf{G}_n,\mathbf{k}} = 0, \tag{2.85}$$

where $\boldsymbol{\varphi}^{(H)}_{\mathbf{G}_n,\mathbf{k}}$ is the G_n-th Fourier component of the plane wave expansion of the Bloch magnetic field:

$$\boldsymbol{\varphi}^{(H)}_{n,\mathbf{k}}(\mathbf{r}) = \sum_{\mathbf{G}_n} e^{i(\mathbf{k}+\mathbf{G}_n)\cdot\mathbf{r}} \boldsymbol{\varphi}^{(H)}_{\mathbf{G}_n,\mathbf{k}}, \tag{2.86}$$

and where $\boldsymbol{\varphi}^{(H)}_{n,\mathbf{k}}(\mathbf{r})$ is the Bloch function as defined in **Equation 2.74**. Geometrically, **Equation 2.85** restricts field solutions to lie in the tangent plane of a 3D sphere with radius $|\mathbf{k} + \mathbf{G}_n|$ centered around the Γ point.

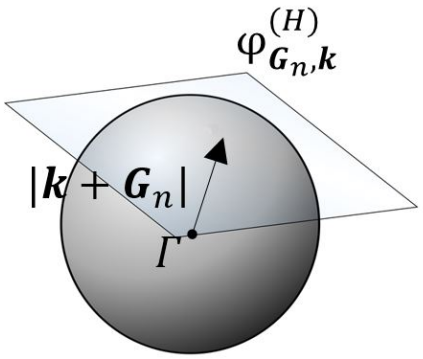

Figure 2.1: Transversality constraint for Bloch magnetic fields in 3D PhC. Solutions are restricted to lie in the tangent plane of a 3D sphere with radius $|\mathbf{k} + \mathbf{G}_n|$ centered around the Γ point. $\boldsymbol{\varphi}^{(H)}_{\mathbf{G}_n,\mathbf{k}}$ is the G_n-th Fourier component of the plane wave expansion of the Bloch magnetic field.

If we take the limit of $\mathbf{k} \to 0$, then for the lowest bands of the PhC, only the $\mathbf{G}_n = 0$ components of $\boldsymbol{\varphi}^{(H)}_{\mathbf{G}_n,\mathbf{k}}$ are nonzero to leading order [124, 125]. This means that for the lowest bands near the Γ point, which disperse linearly ($\omega \propto |\mathbf{k}|$), the Bloch fields are constrained to be tangent to a small sphere in momentum space surrounding Γ. Notably, since according to the so-called hairy-ball theorem the Euler characteristic

of the tangent space of a 3D sphere is nonzero [126, 127], it is impossible to select a continuous basis for it. As we will see in further sections, the lack of analyticity in the Bloch basis has a series of relevant consequences:

- It precludes the construction of exponentially localized Wannier functions [121] for the lowest photonic bands of 3D PhCs.

- It renders ill-defined polarization and symmetry content of long-wavelength electromagnetic fields at zero frequency in 3D [23, 122].

This poses a challenge when applying standard Topological Quantum Chemistry (TQC) methods [128, 129] to 3D PhCs, since TQC conventionally necessitates knowledge of the symmetry content at Γ. To overcome this challenge, a recent study by Ref. [23] introduced a regularization procedure enabling the topological characterization of 3D PhCs using transverse symmetry indicators [130]. This advancement has extended TQC to 3D PhCs and introduced the concept of topological non-gaps, i.e. gaps along high-symmetry lines that signify Γ-enforced band closings within the BZ. The Γ-point vortex has also relevant implications for the development of tight-binding models since it prevents the construction of maximally localized orbitals. We will address this issue in **Section 3.2**, by introducing the so-called "transversality-enforced" tight-binding method for 3D PhCs.

2.3.1.4 TM and TE polarizations

In stark contrast to 3D, in 2D PhCs, it is possible to circumvent the vectorial nature of light and avoid the Γ problem. More specifically, in 2D PhCs, it is possible to decouple the field polarizations into Transverse-Electric (TE) polarized fields of the form:

$$\psi_{\mathrm{TE}} = \begin{pmatrix} \psi_{\mathrm{TE}}^{(E)} \\ \psi_{\mathrm{TE}}^{(H)} \end{pmatrix} = \begin{pmatrix} \psi^{(E_x)} \\ \psi^{(E_y)} \\ 0 \\ 0 \\ 0 \\ \psi^{(H_z)} \end{pmatrix}, \tag{2.87}$$

and Transverse-Magnetic (TM) polarized fields of the form:

$$\psi_{\mathrm{TM}} = \begin{pmatrix} \psi_{\mathrm{TM}}^{(E)} \\ \psi_{\mathrm{TM}}^{(H)} \end{pmatrix} = \begin{pmatrix} 0 \\ 0 \\ \psi^{(E_z)} \\ \psi^{(H_x)} \\ \psi^{(H_y)} \\ 0 \end{pmatrix}, \tag{2.88}$$

and, in the absence of bianisotropy, express Maxwell's equations as two separate scalar eigenproblems [16, 17].

Separability of TE/TM polarizations 2D PhCs consist of dielectric elements periodic in the x, y plane, ideally infinite and continuous along z. This means that both ε and μ can be written as z-independent tensors of the form:

$$v = \begin{pmatrix} v_{2D} & 0 \\ 0 & v_3 \end{pmatrix}, \tag{2.89}$$

where $v = v(x, y)$ and where v_{2D} is 2×2. Because of the block-diagonal structure, the electric fields in the x, y-plane, of the form $\psi^{(E)} = \begin{pmatrix} \psi^{(E_x)} \\ \psi^{(E_y)} \\ 0 \end{pmatrix}$ induce the time-dynamics only for the $z-$component of the magnetic field $\psi^{(H)} = \begin{pmatrix} 0 \\ 0 \\ \psi^{(H_z)} \end{pmatrix}$. This means that TE modes only evolve into TE modes. The same applies to TM modes. The z-independence of the dielectric tensor allows to further factor the fields into a product via a plane-wave in z:

$$\psi(x, y, z) = \psi(x, y)e^{ik_z z}, \tag{2.90}$$

making therefore possible to define a 2D Maxwell scalar eigenproblem for TM and TE polarizations, separately [16, 17].

The polarization-decoupled wave equations in 2D become particularly simple when we consider isotropic, real-valued dielectric media, having diagonal $\varepsilon_{2D} = \mathrm{diag}[\varepsilon, \varepsilon]$ and $\mu_{2D} = \mathrm{diag}[\mu, \mu]$. In the second-order formulation of **Equation 2.56**,

we have, for TE modes:

$$\frac{1}{\mu}\left(\partial_x \frac{1}{\varepsilon}\partial_x + \partial_y \frac{1}{\varepsilon}\partial_y\right)\psi^{(H_z)} + \omega^2\psi^{(H_z)} = 0 \tag{2.91}$$

and, for TM modes:

$$\frac{1}{\varepsilon}\left(\partial_x \frac{1}{\mu}\partial_x + \partial_y \frac{1}{\mu}\partial_y\right)\psi^{(E_z)} + \omega^2\psi^{(E_z)} = 0. \tag{2.92}$$

Note that, for non-magnetic media ($\mu = 1$), the TM wave equation exactly map to the Poisson equation with refractive contrast $n^2 = \varepsilon$:

$$\left(\partial_x^2 + \partial_y^2\right)\psi^{(H_z)} + (n\omega)^2\,\psi^{(H_z)} = 0. \tag{2.93}$$

which establishes an parallelism between 2D acoustic waves with mass stiffness profile $\sigma(x, y)$ [118] and 2D TM electromagnetic waves with refractive index profile $n(x, y)$. TE and TM solutions to **Equations 2.91** and **2.92** circumvent the Γ-point issue since they automatically satisfy the transversality constraint: at Γ and zero frequency, any TE or TM mode with constant amplitude and polarization vector $\hat{u}$ aligned with the $\hat{z}$ direction qualifies as a valid solution. This alignment with $\hat{z}$ ensures orthogonality to k_x and k_y. In practice, the TE/TM decoupling has allowed to transformation of the Maxwell vector eigenproblem into a scalar one. As a result, 2D PhCs admit photonic counterparts of maximally localized Wannier functions, derived via solid-state Wannierization techniques [131–133]. These functions can serve as a basis set for constructing a robust 2D tight-binding model of the 2D PhCs. As well, the scalar nature of 2D PhCs allows the application of standard TQC methods [33, 134], which have proven useful for the definition and the study of fragile topology in either TE or TM modes [33, 135].

2.3.2 Symmetry Classification of Topological PhCs

In **Section 2.3.1.1**, we explored how the spatial variation of the dielectric function in PhCs can create photonic bandgaps—frequency regions where light propagation is forbidden due to interference within the periodic structure. Now, our focus shifts to understanding the possible topological invariants associated with these bandgaps in PhCs. The Cartan-Altland-Zirnbauer (CAZ) classification scheme, also known as the Ten-Fold Way, is a standard framework used for categorizing topological phases in various physical systems, including topological insulators and superconductors. This

classification is based on the symmetries of a gapped Hamiltonian and comprises ten distinct topological classes. Each class hosts different topological phases distinguished by specific invariants, such as Chern numbers or Kane-Mele invariants. The calculation of these invariants is approached through cohomological methods, involving the analysis of mappings from the BZ's torus ($\mathbb{T}^d$) to the Bloch sphere of two-band gaps ($\mathbb{S}^2$). The nature and quantity of these invariants depend on both the system's symmetries and its dimensionality (d). In this section, we briefly review the CAZ classification of gapped Maxwell operators in PhCs. The resulting periodic table of PhCs will allow us to highlight key peculiarities of topological photonics as compared to the conventional classification theory in condensed matter systems. These differences arise from the real-valued nature of electromagnetic fields, the presence of electromagnetic duality symmetries, and the absence of either Kramers degeneracy or charge.

2.3.2.1 Dielectric or material symmetries

Topological PhCs are classified on the basis of the possible symmetry transformations of the Maxwell operator $\mathcal{M}$, which we denote as dielectric or material symmetries. In the spirit of the CAZ scheme, symmetries of the Maxwell operator are distinguished on the basis of them being unitarity/antiunitary and commuting/anticommuting, considering:

- Unitary operators U with $U^2 = \mathbb{1}$, that implement:
  - Regular or isospin type of symmetries, when commuting:

$$U\mathcal{M}U^{-1} = +\mathcal{M} \tag{2.94}$$

  - Chiral or sublattice type of symmetries (S), when anticommuting:

$$U\mathcal{M}U^{-1} = -\mathcal{M} \tag{2.95}$$

- Antiunitary operators T (which can be even or odd $T^2 = \pm\mathbb{1}$), that implement:
  - Time-reversal type symmetries (T), when commuting, similarly to **Equation 2.94**
  - Particle-hole symmetries (C), when anticommuting, similarly to **Equation 2.95**.

Following the approach guiding the CAZ scheme [24, 25], at the basis of the periodic table of topological insulators, the initial classification of topological PhCs will exclude those symmetries which are both commuting. This exclusion is based on the premise that these symmetries are assumed to commute with the other types of symmetries mentioned earlier in the CAZ scheme.

Maxwell Linear Formulation The distinction between commuting and anticommuting symmetries is a key aspect for the CAZ topological classification, and it has been often overlooked in the analysis of PhCs [30]. In order to correctly classify the Maxwell operator, it is necessary to employ the first-order formulation, instead of the quadratic formulation, described in **Section 2.2.9**. The reason is that in the second-order one, one can no longer distinguish between operators U which commute or anti-commute with the quadratic Maxwell operator, because in both cases:

$$U\mathcal{M}^2U^{-1} = (\pm 1)^2\mathcal{M}^2. \tag{2.96}$$

In order to study the action of the symmetries on the (linear) Maxwell operator, we will represent the transformations in terms of Pauli matrices, with unitary operations written as:

$$U_i = (\sigma_i \otimes \mathbb{1}), \tag{2.97}$$

and antiunitary ones as:

$$T_i = (\sigma_i \otimes \mathbb{1})K, \tag{2.98}$$

where σ_i, $i = 1..3$ are the Pauli matrices, equipped with the identity $\sigma_0 = \mathbb{1}$.

	Commuting	Anticommuting
Unitary (U_i)	Regular, e.g. isospin	Chiral, e.g. sublattice (CAZ ✓)
Antiunitary (T_i)	Time Reversal (CAZ ✓)	Particle Hole (CAZ ✓)

Table 2.4: Distinction of possible material symmetries employed in the CAZ classification, in terms of their commutation and unitarity properties. Commuting unitary symmetries are usually excluded from the CAZ scheme. Note that antiunitary transformations can be of two types: even or odd ($T^2 = \pm\mathbb{1}$).

Correspondingly, we will express the free Maxwell operator:

$$\mathcal{M}_{\text{free}} = \text{Rot} = \begin{pmatrix} 0 & +i\boldsymbol{\nabla}\times \\ -i\boldsymbol{\nabla}\times & 0 \end{pmatrix} = -\sigma_2 \otimes (\boldsymbol{\nabla}\times) \tag{2.99}$$

where $\boldsymbol{\nabla}\times$ is the curl. Similarly, for the constitutive tensor:

$$\mathcal{K} = \begin{pmatrix} \varepsilon & \xi \\ \xi^{\dagger} & \mu \end{pmatrix} = \begin{pmatrix} v_0 + v_3 & v_1 - iv_2 \\ v_1 + iv_2 & v_0 - v_3 \end{pmatrix} = \sum_{i=0}^{3} \sigma_i \otimes v_i \tag{2.100}$$

where v_i are 3x3 Hermitian matrices, defined as:

$$v_0 = \frac{\varepsilon + \mu}{2} \qquad v_3 = \frac{\varepsilon - \mu}{2} \tag{2.101}$$

$$v_1 = \frac{\xi^{\dagger} + \xi}{2} \qquad v_2 = \frac{\xi^{\dagger} - \xi}{2i}. \tag{2.102}$$

2.3.2.2 Admissible symmetries in PhCs

All the symmetries which map positive frequency states into negative frequency states need to be discarded since they can break the physical real-valuedness constraint of the electromagnetic fields, discussed in **Section 2.2.7**. With these assumptions, together with the hypothesis about Hermiticity and positive index of $\mathcal{K}$ adopted in **Section 2.1**, it is easy to show that only three operations are admissible:

$$T_1, T_3, U_2. \tag{2.103}$$

As we will see in **Section 2.3.2.3**, T_1 and T_3, implement two physically distinct types of time-reversal symmetries. As we will see in **Section 2.3.2.6** the U_2 transformation, represents electromagnetic duality symmetry. The specific conditions on v_i which arise from imposing the commutation/anticommutation relations with $\mathcal{K}$, have been derived by Ref. [28, 39], and are summarized in **Table 2.5**.

	$(v_0 =)$	$(v_1 =)$	$(v_2 =)$	$(v_3 =)$
T_1	$\mathrm{Re}(v_0)$	$\mathrm{Re}(v_1)$	$\mathrm{Re}(v_2)$	$\mathrm{iIm}(v_3)$
T_3	$\mathrm{Re}(v_0)$	$\mathrm{iIm}(v_1)$	$\mathrm{Re}(v_2)$	$\mathrm{Re}(v_3)$
U_2	v_0	0	v_2	0

Table 2.5: Constraints on the components of the consitutive tensor $\mathcal{K}$, in presence of the three admissible material symmetries: T_1, T_3, U_2. Adapted from Refs. [28, 39]

2.3.2.3 Even time reversal symmetry

PhCs can present two types of time-reversal symmetries (TRS), denoted as T_3 and T_1. T_3 is a symmetry characteristic of non-gyrotropic and non-magnetoelectric media, which comprise most of the well-known dielectric media, of the silicon type. Instead,

T_1 hold in certain type of bianisotropic structures, where electric and magnetic fields are coupled. Both T_1 and T_3 are classified as TRS operators since they are implemented in an anti-commuting and anti-unitary way [24,25]. As well, both of these symmetries are even-type, bosonic symmetries, squaring to identity. Let's analyze briefly each of them individually.

2.3.2.4 T_3 for real-valued media

$T_3 = (\sigma_3 \otimes \mathbb{1})K$ acts on the complexified fields as:

$$T_3 : \psi = \begin{pmatrix} \psi^{(E)} \\ \psi^{(H)} \end{pmatrix} \rightarrow \begin{pmatrix} \overline{\psi}^{(E)} \\ -\overline{\psi}^{(H)} \end{pmatrix} \tag{2.104}$$

with $T_3^2 = \mathbb{1}$. The invariance under T_3 on the Maxwell operator:

$$T_3 \mathcal{M} T_3^{-1} = +\mathcal{M}, \tag{2.105}$$

imposes constraints on the dielectric tensor's components, specifically that υ_0, υ_2, and υ_3 must be real, while υ_1 must be purely imaginary. In more practical terms, this constraint results in the dielectric and magnetic permeability (ϵ and μ) being real-valued. Non-bianisotropic materials meeting these conditions for υ_i represent are non-gyrotropic, also denoted as real-valued dielectric media. Many well-known dielectrics, fall into this category [136–138] and are referred to as type-AI media in the CAZ scheme [25].

Complex Conjugation The breaking of T_3 is a pivotal factor enabling the existence of unidirectional edge channels and non-reciprocal properties in PhCs. Otherwise, modes occur in counterpropagating pairs that are linked by time-reversal symmetry. In the microwave regime, PhCs made of yttrium–iron–garnet (YIG) can break T_3 via gyrotropy [98, 139, 140]. Strictly speaking TRS in PhCs isn't realized through complex conjugation (K), as it is sometimes assumed [10, 30]. While this may seem like a formal subtlety with no relevant practical difference, it holds theoretical significance in correctly assigning the CAZ class. In the CAZ scheme, K is an even particle-hole symmetry, associated with class D [24, 25] and not in class AI, as it should correctly be. In addition, as shown in **Section 2.2.7**, K is not even a conven-

tional symmetry of the Schrödinger operator, since it relates positive to negative frequencies. Physical time-reversal symmetry acts on the real electromagnetic fields as follows:

$$T : \begin{pmatrix} \mathbf{E}(t) \\ \mathbf{H}(t) \end{pmatrix} \to \begin{pmatrix} \mathbf{E}(-t) \\ -\mathbf{H}(-t) \end{pmatrix}, \tag{2.106}$$

which, at the level of complex fields ψ is implemented via T_3.

2.3.2.5 T_1 for magneto-electric coupling

Interestingly, T_3 is not the only TRS-type symmetry admissible in PhCs. Together with it, T_1 is another candidate TRS operator:

$$T_1 = (\sigma_3 \otimes \mathbb{1})K. \tag{2.107}$$

T_1 is also a TRS-type operation, which exchanges electric and magnetic fields and then complex conjugates them, therefore playing an important role in the analysis of magneto-electric media. Imposing T_1 to be a symmetry of the Maxwell operator translates on the conditions for which v_3 is imaginary and v_0, v_1, v_2 are real-valued tensors, which are satisfied by certain bianisotropic media, having non-zero magneto-electric coupling ξ [74].

Photonic Analogues of QSHE T_1 is an even, bosonic TRS:

$$T_1^2 = \mathbb{1}. \tag{2.108}$$

In the CAZ classification scheme, the QSHE has a precise definition: the system belongs to class AII [141], indicating the presence of an odd time-reversal symmetry:

$$T_{\text{QSHE}}^2 = -1, \tag{2.109}$$

which directly leads to the phenomenon of spin-momentum locking, due to Kramer's protection [142] i.e. the two-fold degeneracy of energy levels in systems with odd time-reversal symmetry. Electromagnetic media do not support odd time-reversal symmetries: both T_1 and T_3

are even. Various effects have been proposed as photonic counterparts of the Quantum Spin Hall Effect (QSHE) either in magneto-electric media relying on T_1 [143, 144] or in real-dielectric media with T_3, in combination with other symmetries. The even nature of bosonic TRS in PhCs does not allow a strict QSHE identification of these topological phases. In combination with other symmetries, it is possible to emulate the response of photonic QSHE in terms of an effective Hamiltonian, even though neither T_1 or T_2 cannot directly impart Kramer's protection.

2.3.2.6 Electromagnetic duality

The presence of both T_1 and T_3 imply the existence of a third combined symmetry

$$T_1 T_3 = i(\sigma_2 \otimes \mathbb{1}) = iU_2 \tag{2.110}$$

which represents electromagnetic duality (D) [104, 145–147]. When U_2 commutes with M, it implies to the vanishing of $v_1 = 0 = v_3$. This is equivalent to say that electric permittivity and magnetic permeability coincide

$$\varepsilon = \mu. \tag{2.111}$$

Vacuum is the simplest realization of this condition. The presence of this symmetry allows to split our frequency-degenerate solutions into left- or right-handed helicity components. In others terms, the Maxwell operator can be block-decomposed as:

$$M = \begin{pmatrix} \mathcal{M}_{h=+} & 0 \\ 0 & \mathcal{M}_{h=-} \end{pmatrix} \tag{2.112}$$

where the operators $\mathcal{M}_{h=\pm} = H_\pm \mathcal{M} H_\pm$ are obtained via the helicity projectors:

$$H_{h=\pm} = \frac{1}{2}(\mathbb{1} \pm D) \tag{2.113}$$

onto right-handed and left-handed circularly polarized waves.

Duality beyond CAZ Dual symmetric media have two types of even TRS and therefore fall outside of the traditional CAZ scheme. In simple terms, we can think of dual symmetric media as a direct sum of two

class AI bundles [28, 39]:

$$\mathrm{AI} \oplus \mathrm{AI}. \tag{2.114}$$

This is because neither T_1 or T_3 mix left- and right-handed states, and when restricted to helicity components, they are not longer distinct operations. In addition, duality is a unitary commuting operation: such transformations are deliberately left out the CAZ scheme. Whether duality (or antiduality [27]) symmetry can protect other type of invariants beyond the CAZ remains an open question, which we address in more detail in **Section 5.3**.

2.3.2.7 Reduced periodic table of PhCs

In terms of the three admissible symmetries (T_1,T_3 and U_2), it is possible to provide a topological classification of PhCs across various d spatial dimensions, by simple application of the CAZ scheme [24, 25]. This allows to compile a periodic table of *insulating* topological PhCs, **Table 2.6**. Notably, the periodic table of PhCs consists of a subset of the electronic counterpart, as it does not include charge-conjugation (C) nor chiral-type (S) operations of the type described in **Equation 2.95**. The table provides a summary of dielectric media categorized by the material symmetries discussed insofar, along with examples of dielectric realizations falling into each category.

Isospin Symmetries The CAZ classification scheme deliberately leaves out additional material symmetries that are both unitary and commutative (such as isospin-symmetries U_{ISO}). When such symmetries are present, it is important to understand their interplay with the other pre-existing symmetries pertaining to the Maxwell operator, by breaking down the Maxwell operator into block operators that act within the eigenspaces of the extra symmetry U_{ISO}.These extra symmetries can become useful for the definition of isospin-resolved invariants, which arise in topological phases protected by symmetries that are a combination of an extra symmetry and a material symmetry. Examples have been demonstrated in Ref. [30], employing a combination of TRS and a crystalline symmetry (C_6), or in Ref. [149] employing a combination of parity(P), duality (D) and TRS (PDT).

Media	Dielectric Proposal/Realization	Symmetries	CAZ	$d=1$	$d=2$	$d=3$	$d=4$
Gyrotropic	YIG rods (IR) [139]	None	A	0	1st Chern ($\mathbb{Z}$)	three 1st Chern ($\mathbb{Z}^3$)	six 1st, one 2nd Chern ($\mathbb{Z}^6 \oplus \mathbb{Z}$)
Real-valued dielectric	Silicon (VIS) Refs. [38, 148]	T_3	AI	0	0	0	one 2nd Chern ($\mathbb{Z}$)
Magneto-electric	Metamaterials [74, 144]	T_1	AI	0	0	0	one 2nd Chern ($\mathbb{Z}$)
EM Dual	Vacuum [145]	T_1, T_3, U_2	AI $\oplus$ AI	0	0	0	two 2nd Chern ($\mathbb{Z}^2$)

Table 2.6: Topological classification of dielectric media in the CAZ scheme [28, 29]. Topologically trivial is indicated by zero.

2.3.2.8 Bulk-boundary correspondence

Photonic phases with nontrivial topological indices in the CAZ scheme realize topological protection through conventional (first-order) bulk-boundary correspondence (BBC), i.e. present gapped d-dimensional bulk and gapless $d-1$ edges, whose respective topological invariants T_{bulk} and quantized observables O_{boundary} are related:

$$T_{\text{bulk}} \sim O_{\text{boundary}}. \tag{2.115}$$

In practical terms, however, BBC manifests slightly differently in photonics than in electronics. The first challenge is posed by the role of the electromagnetic vacuum. In electronics, the vacuum is inherently a trivial insulator. However, in photonics, due to radiation through the electromagnetic continuum, the vacuum can potentially conduct light. Avoiding this conduction this requires precise parameter tuning of the crystal to confine edge modes within the topological gap, ensuring they fall outside the light cone [17]. Alternative strategies have been successfully explored, like terminating the PhC with quasi-perfect mirrors [11] or employing two different PhCs with overlapping relevant photonic band gaps [50, 144]. The second issue concerns the role of quantization. The photonic Chern number has no clear quantum of conductance associated, except that it determines the number of unidirectional edge states supported by a trivial interface. In this context, Ref. [80] has shown a possible connection between the photonic Chern number and the quantum of the light-angular momentum in a photonic insulator cavity. The question remains still unclear for other types of topological invariants, such as the magnetoelectric angle.

2.3.3 Space-Group Symmetries

In the preceding section, our focus was primarily on material symmetries- those governing the relationships between electric and magnetic field components. In this section, we shift our focus to examining the role of crystalline symmetries, by considering the transformation properties of the Maxwell eigenproblem under spatial transformations. Including spatial symmetries in the topological classification allows the definition of new topological invariants. These invariants are at the basis of the topological protection of crystalline insulators [150,151]. Let's begin by considering a space group denoted as G [152–154]. Within this group, its elements are represented as g and defined as follows:

$$g = \{R|\mathbf{t}\}, \tag{2.116}$$

where R is an orthogonal transformation with $\det R = \pm 1$, where the sign distinguishes proper (+, e.g. rotation around an axis) and improper operations (−, e.g. inversions and reflections), and where $\mathbf{t}$ is a fractional lattice translation $\mathbf{t}$. The transformation of the coordinate vector $\mathbf{r}$ in the Maxwell problem can be expressed as:

$$g\mathbf{r} = \{R|\mathbf{t}\}\mathbf{r} = R\mathbf{r} + \mathbf{t}. \tag{2.117}$$

The $\psi^{(E)}$ electric field transforms a vector and the $\psi^{(H)}$ magnetic field is a pseudovector [16]:

$$g\psi^{(E)} = (R\psi^{(E)})(g^{-1}\mathbf{r}), \tag{2.118}$$

$$g\psi^{(H)} = \det(R)(R\psi^{(H)})(g^{-1}\mathbf{r}), \tag{2.119}$$

transforming both via their components and their coordinates. A PhC belongs to a space group G if the Maxwell eigenproblem remains invariant under all the spatial symmetries $g \in G$. In other words, when the Maxwell operator satisfies **Equation 2.94**:

$$g\mathcal{M}g^{-1} = \mathcal{M}, \tag{2.120}$$

which directly translates on the equivalent conditions for the constitutive tensor $\mathcal{K}$. For a PhC belonging to a space group G, we can define the $x(g)$ symmetry eigenvalue of the electromagnetic fields for an operation $g \in G$ as follows:

$$x(g) = \langle \psi | g\psi \rangle_{\mathcal{K}}, \tag{2.121}$$

where the energy inner-product structure **Equation 2.30** is involved. In the case of non-magneto electric media, $x(g)$ can be equivalently obtained via the electric or the magnetic field only.

2.3.3.1 Irrep characterization of photonic modes

To analyze photonic band structures, we compute symmetry eigenvalues from Bloch eigenmodes $\varphi_{\mathbf{k},n}$ in reciprocal space as:

$$x_{\mathbf{k},n}(g) = \langle \varphi_{\mathbf{k},n} | g\varphi_{\mathbf{k},n} \rangle_{\mathcal{K}}, \tag{2.122}$$

where g is an element in the little group $G_{\mathbf{k}}$ of the high-symmetry point (HSP) $\mathbf{k}$. These symmetry eigenvalues can be used to extract the multiplicity of the irreducible representations (irreps) $\rho_{i[\mathbf{k}]}$ in the HSP class $[\mathbf{k}]$, where i labels the particular irrep.

Using Schur's orthogonality relations [152, 153], we can compile the vector:

$$\mathbf{v}_{\mathbf{k}} = \bigoplus_{i} n_{i[\mathbf{k}]}\rho_{i[\mathbf{k}]}, \tag{2.123}$$

containing the multiplicity $n_{i[\mathbf{k}]}$ of each $\rho_{i[\mathbf{k}]}$ irrep. Obtaining these irreps is crucial for constructing reliable symmetry-adapted models of the photonic bands in the vicinity of $\mathbf{k}$. In **Appendix A**, we demonstrate this by building a $\mathbf{k}\cdot\mathbf{p}$ model of a photonic Weyl point.

2.3.3.2 Ill-defined symmetry content at zero-energy

By collecting $\mathbf{v}_{\mathbf{k}}$ at all HSPs, we can assemble the so-called symmetry vector [128, 129, 155, 156]:

$$\mathbf{v} = \bigoplus_{\mathbf{k}} \mathbf{v}_{\mathbf{k}}, \tag{2.124}$$

which encapsulates all the pertinent space-group symmetry information for the n bands of interest. The procedure has to be carried out on a bundle of bands that can form an isolated set that satisfies the compatibility relations. The symmetry vector serves as the foundation for applying TQC methods to PhCs [33,134] and for developing TB models, capable of reproducing symmetry and topological features throughout the BZ [123]. This step can be realized smoothly in 2D PhCs, via TE and TM modes. Unfortunately, in 3D PhCs, assigning irreps at $\mathbf{k} = 0$ and $\omega = 0$ becomes problematic due to the Γ-point obstruction, originating from the Maxwell transversal constraint as discussed in **Section 2.3.1.3**. In certain cases, we can extrapolate the symmetry content at the Γ point from the asymptotic behavior for the lowest transverse modes in the $\mathbf{k} \to 0$ limit, particularly in space groups without (roto-)inversions, by considering the high symmetry lines and planes intersecting Γ [122]. However, even when this is possible, the symmetry content at Γ can be singular, as it involves a *difference* of irreps. To address this issue, Ref. [23] introduced the concept of a transverse symmetry vector ($\mathbf{v}^T$):

$$\mathbf{v}^T = \bigoplus_{i,[\mathbf{k}]} n_{i[\mathbf{k}]}\rho_{i[\mathbf{k}]} \oplus (\blacksquare)^{2T}, \tag{2.125}$$

which includes the symbolic expression $(\blacksquare)^{2T}$ to denote the ill-defined symmetry content associated with the lowest two transverse (2T) modes at Γ and $\omega = 0$. The singularity in the symmetry content at Γ precludes the construction of 3D TB models for PhCs using standard Wannierization techniques. We will address this issue in **Section 3.2** and propose solutions to circumvent these limitations.

Chapter 3

Methods

In this chapter, we present dimension-specific modeling and characterization techniques designed to explore the topology in 3D PhCs. The vectorial and transversal nature of light makes determining topological invariants and developing analytical models in 3D challenging. While many topological methods have been crafted for scalar waves, they require modifications to extend to vector fields in PhCs. The transversality conditions set by Maxwell's equations in periodic dielectric media add complexity to the Maxwell problem beyond other 3D classical waves. A primary reason is the non-analytic behavior of photonic eigenstates throughout the BZ at the zero energy limit, attributed to the Γ point obstruction. This characteristic makes constructing tight-binding models over the entire BZ difficult and hinders the smooth evaluation of topological invariants, which are defined non-locally in the 3D momentum space. To effectively design and analyze 3D topological phases of light, we intend to develop characterization methods tailored to address and solve these specific challenges. The contents of this chapter are divided into two sections:

- **Electromagnetic Wilson Loops for 3D PhCs** (**Section 3.1.1**). We begin by introducing electromagnetic Wilson loop and hybrid Wannier energy centers as versatile tools for characterizing topology in PhCs. We address our focus on 3D PhCs, highlighting the necessary adjustments to apply these methods in the context of vectorial waves and to overcome the Γ-point obstacle. Finally, we offer a practical tutorial for computing 3D-specific topological invariants using the aforementioned tools. These 3D invariants include the charge of the Weyl points (q_{W}), the Chern vector ($\mathbf{C} = (C_x, C_y, C_z)$), the magnetoelectric axion angle (θ), and the Weyl nodal wall monopole charge (q_{WNW}).
- **Tranversality Enforced Tight Binding Models for 3D PhCs** (**Section 3.2**).

We introduce a novel strategy for modeling 3D topological PhCs using a tight-binding approach, overcoming the absence of maximally localized Wannier functions in 3D PhCs. This technique comprises of two steps: extracting a pseudo-orbital basis through group theoretical arguments and constructing a tight-binding model with enforced transversality. The resulting model efficiently regularizes the singularity at the BZ origin, preserves the PhC's symmetries, and accurately reproduces its topological and energetic traits.

The methods developed in this chapter permit us to overcome the theoretical challenges associated to the vectorial nature of light in 3D PhCs, and will allow us to comprehensively model and characterize the topological properties of the photonic 3D topological phases proposed in **Chapter 4**.

3.1 Computing Topological Invariants in *3D* PhC

This section serves as a practical guide for the topological characterization of 3D PhCs via numerical methods. Our goal is to extend the methodologies presented in our recent tutorial for 2D PhCs: "Tutorial: Computing Topological Invariants in 2D PhC" [1] to the field of 3D PhCs. As highlighted in **Chapter 2**, the nature of 3D electromagnetic waves is significantly different from that of 2D ones, which have scalar electronic analogies. The key distinctions arise from the vectorial nature of light and the presence of the Γ point obstruction in 3D PhCs (see **Section 2.3.1.3**). Therefore, this section will have a special focus on the necessary adjustments needed for this change of dimensionality.

In particular, we offer strategies for computing the following 3D topological invariants:

- the monopole charge of a Weyl point (q_W) in a photonic Weyl semimetal.
- the Chern vector ($\mathbf{C} = (C_x, C_y, C_z)$) characterizing a 3D photonic insulator,
- the topological charge of a Weyl nodal wall (q_{WNW}) in a photonic nodal semimetal,
- the axion angle (θ) of a photonic axion insulator,

The pivotal step in the numerical evaluation of these invariants is the implementation of electromagnetic Wilson loops. As we will show, these represent a very versatile tool able to identify a large variety of 3D topological invariants. The concept of concept of electromagnetic Wilson loops is introduced in **Section 3.1.1**.

3.1.1 Electromagnetic Wilson Loops

An alternative approach to characterize the PhC topology with respect to the Berry phase of **Equation 2.77** is to compute the path-order exponential of the Berry connection defined in **Equation 2.76** for the $m, n = 1...N_{band}$ bands of interest:

$$\mathcal{W}_{m,n}(\ell) = \mathcal{P}e^{i\oint_\ell \mathbf{A}_{m,n}(\mathbf{k})\cdot d\ell}, \tag{3.2}$$

an object also called Wilson Loop (WL) operator for the closed loop ℓ [157, 158]. The WL operator forms a matrix representation of a holonomy [159, 160], acting as a parallel transport for eigenstates along the closed path ℓ. Therefore, it encapsulates crucial topological information concerning the geometric phases accumulated along the loop ℓ.

3.1.1.1 Discrete Limit

From the definition of the Berry connection of **Equation 2.76**, it is easy to show that the Wilson line between two discrete momenta ($\mathbf{k}$ and $\mathbf{k}+\epsilon$) is given by the following:

$$\mathcal{W}_{m,n}^{\mathbf{k}+\epsilon\leftarrow\mathbf{k}}(\epsilon) = \langle u_{m,\mathbf{k}+\epsilon}|u_{n,\mathbf{k}}\rangle_{\mathcal{K}}, \tag{3.3}$$

where ϵ is the momenta separation and the $\leftarrow$ arrow keeps track of the patch-ordering. Reversing the path $\epsilon = \epsilon^T$ gives:

$$(\mathcal{W}_{m,n}^{\mathbf{k}+\epsilon\leftarrow\mathbf{k}}(\epsilon))^{-1} = (\mathcal{W}_{m,n}^{\mathbf{k}\leftarrow\mathbf{k}+\epsilon}(\epsilon^T)) = (\mathcal{W}_{m,n}^{\mathbf{k}+\epsilon\leftarrow\mathbf{k}}(\epsilon))^\dagger. \tag{3.4}$$

The WL discretization via Wilson lines allows to describe the WL operator as a path-order product of overlap matrices. Specifically, for a closed loop that starts at a base-point $\mathbf{k}_{(0)}$ and ends at $\mathbf{k}_{(F)} = \mathbf{k}_{(0)}$, we can express the m, n matrix element of the Wilson loops as:

$$\mathcal{W}_{m,n}(\ell) = \mathcal{W}_{m,p}^{\mathbf{k}_{(F)}\leftarrow\mathbf{k}_{(N)}}\mathcal{W}_{p,q}^{\mathbf{k}_{(N)}\leftarrow\mathbf{k}_{(N-1)}}...\mathcal{W}_{r,s}^{\mathbf{k}_{(2)}\leftarrow\mathbf{k}_{(2)}}\mathcal{W}_{s,n}^{\mathbf{k}_{(1)}\leftarrow\mathbf{k}_{(0)}}, \tag{3.5}$$

where the points of the path are ordered as $\{\mathbf{k}_{(F)}, \mathbf{k}_{(N)}, \mathbf{k}_{(N-1)}, .., \mathbf{k}_{(2)}, \mathbf{k}_{(1)}, \mathbf{k}_{(0)}\}$ with $N >> 1$, and where $p, q, r, s = 1...N_{band}$ label the band index. Since overlap matrices in **Equation 3.2** can be easily evaluated numerically, this expression gives a computationally efficient way to obtain the WL and the associated topological invariants.

3.1.1.2 Gauge Invariance and Band Projectors

Here we aim to highlight some key properties of the WL operator and its spectrum. From the **Equation 3.5**, we can compactly write the WL operator as a path-order product of projectors:

$$\mathcal{W}_{m,n}(\ell) = \langle u_{m,\mathbf{k}_{(F)}} | \prod_{j}^{\mathbf{k}_{(F)} \leftarrow \mathbf{k}_{(0)}} P_{\mathbf{k}_{(j)}} | u_{n,\mathbf{k}_{(0)}} \rangle_{\mathcal{K}}, \tag{3.6}$$

where $P_{\mathbf{k}}$ is the projector over the bands of interest N_{band}, at momentum $\mathbf{k}$:

$$P_{\mathbf{k}} = \sum_{m=1}^{N_{band}} |u_{m,\mathbf{k}}\rangle_{\mathcal{K}} \langle u_{m,\mathbf{k}}|. \tag{3.7}$$

Clearly, these projectors are left invariant under a general $U_{\mathbf{k}}(N_{band})$ gauge transformation of the subspace of the bands of interest, i.e. a rotation in the N_{band} dimensional space of the bands below a bandgap:

$$|u_{n,\mathbf{k}}\rangle \rightarrow \sum_{m=1}^{N_{band}} U_{\mathbf{k}}^{m,n} |u_{m,\mathbf{k}}\rangle. \tag{3.8}$$

As a result, the WL is gauge-covariant, meaning that it transforms as an operator, while its spectrum is gauge-invariant. Moreover, the Wilson loop eigenvalues do not depend on the choice of base point $k_{(0)} = k_{(F)}$, as can be deduced from **Equation 3.4**).

3.1.1.3 Spectral Properties

The WL eigenvalues consist of phase factors, as follows from the WL definition in terms of the path-ordered exponential of the Berry connection:

$$\text{spec}[\mathcal{W}(\ell)] = \{e^{iw_n(\ell)}\}_{n=1}^{N_{band}}. \tag{3.9}$$

The Wilson loop $w_n(\ell)$ phases, defined modulo 2π, represent the "geometrical" phase accumulated along the ℓ loop. For $N_{band} = 1$, these quantities coincide with the Berry's phases. For more general N_{band}, the WL spectrum represents the non-Abelian Berry phases for multi-band system. A total Berry phase for the entire subspace be defined as:

$$\phi(\ell) = \sum_{n=1}^{N_{band}} w_n(\ell), \tag{3.10}$$

which becomes relevant in the case of multi-band systems.

3.1.1.4 Hybrid Wannier Centers

A spectral mapping can be established between the eigenvalues of the **x**-directed WL and those of the $\hat{\mathbf{x}}$ position operator, providing a physical interpretation of the WL in the context of hybrid Wannier centers [161, 162]. Note that, for simplicity of presentation, we will illustrate this fact focusing on the **x**-direction with orthogonal (k_y, k_z) momenta. However, these results hold also for non-orthogonal lattices, replacing **x** with $\mathbf{a}_1$ and substituting the orthogonal momenta with their projected components $(\mathbf{k}\cdot\mathbf{a}_2, \mathbf{k}\cdot\mathbf{a}_3)$ where $\mathbf{a}_m$ are the primitive lattice vectors defined in **Equation 2.64**. To demonstrate the spectral equivalence just mentioned, we consider a closed path parallel to the k_x axis. We label the WL computed along this $\hat{\mathbf{x}}$-directed path, with the remaining $(d-1)$-dimensional momenta orthogonal to it as $\mathbf{k}_\perp$:

$$\mathcal{W}_X = \mathcal{W}(\mathbf{k}_\perp). \tag{3.11}$$

The phases of this object $(w_n(\mathbf{k}_\perp))$ constitute an effective $(d-1)$-dimensional bandstructure in $\mathbf{k}_\perp$. However, unlike a traditional band structure, the WL phases are defined only modulo 2π. It is possible to show that eigenvalues of the $\mathcal{W}_X$ are related to those of the $\hat{\mathbf{x}}$ position operator, projected over the bands of interest [163]:

$$P_{\mathbf{k}_\perp}\hat{\mathbf{x}}P_{\mathbf{k}_\perp}, \tag{3.12}$$

where the projectors:

$$P_{\mathbf{k}_\perp} = \int_{-\pi/a_x}^{\pi/a_x} \frac{dk_x}{2\pi} P_{\mathbf{k}} \tag{3.13}$$

are defined similarly as in **Equation 3.7**. These $x_n(\mathbf{k}_\perp)$ eigenvalues of $P_{\mathbf{k}_\perp}\hat{\mathbf{x}}P_{\mathbf{k}_\perp}$ have the interpretation of hybrid Wannier centers, and the corresponding eigenstates are known as $\hat{\mathbf{x}}$-localized hybrid Wannier functions $|X_{n,\mathbf{k}_\perp}\rangle$. Hybrid Wannier Functions (HWF) are confined in the $\hat{\mathbf{x}}$-direction, and extend as Bloch-waves perpendicular to $\hat{\mathbf{x}}$ [164, 165]:

$$|X_{n,\mathbf{k}_\perp}\rangle = a_x \int_{-\pi/a_x}^{\pi/a_x} \frac{dk_x}{2\pi} e^{-ik_x a_x} U_{\mathbf{k}}^{m,n} |\psi_{m,\mathbf{k}}\rangle. \tag{3.14}$$

When the mixing matrix $U_{\mathbf{k}}^{m,n}$ is chosen to maximally localize the Wannier function along $\hat{\boldsymbol{x}}$ by minimizing the quadratic spread functional [164], the corresponding Wannier centers $(x_n(\mathbf{k}_\perp))$ coincide with the phases of the WL operator. To be precise, a spectral mapping can be established between the phases of the $\mathcal{W}_X$ operator $(w_n(\mathbf{k}_\perp))$

and the eigenvalues of the $\hat{\mathbf{x}}$ projected position operator ($x_n(\mathbf{k}_\perp)$), according to:

$$\frac{w_n(\mathbf{k}_\perp)}{2\pi} = \frac{x_n(\mathbf{k}_\perp)}{a_x} \pmod 1, \tag{3.15}$$

which is valid up to possible reordering.

Energy vs Charge Centers For electromagnetic waves, the interpretation of hybrid Wannier centers differs significantly from their counterparts in electronic systems. Instead of characterizing them as "charge" centers, the correct interpretation is in terms of "energy" centers. More specifically, the winding behavior of hybrid Wannier centers signifies the transport of energy, linked to the Poynting vector, in contrast to the charge transport typically discussed in electronic systems. This distinction emerges from the formulation of the electromagnetic WL, which employs an energy inner product, weighted by the constitutive tensor matrix:

$$\mathcal{K} = \begin{pmatrix} \varepsilon & \xi \\ \xi^\dagger & \mu \end{pmatrix},$$

This weighting is not a formal detail, but it represents a crucial point in order to ensure the quantization of topological invariants [118, 119, 166]. Consequently, when dealing with PhCs, we will denote the hybrid Wannier centers as Hybrid Wannier Energy Centers (HWECs) instead of Hybrid Wannier Charge Centers (HWCCs).

3.1.1.5 Chern Number: Flow of hybrid Wannier centers

The connection between the WL and HWECs gives rise to a physical interpretation of the electromagnetic Berry phase. As the momentum k_y is varied across the BZ, the average energy centers in the orthogonal direction to k_y (x) can move into a different unit cell. This represents an energy pumping process, where each cycle of k_y moves the energy centers transversally across unit x cells.In 2D, this description allows to express the electromagnetic Chern number as the winding of x-HWECs along the $\mathbf{k}_\perp$ direction (k_y):

$$C = \sum_{n=1}^{N_{band}} \int_{-\pi/a_y}^{\pi/a_y} \frac{dx_n(k_y)}{a_x}. \tag{3.16}$$

or, equivalently for a periodic gauge choice (se **Section 3.1.2.2**):

$$C = \frac{1}{a_x} \sum_{n=1}^{N_{band}} \left(x_n(k_y = 2\pi/a_y) - x_n(k_y = 0) \right) \tag{3.17}$$

where the $x_n(k_y)$ are assumed to be smooth functions of k_y. The periodicity in **Equation 3.17** is intended modulo a lattice vector a_x. Therefore, solely from the winding of the x-localized HWEC as a function of k_y, it is possible to extract the Chern number of the 2D PhC. Other 2D topological invariants such as the valley-Chern number [167] or the $\mathbb{Z}_2$ fragile index [33] can be also deduced for 2D PhCs using HWECs [1]. In the next section, we will demonstrate how to extend these results from 2D to 3D, using the WLs to compute topological invariants for 3D PhCs.

3.1.2 Numerical Implementation

In this section, we emphasize the essential modifications required for evaluating electromagnetic WLs in 3D, relative to the 2D approach, to accommodate this dimensional change. Similar to the methods detailed in Ref. [1], we will use electromagnetic solutions derived from the MIT Photonic Bands (MPB) [168] package as the foundation for our topological analysis.

3.1.2.1 Overlap Matrices for Vector Fields

The fundamental objects for the numerical evaluation of electromagnetic WLs are the overlap matrices defined in **Equation 3.3**. In the case of 3D PhCs, these involve the use of the full vector field:

$$u_{m,\mathbf{k}} = \begin{pmatrix} u^{(E)}_{m,\mathbf{k}} \\ u^{(H)}_{m,\mathbf{k}} \end{pmatrix}, \tag{3.18}$$

where the eigenstates, the periodic part of the Bloch modes, are considered to be already normalized. For non-bianisotropic media, the problem can be separated into electric ($u^{(E)}_{m,\mathbf{k}}$) or magnetic ($u^{(H)}_{m,\mathbf{k}}$)-field components and the computation of overlap matrices is accomplished through:

$$\mathcal{W}_{m,n\,3\mathrm{D},E}^{\mathbf{k}'\leftarrow\mathbf{k}} = \langle u^{(E)}_{m,\mathbf{k}'} | u^{(E)}_{n,\mathbf{k}} \rangle_{\varepsilon}, \quad \text{where } u^{(E)}_{n,\mathbf{k}} = \begin{pmatrix} u^{(E_x)}_{n,\mathbf{k}} \\ u^{(E_y)}_{n,\mathbf{k}} \\ u^{(E_z)}_{n,\mathbf{k}} \end{pmatrix}, \tag{3.19}$$

and

$$\mathcal{W}_{m,n\,\mathrm{3D},H}^{\mathbf{k}'\leftarrow\mathbf{k}} = \langle u_{m,\mathbf{k}'}^{(H)} | u_{n,\mathbf{k}}^{(H)} \rangle_{\mu}, \quad \text{where } u_{n,\mathbf{k}}^{(H)} = \begin{pmatrix} u_{n,\mathbf{k}}^{(H_x)} \\ u_{n,\mathbf{k}}^{(H_y)} \\ u_{n,\mathbf{k}}^{(H_z)} \end{pmatrix}, \tag{3.20}$$

for the electric and magnetic field solutions respectively. The transition from a scalar to a vectorial problem becomes evident as we consider the inner product's vectorial structure, which involves the three Cartesian components as follows:

$$\mathcal{W}_{m,n\,\mathrm{3D},E}^{\mathbf{k}'\leftarrow\mathbf{k}} = \overline{u_{m,\mathbf{k}'}^{(E_x)}} u_{n,\mathbf{k}}^{(D_x)} + \overline{u_{m,\mathbf{k}'}^{(E_y)}} u_{n,\mathbf{k}}^{(D_y)} + \overline{u_{m,\mathbf{k}'}^{(E_z)}} u_{n,\mathbf{k}}^{(D_z)}, \tag{3.21}$$

where the overline indicates complex conjugation, and:

$$\mathcal{W}_{m,n\,\mathrm{3D},H}^{\mathbf{k}'\leftarrow\mathbf{k}} = \overline{u_{m,\mathbf{k}'}^{(H_x)}} u_{n,\mathbf{k}}^{(B_x)} + \overline{u_{m,\mathbf{k}'}^{(H_y)}} u_{n,\mathbf{k}}^{(B_y)} + \overline{u_{m,\mathbf{k}'}^{(H_z)}} u_{n,\mathbf{k}}^{(B_z)}. \tag{3.22}$$

In contrast, in 2D PhCs band-topology can be assessed solely using scalar fields [1], either with the z-polarized electric field for TM modes:

$$\mathcal{W}_{m,n\;TM}^{\mathbf{k}'\leftarrow\mathbf{k}} = \langle u_{m,\mathbf{k}'}^{(E_z)} | u_{n,\mathbf{k}}^{(E_z)} \rangle_{\varepsilon}, \tag{3.23}$$

or with the z-polarized magnetic field for TE modes:

$$\mathcal{W}_{m,n\;TE}^{\mathbf{k}'\leftarrow\mathbf{k}} = \langle u_{m,\mathbf{k}'}^{(H_z)} | u_{n,\mathbf{k}}^{(H_z)} \rangle_{\mu}, \tag{3.24}$$

This marks the initial transition from the scalar to the vectorial nature of the problem.

3.1.2.2 Componentwise Gauge Fixing

When the periodic part of the Bloch fields ($u_{m,\mathbf{k}}$) is obtained by frequency-domain solvers, random phases can originate at different $\mathbf{k}$ points, due to the diagonalization procedure. These arbitrary phases automatically cancel pairwise in the WL evaluation when taking products of neighboring states within the closed path of **Equation 3.5**, since every state appears twice as a ket-bra form. However, at the endpoints of the path, $\mathbf{k}_0$ and $\mathbf{k}_{(F)}$, a periodic-gauge choice must be explicitly enforced to ensure the smoothness of the Wilson loops eigenvalues in the BZ [169]. Let us consider a non-contractible path that traverses the BZ along a reciprocal vector $\mathbf{G}$, where:

$$\mathbf{k}_{(F)} = \mathbf{k}_{(0)} + \mathbf{G}. \tag{3.25}$$

We want to ensure that the Bloch states (ψ) satisfy the periodic gauge condition:

$$\psi_{\mathbf{k+G}} = \psi_{\mathbf{k}}, \tag{3.26}$$

or, equivalently, that the periodic part of the Bloch fields (u) respects:

$$u_{\mathbf{k+G}} = e^{-i\mathbf{G}\cdot\mathbf{r}} u_{\mathbf{k}}. \tag{3.27}$$

A way to enforce this constraint is to formally redefine the periodic part of the fields, at $\mathbf{k} + \mathbf{G}$ as:

$$u'_{\mathbf{k+G}} = \frac{u_{\mathbf{k+G}}}{\psi_{\mathbf{k+G}}} \psi_{\mathbf{k}}, \tag{3.28}$$

where the righthand side of the equation is composed of solely states obtained directly from the numerical solver. For 3D vector fields, this operation has to be done componentwise, for each Cartesian component of the fields, e.g. for the x-electric field component:

$$u^{(E_x)'}_{\mathbf{k+G}} = \frac{u^{(E_x)}_{\mathbf{k+G}}}{\psi^{(E_x)}_{\mathbf{k+G}}} \psi^{(E_x)}_{\mathbf{k}}. \tag{3.29}$$

This gauge-fixing is relevant to guarantee the smoothness of the Wilson loop eigenvalues in the BZ.

3.1.2.3 Polarization Vortex and Wilson Loops

So far, the differences with respect to the 2D scenario have manifested as a simple increase of vectorial components within the problem. Yet, the most profound and conceptually fundamental distinction emerges when we consider the role of the Γ point. When implementing WL calculations for photonic bands, special care should be given at the $\omega = 0$ states, where 3D PhCs present a vortex-like singularity in the polarization. Numerical solvers such as MPB usually give a null eigenfunction as the default solution at $\omega = 0$, which can result in discontinuities in the WL spectrum. In 2D, this issue can be resolved by noticing that, at $\omega = 0$, any constant, normalized eigenfunction is a valid solution for the dynamical equations, **Equations 2.92** and **2.91**. In Ref. [1] we showed that this replacement allows to avoid singularities, without affecting the topological characterization. The situation is more complicated in 3D PhC since no well-defined polarization can be assigned to the $\omega = 0$ states. To address this problem, we propose two distinct strategies, and we elaborate on them in the next two subsections with practical 3D PhC examples, proposing:

- The calculation of Γ-avoiding section Chern numbers, suited for gapped and (some) gapless 3D PhCs (**Section 4.1.3.3**).
- The calculation of a Γ-encircling Berry Flux, for gapless 3D PhCs (**Section 3.1.4**).

Both approaches are designed to circumvent the Γ point, allowing the topological characterization of 3D PhCs.

3.1.3 Γ-Avoiding Section Chern Number

The Chern number is an invariant defined for gapped systems on closed, even dimensional manifolds. In 2D, this invariant is related to a specific mapping from the BZ, which has the topology of a torus ($\mathbb{T}^2$), to the Bloch sphere ($\mathbb{S}^2$) representing the gapped energy bands. This mapping, denoted as

$$h : \mathbb{T}^2 \to \mathbb{S}^2, \tag{3.30}$$

takes each point $\mathbf{k}$ in the BZ to a point $\mathbf{h}(\mathbf{k})$ on the Bloch sphere. As $\mathbf{k}$ traverses the BZ, the unit vector on the Bloch sphere may wind around multiple times. The Chern number quantifies this winding behavior, which is akin to measuring how many times the unit vector wraps around the Bloch sphere as $\mathbf{k}$ varies across the BZ. Mathematically, this corresponds to the Brouwer degree of the mapping [170], providing a numerical measure of the winding. It's essential to note that the standard definition of the degree of a map requires the map to be continuous in $\mathbf{k}$. As we already mentioned in **Section 3.1.2.3** this continuity in the BZ can be guaranteed for the eigenstates of a 2D PhC, while in 3D PhCs the lack of analyticity at Γ cannot be avoided. In 3D PhC, each gapped 2D cross section of the 3D momentum space:

$$\mathbf{k} = (k_x, k_y, k_z) \tag{3.31}$$

can be associated to a section Chern number C_l [171, 172], as long as $k_l \neq 0$, with $l \in \{x, y, z\}$. This is because $k_l = 0$ cross sections contain the Γ vortex singularity and, differently from 2D, no polarization state can be assigned to zero-energy Γ states. Fortunately, in a 3D BZ, we have always the option to consider 2D planar subdomains that bypass the Γ point, a possibility that clearly does not exist in a 2D BZ. As we will demonstrate shortly, excluding the $k_l = 0$ plane results in the removal of a 0-D interval from the domain of a piece-wise defined function, which we will introduce in order to

calculate Chern and Weyl topological invariants. As we will see, this will discontinuity will not affect the topological characterization of the 3D PhC. To numerically obtain the section Chern number C_l for a l cross section, we consider, for fixed $k_l \neq 0$, the WL operator computed in the i direction:

$$\mathcal{W}_i(k_j, k_l) = \mathcal{W}_i(k_j), \tag{3.32}$$

and track the flow of the $i_n(k_j, k_l)$ HWECs with respect to k_j. Here, i, j, l can take values in the cyclic permutations of x, y, z. Explicitly, the C_l section Chern number can be evaluated from the winding of the HWECs, according to:

$$C_l = \sum_{n=1}^{N_{band}} \int_{-\pi/a_j}^{\pi/a_j} \frac{d i_n(k_j)}{a_i}. \tag{3.33}$$

or, equivalently, for a smooth gauge:

$$C_l = \sum_{n=1}^{N_{band}} \frac{i_n(k_j = -\pi/a_j) - i_n(k_j = \pi/a_j)}{a_i}. \tag{3.34}$$

Non-Zero Chern Numbers with TRS Here we want to highlight another important difference from 2D. A non-zero Chern number of a 2D BZ is always associated with the breaking of TRS. Differently, the section Chern number taken on a 2D cross-section of a 3D BZ can be non-zero also in the presence of TRS. This situation can, for example, occur in chiral crystals that support Weyl points arising from inversion breaking, e.g. the woodpiles PhCs of Ref. [67, 173]: a section Chern number taken in between the Weyl points can be non-zero, even though the system does not break TRS.

3.1.3.1 Discontinuities at Weyl Nodes

The section Chern number C_l is a topological invariant of gapped bands. Therefore, it can change only when the band gap closes at a certain point on the k_l plane -that is, when the k_l planes host nodal features. Because of this, the section Chern numbers can be used to detect the existence of nodal features in 3D momentum space, such as Weyl Points, which are source and sink of Berry curvature [174–178], and extract their topological charge. The section Chern number is in general represented by

a piece-wise constant function in k_l, with possible discontinuities on the planes that contain gap closings. For example, let us assume the system has only Weyl points in the open interval $(-\frac{\pi}{a_l}, \frac{\pi}{a_l})$, located on different P planes $k_l = k_{l,W_p}$, with $p = 1..P$. The corresponding section Chern number is going to be a piece-wise constant function of the type:

$$C_l = C_l(k_l) = \begin{cases} C_1 & k_l \in \left[-\frac{\pi}{a_l}, k_{l,W_1} \right) \\ \vdots & \\ C_p & k_l \in \left(k_{l,W_{p-1}}, k_{l,W_p} \right) \\ C_{p+1} & k_l \in \left(k_{l,W_p}, k_{l,W_{p+1}} \right) \\ \vdots & \\ C_P & k_l \in \left(k_{l,W_{P-1}}, k_{l,W_p} \right) \\ C_{P+1} & k_l \in \left(k_{l,W_p}, \frac{\pi}{a_l} \right) \end{cases} \tag{3.35}$$

where $C_{P+1} = C_1$. As we will show now, this piece-wise defined function can be used to detect the existence of Weyl nodes, and extract the net topological charge (q_{W_p}) from Chern number discontinuities:

$$q_{W_p} = C_{p+1} - C_p, \tag{3.36}$$

at each plane $k_l = k_{l,W_p}$. To handle the discontinuities numerically, a cutoff is needed. More specifically, we have to evaluate the section Chern number around the plane containing the Weyl point $k_{l,(W)}$, excluding a specific range $[k_{l,(W)} - \epsilon, k_{l,(W)} + \epsilon]$ where $0 < \epsilon << 1$. The choice for ϵ balances two different criteria: it should be smaller than the separation from other nodal features yet larger than a lower bound, which depends on the WL discretization, to ensure convergence. For example, in the calculation considered in **Section 4.1** a 81×81 grid in (k_x, k_y) is employed, and a $\frac{\epsilon}{2\pi} \sim 0.03$ interval around Weyl nodes is excluded. In **Figure 3.1**, we consider the case of a single pair of oppositely-charged Weyl points (a Weyl dipole with $q_\pm = \pm 1$), having symmetric nodes at $k_z^\pm$. To identify the Weyl point topological charge, we compute the C_z section Chern number on 2D k_z planes, away from $k_z = k_z^\pm$. The resulting $C_z(k_z)$ is a piece-wise continuous function, that jumps from 0 to 1 (with a net $+1$ discontinuity) at $k_z = k_z^+$, and from 1 to 0 (with a net -1 discontinuity) at $k_z = k_z^-$. These discontinuities signify a net ± 1-charge for Weyl points located on the $k_z = k_z^\pm$ planes, acting as as a source and sink of Berry curvature.

On the other hand, no discontinuity is observed at Γ, confirming that the vortex

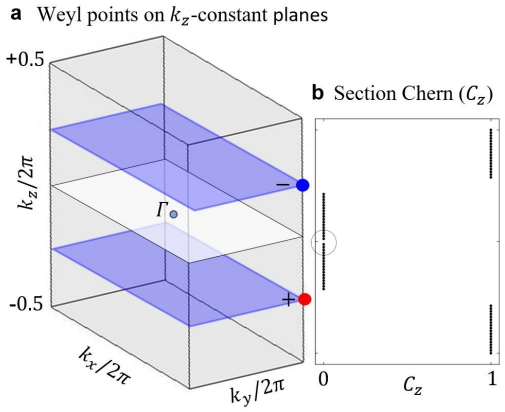

Figure 3.1: Section Chern number approach to identify the charge of a Weyl dipole in the 3D BZ. Panel a): Location of the charge ±1 Weyl nodes ($\mathbf{k}^{\pm} = (\frac{\pi}{a}, \frac{\pi}{a}, \pm\frac{\pi}{2a})$) in the 3D BZ. 2D k_z cross sections, with the Γ-avoiding cross section displayed in white. Panel b): Discontinuity in the section Chern number at the planes which contain the Weyl nodes $k_z = \pm\frac{\pi}{2a}$.

singularity does not affect the calculation of the section Chern number. In this example, with a single pair of Weyl points split along the k_z line, the topological charge can be computed solely using the C_z invariant. For more complicated Weyl point configurations, such as multiple or coplanar Weyl points, it may be necessary to evaluate other section Chern numbers (C_i) to fully determine the individual topological charge of the individual nodes. The section Chern number method proposed here can also be used to compute the three components of the Chern vector of 3D Chern insulators. A 3D Chern insulator is a 3D TRS-broken topological phase characterized by a triplet of three first Chern numbers ($\mathbf{C} = (C_x, C_y, C_z)$) [179–184]. In a layer construction picture [45,185], 3D Chern insulators can be interpreted as a stack of 2D Chern insulators, with each k_i section in the BZ having a constant value C_i. The section Chern number allows to evaluation of the components of the Chern vector in a straightforward way. We will employ the section Chern number method to characterize a topological Weyl to 3D Chern transition in the PhC designed in **Section 4.1**.

3.1.4 Γ-Encircling Wilson Loops

The section Chern number approach for characterizing PhC topology relies on the assumption of the existence of gapped 2D cross-sections within the BZ. However, in certain situations, no such gapped domains can be identified. This scenario can arise, for instance, when dealing with extended nodal walls, which make every planar cross section gapless. Additionally, up to this point, our discussion has primarily revolved around cross-sections that avoid the Γ point within the BZ. We haven't yet addressed

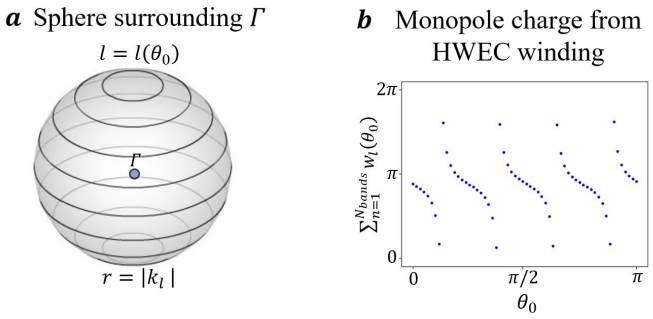

Figure 3.2: **a**: Small sphere of $|k_r|$ surrounding a photonic Weyl point at Γ.**b**: The Weyl point charge can be extracted from winding in θ_0.

situations where topological charges are precisely located at the Γ point itself. Herewith, we aim to show how to proceed in these two cases. Specifically, we will introduce an alternative approach for extracting:

1. the monopole charge associated with a Weyl point positioned at the Γ point in the lowest transversal bands

2. the topological charge of a Weyl nodal wall situated along the boundary of the BZ.

We do this by tracking the Wilson loop flow on closed 2D manifolds that enclose the monopole charge (the Weyl point or the nodal wall). Since a Chern number can be defined for this 2D closed manifold, the Berry flux q_{IN} piercing through it can be deduced from the winding of the Wilson loop on its surface. More specifically, this can be done by parametrizing the surface of the closed manifold with parallel loops:

$$l = l(p) \tag{3.37}$$

that cover the entire manifold as the p parameter varies in a closed interval, $p \in [0, 1]$, and by tracing the flow of this WL operator:

$$\mathcal{W}_l = \mathcal{W}_l(p), \tag{3.38}$$

as a function of p. Because the net charge in the BZ must be zero, the total monopole charge of nodes falling outside the manifold can be obtained as:

$$q_{\text{IN}} = -q_{\text{OUT}}. \tag{3.39}$$

By choosing a closed surface that encircles the Γ point, it is possible to explicitly ex-

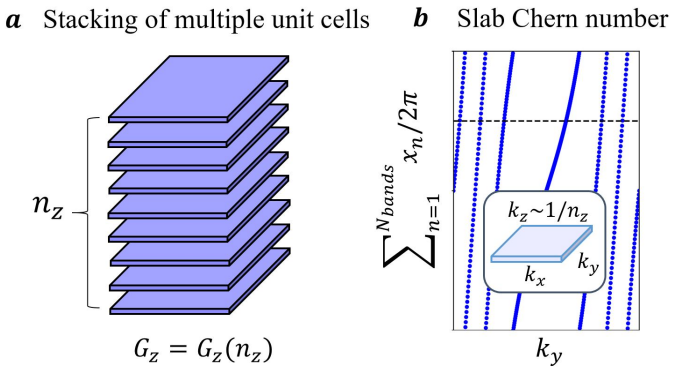

Figure 3.3: Layer Chern number. **a**: Slab with n_z layer. **b**: Winding of the HWEC in the 2D BZ of the slab.

clude the $\mathbf{k} = 0$ eigenstates from the calculation. This allows to simultaneously characterize the topology of nodes where the previous approach fails, while at the same time avoiding the necessity of assigning a well-defined polarization state to the $\omega = 0$ fields. We will use this method to characterize the topology of the 3D PhC of **Section 4.3**, which simultaneously presents a Weyl nodal wall and a Weyl point located at Γ.

3.1.5 Layer Chern Numbers via 3D Effective Models

The 3D topological invariants computed so far can be obtained in a straightforward way from WLs computed in the bulk of the 3D PhC. However, there exist certain 3D invariants which are convenient to be evaluated in a slab configuration. An example of these invariants is the layer Chern number G [59, 186–188]. This quantity becomes relevant for the topological characterization of certain 3D topological phases, which display bulk-hinge correspondence, in contrast to bulk-boundary correspondence, such as in the example described in **Section 4.2**. The layer Chern number G is nothing but the Chern number computed for a 2D slab of a 3D crystal. For a z-normal slab with $n_z >> 1$ layers, the G_z layer chern number can be obtained computing the x-directed WLs for the slab:

$$\mathcal{W}_x^{(\mathrm{SLAB})} = \mathcal{W}_x(k_y), \tag{3.40}$$

and tracking the flow in k_y. Note that, since k_z is no longer a well-defined momentum component for a slab, the k_z dependence of the WL is ignored. More specifically, the k_z axis folds to $2\pi/n_z \to 0$ in the $n_z >> 1$ limit, and the Wilson loop must be evaluated at $k_z = 0$. While the implementation of the layer Chern number is conceptually straightforward, its practical execution can be computationally intensive, especially when using exact electromagnetic solvers. In the system studied in **Chapter 4**, deal-

ing with a 3D PhC solved in MPB, even a thin slab calculation with just $4 + 4$ layers, 4-bands, and a 24×24 $\mathbf{k}$ grid points was already beyond the available computational resources in a state-of-the-art high-performance computing cluster. In general, conducting electromagnetic simulations for confined slab and rod geometries of 3D PhCs can be computationally demanding. To overcome these numerical difficulties, condensed matter systems often rely on tight-binding models. Unfortunately, extending a tight-binding approach from electronic systems to 3D PhCs presents its own challenges, due to the absence of a maximally localized Wannier basis, stemming from the Γ point singularity described in **Section 2.3.1.3**. In **Section 3.2**, we will detail how to circumvent these conceptual difficulties and create effective tight-binding models of 3D PhCs, that accurately reproduce their topological properties, while using a reduced set of parameters and basis functions compared to traditional brute-force simulations. Once an effective model for the 3D PhC is obtained, the layer Chern number G can be easily be computed. In **Section 4.2**, we will illustrate how to use the layer Chern number G for the topological characterization of a 3D PhC, displaying (higher-order) axion topology.

3.1.6 Discussion and outlook

In this section, we have demonstrated the possibility of computing several 3D topological invariants using a single tool: the electromagnetic Wilson loop and the associated hybrid Wannier energy centers. It's essential to emphasize that the Wilson loop is a versatile and powerful approach capable of identifying a wide range of 3D topological invariants, beyond the specific examples presented here. The methods introduced in this section could be readily extended for other applications, such as, just to name a few possibilities, assessing the braiding of multigap photonic nodal links [189] or detecting fragile topology [190] within the fundamental gap of 3D PhCs.

3.2 Transversality-Enforced Tight-Binding Models

In this section, we aim to extend the tight-binding modeling approach to 3D PhCs. The tight-binding, heavily used in solid-state physics, can describe a crystal's band structure and topological properties while using a small set of parameters and basis functions as compared to ab initio models or exact solvers, allowing the simulation of much larger systems using fewer computational resources. Unfortunately, the extension of such models to 3D PhCs has been so far elusive. The main reasons are the

irregular symmetry content of the zero frequency states in 3D PhCs and the impossibility of directly constructing a basis of maximally localized TB basis functions due to the vectorial nature and transversality of Maxwell's equations. In the following section, we explore these obstacles in depth, outlining a potential approach to overcome them.

3.2.1 Obstructions to 3D Photonic TB Models

The development of highly efficient simulation techniques is in high demand to advance the field of 3D photonics [18–21, 148]. 3D topological PhCs, when interfaced with trivial dielectric materials, can sustain surface and hinge states within the bulk band gap. These states are topologically protected and constrain light propagation on confined regions, leading, just a name a few, to an enhanced local density of states capable of boosting light-matter interactions [191] or to non-reciprocal propagation properties of light via unidirectional hinge channels [36]. The study of these photonic architectures requires the simulation of very large supercells, which often reach the limits of state-of-the-art high-performance computing resources.

For this reason, in solid-state physics, the common strategy is to use Tight-Binding (TB) models [192–194] to replicate the topological properties of the crystal. Those models are built from a small set of basis functions based on maximally localized Wannier functions and some hopping parameters. This reduced dimensionality, lowers the computational effort required to perform extensive calculations substantially in comparison with the requirements of ab initio techniques. Unfortunately, extending a TB approach from electronics to PhCs is not straightforward. Electronic systems naturally display a set of atomic orbitals that can be mathematically mapped to a set of exponentially localized states known as Maximally Localized Wannier Functions (MLWFs) [164]. This set of functions can be directly used as a basis for a TB model. Finding such a basis of localized states for 3D PhCs is not obvious. In 1D and 2D PhCs, it's always possible to separate the solutions of the wave equation into scalar TE and TM modes. This separation allows us to express Maxwell's equations as a scalar eigenproblem, closely resembling the spinless Schrödinger equation. In these cases, it is possible to find photonic counterparts of MLWFs through well-established solid-state Wannierization techniques [131–133]. These MLWFs can then serve as a basis set of states for constructing a robust TB model of the crystal, facilitating the analysis of its properties. However, the situation differs in 3D PhCs due to a fundamental obstacle stemming from the transversality constraint. As discussed in **Section 2.3.1.3**, the

divergence-free nature of source-free Maxwell equations leads to non-analyticity in the Bloch basis across the entire BZ. This non-analyticity makes it impossible to construct exponentially localized Wannier functions for the lowest photonic bands [22, 23, 121]. Consequently, it prevents the establishment of a standard Wannier basis for a 3D photonic TB model. To understand this fact, we remind that, to maximally localize a Wannier function, we need to select a specific mixing gauge matrix in **Equation 3.14**, capable of minimizing the spread of the quadratic spread functional [164] along a given direction. In 3D PhCs, this localization becomes problematic due to the lack of analyticity in the Bloch basis. In addition, the irregular symmetry content at the Γ point apparently creates on obstruction in the development of a symmetry-adapted model valid all across the BZ, also in the zero-energy, long-wavelength limit. To overcome these limitations, we propose a novel method for constructing a reliable TB representation of 3D PhCs that doesn't rely on the existence of MLWFs. We accomplish this by introducing auxiliary longitudinal modes to the physical transverse bands of the PhC, effectively addressing the singularity at the Γ point. Our inspiration for using longitudinal modes in the Γ point context came from Ref. [23], where the potential of these modes for regularization was first demonstrated in extending topological characterization via symmetry indicators [45, 67, 195–198] to 3D PhCs. The method proposed here is based solely on group theoretical arguments, exploiting the formalism of TQC for non-fermionic systems [23, 199–201], and it comprises two steps:

- We use TQC to identify and define a set of pseudo-orbitals and their corresponding real space locations, providing us with a starting basis for the construction of a photonic TB.

- We enforce transversality on the effective TB model of the 3D PhC built from the pseudo-orbitals obtained in the previous step. By distinguishing physical transverse modes and auxiliary longitudinal modes, we trace out the latter from the final TB description.

This results in a Transversality-Enforced-Tight-Binding (TETB) which can replicate all the energetic features, symmetry content, and topology of the 3D PhC. Additionally, we explain how to introduce the effects of a static magnetic field into the model. We use the TETB method developed to model the topological transition in **Section 4.2**.

3.2.2 Selecting Pseudo-Orbitals Candidates

As previously stated, our first objective is to identify a basis of orbitals that can be used to build a TB model for a 3D PhC. In this section we describe how to obtain such a basis most effectively, by minimizing the basis dimensionality, and therefore the complexity of resulting TB. We will use the term pseudo-orbitals to refer to the localized, symmetric functions that induce the photonic bands, and we will highlight the key differences from conventional orbitals commonly used in solid-state physics.

3.2.2.1 Transverse symmetry vector

To start, we need to pinpoint the symmetry content of the band structure at all HSPs in the BZ. This is determined by the irreps of the eigenvectors at the HSPs. These irreps constitute the first stage of studying the system's topology via TQC. Any reliable TB model of a crystal, which replicates the system's topology, must reproduce such irreps at the HSPs. The irreps of the electromagnetic fields at the HSPs are computed numerically, using the methods described in **Section 2.3.3**. We use the functions provided in the last version of MPB (v1.11.1) dedicated to the computation of overlap integrals. Then, we apply Schur's Orthogonality Relations [152] to obtain the irrep decomposition. The irreps are labeled following the Bilbao Crystallographic Server (BCS) [154, 202] notation. Each irrep is denoted as $\rho_{i[\mathbf{k}]}$ where i labels the particular irrep at each class of HSP [$\mathbf{k}$]. In 3D PhCs, the irrep contents can be computed at every HSP except for the zero-frequency modes at Γ, where the symmetry identification is either ill-defined or irregular. In the following, the symbol $(\blacksquare)^{2T}$ will represent the Γ irrep content, consistent with the notation introduced by Ref. [23]. This symmetry identification procedure has to be carried out on a bundle of bands that can form an isolated set that satisfies the compatibility relations. The bundling procedure for transverse bands is described in **Section B.1**. These steps return the transverse symmetry vector ($\mathbf{v}^T$), expressed as:

$$\mathbf{v}^T = \bigoplus_{i,[\mathbf{k}]} n_{i[\mathbf{k}]}\rho_{i[\mathbf{k}]} \oplus (\blacksquare)^{2T}, \tag{3.41}$$

where $n_{i[\mathbf{k}]}$ labels the multiplicity of each irrep.

3.2.2.2 Infinite Pseudo Orbital Solutions

Using TQC, we aim to decompose the transverse symmetry vector $\mathbf{v}^T$ into Elementary-Band Representations (EBRs) [128, 129, 155, 156], which will constitute the building blocks of our TB model. Roughly speaking, an EBR describes the transformation properties of the bands obtained by placing a set of orbitals, which transform under a certain irrep $\rho_{\mathbf{q}}$ of the site-symmetry group, at a particular maximal Wyckoff position $\mathbf{q}$. Thus, a certain EBR can be specified by the pair "$\rho_{\mathbf{q}}@\mathbf{q}$". In PhCs, the concept of orbital is not technically precise and we use pseudo-orbitals to refer to the localized, symmetric functions that induce the photonic bands. All EBRs for all SGs and the irreps at the HSPs they induce are tabulated in the BCS. Then, the initial problem reduces to finding a linear combination of EBRs such that $\mathbf{v}^T = \sum_i n_i \mathrm{EBR}_i$, with $n_i \in \mathbb{Z}$. Therefore, we collect all the EBRs of the SG of the crystal into a matrix $\mathbf{A}$. Denoting the number of EBRs in the SG by N_{EBR} and the total number irreps at all HSPs by N_{irr}, $\mathbf{A}$ has a size of $N_{irr} \times N_{EBR}$. The i-th column of $\mathbf{A}$ will represent the symmetry vector of the i-th EBR, as tabulated in the BCS. To find a linear combination of EBRs that describes the symmetry content of $\mathbf{v}^T$, we must obtain an integer solution to:

$$\mathbf{v}^T = \mathbf{An}, \tag{3.42}$$

where $\mathbf{n}$ is an integer vector describing the multiplicities of each EBR. In general, $\mathrm{rank}(\mathbf{A}) \leq \min(N_{EBR}, N_{irr})$, which means that we can, in principle, find infinite solutions to **Equation 3.42**. Such indeterminate problems with solutions over the integers are known as Diophantine equations.

> **Equivalence of the infinite solutions** From a physical perspective, the existence of multiple solutions is attributable to the fact that different linear combinations of EBRs can yield the same symmetry vector, resulting in an equivalent description of the photonic band structure. Physically, this is possible because a set of orbitals localized at some Wyckoff positions can be adiabatically moved to other Wyckoff positions in a symmetry-allowed way, i.e., the linear combinations of EBRs induced from the pseudo-orbitals before and after this symmetric deformation are topologically equivalent.

Note that standard methods to solve linear systems of equations are not well suited for solving **Equation 3.42** since they yield real-valued solutions while we need

integer solutions. A convenient way to solve this equation is to compute the Smith decomposition of the integer matrix **A**:

$$\mathbf{A} = \mathbf{U}^{-1}\mathbf{D}\mathbf{V}^{-1}, \tag{3.43}$$

where **U** and **V** are matrices invertible over the integers and **D** is an integer diagonal matrix, whose non-zero entries are called divisors of **A** [203]. Now, the general solution **n** can be computed as:

$$\mathbf{n} = \mathbf{V}\mathbf{D}^{+}\mathbf{U}\mathbf{v}^{T} + (\mathbb{1}_{N_{EBR}} - \mathbf{V}\mathbf{D}^{+}\mathbf{U}\mathbf{A})\mathbf{z} \tag{3.44}$$

where $\mathbf{D}^{+}$ denotes the pseudo-inverse of **D** and **z** is an arbitrary integer vector. **Equation 3.44** (or equivalently, **Equation 3.42**) gives an infinite number of solutions. This means that, for a given symmetry vector $\mathbf{v}^{T}$, there can be many equivalent EBR decompositions, as many as **z**.

3.2.2.3 Minimization of the TB Basis

These multiple solutions can result in a different number of bands depending on the EBRs used and their associated dimension. The number of bands μ that result from the EBR decomposition can be obtained using the norm:

$$\mu = ||\mathbf{n}|| = \sum_{j=1}^{N_{EBR}} g_j |n_j| \tag{3.45}$$

where $|\cdot|$ indicates the absolute value and g_j is the dimension of the EBR n_j. Minimizing the norm of the vector solution **n** is equivalent to minimizing the number of bands employed for the construction of the TB model. Therefore, choosing solutions with minimal norms can enable a simpler construction of a TB model for the 3D PhC. Other norms can be equivalently defined, to estimate the complexity of the associated TB, depending on convenience.

In **Section B.3** we describe the necessary steps for obtaining pseudo-orbitals which are simultaneously optimal and physical solutions to Eq. **3.42**. As we will show, the pseudo-orbital are *minimal* because they minimize the number of auxiliary modes introduced to regularize the Γ point singularity, and they are *physical*, because they satisfy the transversality constraint, which discards longitudinal wave solutions.

3.2.2.4 Negative EBR Coefficients

The vector solution **n** of **Equation B.3** in general contains certain negative EBR coefficients. For the lowest bands of a trivial 3D PhC, this situation can never be avoided since it relies on the intrinsic obstruction due to the Γ point problem [23], which enforces the presence of at least one minus sign in the decomposition.

> **Fragility and transverse bands** The impossibility of expressing the lowest bands of a 3D PhC as a linear combination of EBRs using strictly positive coefficients is reminiscent of the concept of 'fragility' in topological band theory [1,33,204]. Unlike fragile topology, which involves a difference of *EBR*, here the decomposition involves a difference of *irreps*. The concept of fragile topology in the lowest fundamental gap of 3D photonic bands remains an open problem, along with its relation to the gamma vortex. We will return to this point in **Section 5.3**.

The seeming fragility of the transverse band can be exploited in the development of the TB model by reinterpreting the EBR with a negative coefficient as a set of 'auxiliary' longitudinal modes ($\mathbf{v}^L$) which regularize Γ point problem (see **Section 3.2.3** for more details). This reorganization of the modes can be formalized through the following expression:

$$\mathbf{v}^T = \mathbf{v}^{T+L} - \mathbf{v}^L, \tag{3.46}$$

where $\mathbf{v}^{T+L}$ is a linear combination of EBRs with integer positive coefficients. This reorganization of the modes can be formalized through the following expression

$$\mathbf{v}^T + \mathbf{v}^L = \mathbf{v}^{T+L}, \tag{3.47}$$

where $\mathbf{v}^{T+L}$ is a linear combination of EBRs with integer positive coefficients and describes a regular set of modes that include all the symmetry content of the transverse, physical band structure while avoiding the singularity at Γ. Later, we will prove that spectral filtering can remove the auxiliary longitudinal bands $\mathbf{v}^L$ by tuning the TB parameters *a posteriori*. Note also that, using the function *BandRep* at the BCS to obtain the irrep content of the EBRs at Γ, Eq. **B.15** assigns a well-defined value to $(\blacksquare)^{2T}$.

3.2.3 Constructing a Photonic TETB

Once a set of candidate pseudo-orbitals has been determined, we look for a TB model that satisfies the following conditions: the additional degrees of freedom introduced as longitudinal modes ($\mathbf{v}^L$) represent energy bands away from the physical bands, the TB model captures the features of the transverse bands ($\mathbf{v}^T$) in the energy window of interest, and the model reproduces the $(\blacksquare)^{2T}$ obstruction at Γ and all the symmetry, topology, and energetic features of the active bands in the PhC.

3.2.3.1 Quadratic Mapping and Spectral Filtering

To proceed, we exploit a formal mapping between the cell-periodic Schrödinger and Maxwell wave equations, respectively linear and quadratic in time. This allows us to relate the energy λ of the electronic wavefunction $\phi(\mathbf{r})$ in presence of a crystal periodic potential $V(\mathbf{r})$:

$$\left[\frac{-\hbar^2}{2m}\boldsymbol{\nabla}^2 + V(\mathbf{r})\right]\phi(\mathbf{r}) = \lambda\phi(\mathbf{r}), \tag{3.48}$$

and the frequency of light ω in media with periodic dielectric permittivity $\varepsilon(\mathbf{r})$ and permeability $\mu(\mathbf{r})$:

$$\left[\varepsilon(\mathbf{r})^{-1}\boldsymbol{\nabla}\times\mu(\mathbf{r})^{-1}\boldsymbol{\nabla}\times\right]\psi^{(E)}(\mathbf{r}) = \omega^2\psi^{(E)}(\mathbf{r}) \tag{3.49}$$

according to $\lambda \sim \omega^2$ [205]. The validity of this mapping was already discussed in **Chapter 2**. This quadratic mapping allows us to construct an effective solid-state inspired optical 3D TB model by enforcing the eigenvalues (λ) of the set of transversal bands to be positive, $\lambda = \omega^2 \geq 0$, while the lowest set of longitudinal bands to be negative, $\lambda = \omega^2 \leq 0$. Note that since the frequency of the electromagnetic solutions is $\omega = \sqrt{\lambda}$, the final real spectra will not contain the auxiliary nonphysical modes. Forcing the longitudinal modes and active transverse modes to be isolated from each other except at $\lambda = 0$ enables us to achieve all the previous points.

3.2.3.2 Enforcing Transversality

To construct a reliable TB that satisfies the abovementioned constraints, we proceed as follows:

1. From the EBR decomposition obtained in as in the previous section (**Section 3.2.2**), we identify $\mathbf{v}^L$, $\mathbf{v}^T$, and $\mathbf{v}^{T+L}$.

2. We build a TB model with generic free parameters from the set of pseudo-orbitals and Wyckoff positions dictated by the EBRs in $\mathbf{v}^{T+L}$.

3. We analyze the symmetry content of the bands induced by these orbitals and identify which modes can be associated uniquely to $\mathbf{v}^{L}$ and $\mathbf{v}^{T}$.

4. We tune the parameters of the TB (onsite energies and hoppings) so that the set of longitudinal bands become the lowest energy modes, with negative frequency ($\lambda = \omega^2 \leq 0$). Then, we fit the $\lambda = \omega^2 \geq 0$ bands to the square of the electromagnetic frequencies obtained numerically for the PhC.

This will result in a TETB model, with Hamiltonian $H(\mathbf{k})$, which captures all the symmetry, topology, and energetic features of the transverse bands in the PhC.

Invariance under any space group transformation g imposes the following constraint on $H(\mathbf{k})$:

$$gH(\mathbf{k})g^{-1} = H(g\mathbf{k}), \tag{3.50}$$

where $g\mathbf{k} \equiv R\mathbf{k}$ for $g = \{R|\mathbf{t}\}$. Similarly, invariance under TRS implies

$$H(-\mathbf{k}) = H^{*}(\mathbf{k}), \tag{3.51}$$

where * denotes complex conjugation.

3.2.3.3 Introduction of a magnetic field perturbation

Some of the essential applications of topological photonics rely on TRS breaking since it stabilizes strong topology in the CAZ ten-fold classification of topological materials [25, 206]. Usually, TRS breaking in PhCs is achieved using gyroelectric or gyromagnetic materials, applying an external static magnetic field, or equivalently through intrinsic remnant magnetization. To mimic such effects, we develop a general method to simulate in our TETB models the interaction of an external and static magnetic field with a PhC. In TB models for electronic bands, the effects of a static magnetic field can be introduced via minimal interaction of the electrons with the vector potential $\mathbf{A}$, usually through Peierls substitution [207, 208], but this is forbidden for photonic systems due to the uncharged nature of photons. This forces us to use non-minimal couplings, where the magnetic field $\mathbf{H}$ is treated as a perturbation in the system's response. Accordingly, the Hamiltonian, including the effects of a magnetic field, can be represented by

$$H_M(\mathbf{k}, \mathbf{H}) = H(\mathbf{k}) + f_M(\mathbf{k}, \mathbf{H}), \tag{3.52}$$

where $H(\mathbf{k})$ is the TETB Hamiltonian of the previous section and $f_M(\mathbf{k}, \mathbf{H})$ is a magnetic field depending perturbation.

Crystal-field joint transformations Here, we would like to comment on the following subtlety, which sometimes is a source of confusion. Even though coupling to an external magnetic field breaks the TRS of the crystal, we must still impose invariance under joint transformations of the crystal *plus* the magnetic field. The symmetry constraints of **Equation 3.50** and **3.51**, generalized to include the magnetic field, become:

$$g f_M(\mathbf{k}, \mathbf{H}) g^{-1} = f_M(g\mathbf{k}, g\mathbf{H}) \tag{3.53}$$

for any space group transformation g and, for TRS:

$$f_M(-\mathbf{k}, -\mathbf{H}) = f_M^*(\mathbf{k}, \mathbf{H}). \tag{3.54}$$

In most cases, taking $f_M(\mathbf{k}, \mathbf{H})$ as a linear function in the components of $\mathbf{H}$ is enough to model the effects of the magnetic field. Higher orders of $\mathbf{H}$ could easily be added to model the effects of higher magnetic field intensities.

3.2.4 Discussion and outlook

In this section, we proposed a method to construct a reliable TB representation of 3D PhCs, even if maximally localized WFs do not exist for such systems [121] and even in the presence of an irregular content at zero energy. To our knowledge, this represents the first method able to provide a reliable tight-binding representation of 3D dielectric periodic structures, all across the 3D BZ. This TETB is capable of capturing and regularizing the Γ-point electromagnetic obstruction that arises due to the transversality constraint of Maxwell's equations while accurately reproducing all the symmetry, topology, and energetic dispersion of the transverse bands in the PhC. Finally, we showed how to model gyrotropy by providing a magnetic version of our TETB model using non-minimal coupling. The lower computational cost of TB models compared to exact solvers can allow to increase in the complexity of future theoretical developments in the field of topological photonics via the calculation of extensive supercells. For example, recently, this method allowed us to simulate the higher-order response on the hinges of photonic axion insulators [36], and to extract the layer Chern number of 3D PhC slabs (see **Section 4.2** for more details). This development was only possible using TETB models because calculating xy-confined rod geometries of 3D

supercells was beyond state-of-the-art high-performance computing clusters. Therefore, we hope that our TETB can facilitate the study of boundary responses of future 3D photonic topological phases.

Chapter 4

Results

In this chapter, we propose the design of three distinct PhCs displaying three distinct topological phases: the 3D Chern photonic insulator, the photonic axion insulator, and the nodal-wall Weyl semimetal featuring unpaired photonic Weyl points. These phases exhibit unique bulk-boundary properties, including vectorial bulk-boundary correspondence, closed Fermi loops, chiral hinge channels, and forbidden surface Fermi arcs. We characterize the topological properties of these 3D PhCs using methods introduced in **Chapter 3**, specifically the electromagnetic Wilson loops and the transversality-enforced tight-binding model. These methods are tailored to address the challenges specific to electromagnetic wave systems in 3D PhCs. For each proposed topological phase, we briefly discuss potential applications. These applications range from magnetic switching of light, unidirectional light propagation, manipulation of quantum emitter interactions, and axionic dark matter detection.

The chapter is divided as follows:

- **3D Chern Photonic Insulator** (**Section 4.1**). We introduce a TRS-broken 3D topological phase in class A: the 3D Chern photonic insulator, characterized by a Chern vector -a triplet of first Chern numbers. Utilizing Weyl point annihilation, our design scheme tailors this Chern vector in magnitude, sign, and direction. These topological phases demonstrate high Chern numbers, vector orientability, and TRS protection under minimal magnetic conditions. The bulk properties correlate with a finite number of closed Fermi loops winding on the surface BZ torus, establishing the 3D Chern insulator's bulk-boundary correspondence. We elucidate that these loops evolve from the open Fermi arcs of the Weyl semimetal phase during a gapless-to-gapped transition. The increase in the values of the Chern vector components comes accompanied by an increase in the number of

the Fermi loops, while the orientability of the Chern vector gives rise to a modification of the Fermi loop winding, originating a vectorial bulk-boundary correspondence across domain walls with different Chern vectors. We finally show how the dispersion characteristics of these loops are tied to the PhC's anomalous surface states and their non-reciprocal propagation dynamics.

- **Photonic Axion Insulator** (**Section 4.2**). We propose a possible approach to induce axionic band topology in gyrotropic 3D Weyl PhCs gapped by SM. To quantize an axionic angle, we create domain walls across inversion-symmetric PhCs, incorporating a phase obstruction in the SM of their dielectric elements. This allows us to bind chiral channels on inversion-related hinges, ultimately leading to the realization of an axionic chiral channel of light. By controlling the gyrotropic response of the material, we demonstrate a physically accessible way of manipulating the axionic modes through a small external magnetic bias, which provides an effective topological switch between different 1D chiral photonic fiber configurations. We show that the unidirectional axionic hinge states supported by the photonic axion insulator are buried in a fully connected 3D dielectric structure, thereby being protected from radiation through the electromagnetic continuum.

- **Unpaired Photonic Weyl Semimetal** (**Section 4.3**). We outline a scheme to design a nodal-wall 3D PhC that features a single, isolated, Weyl point at the Γ point. The high-monopole charge of this unpaired Weyl point is balanced by an absorbing nodal wall at the boundary of the cubic BZ. The symmetry of the nodal wall, combined with the maximal topological charge of the Weyl point, gives rise to a nodal configuration with topological properties that are distinctly different from those of standard Weyl-dipolar systems.

We propose these 3D phases in all-dielectric periodic structures, i.e. structures that contain no metallic or plasma components. To model TRS-invariant phases, we consider high-dielectric, isotropic media. In magnetic scenarios, we use gyrotropic media with parameters aligned with realistic microwave implementations [11, 41, 139].

4.1 3D Chern Photonic Insulator

4.1.1 Introduction

TRS-broken topological materials, like Chern Insulators (CI) [9, 10] and Chern lasers [88], stand out among topological states of matter for their topologically protected, non-reciprocal edge states. In these systems, scattering processes from one boundary state into another are strongly suppressed, due to the decoupling of counter-propagating 1D chiral edge channels [209, 210]. As established in **Chapter 2**, strong topology in PhC is limited to class A with broken TRS for spatial dimensions $d \leq 3$. Pioneering studies in 2D photonics have shown that TM modes in gyro-magnetic PhCs can emulate the Chern insulating state for light [11, 139]. Owing to a non-zero Chern number, these systems support topologically protected one-way edge states with minimal dissipation and no back-scattering, resilient to impurities and lattice defects disrupting translational symmetry. At the same time, significant Chern numbers have been detected in 2D square PhC bandgaps [98, 211]. Photonic systems with elevated Chern numbers can sustain multiple spatially separated edge states [211]. These edge states allow a plethora of applications, including unidirectional multimode waveguides where information can be multiplexed through the different edge states allowing for photonic on-chip communications with higher channel capacity [211]. Nevertheless, the value of the Chern number in these 2D systems was not determined by design, but a consequence of the particular system under study. A systematic design strategy able to dictate the Chern number's value remained elusive. *B. I. Halpherin* [212] initially highlighted in the electronic context that extending Chern topology to 3D is feasible, albeit under stricter prerequisites. For instance, while maintaining lattice translational symmetry, a 3D Chern insulating phase is anticipated to support anomalous surface states with unidirectional properties [179–184]. In contrast to 2D, a 3D Chern insulator (3D CI) is a topological phase that can be characterized by three first Chern invariants - or a Chern vector $\mathbf{C} = (C_x, C_y, C_z)$ - defined on lower dimensional manifolds [45–50]. The existence of a triplet of Chern invariants leads to vectorial aspects of BBC which outpass those usually predicted by conventional "scalar" BBC typical for 2D CIs. In 2D, the Chern vector is always fixed along the axis of the reduced dimensionality, i.e. orthogonal to the plane of the system. On the contrary, the possibility of orienting Chern vectors in space, opens up the possibility of constructing domain walls between different orientations, thus requiring for a "vectorial" BBC to be defined. In condensed matter systems, the 3D quantum Hall effect is usually discussed

in layered systems [213–220]. Since layered systems have a preferred axis, and since the magnetic field needs to be along this axis, the orientability of the Chern vector doesn't come up. Other 3D proposals in photonics [221] have also been limited to unit and uniaxial Chern numbers and did not manifest the full topological properties associated to the Chern vector. Motivated by previous insights, in this chapter, we develop a general design strategy allowing to tailor the Chern vector of a 3D PhC in terms of magnitude, sign, and direction. This strategy uses Weyl point manipulation and multifold Supercell Modulations (SM) [222] to realize the following different topological scenarios:

- The Chern number's additivity with band-folding over large supercells enables the system to support large Chern numbers, allowing for multimodal unidirectional surface states.

- Adjusting the amplitude of the SM, it becomes possible to reduce the magnetic requirements, which can be beneficial for specific photonic applications.

- Activating orthogonal components of the Chern vector offers a broader array of boundary interfacing possibilities as compared to 2D systems.

We characterize the propagation properties of the anomalous surface states in the 3D Chern insulators, unveling the emergence of photonic Fermi loops. By orienting the Chern vector in different spatial directions across domain walls, we discuss vectorial aspects of their bulk-boundary correspondence. These ideas were initially presented in our recent theoretical works, "Cubic 3D Chern photonic insulators with orientable large Chern vectors" [50] and "Vectorial Bulk-Boundary Correspondence for 3D Photonic Chern Insulators" [42]. While Ref. [50] develops the design strategy centered around SM and Weyl point annihilation for Chern vector engineering, Ref. [42] explores anomalous surface states for different boundary configurations of 3D Chern insulators, especially addressing non-collinear Chern vector orientations, in a vectorial bulk-boundary correspondence picture. We refer to the experimental study carried out by the *Baile Zhang* group [41], for a realistic implementation in a 3D PhC setup. In their work, they realized a photonic 3D Chern insulating phase via Weyl point annihilation, featuring high Chern numbers and orientable Chern vectors. Vectorial bulk boundary correspondence was observed in a gyrotropic PhCs at microwave frequencies, demonstrating the adaptability of these theoretical ideas into experimental settings.

4.1.2 Initial setup

The starting point of our design is a PhC with a unit cell containing four dielectric rods directed along the main diagonals of a cubic crystal (scalable lattice parameter $|a|$). The rods meet at the origin of the unit cell, and the structure is invariant under the operations of the centrosymmetric and non-symmorphic space group (SG) $Pn\bar{3}m$ (No. 224) [223]. Since we will later consider modulations of this structure, it is convenient to simulate the dielectric rods by assembling dielectric spheres with radius $r = r_0$ along $(x, y, z)_0/|a| = (t, t, t), (t, 1-t, 1-t), (1-t, t, 1-t), (1-t, 1-t, t)$ with $0 < t < 1/2$, i.e. employing a spherical covering approximation [224]. The resulting design is shown in **Figure 4.1(a)**. Starting in a TRS-preserving system, the dielectric material is described by a diagonal (isotropic) permittivity tensor, $\varepsilon_{TRS} = \varepsilon \mathbb{1}_3$, where $\mathbb{1}_3 = \hat{\mathbf{x}} \otimes \hat{\mathbf{x}} + \hat{\mathbf{y}} \otimes \hat{\mathbf{y}} + \hat{\mathbf{z}} \otimes \hat{\mathbf{z}}$ and $\varepsilon \in \mathbb{R}$ (no losses), and by unit magnetic permeability $\mu = \mathbb{1}_3$. To simulate the optical response of the system, we employ the MIT Photonic Bands (MPB) software package [168]. As shown in **Figure 4.1(a)**, with TRS, the photonic band-structure presents a three-fold degeneracy between the three lowest energy bands at the high symmetry point $\mathbf{R} = \frac{2\pi}{|a|}(1/2, 1/2, 1/2)$; note that, in the displayed energy window, the two lowest bands are fully degenerate. Everywhere else in the BZ, there is a gap between the second and third bands. The dispersion reflects the three-fold rotational symmetry of the crystal, and is invariant under cyclic permutations of the three k_i $(i = x, y, z)$ directions. In order to keep the notation consistent throughout the section and to capture all the variety of symmetry designs, we label the high symmetry points in the BZ according to a Cartesian orthorhombic convention, see **Figure 4.3**, using the BCS notation.

4.1.2.1 Weyl points formation

To split the three-fold degeneracy at $\mathbf{R}$ into two Weyl points [223], we break TRS. This can be achieved by either applying an external magnetic field bias to a gyro-electric crystal [9, 10] as we proceed here, or by exploiting the internal remnant magnetization of ferrimagnetic materials [139]. TRS breaking is implemented by introducing off-diagonal imaginary elements in the permittivity tensor: for the specific case of an applied magnetic field $\mathbf{H} = H_z\hat{\mathbf{z}}$, the induced gyro-electric tensor is:

$$\varepsilon_{\eta_z} = \begin{pmatrix} \varepsilon_\perp & i\eta_z & 0 \\ -i\eta_z & \varepsilon_\perp & 0 \\ 0 & 0 & \varepsilon \end{pmatrix}, \tag{4.1}$$

where $\eta_z = \eta_z(H_z)$ the bias-dependent gyro-electric parameter and $\varepsilon_\perp = \sqrt{\varepsilon^2 + \eta_z^2}$. The gyro-electric tensor corresponding to magnetic fields in other directions can be obtained by orthogonal rotations of **Equation 4.1**. Under these conditions, the three-fold degeneracy splits into a pair of Weyl points (or a "Weyl dipole"). In order to analyze the formation and splitting of the Weyl points under TRS breaking and to predict the direction of their displacement in the BZ, we develop a $\mathbf{k}\cdot\mathbf{p}$ model around the three-fold degeneracy at $\mathbf{R}$. The model, based on the group theoretical method of invariants (see **Appendix A**), allows us to conclude that Weyl points appear at inversion-symmetric positions with respect to $\mathbf{R}$ along the k_z direction, with a separation that can be adjusted by choosing the bias field H_z appropriately. Our MPB simulations, presented in **Figure 4.1(b)**, confirm this predictions accurately. More generally, for a magnetization applied along any of the main coordinate axes x_i, the Weyl dipole is oriented along the line joining $\mathbf{R}$ to $\mathbf{R}' = \mathbf{R} - \mathbf{b}_i$, where $\mathbf{b}_i$ is the corresponding primitive reciprocal lattice vector.

4.1.2.2 Topological charge of photonic Weyl points

Next we calculate the chiral topological charge $q_\pm$ of the Weyl points. For the $\mathbf{k}\cdot\mathbf{p}$ model we use the *Z2Pack* numerical tool [225, 226], concluding that the Weyl points have opposite valued unit charges ($q_\pm = \pm 1$). We confirm these predictions by computing the topological charges directly from the MPB eigenstate solutions. To do so, we implement a numerical approach based on the analysis of the winding properties of photonic hybrid Wannier energy centers as defined in the **Chapter 3**. There, we establish a mapping from electronic hybrid Wannier charge centers [164, 227] to photonics and we perform a generalization of the photonic Wilson loop approach of Ref. [1] (initially implemented for 2D scalar waves) applicable to fully 3D electromagnetic vector fields. The results of this analysis are summarized in **Figure 4.1(c)**: the top panel shows the electromagnetic Chern number C_z of the two lowest bands calculated on 2D planes orthogonal to the magnetization axis. We observe a sharp discontinuity $\Delta C_z = \pm 1$ at the wavevector of each Weyl point. This is similarly reflected in the winding of the Wilson loop eigenvalues on two selected planes, as shown in the bottom panel. The Weyl points of the WS phase have the same frequency and occur between bands 2 and 3. These bands directly connect to the Γ states at frequency zero, as shown in **Figure 4.1(b)**. Therefore the entire $N_{band} = 2$ needs to be involved in the calculation. The Weyl dipole orientation in the 3D BZ is shown in **Figure 4.1(b)**. On the other hand, no discontinuity is observed at Γ, confirming that the vortex singularity

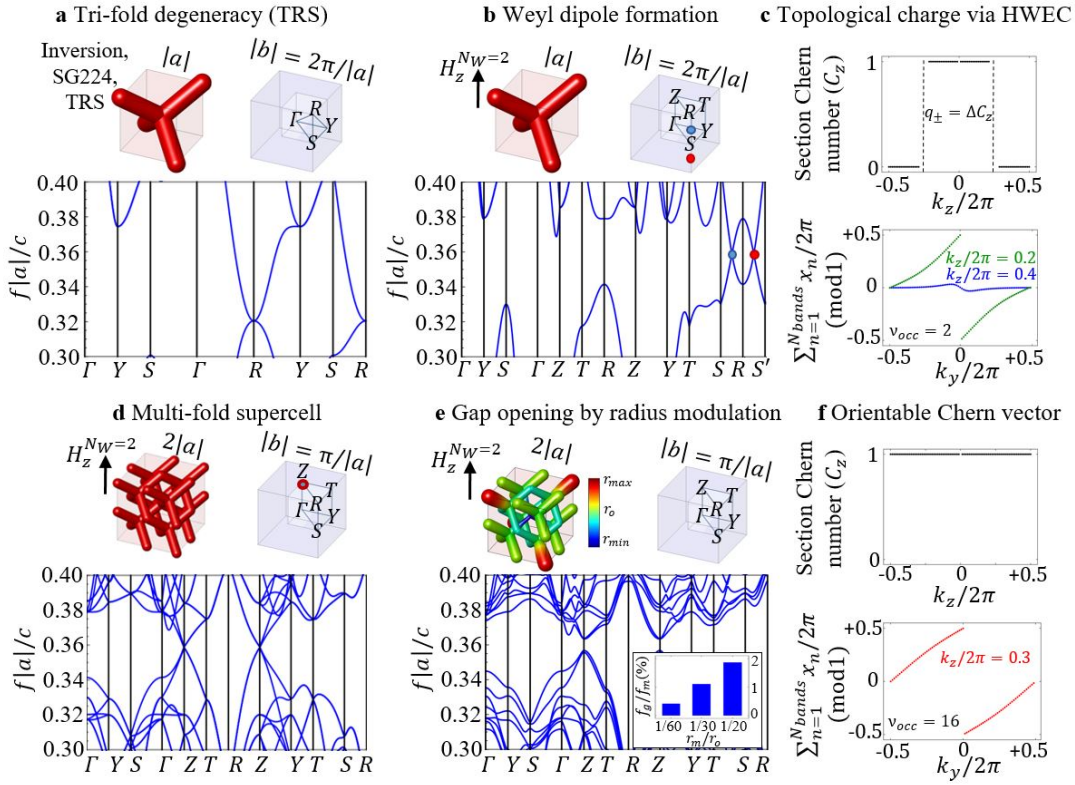

Figure 4.1: Cubic SM at $N = N_W = 2$. Each **a,b,d,e** panel shows the crystal unit cell, the irreducible Brillouin zone (IBZ) and the corresponding band-structure (BS). Frequencies f are given in reduced units, $|a|$ being the scale invariant lattice parameter and c the speed of light. Panels **c** and **f** contain the topological characterization from analysis of the photonic Wilson loops (WL), for the system in the Weyl semimetallic (WS) phase and in the topological insulating 3D CI phase, respectively. **a**: PhC constructed from cylinders of radius $r_0 = 0.15$ and dielectric constant $\varepsilon = 16$ at TRS. The three lowest photonic modes display a three-fold degeneracy at **R** and the two lowest bands are fully degenerate in the displayed energy window. **b**: TRS breaking implemented via a gyro-electric response with $\eta_z^{N_W=2} = 16$: the bias field is adjusted in order to split the Weyl points of approximately half the BZ, i.e. at $k_z^{\pm} = \pm\frac{\pi}{2|a|}$, along the **SRS′** line where $\mathbf{S'} = \mathbf{S} - \mathbf{b}_z$. **c**: Electromagnetic section Chern number calculated on 2D k_z planes normal to the magnetization (upper panel) and transverse flow of the θ_y eigenvalue of the WL matrix summed over the entire subset of ν_{occ} bands lying below the local gap at k_z (lower panel). The discontinuity of the section Chern number at the wavevector of each Weyl point $k_z^{\pm}$ is used a measure its topological charge ($q_\pm = 1$). **d**: Artificial folding of the bands on a $N = 2$ cubic supercell: Weyl points superimpose at **Z** in the new BZ. **e**: Coupling and annihilation of Weyl points through a $N = 2$ SM with parameter $r_m = r_0/20$ which is graphically visualized via a colorbar where $r_{max} = r_0 + r_m$ and $r_{min} = r_0 - r_m$. This results in a topological direct gap (f_g) at **Z** with gap-to-midgap (f_g/f_m) ratio of 1.86%. The size of gap can be appropriately tuned by choosing the value of the modulation, as shown in the inset. **f**: The section Chern C_z number is constant everywhere in the BZ confirming the absence of any gap closure and it displays unit value establishing the system to be in the 3D CI phase.

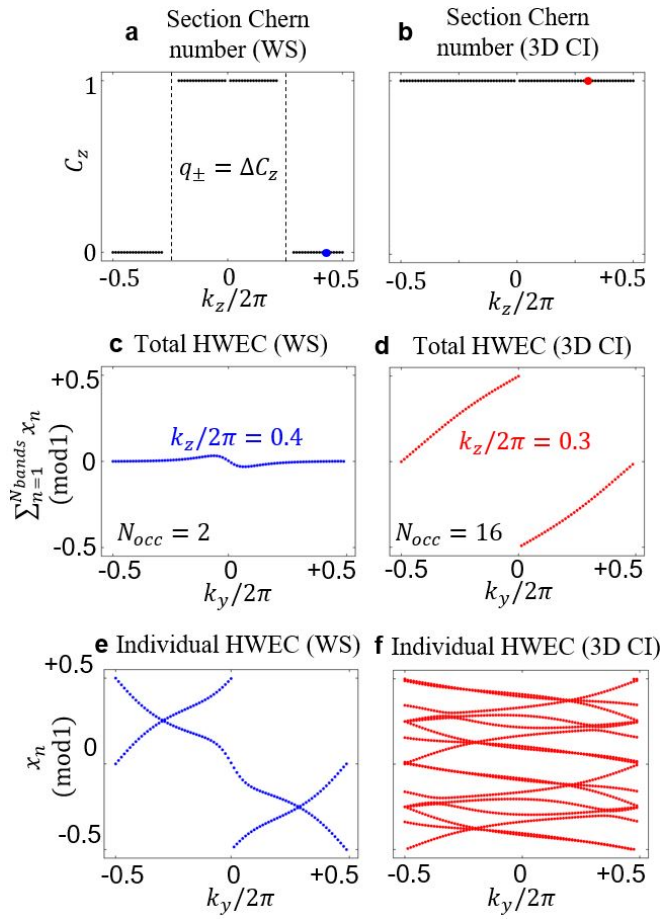

Figure 4.2: Comparison of section Chern number and hybrid Wannier energy center characterization for the WS (left) and the 3D CI (right). **a,b**: Section Chern number $C_z = C_z(C_z)$, showing discontinuities at the planes that intersect the Weyl nodes ($k_z^{\pm} = \pm\frac{\pi}{2a}$) for the WS phase, and no-discontinuities for the 3D CI phase. **c,d**: Cumulative flow of the x-HWEC as a function of k_y, taken at fixed k_z. **e,f**: Individual x-HWEC for the $N_{band} = 2$ bands below the Weyl nodes and the $N_{band} = 16$ bands below the 3D Chern gap.

does not affect the calculation of the section Chern number. From the discontinuity in the section Chern number at each Weyl point, we deduce the associated topological charge [172], confirming that $q_\pm = \pm 1$, as predicted by the $\mathbf{k} \cdot \mathbf{p}$ model.

4.1.2.3 Weyl points annihilation

The $\mathbf{k}\cdot\mathbf{p}$ model allows us to identify a geometrical perturbation able to open a bandgap. In **Appendix A** we study the coupling of the Weyl points and show that the only possible deformations of the geometrical structure leading to Weyl annihilation and to the opening of a topological gap are lattice commensurate SMs. In particular, we find that it is possible to independently activate the SM along the x_i Cartesian directions and couple Weyl points generated by the corresponding external magnetic field H_i. When

we couple the Weyl nodes by a lattice commensurate modulation, we backfold the BZ into a region commensurate with the Weyl node separation vector, which is a reciprocal lattice vector in the folded BZ. The additivity of the Chern number then ensures that every plane in the reduced BZ carries a nonzero Chern number, resulting in a 3D CI when the gap is opened [222]. This expresses the fact that the Chern number *density* of our 3D system does not change as a function of the (TR-even) SM; it simply goes from being unquantized in the original system (necessitating the existence of Weyl points), to being a quantized multiple of a reciprocal lattice vector in the modulated system.

4.1.3 Engineering of the 3D CI gap and its Chern vector

4.1.3.1 Three-step procedure

With this starting setup, in order to obtain 3D Chern insulating phases, we outline a general three-step strategy:

1. First, using the external magnetic field we move the Weyl points at fractional distances of the Brillouin zone (BZ), i.e. at positions $\mathbf{K}_{1,2} = \mathbf{R} \pm \frac{\mathbf{x}_i}{N_W}$ where $N_W \in \mathbb{N}$ and $N_W > 1$. In this way, in a further step, we will be able to couple and gap the Weyl points with a commensurate modulation of a supercell structure. Notice that larger N_W are associated to smaller splittings.

2. Secondly, we fold the BZ by creating multifold ($N > 1$) supercells; this is achieved by replicating the original unit cell either in a cubic supercell of dimensions (N, N, N) or in a uniaxial supercell of size N directed along the magnetic field direction. This step of the procedure will merge the Weyl points, originally at $\mathbf{K}_{1,2}$ in the natural BZ, to the same $\mathbf{k}$ point in the new reduced BZ, forming a four-fold degeneracy. In **Appendix C**, we show that fine-tuning and perfect band folding are not strictly necessary for opening a gap at the Weyl points. This endows our system with robustness and tolerance against reciprocal lattice vector mismatches.

3. As a third and last step, we couple and gap the opposite-charge Weyl points by spatially modulating the crystal geometry with a periodicity commensurate to the designed supercell. More specifically, we vary the radius of the cylinders through the entire supercell: numerically, this is achieved by locally changing the radius of the spheres in the covering approximation, from their original r_0

radius to the new local one $r(x, y, z)$. Coherently to the choice made in the previous point 2, this is either done with a cubic modulation of the type: $\Delta r(x, y, z) = r(x, y, z) - r_0 = r_m[\cos(2\pi x/N|a|) + \cos(2\pi y/N|a|) + \cos(2\pi z/N|a|)]$ when all the Cartesian components of the modulation are turned on or with a uniaxial modulation, where only the component-oriented along the magnetic field is activated, e.g. $\Delta r(x, y, z) = r_m \cos\left(2\pi x_i/N|a|\right)$ for a field with $H_i \neq 0$ field (more details are given in **Appendix C**).

Depending on the relative values of the supercell period (N), the Weyl dipole splitting (N_w), the intensity of the SM (r_m), and the external magnetic field direction (H_i), it is possible to design different tailored 3D CI phases, in particular: a cubic 3D CI with orientable Chern vectors, a 3D CI in a reduced magnetization environment and a 3D CI with tunable large Chern numbers. We stress that the argument of gap opening by folding and SM is very general, and can be applied as long as the constraints of commensurability between the Weyl displacement and the supercell size are satisfied. Therefore, other crystal structures exhibiting a pair of Weyl points could be suited to their annihilation via the mechanism proposed, see**Appendix C**.

4.1.3.2 Cubic 3D CI

Our first objective is to design a cubic 3D CI with orientable Chern vectors. As we will show, this can be achieved using a cubic SM with $N = N_W > 1$. In order to keep the MPB simulations computationally affordable we consider the simplest case of $N = N_W = 2$, which requires to separate the Weyl points to half the BZ as in **Figure 4.1(b)**. The effect of band folding in such a system is visualized in **Figure 4.1(d)**: for a field oriented as H_z, the two Weyl points superimpose to form an artificial four-fold degeneracy at $\mathbf{X}_3 \equiv \mathbf{Z}$. More generally, on a $N = N_W$ cubic supercell and from simple folding considerations, we expect the opposite-charge Weyl points to merge at $\mathbf{X}_i$ when $N = N_W$ is even, at $\mathbf{R}_i - \mathbf{X}_i$ when $N = N_W$ is odd, where $\mathbf{X}_i = \frac{\mathbf{b}_i}{2} \equiv \mathbf{X}, \mathbf{Y}, \mathbf{Z}$. From this starting point, in order to realize a cubic 3D CI phase with orientable Chern vectors, all three Cartesian components of the cubic commensurate modulation need to be simultaneously turned on, according to the most general relation given previously. The resulting photonic band structure of the $N_W = N = 2$ supercell modulated structure is shown in **Figure 4.1(e)**: as it can be seen, the Weyl points annihilate and open up a gap.

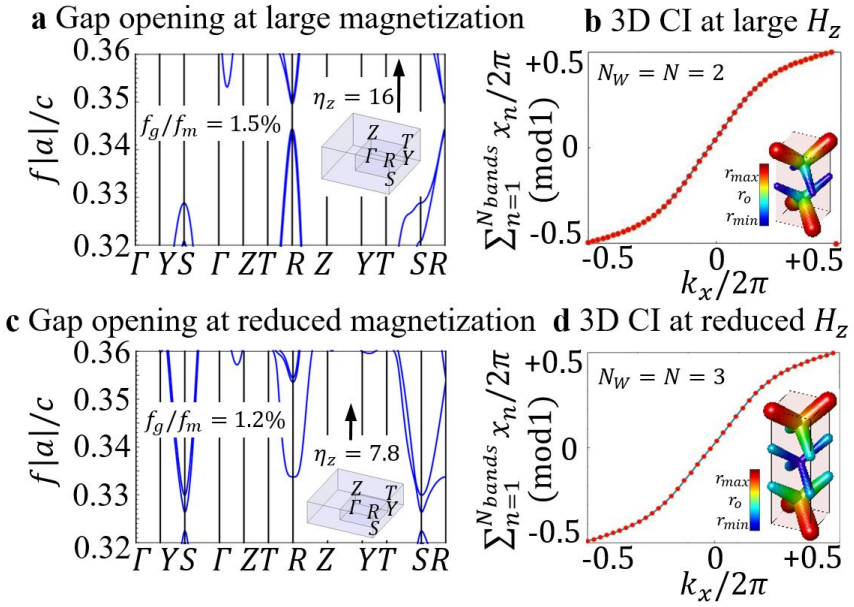

Figure 4.3: Orientability of the Chern vector $\mathbf{C} = (C_x, C_y, C_z) \equiv C_x\hat{\mathbf{x}} + C_y\hat{\mathbf{y}} + C_z\hat{\mathbf{z}}$ with the external magnetic field. **a**: Labeling convention of the BZ adopted in the main text, to capture all symmetry and orientations of the designed unit cells: each point $\mathbf{X}_i = \frac{\mathbf{b}_i}{2}$ is indicated according to the corresponding primitive reciprocal lattice vector $\mathbf{b}_i$, i.e. in a orthorhombic notation. **b,c,d**: Supercells of size $(2, 2, 2)$. Owing to cubic symmetry of the SM, a 3D Chern insulating phase can be obtained for any choice of the magnetization along the three principal axes; shown the corresponding tetragonal IBZs for $\hat{\mathbf{x}}, \hat{\mathbf{y}}, \hat{\mathbf{z}}$ respectively.

4.1.3.3 Topological characterization

To numerically verify the topological properties of this bulk gap in our design we compute photonic Wilson loops and analyze their winding in the BZ, via the methods developed in **Chapter 3**. Our results, summarized in **Figure 4.1(f)**, determine that the obtained insulating phase acquires a nonzero Chern number along every plane perpendicular to the magnetization axis as predicted by the $\mathbf{k} \cdot \mathbf{p}$ model. Since the system is fully gapped in all the three $\mathbf{k}$ directions, no discontinuity is observed in k_i in any of the three section Chern numbers $C_i(k_i)$, $i = x, y, z$. As shown in the right panels of **Figure 4.2**, the $C_z(k_z)$ is indeed continuous and equal to $+1$ independently of k_z. This means that we can identify the z component of the Chern vector with the constant value of C_z in the BZ. The same can be done for the other x and y components. For the example considered here $C_x(k_x) = 0 = C_y(k_y)$, and we deduce the Chern vector $\mathbf{C} = (0, 0, 1)$. Therefore, by simply changing the orientation of the magnetization axis, it is possible to select each Cartesian component in a first Chern class vector (C_x, C_y, C_z), due to the the cubic nature of the underlying system and modulation. Note that the existence of three weak indices in 3D allows for more interfacing possibilities as compared to

the 2D case, where only the trivial/TI and the opposite (or different) Chern number combinations are realizable. The analysis of these other interfacing possibilities is left for **Section 4.1.5**, dedicated to bulk-boundary correspondence.

4.1.3.4 Magnetic bias reduction

In our previous example, we required the Weyl points to be displaced to the half of the BZ. Achieving such a condition requires large TRS-breaking parameters. In our simulations, fulfilling this requirement implied using a magnetization bias corresponding to $\eta^{N_W=2} = 16$. Note that, to date, large gyrotropic parameters have been experimentally achieved in PhCs only in the microwave frequency regime via ferri-magnetic materials [139, 139, 228] and that the gyrotropic response of most currently known dielectric materials is weak. Therefore, in this section, we suggest a way to reduce the magnetization requirements for obtaining CI phase by employing multifold supercells and by increasing the intensity of the modulation. Instead of displacing the Weyl points to half the BZ and applying a SM over two original unit cells, we now move the Weyl points to a smaller fractional distance of the BZ and apply a SM over a larger number of original supercells to merge and gap the Weyl points appropriately. The resulting 3D CI phase still displays the same Chern number as in the maximally TRS broken system with $N = N_W = 2$, but it occurs in a largely reduced magnetic field environment due to the smaller **k**-space displacement of the Weyl points. For example, making $N = N_W = 3$, which corresponds to a dipole separation of one-third of the BZ and spatially modulating the structure over 3 original unit cells, one can get the same topological phase as in the previous example. Under this construction, the CI phase is achieved at $\eta_z^{N_W=3} = 7.8$, as shown in **Figure 4.4**. As can be naturally expected, the resulting 3D CI suffers a moderate reduction in the bandgap. But when we compare the designs for $N = N_W = 2$ and $N = N_W = 3$, showcased in **Table 4.1**, the latter offers a balanced trade-off between gap size and TRS-breaking intensity. This is evident from the significant reduction in the needed magnetization bias (from $\eta^{N_W=2} = 16$ to $\eta^{N_W=3} = 7.8$), making it an appealing strategy for photonics where the magnetic response isn't strong. The gyrotropic parameter can be further lowered, detailed in**Appendix C**. By exploiting larger supercells like $N_W = 5, 6, 7$ and adjusting the modulation intensity (r_m), the bandgap decrease can be partially compensated. The Chern gap, at linear order, scales with the SM intensity, as shown in **Figure 4.1(e)**. This fact can help mitigate the bandgap reduction. Clearly, we cannot iterate this procedure to infinity. Pushing to near-zero bias always involves a trade-off with

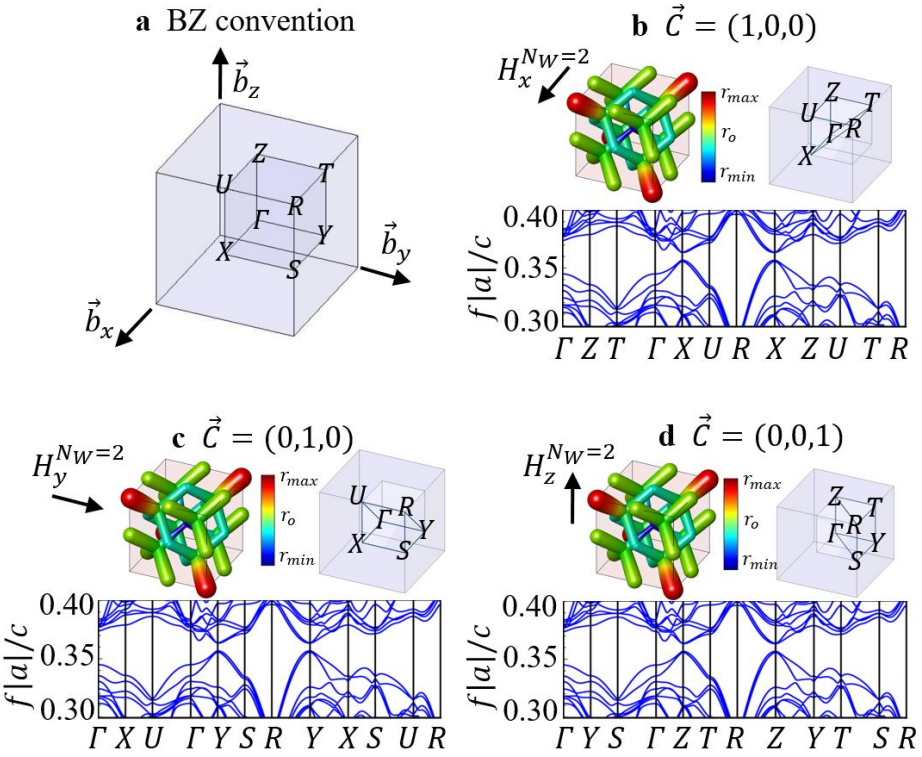

Figure 4.4: 3D CI in a reduced magnetization environment. Uniaxial supercells $(1, 1, N)$ with modulation parameter $r_m = r_0/20$ and WLs on selected planes for $k_z/2\pi = 0.3$. **a,b**: 3D CI with C=1 at large magnetization $\eta^{N_W=2} = 16$, corresponding to the maximum Weyl dipole separation and bandgap. **c,d**: 3D CI in a largely reduced magnetic environment $\eta^{N_W=3} = 7.8$. The bandgap only suffers a moderate contraction, yet the Chern vector and the topological properties are preserved.

$N = N_W$	2	3
C	1	1
η	16	7.8
$f_g/f_m(\%)$	1.5	1.2

Table 4.1: Reduction of the magnetic bias and of the topological gap-to-midgap ratio. Under a large drop in the magnetizing bias η, the bandgap suffers only a moderate reduction. Both PhCs are in the same $C_z = 1$ topological phase.

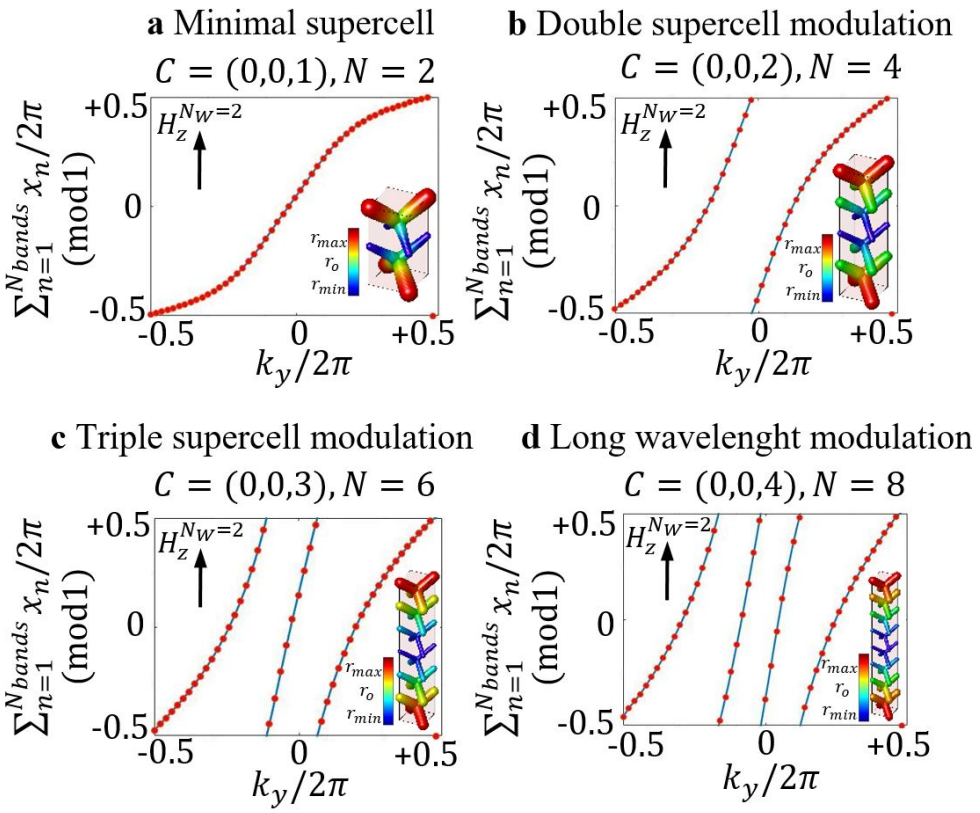

Figure 4.5: Generating larger Chern numbers: annihilation of Weyl points with $N_W = 2$ over multifold supercells of even N. **a**: Unit Chern number 3D CI. **b,c,d**: Increasing Chern numbers C according to the relation $C = N/2$. Calculations performed on 1D supercells $(1, 1, N)$ with modulation parameter $r_m = r_0/20$ and WL on selected planes for $k_z/2\pi = 0.3$.

the bandgap. Specifically, for very large N, Weyl point splitting becomes negligible, making it clearly challenging to open the TRS broken gap, since $\lim_{N\to\infty} f_g = 0$.

4.1.3.5 Arbitrarily large Chern vectors

Lastly, we show that our design strategy can also be used to obtain 3D CIs with larger Chern numbers. This can be achieved by modulating over even multifold supercells with $N = 2n > 2$, $n \in \mathbb{N}$, while keeping $N_W = 2$. The use of larger supercells permits the folding of the BZ multiple times. In the band-folding process, the Chern number contribution in each folded region of the BZ adds up. We thus expect the gap resulting for such a modulated system to achieve larger Chern numbers C_i according to the following relation: $C_i = n$. To prove this, we build uniaxial supercells of size $(1, 1, 2n)$ with $n = 1, 2, 3, 4$. These crystalline supercells are magnetized along the $\hat{\mathbf{z}}$ direction, creating Weyl points at half of the original BZ ($N_W = 2$). After folding, we find that the Weyl points are superimposed at $\mathbf{R} - \mathbf{Z} \equiv \mathbf{S}$ if n is even and at $\mathbf{R}$ is n is

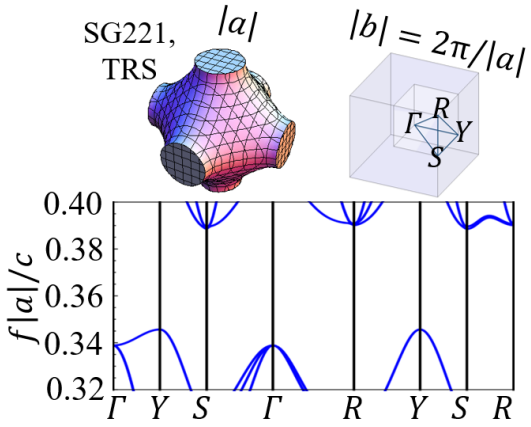

Figure 4.6: Insulating trivial interface consisting of dielectric material $\epsilon_{triv} = 16$ embedded in a "plumber" Schwarz P minimal surface (SG 221) with $g_0 = 0.5$. The trivial gap contains completely the gap of the topological system.

odd. As a final step we activate the modulation along the z direction. In **Figure 4.5** we calculate the Chern number of the band gaps in these systems using hybrid Wannier energy centers and analyzing their winding in the BZ. The modulated supercells with $n = 1, 2, 3, 4$ under the appropriate TRS breaking acquire, as predicted, Chern numbers $C_z = 1, 2, 3, 4$ respectively.

4.1.4 Surface characterization

4.1.4.1 Trivial/Topological domain wall

In order to analyze the boundary response at the interface formed by a trivial insulator and the 3D CI, we search for a PhC with a bandgap completely overlapping the topological system one. Other CI/CI interfacing possibilities are discussed in **Section 4.1.5**. Finding a proper insulating interface is a necessary requirement in order to prevent propagation of edge modes in free space due to modes living in the light cone and to avoid the formation of defect states due to lattice mismatches: this is usually a quite difficult task in 3D, due to limited available bandgap geometries as compared 2D. In this work, this is achieved by means of a triply periodic minimal surface (the "plumber" Schwarz P [229]) having the spatial symmetries of SG No. 221 and displaying a large trivial gap. This PhC consists of an isotropic TRS dielectric material $\varepsilon{=}\varepsilon_{triv}\mathbb{1}_3$ embedded in the region of space defined as $g(x, y, z) < g_0$ where $g_0 \in \mathbb{R}$ and $g(x, y, z)$ is the triply periodic minimal surface: $g(x, y, z) = \cos(2\pi x/|a|) + \cos(2\pi y/|a|) + \cos(2\pi y/|a|)$. As shown in **Figure 4.6**, the trivial photonic gap contains the topological bandgap of 3D CI completely.

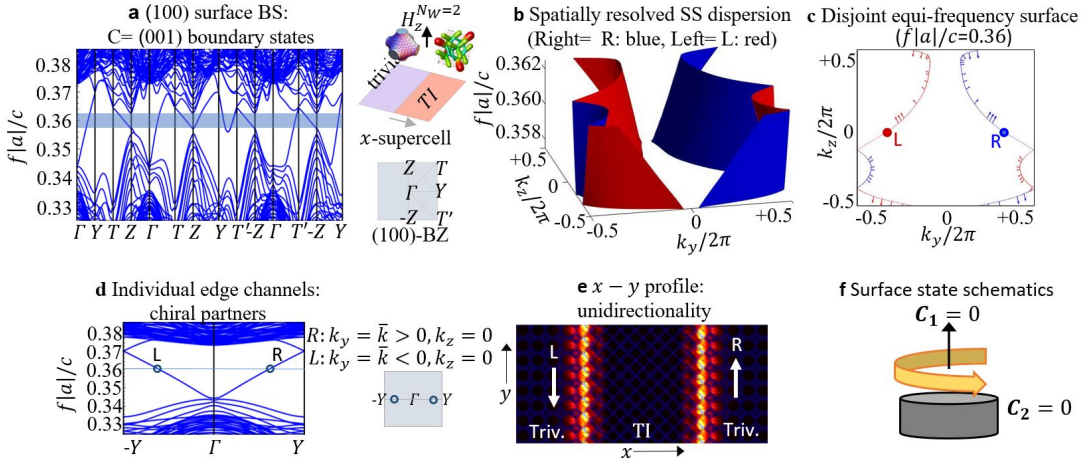

Figure 4.7: **a**: Projected band-structure on the surface BZ with Miller index (100), for the interface between $N_{triv} = 8$ cells of trivial insulator and $N_{TI} = 8$ cells of TI, under a $\mathbf{H} = H_z\hat{\mathbf{z}}$ field and with unit Chern number. Edge states cross the topological gap, highlighted in the shaded region. The extended BZ is fully displayed from $-\mathbf{Z}$ to $\mathbf{Z}$, since it lacks of TRS due to the application of a $\hat{\mathbf{z}}$ directed bias field. **b**: 2D dispersion of topological surface states on the projected BZ, in the energy range of the topological bandgap. **c**: Equifrequency loops for a cut taken at midgap: the arrows on the plot indicate the direction of the group velocity $\mathbf{v}_g = \nabla_{\mathbf{k}} f|a|/c = (v_y, v_z)$. Blue and red colors correspond to chiral partners with opposite v_y and same optical chirality $\bar{c}$ which are located on opposite left/right sides of the interface (L, R). **d**: Edge states dispersion along a direction normal to both the interface and the external magnetic field; highlighted in circles is a pair of counterpropagating $m-th$ edge channels with $\pm k_y$: the spatial profile of their total electric field is shown in two following panels. **e**: Counterpropagating chiral partners located on the two opposite left/right surfaces of the sample (L, R): wavefront propagation in the $\mathbf{k}$ direction indicated by White arrows on a xy cross-section. **f**: Schematics of the conveyor belt anomalous surface states wrapping around the Chern vector.

4.1.4.2 Anomalous Hall surface states

To keep the simulations numerically affordable, we stick to the case of a cubic supercell with $N = N_W = 2$ and analyze a topological slab with normal vector oriented along $\hat{\mathbf{x}}$, in the presence of a H_z field and with a unit Chern vector $C_z = 1$. From conventional bulk-boundary considerations, we expect anomalous surface states to appear on the planes parallel to the magnetization (i.e., with normal vectors perpendicular to the magnetization direction). Surface states are considered unidirectional in the following sense: The component of the group velocity (or Poynting vector) normal to the magnetization direction has a well-defined sign i.e. surface states cannot back-scatter along this specific direction. This component will be later denoted as a conserved component of the conveyor belt surface state **Figure 4.7(f)**. With this setup, we characterize the hallmarks of unidirectional surface state propagation using a combined real-reciprocal space analysis. **Figure 4.7(a)** shows the band-structure for the (100)-surface, confirming the emergence of anomalous surface states connecting the lower and upper bands

and fully crossing the bandgap. To better visualize the surface state energy dispersion, in **Figure 4.7(b)** we consider a 3D surface plot, out of which we take the midgap equifrequency cut shown in **Figure 4.7(c)**. We observe the emergence of 3D Chern Fermi Loops (FLs) which are the natural evolution of the Fermi Arcs (FAs) of the photonic Weyl semimetallic phase. In **Section 4.1.4.3**, we show how the open FAs of the WS phase evolve into the closed 3D Chern FLs as a consequence of Weyl points annihilation. In a 3D CI, the FLs come in "disjoint" partners, that be separated in real space, i.e. we can- associate those with positive group velocity components normal to the magnetization to a surface of the slab and those with negative ones to the other surface. In order to establish the relation between counter-propagating modes with respect to the direction orthogonal to the magnetization axis $\hat{\mathbf{z}}$ and the interface normal $\hat{\mathbf{x}}$, i.e. $\hat{\mathbf{y}} = \hat{\mathbf{z}} \times \hat{\mathbf{x}}$, we analyze the propagation of individual edge channels at fixed k_z. As indicated by red/blue colors in **Figure 4.7b–c**, modes propagating with positive transverse group velocity $v_y > 0$ appear on one side of the topological slab, their flow being compensated by counter-propagating $v_y < 0$ partners located on the other surface of the slab. We define chiral partners, the pair of surface states living on opposite sides of the slab, moving with opposite components of the group velocity which is normal to the magnetization axis. This feature is visualized in **Figure 4.7b–e** where we select a pair of chiral partners for explanatory purposes and display their electric field profile in real space on a cross-sectional view of the crystal slab. We conclude that each disjoint piece of the surface states energy sheet in **Figure 4.7(c)** corresponds to $v_y > 0$ and $v_y < 0$: this spatial separation of chiral partners, provided by the bulk, is the protection mechanism which prevents the back-scattering of one state into the other. Because of this, the presence of touching points in the dispersion between different chiral partners (red and blue lines in **Figure 4.7(c)**), is purely accidental. As so, these crossings occur between states that reside on opposite sides of the slab and are physically separated in real space by the bulk. Therefore they cannot gap out, up to exponentially small finite size effects, and are protected by the spatial separation separation of chiral partners on opposite surfaces. Interestingly, even if individual edge channels display nonzero propagation along the magnetization direction, integrating the total contribution of entire surface states yields no net energy transport along the bias field, as expected due to equilibrium conditions. The chiral propagation of photonic surface states was experimentally observed in the PhC realization designed by the group of *Baile Zhang* [41]. To confirm the topological protection, several copper pillars were inserted to function as metallic obstacles. They showed that, when the

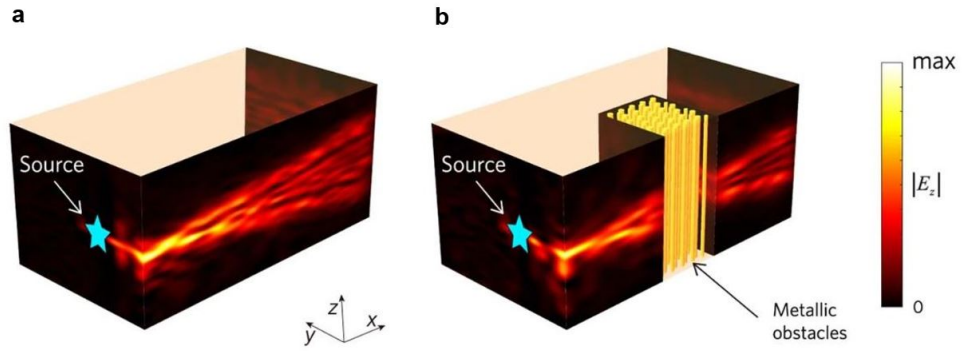

Figure 4.8: Adapted from Ref. [41]. Measured field distribution of chiral surface states. The surface states are excited by a point source (cyan star). Comparison of the measured field distribution without and with copper pillars (yellow rods) inserted into the sample as metallic obstacles. The samples are biased along the z-axis. The chiral surface states can propagate smoothly around the sharp corners and obstacles without scattering. The surface waves are mainly confined at their individual layers when passing around the copper pillars due to the weak dispersion along the z-axis.

dispersion along the Chern vector axis is limited, the surface waves are mainly confined in the vertical direction when passing around the copper pillars, and propagate in a unidirectional fashion, see **Figure 4.8**.

4.1.4.3 Evolution of FAs into loops

The FLs of the 3D Chern phase originate from the FAs [230] of the starting photonic Weyl semimetal setup as the Weyl points undergo annihilation. **Figure 4.9** describe the evolution of the FAs during the supercell folding and modulating process, for an uniaxial system with $N = N_W = 2$. **Figure 4.9(a)** shows the FAs of the Weyl semimetallic phase. Opposite charged Weyl points are located at $(k_y^{\pm}, k_z^{\pm}) = (\pm\frac{\pi}{2}, \pi)$, i.e. midway along the **SR** line. After supercell folding, the Weyl points are superimposed and their FAs display a folding as well, as in **Figure 4.9(b)**. Finally, by turning on the SM, a gap is opened in the BZ and the FAs sharply evolve into disjoint FLs of the 3D CI system, as in **Figure 4.9(c)**. This "arc" to "loop" transition was experimentally observed in Ref. [41], as shown in **Figure 4.10**. In **Section 4.1.3.5**, we demonstrated it is possible to achieve high Chern numbers by increasing the modulation period. We showed that the increase in Chern number can be tracked via Wilson loop winding. More specifically, according to bulk-boundary correspondence, large Chern numbers correspond to an increase in the number of FLs on the surface's BZ. This predicted increase in FLs with the Chern number was confirmed in Ref. [41]. These experiments could resolve Chern numbers up to $C_z = 6$, confirming the possibility of increasing the Chern num-

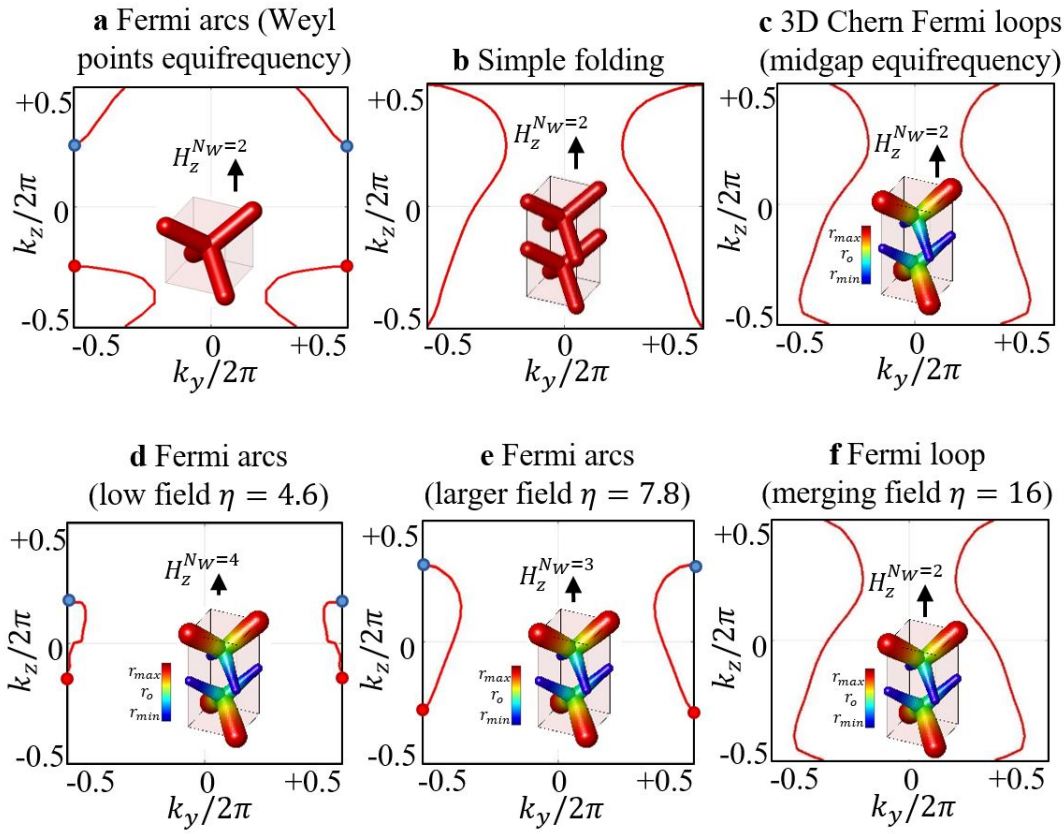

Figure 4.9: Evolution of the FAs. **a**: Starting FAs of the Weyl semimetal phase. **b**: Brillouin zone folding. **c**: SM. The FAs of the Weyl semimetal are transformed into the FLs of the 3D CI system as a result of the supercell folding and modulation. Panels **d-f** show that same situation from a different point of view: first, the SM is introduced and later the Weyl points are brought together.

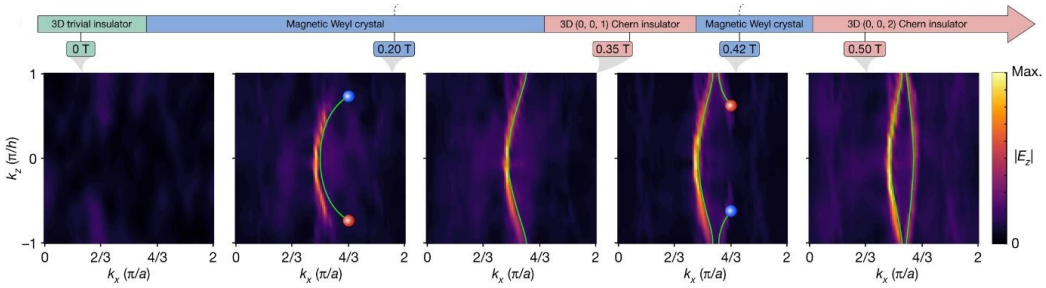

Figure 4.10: Adapted from Ref. [41]. FA or FL surface states, where red and blue dots represent projected Weyl points carrying opposite topological charges. To visualize these states, the field distributions on the surface were mapped using a near-field scanning probe and, subsequently, Fourier transformed to form surface dispersion contours.

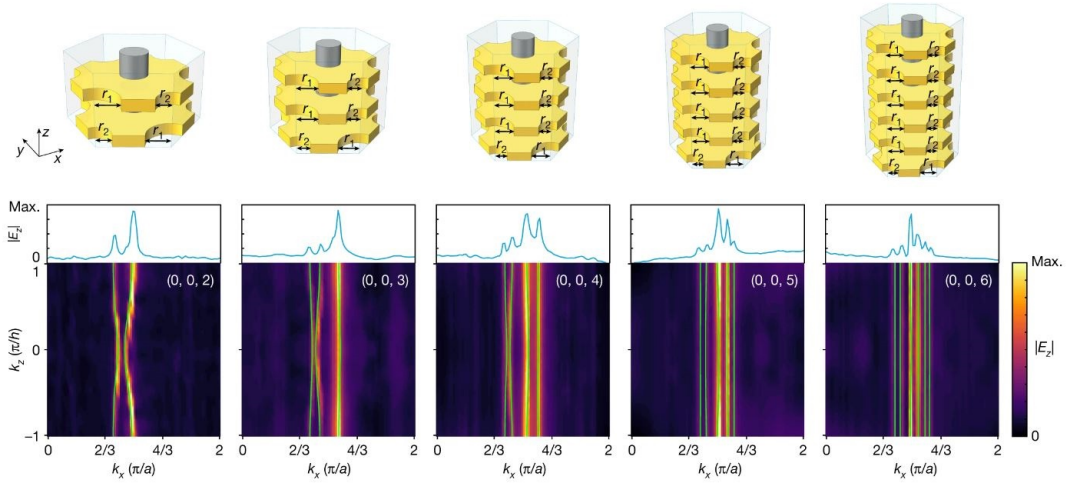

Figure 4.11: Adapted from Ref. [41]. Bottom: measured surface intensity for biasing magnetic field along the z axis at frequency 19.6 GHz. Middle: measured surface intensity extracted from bottom panels at fixed k_z. Top: PhC unit cell of the PhC with increasing Chern vectors from $C_z = 1$ to $C_z = 6$.

ber from a starting value of $C_z = 1$ by the addition of further modulation periods, as shown in **Figure 4.11**.

4.1.5 Vectorial bulk boundary correspondence

In this section, we investigate vectorial aspects of bulk-boundary correspondence at the interface of 3D CIs with different Chern vectors $\mathbf{C}_1 \neq \mathbf{C}_2$. In particular, we analyze the emerging surface states and show what occurs when the Chern vectors across the boundary are not parallel to each other. The analysis of interfaces where Chern vectors have a different orientation in space allows us to promote the "scalar" bulk-boundary correspondence (sBBC) from 2D to a "vectorial" bulk-boundary correspondence (vBBC) for 3D CIs. In 2D, the Chern vector aligns orthogonal to the system's plane. In 3D, the quantum Hall effect in condensed matter is typically associated with layered systems [213–220]. Since layered systems have a preferred axis, with the magnetic field along this axis, the vectorial nature doesn't play any role in such a system. However, the possibility of orienting Chern vectors in space, demonstrated in 3D PhCs in the previous section, allows to construction of domain walls between different Chern orientations, thus necessitating a vBBC. An illustrative case is when a domain wall has Chern vectors orthogonal to one another, i.e., $\mathbf{C}_1 \cdot \mathbf{C}_2 = 0$. We seek answers to the following: Do individual components of the Chern vector independently contribute to surface modes? How do multiple photonic surface modes hybridize given different orientations of the Chern vector? Can we systematically count surface modes or pre-

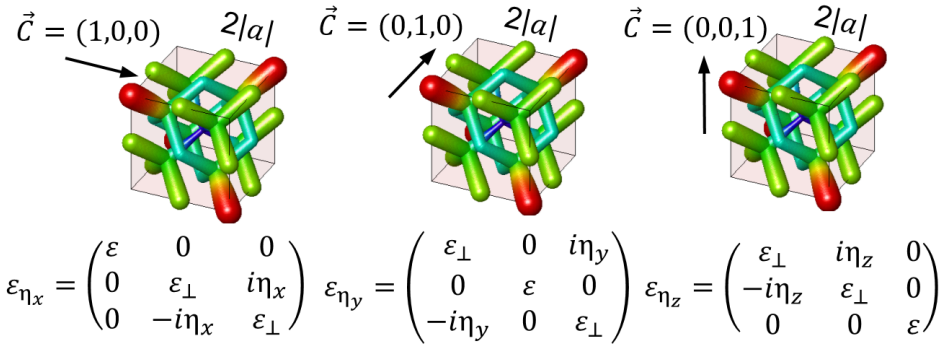

Figure 4.12: Orientability of the Chern vector along the gyrotropic axis.

dict their direction? Exploring the link between FL connectivity and the change in the Chern vector at the interface is a primary goal of this section.

4.1.5.1 Orientable Chern vectors

The Chern vector for our 3D CI cubic model is fixed by the magnetization direction of **Equation 4.1**, as shown in **Figure 4.12**. Therefore, by choosing gyrotropic materials, it is possible to arrange magnetized samples in the desired configuration to construct domain-wall interfaces.

4.1.5.2 Domain-wall planar interfaces

To analyze planar interfaces at the boundary of different 3D CIs, we construct 1D supercells and obtain topological slabs with normal vector oriented along $\hat{\mathbf{x}}$. In particular, we analyze the following 3D CI/3D CI interfacing configurations:

1. $\mathbf{C}_1 = C_{z_1}\hat{\mathbf{z}}$ and $\mathbf{C}_2 = C_{z_2}\hat{\mathbf{z}}$, with $C_{z_1} = -C_{z_2} = C_z$: anti-parallel Chern vectors, both parallel to the interface plane. We call this configuration anti-ferromagnetic C_zI/C_zI.

2. $\mathbf{C}_1 = C_x\hat{\mathbf{x}}$ and $\mathbf{C}_2 = C_z\hat{\mathbf{z}}$: Chern vectors orthogonal to each other, one parallel to the interface plane, the other orthogonal to the interface plane. We call this configuration C_xI/C_zI.

3. $\mathbf{C}_1 = C_y\hat{\mathbf{y}}$ and $\mathbf{C}_2 = C_z\hat{\mathbf{z}}$: Chern vectors orthogonal to each other, both parallel to the interface plane. We call this configuration C_yI/C_zI.

There are two additional interface conditions: (4) The case for which $\mathbf{C}_1 = 0$ and $\mathbf{C}_2 = C_{z_2}\hat{\mathbf{z}}$, i.e. a non-null Chern vector parallel to the interface with a trivial insulator;

(5) The case where $\mathbf{C}_1 = C_{z_1}\hat{\mathbf{z}}$ and $\mathbf{C}_2 = C_{z_2}\hat{\mathbf{z}}$, with $C_{z_1} = C_{z_2} = C_z$, i.e. identical Chern vectors, both parallel to the interface plane. Case (4) was already extensively studied in **Section 4.1.4.1** and it here is referred to as Trivial/C_zI configuration. Case (5) will not have protected chiral modes by the scalar bulk-boundary correspondence, and so will not be of further interest here. However such interfaces may be interesting from the point of view of higher order topology [222], and will be explored in **Section 4.2**. For each interface (1)–(3), we characterize the number and propagation direction of the emerging surface states and investigate the vectorial aspects of BBC using a combined real-reciprocal space analysis. First, we analyze the surface states in the frequency domain, showing the surface states energy sheets as a function of surface momenta k_y, k_z on the (100) plane. We then look at midgap equifrequency cuts to extract FLs. Second, we analyze the direction of the associated group velocity (or Poynting vector) and the spatial localization of the fields on the boundary. Note that, for numerical convenience, we analyze only systems with unit Chern vectors, i.e. where C_x, C_y, C_z are either 1 or -1. Extending our considerations to larger Chern vectors would require larger supercells that are computationally too challenging for our resources. Nevertheless, unit Chern vectors allow us to derive general principles of the vBBC that generalize to Chern vectors of arbitrary magnitude and direction. **Figures 4.13**,**4.14**, **4.15** summarize the surface states analysis for the C_zI/C_zI, C_xI/C_zI and C_yI/C_z configurations, respectively. Each figure displays: in panel **a**, the orientation of the Chern vectors as shown by arrows together with the unit cell of the 3D Chern PhCs; in panels b-c, the band dispersion, for the surface states (light blue) and for the nearby bulk bands (orange); in panel **d**, the equi-frequency FLs in momentum space, with arrows indicating the direction of the group velocity (or, equivalently, the Poynting vector [231]). Red and green lines label the localization of surface modes, respectively, on the left or right side of the interface.

4.1.5.3 Case C_zI/C_zI

In the case where the Chern vectors are anti-parallel, along $\hat{\mathbf{z}}$, and both parallel to the interface surface, the configuration is similar to an anti-ferromagnetic arrangement of opposite Chern numbers for a 2D system in the (001) plane [19]. Therefore, for this simple case, we can expect sBBC to naturally extend to 3D. Specifically, when $C_{z_1} = -C_{z_2} = C_z$, we have $|2C_z|$ chiral boundary modes. Indeed, the configuration with anti-parallel unit Chern vectors $C_{z_1} = -C_{z_2} = 1$ results in two co-propagating surface states on each side of the supercell slab, as in **Figure 4.13**. Note that the con-

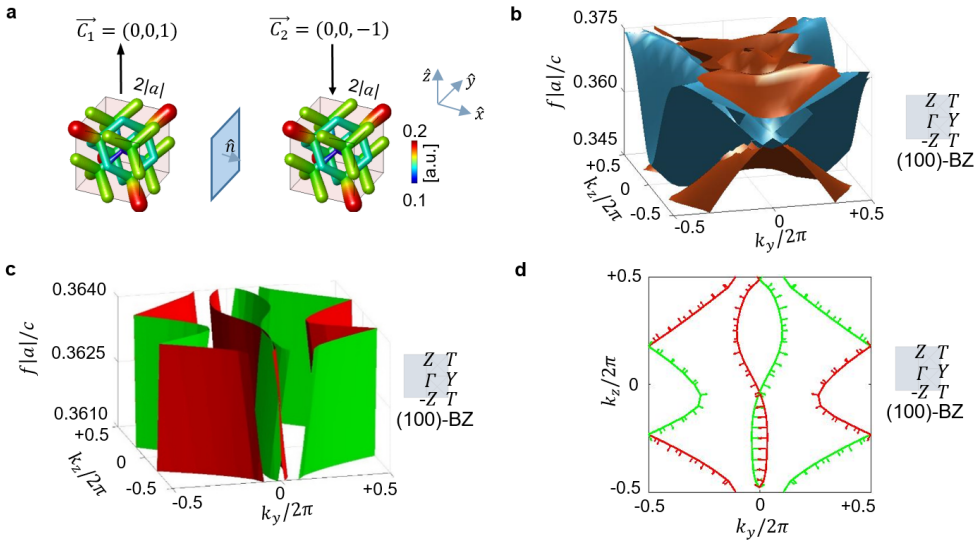

Figure 4.13: C_zI/C_zI interface. $C_{z_1} = -C_{z_2} = 1$. Two co-propagating surface states on each side of the slab. **a**: shows the orientation of the Chern vectors (by arrows) together with the PhC unit cell on each side of the interface. The color code indicates the value of the local radius of the cylinders that constitute the rods of the PhC. The radii of the dielectric rods are locally modulated in order to induce a SM effect able to open up the 3D Chern gap in the underlying crystals. **b** shows the surface (light blue) and bulk (orange) state dispersion as a function of k_y and k_z for frequencies near the topological gap. **c** shows the surface state dispersion over a narrow frequency range in the bulk band gap. Green (red) colors denote states on the right (left) interface. **d** shows an equi-frequency cut of the surface states. The direction of the Poynting vector is denoted by arrows.

served propagation component for these surface states coincides with the propagation direction of the chiral edge modes that would live in the 2D analog system. The 2D analogy employed here works because 3D CIs can be interpreted, in a layer construction picture [45, 185], as a stack of 2D CIs.

4.1.5.4 Case C_xI/C_zI

In 3D CIs, unidirectional surface states can emerge only on the planes parallel to the magnetization [45,46,185]. Therefore, we can expect the 3D CIs with the Chern vector normal to the interface plane (the C_xI side) not to contribute to the spectral flow on the boundary. As a confirmation of this, we observe that both the surface states dispersion and the FL displayed in **Figure 4.14** constitute an adiabatic deformation of those found on the 3D C_zI/trivial interface of Ref. [50]. In particular, the conserved propagation component is determined by C_z only, yielding a surface mode with velocity along k_y. Effectively, the C_xI side does not alter the number of surface modes on the $\hat{\mathbf{x}}$ interface. Therefore, the propagation and the spectral properties of the surface modes do not change even when reversing the sign of C_x. Note, however, that the presence of a

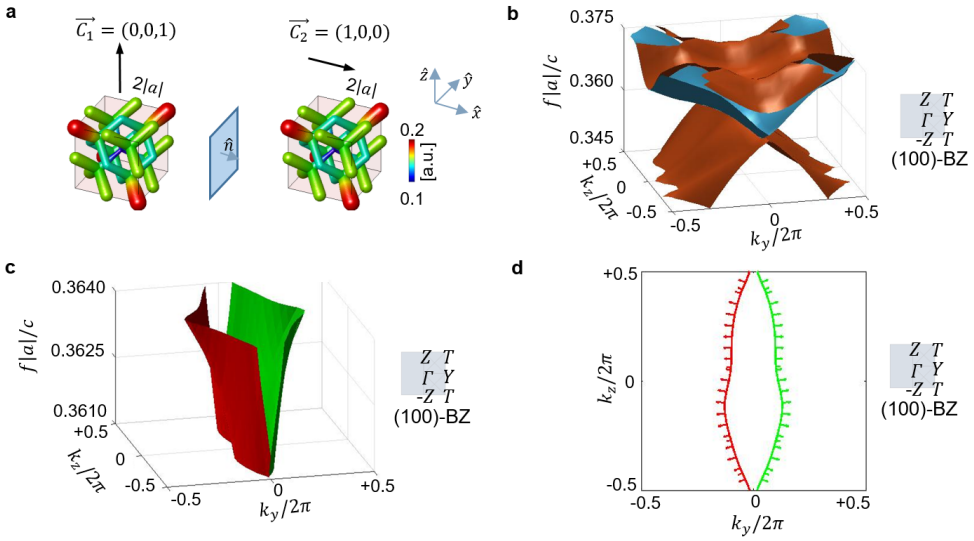

Figure 4.14: 3D C_zI/3D C_xI interface. $C_z = 1$ and $C_x = -1$. Identical when $C_z = 1$ and $C_x = 1$. A single unidirectional surface state: lack of contribution from the Chern vector normal to the interface plane. **a** shows the orientation of the Chern vectors (by arrows) together with the PhC unit cell on each side of the interface. The color code indicates the value of the local radius of the cylinders that constitute the rods of the PhC. The radii of the dielectric rods are locally modulated in order to induce a SM effect able to open up the 3D Chern gap in the underlying crystals. **b** shows the surface (light blue) and bulk (orange) state dispersion as a function of k_y and k_z for frequencies near the topological gap. **c** shows the surface state dispersion over a narrow frequency range. Green (red) colors denote states on the right (left) interface. **d** shows an equi-frequency cut of the surface states. The direction of the Poynting vector is denoted by an arrow.

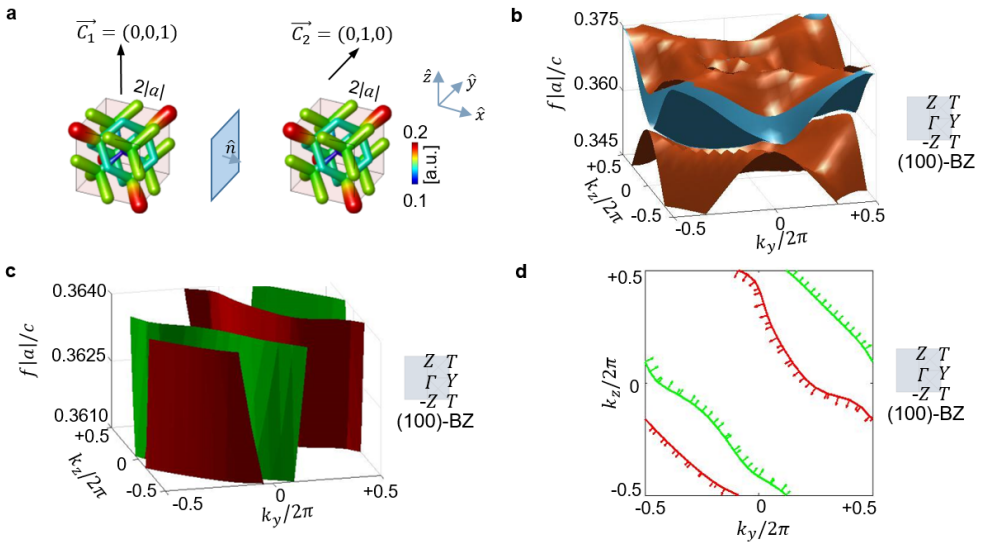

Figure 4.15: 3D C_zI/3D C_yI interface. A single surface state propagating along (011), i.e. along the vectorial sum of the unit Chern vectors. **a** shows the orientation of the Chern vectors (by arrows) together with the PhC unit cell on each side of the interface. The color code indicates the value of the local radius of the cylinders that constitute the rods of the PhC. **b** shows the surface (light blue) and bulk (orange) state dispersion as a function of k_y and k_z for frequencies near the topological gap. **c** shows the surface state dispersion over a narrow frequency range. Green (red) colors denote states on the right (left) interface. **d** shows an equi-frequency cut of the surface states. The direction of the Poynting vector is denoted by an arrow.

band-gap in the C_xI side (in this case a Chern gap) is fundamental for it to behave as an insulator. In conclusion, due to the orientation of its Chern vector, the C_xI side acts as a trivial insulator from the perspective of surface states, even though the Chern vector itself is not zero. A C_xI/C_yI configuration for the same $\hat{\mathbf{x}}$ boundary can be treated very similarly. In such a case, the FLs would be rotated in the $k_y - k_z$ plane relative to **Figure 4.14** , propagating along z. These facts will be exploited in the following subsection.

4.1.5.5 Case C_yI/C_zI

In this configuration, the Chern vectors are orthogonal to each other, and both parallel to the interface plane. This is a fully 3D configuration of Chern vectors, and so a 2D scalar analogy cannot be applied. To understand the correct counting of surface modes and their propagation on the boundary, we need to consider how surface states can hybridize with each other. Following what was observed in the previous subsections, both the C_yI and C_zI side should contribute to surface modes with, respectively, propagation along k_z and k_y. However, in the plot of **Figure 4.15** we observe a single surface state propagating along (011), i.e. along the vector sum of the unit Chern

vectors. This can be understood as follows. In a layer construction picture, the surface modes can never scatter along the propagation direction [46], but they can hybridize along the Chern vector direction. This reasoning will be supported by topological considerations and by a simple model in **Section 4.1.5.6**. Therefore, if we superimpose the plot of **Figure 4.14 (d)**, i.e. for the C_zI side, with a 90 degrees tilted version of it, i.e. for the C_yI side, and if we allow only states on the same side of the sample to hybridize, we obtain the FL connectivity of **Figure 4.15(d)**. Therefore, it can now be interpreted via a linear combination of unit Chern vectors, as summarized in **Figure 4.16 b,d**.

4.1.5.6 Topology of Fermi loops and vBBC

From our previous considerations, it is possible to gain more insight into the topological properties of the FLs and infer some general statements about vBBC for the case of a 3D CI. In **Section 4.1.4.2** we showed that FLs can split in disjoint chiral partners located on opposite sides of the interface slab [46,50], which is reproduced here as well, as confirmed by the fields localization analysis. When residing on the same side of the sample, overlapping FLs can hybridize giving rise to a single, continuously connected FL, as sketched in **Figure 4.16 (d–e)** . The hybridization results in a local change of Poynting vector, for each specific momentum component. However, the winding of the resulting loop around the surface BZ is the same as that of the individual loops before hybridization. To see how this works quantitatively, we can consider a simple model for the interface between a $C_z = 1$ and a $C_y = 1$ 3D Chern system, again with the interface normal to the $\hat{\mathbf{x}}$ direction. Without any hybridization, we will have two chiral surface modes propagating on the interface: $\Delta C_z = 1$ across the interface implies the existence of a state whose Hamiltonian can be written as $H_z = v_z k_y$, describing a chiral mode propagating in the $\hat{\mathbf{y}}$ direction. Similarly, $\Delta C_y = -1$ at the interface implies the existence of a mode with low energy effective Hamiltonian $H_y = v_y k_z$, describing a chiral mode propagating in the $\hat{\mathbf{z}}$ direction. The model employed here represents an effective model for the dispersion of a unidirectional mode on the surface, with broken TRS and at the lowest order in $\mathbf{k}$. Ignoring any hybridization between these modes, we can write the combined surface effective Hamiltonian as:

$$H_0 = \begin{pmatrix} v_z k_y & 0 \\ 0 & v_y k_z \end{pmatrix}. \tag{4.2}$$

The effective Hamiltonian description allows us to find an expansion in powers of the wave vector **k** of the photonic energy bands ω, able to replicate the photonic modes dispersion obtained by numerically solving the Maxwell equations. The constant frequency contours of H_0 consist of one horizontal and one vertical line at each point in the surface Brillouin zone. The two modes at frequency ω intersect at $(k_y, k_z) = (\omega/v_z, \omega/v_y)$ Furthermore, there is spectral flow from negative to positive frequency in H_0, in that we can continuously follow each surface band from $-\infty$ to $+\infty$ in frequency. However, the twofold degeneracy of states at $(k_y, k_z) = (\omega/v_z, \omega/v_y)$ is generically unstable to surface perturbations. To the lowest order, we can model such a perturbation as a constant off-diagonal term added to the effective surface Hamiltonian, **Equation 4.2**,

$$H = H_0 + V = \begin{pmatrix} v_z k_y & r \\ r^* & v_y k_z \end{pmatrix}, \tag{4.3}$$

where $|r|$ parametrizes the strength of the hybridization between modes. The eigenfrequencies of H are given by

$$\omega_\pm = \frac{1}{2}(v_z k_y + v_y k_z) \pm \frac{1}{2}\sqrt{(v_z k_y - v_x k_z)^2 + 4|r|^2}. \tag{4.4}$$

We see immediately that $\omega_+ \neq \omega_-$ for any (k_y, k_z), so there is no longer degeneracy between states. The constant energy contours are now hyperbolic, just as in **Figure 4.16**. Although there is a gap between ω_+ and ω_- at each momentum in the surface Brillouin zone, however, there is still spectral flow from the valence states to the conduction states in frequency and the edge state dispersion extends throughout the entire gap. To see this, we can consider the line $t = v_z k_y = v_y k_z$ in the surface Brillouin zone. Along this line, we have $\omega_\pm = t \pm |r|$; Thus both ω_+ and ω_- interpolate from $-\infty$ to $+\infty$ as a function of t, consistent with the bulk-boundary correspondence. To generalize this hybridization picture to interfaces with larger Chern vectors, we can employ a circuit- or network-type analogy, where the loop states are viewed as wires. If we consider a $\hat{\mathbf{x}}$ interface with M loops directed along k_y and N loops directed along k_z, we can picture the BZ as sort of a black box with M leads on the left and right edges, and N leads on the top and bottom edges. If we want to wire up this box so that current can flow through all the leads, the only way to do this with no intersections is to have a single wire that winds from left to right M times and from bottom to top N times. Since the surface BZ has the topology of a torus, we have $(T_1, T_2) = (M, N)$, where T_1, T_2 denote the winding around the two handles of the surface BZ torus. Therefore,

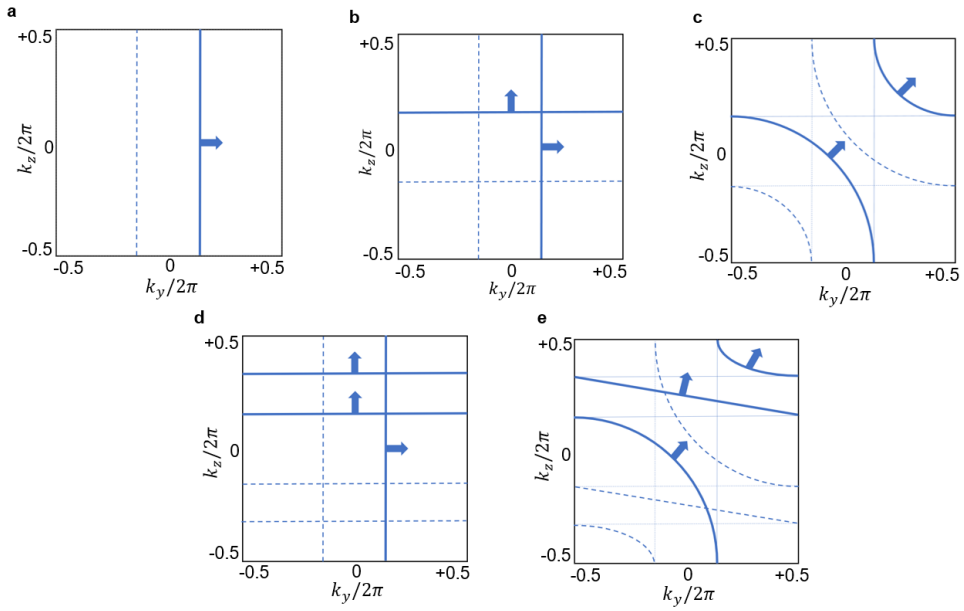

Figure 4.16: Topology of the FLs and their hybridization. Solid and dashed lines label states residing on opposite side of the sample. Thick and thin lines indicate states before and after hybridization, respectively. **a**: FLs with $(T_1, T_2) = (0, 1)$. **b,c**: FLs with $(T_1, T_2) = (1, 1)$ before and after hybridization. d,e) FLs with $(T_1, T_2) = (2, 1)$ before and after hybridization.

given a difference of Chern numbers equal to:

$$\Delta\mathbf{C} = \mathbf{C}_1 - \mathbf{C}_2 = (C_{x_1} - C_{x_2}, -M, N), \tag{4.5}$$

we can expect $M = C_{y_1} - C_{y_2}$ loops directed along k_y and $N = C_{z_1} - C_{z_2}$ loops directed along k_z, since, as observed in **Section 4.1.5.4** , the individual values of C_x do not contribute to any mode on a $\hat{\mathbf{x}}$ interface. In conclusion, the non-zero components of the discontinuity of Chern vectors parallel to the interface correspond to the winding numbers of the surface FLs around the two handles of the surface BZ torus, which completes our vBBC picture for 3D CIs. A $(M, N) = (2, 2)$ type of interface configuration was experimentally constructed by the group of *Baile Zhang* [41] in their vBBC demonstration experiment. Note that the symmetry of a FL in $\mathbf{k}$ is not a universal property and depends on the geometry of the crystal. As discussed in**Appendix C**, the BBC relations are not modified by an asymmetry of the FLs. As well, we stress that the number of loops is not the topologically protected quantity. vBBC only establishes a link between the Chern vector discontinuity and the winding of the FLs on the surface BZ, not with their number. For example, two FL states propagating along k_y and k_z, as represented in **Figure 4.16(b)**, are topologically equivalent to a single FL propagating along a tilted direction, as in **Figure 4.16(c)**: their winding across the two handles of

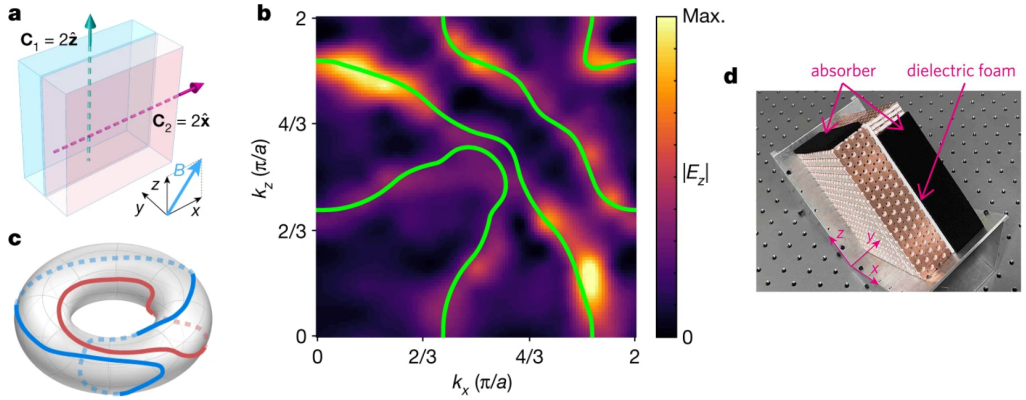

Figure 4.17: The interface between two photonic 3D Chern insulators with perpendicular Chern vectors and magnetic field applied along the diagonal formed by the sum of the two Chern vectors. The FLs wrap around the surface BZ torus to form a $(2, 2)$-torus link (Hopf link).

the BZ is the same, and thus the net propagation direction. This is important because it means that surface states on the same surface of the slab are allowed to scatter and interfere, changing the counting of closed loops on the BZ. Due to topological protection, the scattering result is still a closed loop, with the same number of crossing points for a fixed momentum line and the same winding across the BZ. Finally, note that the vBBC conditions derived here can also be applied to diagonal orientations of the interface normal with respect to the Chern vector, provided moving in a new reference frame. In these regards, a detailed explanation of the vBBC for diagonal cuts of the crystal is provided in **Appendix C**, where a guiding example is provided.

4.1.6 Discussion and outlook

In this section, we developed a strategy to induce the annihilation of Weyl points through cubic and multifold SMs, allowing us to achieve a photonic 3D CI phase with the following novel characteristics: high Chern numbers, reduced magnetic constraints, and orientable Chern vectors. We showed that 3D CI photonic phase obtained displays anomalous surface states on the planes orthogonal to the net magnetization, with non-reciprocal properties. As a remarkable signature of this, we observed the formation of disjoint equifrequency loop structures associated to the spatial separation of chiral and counter-propagating partners. The closed loops emerge from the open FAs of the Weyl semimetal phase, as a result of the topological transition into the 3D Chern insulating phase. From the analysis of interfaces where Chern vectors have a different orientation, we could discuss vectorial aspects of bulk-boundary correspon-

dence, establishing a link between the Chern vector discontinuity and the winding of the FLs on the surface BZ. More in detail, we targeted the following three topological features: First, arbitrarily large Chern numbers can be achieved by design, allowing for multi-modal propagation of topological surface states [98], [211]. On the one hand, the system with Chern number N supports N equifrequency loops. These N equifrequency loops are compressed into a folded BZ that is $1/N$ the size of the original BZ. In this sense, if we are interested in quantities integrated over the BZ, we cannot expect an increase in extensive quantities such us the total field intensity. However, if we are interested in addressing states at a particular wavevector, which is a reasonable constraint in photonic systems, then the modulation has allowed us to address N chiral surface modes with equivalent reciprocal lattice vectors, i.e. achieve unidirectional multiple surface mode operation. The capability of designing photonic systems with large Chern numbers in 3D could find interesting applications in the development of the emergent field of topological lasers [88,232] with a larger number of unidirectional surface states. Second, we showed the TRS breaking parameters required to induce this 3D CI phase can be substantially diminished by the use of larger supercells, which can enable the realization of a 3D CI phase in photonic systems where the magnetic response is weak or it is not possible to manipulate largely the Weyl points in the BZ. We also intend to emphasize that the strategy we devised in our method is material agnostic, and can be easily adapted to any to-be-discovered experimental platform. In that sense, our work provides a roadmap to future experimental exploration of topological PhCs by showing how to reduce the needed magnetic response. Third, we showed that any element of the first Chern class vector can be selected by simply changing the magnetization direction, allowing for unique 3D CI/3D CI interfacing combinations as compared to 2D. This allowed us to investigate vectorial aspects of bulk-boundary correspondence for photonic 3D CIs with Chern vectors differently oriented in space. We showed that, for a 3D CI crystal, the Chern vectors across the interface no longer need to be parallel or anti-parallel to each other, which may render the scalar analogy with 2D difficult to apply. We concluded that vectorial features of the BBC need to be taken into account to correctly capture the number and the propagating properties of the photonic surface modes, in perspective of promoting sBBC from 2D to a vBBC for 3D CIs. Specifically, we analyzed the variety of possible surface states that can emerge on the boundary of photonic 3D CIs, depending on the orientation of Chern vectors across, and with respect to the interface. We showed that: (1) Any discontinuity in the Chern vector components normal to the plane of the interface does not contribute to the num-

ber of surface modes; (2) Multiple unidirectional photonic surface modes arising from different Chern vectors across the interface can hybridize with each other, preserving their winding around the surface BZ; (3) The number and propagation direction of the surface modes can be related to a difference of Chern vectors parallel to the interface. Our observations can summarized via the following statement: the winding numbers of the surface FLs around the surface BZ correspond to the non-zero components of the discontinuity of Chern vectors parallel to the interface. In other words, we derived a link between a bulk topological quantity, the Chern vector, and a boundary observable, the winding of the FLs on the surface, which completes the vBBC picture for 3D CI PhCs. The present work remains open to new developments and research lines: First, as already noted in the previous sections, a 3D CI can be thought of as a stack of 2D CIs from a layer construction point of view [45, 185]. An obstruction in this layer structure across the interface can give rise to extra chiral boundary modes [65, 222], even without a discontinuity in the Chern vector [222], beyond what is expected from a simple extension of 2D sBBC to 3D. The concept of obstructed 3D Chern Insulators (o3D CI) and their chiral photonic hinge modes will be explored in the next section. Moreover, our analysis was performed using 1D linear supercells, due to numerical limitations. However, more complex supercells and Chern vector configurations may be worth to be considered (2D rod-, 3D core- geometries made of 3D CIs, etc.). An interesting design could consist of 3D CI arranged around a trivial core with Chern vectors pointing inwards (e.g. fixing a 3D $+C_x\mathrm{I}$ on a left $\hat{\mathbf{x}}$ panel). Such a 3D interfacing arrangement, originally proposed in Ref. [46] as a possible realization of a magneto-electrical (ME) coupler in the field of electronics, has not yet a realization or equivalent in photonics. Analysis of all these designs is left for further investigation.

4.2 Photonic Axion Insulator

Axion insulators (AXIs) [48, 51–57, 57–59, 59–68] are 3D inversion ($\mathcal{I}$)-symmetric magnetic Higher-Order Topological Insulators (HOTIs) [233, 234] which induce various topological magnetoelectric effects, such as the quantized magneto-optical Faraday and Kerr rotation, the image magnetic monopole effect, and half-quantized surface Hall conductance [56–59]. The topological properties of AXIs arise from the quantization of their electromagnetic coupling term, the so-called topological θ-angle [48, 51, 52], which is pinned to π in presence of $\mathcal{I}$-symmetry (or other θ-odd operations such as roto-inversions and time-reversed rotations). [235]. AXIs are of significant interest

because, acting as HOTI, they are able to support hinge-localized chiral modes, which propagate in the form of unidirectional axionic channels [236–238]. These hinge-states are expected to emerge at the 1D facets of an AXI crystallite or in the presence of 1D dislocations in the AXI lattice, where gradients of the θ angle arise, inducing the formation of axionic strings [59, 237, 239]. Recent studies [59, 65] have shown that the chiral propagation of the AXI hinge-localized modes is highly tunable. Especially in the presence of a ferromagnetic order, it is possible to switch between different hinge-mode configurations via external magnetic control, allowing magnetic re-routing of conducting channels from one input into one or more outputs. In the context of PhCs (PhCs), this remarkable property of AXIs could allow for magnetic manipulation, guiding, and rerouting of the 1D non-reciprocal flow of light, with relevant applications for optical communication technologies and for the development of magnetically-tunable photonic switch devices. So far, no proposals have been presented for axion-based PhCs or axion-protected light propagation. In addition to this, recent studies have suggested that AXI materials may be capable of detecting axion-like particles, that constitute dark-matter candidates [240–242]. This is due to the fact that emergent axionic excitations in AXI couple with electromagnetism, $\mathcal{L} \propto \theta \mathbf{E} \cdot \mathbf{H}$, similar to the axion ($a$)-photon coupling observed in high-energy physics for light dark-matter, which follows $\mathcal{L} \propto a\mathbf{E} \cdot \mathbf{H}$. In PhCs, photons can interact with external magnetic fields via gyrotropy, they display a non-zero effective mass, and they are wavelength-tunable via lattice size-scaling, all of which are essential ingredients for the realization of an axion haloscope [240, 243–245]. The demonstration of an AXI in a PhC could represent an opportunity to bridge these two different approaches in the study of axion-photon coupling. Despite the theoretical significance and potential applications of AXIs, no proposals have been put forward yet for their implementation in PhCs: this section aims to propose and demonstrate the first theoretical model and general design strategy for photonic AXIs in 3D PhCs. To induce axionic band topology ina 3D PhC, we incorporate a phase obstruction in the SM of the dielectric elements within gyrotropic Weyl PhCs [42, 50]. The SM is designed as an $\mathcal{I}$-symmetric, static, geometric deformation of the PhC lattice, enabling an experimental implementation of the PhC without necessitating any dynamic driving. Serving as a photonic analog of a Charge-Density-Wave (CDW) [222, 238, 246, 247], the SM couples Weyl points with opposite topological charges while maintaining the $\mathcal{I}$-symmetry of the model. The resulting AXI is dubbed *relative*, because it is only exhibited at the interface of two PhCs with a quantized *relative* axionic angle $\delta\theta$ and vanishing *relative* Chern numbers. This ap-

proach is grounded in the concept that a dislocation of the CDW phase in a specific class of $\mathcal{I}$-symmetric Weyl Semimetals (WS) acts as a source of axion field gradients [222, 238, 239]. Consequently, the domain wall separating the phase-obstructed CDW-WS can be interpreted as the critical point between a trivial insulator and an AXI. By employing this strategy, we successfully realize a photonic *relative* Axion Insulator (*r*AXI) in a realistic gyrotropic setup. By inserting planar dislocations in the SM phase, we bind 1D chiral channels on $\mathcal{I}$-related hinges, that provide a PhC realization of an axion domain wall protected by $\mathcal{I}$-symmetry. Remarkably, the 1D channels supported by the *r*AXI are buried in a fully connected 3D dielectric structure, thus protected from radiation through the electromagnetic continuum [248]. This design not only represents the first instance of a tunable HOTI with chiral hinge states in 3D PhCs [19], but the observed 1D-modes are also consistent with a single, unidirectional axionic channel that wraps around the central phase-obstructed core, endowing the photonic hinge-channels with non-reciprocal propagation properties. Lastly, we propose a physically viable method for manipulating these axionic hinge modes by controlling the PhC gyrotropic response using a small external magnetic bias. Specifically, we induce gyrotropy-induced transitions in the photonic AXI, which can function as an efficient topological switch between various 1D photonic fiber configurations. Interestingly, recent experimental advancements in 3D gyrotropic crystals have demonstrated that manipulating Weyl points via external fields is possible, with a high degree of control and intensity [41,249]. These findings suggest the possibility of manipulating, directing, and deviating the 1D non-reciprocal flow of light in a photonic AXI using state-of-the-art experimental setups. The capability of manipulating the HOTI hinge states in the photonic AXI via gyrotropy underscores the potential of the proposed design for creating magnetically tunable photonic switch devices, thereby paving the way for advancements in axion-based photonics. These ideas were initially presented in our recent theoretical work, "Axion Topology in PhC Domain Wall" [36].

4.2.1 Inversion-symmetry pinning

Our starting setup for inducing photonic AXI band topology consists of an $\mathcal{I}$-symmetric gyrotropic PhC [42,223,250] under an external magnetic field $\mathbf{H} = (0, 0, H_z)$, as shown in **Figure 4.18(a)**. The starting point is the Weyl PhC studied in the previous chapter at **Section 4.1.2**. However, differently from before, we now want to preserve $\mathcal{I}$-symmetry, the fundamental symmetry for inducing AXI topology. As we already discussed in **Section 4.1**, in the presence of a gyroelectric medium the external magnetic field induces

an off-diagonal imaginary component in the permittivity tensor [9, 10], as expressed by **Equation 4.1**, where $\eta_z = \eta_z(H_z)$ is the bias-dependent gyroelectric parameter. As a consequence of TRS breaking due to gyrotropy, a photonic Weyl dipole is generated in the Brillouin zone, along the direction of the H_z magnetic field, as shown in **Figure 4.18(a)**. The Weyl dipole separation increases proportionally to the external H_z and can be magnetically tuned. In order to emulate the effect of a CDW in condensed-matter systems [236, 238, 246] to open a topological gap, we introduce a z-directed SM of lattice period $N \in \mathbb{N}$ and $N \geq 2$, commensurate with the Weyl dipole separation $\mathbf{Q} = \mathbf{q}_+ - \mathbf{q}_-$, where $\mathbf{q}_\pm$ are the locations of Weyl points with chirality ± 1 in Brillouin zone. Accordingly, we fix the Weyl points of opposite topological charge at approximately $\mathbf{q}_\pm = (\pi, \pi, \pi \pm \pi/N)$. This results in a folding of the BZ, as shown in **Figure 4.18(b)**, and couples the Weyl points to open a non-trivial gap, as shown in **Figure 4.18(c)**. The SM is introduced as a local deformation Δr of the radius r of the dielectric rods, according to the relation:

$$\Delta r = r_m \cos(2\pi z/N|a| + \phi), \tag{4.6}$$

where $|a|$ is the lattice parameter of the starting PhC, while r_m and ϕ control, respectively, the amplitude and the phase of the dielectric modulation. Note that this represents a static geometric deformation of the PhC structure which can be stably implemented during the fabrication process and does not require any dynamical driving. The ϕ phase of the SM is the fundamental design parameter that we will set in order to induce axionic band topology. For the purpose of preserving the $\mathcal{I}$-symmetry of the unperturbed PhC of **Figure 4.18(a)**, which is crucial for axion behavior, we pin the modulation at the $\mathcal{I}$-center and target only two specific values of the SM phase: $\phi = 0$ and $\phi = \pi$. The corresponding modulated dielectric structures are shown in **Figure 4.18(c–d)** in a 3D rendering, and in **Figure 4.19** in a side view, for a $N = 3$ modulation period. We observe that both $\phi = 0$ and $\phi = \pi$ phases display the same insulating spectrum. However, we will now demonstrate that their 3D photonic bulk gaps exhibit a different topological obstruction in the $\mathcal{I}$-symmetry indicators associated to the quantization of their *relative* axion angle $\delta\theta$.

4.2.2 Transversality-enforced TB for the *r*AXI

In this section, we develop a TETB model [250] of the photonic *r*AXI with the methods described in **Chapter 3**. The model, enabling the simulation of the electromagnetic re-

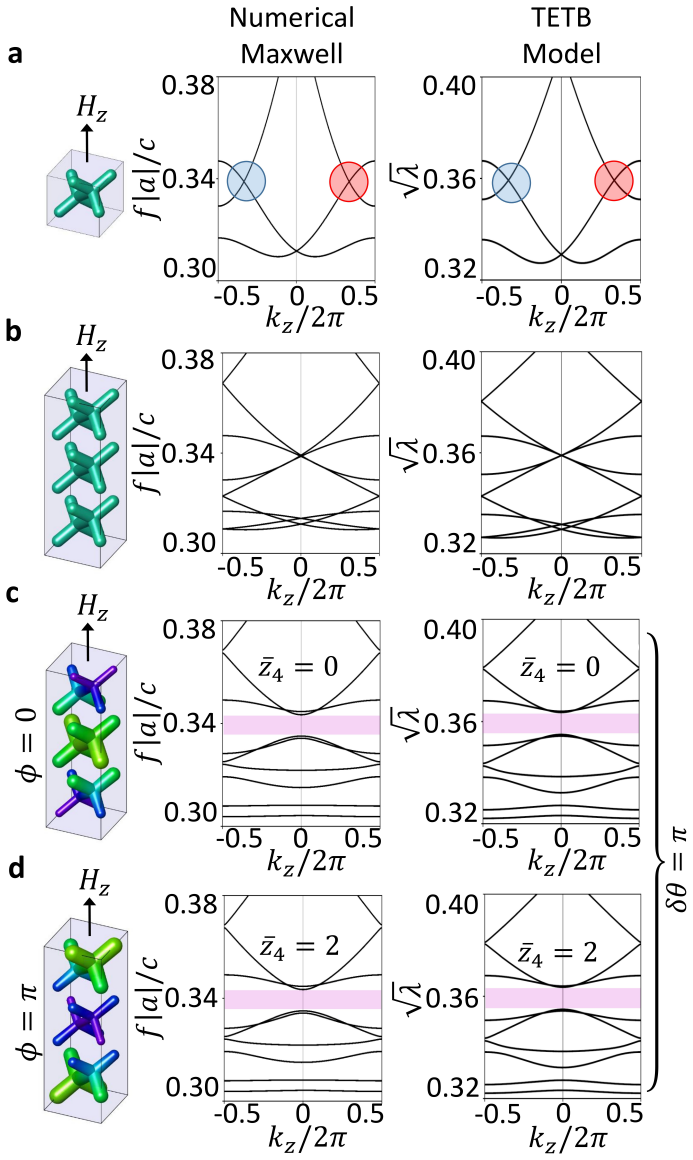

Figure 4.18: Effect of a SM on the photonic Weyl bands. The left panels show the PhC geometry and the reduced frequencies $f|a|/c$, where c is the speed of light and $|a|$ the scale-invariant lattice parameter, obtained by solving numerically the Maxwell equations. The right panels show the square root of the transversality-enforced tight-binding model eigenvalues $\sqrt{\lambda}$, consistent with the mapping between the Schrödinger and electromagnetic wave equations, that relates energies and frequencies quadratically ($\lambda \sim \omega^2$, see [250]). In these plots, we show the k_z line, for fixed $k_x = \pi$ and $k_y = \pi$. Weyl points which are separated by a $|\mathbf{Q}| = 2\pi/N$ distance in momentum space as in panel **a**, are superimposed on an artificial supercell in panel **b**, and then coupled by a commensurate SM of period $N = 2\pi/|\mathbf{Q}|$ as in panels **c–d**. The supercell amplitude is $r_m/r_0 = 1/20$ for the PhC and $V_{4c} = -V_{4b} = 1/150$ for the TETB. The relative gyrotropic parameter is $\eta_z = 7.8$ for the PhC, which corresponds to an adimensional magnetic perturbation of $H_z = 5.45$ in the TETB. Panel **c** and **d** differ solely for the angular phase of the SM ϕ, with $\phi = 0$ in panel **c**, and $\phi = \pi$ in panel **d**.

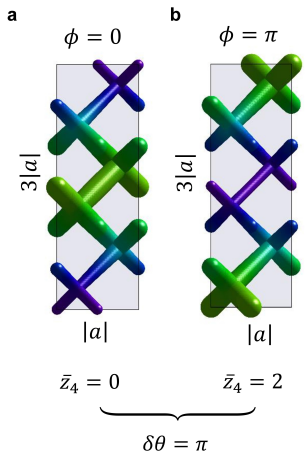

Figure 4.19: 3D photonic *r*AXI resulting from a $N = 3$ periodic SM imposed on a gyrotropic Weyl photonic semimetal (side view). The SM acts as a local deformation of the diameter of the dielectric rods. The z-directed modulation is along the magnetization axis. The SM is centered at the inversion center of the unperturbed lattice: panels (**a** and **b** correspond to an angular phase ϕ of the SM of 0 and π, respectively.

sponse of the photonic *r*AXI, allows the demonstration of HOTI bulk-hinge correspondence of the *r*AXI through cost-effective calculations of large-scale rod geometries. Moreover, it facilitates efficient computation of the axion topological invariants and provides an analytical model that is well-suited for identifying symmetries in the topological phase, while capturing and regularizing the Γ-point electromagnetic obstruction that arises due to the transversality constraint of the Maxwell equations [23, 250]. Before the introduction of the z-directed external magnetic field and SM, the crystal structure belongs to SG #224 ($Pn\bar{3}m$) [42, 50, 250]. The symmetry content of the photonic bands can be deduced by analyzing the Bloch electric modes (**E**), obtained in MPB via numerical solution of the Maxwell equations. The **E** field transforms as a vector:

$$g\mathbf{E}(\mathbf{r}) = (R\mathbf{E})(R^{-1}(\mathbf{r} - \mathbf{t})), \tag{4.7}$$

for each SG operation $g = \{R|\mathbf{t}\}$, where R is a point group element and $\mathbf{t}$ a translation. For each band n with $\omega \neq 0$ and every high-symmetry point $\mathbf{k}_h$, we compute the $x_{n,\mathbf{k}_h}(g)$ diagonal elements of the representation matrix corresponding to g in the little group of $\mathbf{k}_h$, from the overlap integrals:

$$x_{n,\mathbf{k}}(g) = \langle \mathbf{E}_{n,\mathbf{k}_h} | g\mathbf{D}_{n,\mathbf{k}_h} \rangle \tag{4.8}$$

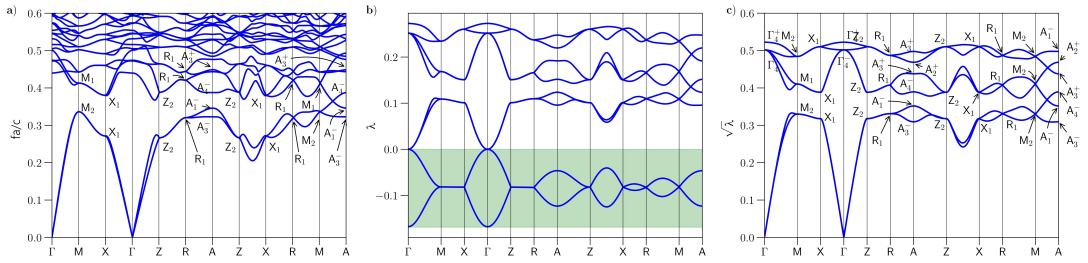

Figure 4.20: TETB for the non-magnetic case. **a**: Photonic bands and associated dielectric structure of the 3D PhC with SG $Pn\bar{3}m$ (No. 224). Irreps are labeled at HSP according to BCS notation. **b**: Band structure of the TB model built from the photonic pseudo-orbitals. The bands enclosed by the green-shaded region belong to the additional modes included to regularize the symmetry content at Γ. **c**: TETB obtained after applying the spectral mapping and imposing the transversality constraint.

where $\mathbf{D} = \varepsilon\mathbf{E}$ is the displacement field and ε the dielectric constant. From Schur's Orthogonality Relations [152], we are able to extract the symmetry vector $\mathbf{v}^T$ that gives the multiplicity of each irreducible representation (irrep) in the little group of each high symmetry point. We label the irrep according to the notation of Bilbao Crystallographic Server (BCS) [202] This analysis returns, for the six lowest-electromagnetic modes:

$$\mathbf{v}^T = [(\blacksquare)^{2T} + \Gamma_2^- + \Gamma_4^-, R_4^- + R_5^+, \quad M_1 + 2M_4, X_1 + X_3 + X_4] \tag{4.9}$$

where $(\blacksquare)^{2T}$ indicates the irregular symmetry content at Γ and $\omega = 0$ arising from transversality of the electromagnetic waves [23, 250], with $()^T$ labeling the transverse bands. The entire transverse bundling procedure is described in **Section B.1**. A symmetry-constrained, tight-binding Hamiltonian $H(\mathbf{k})$ can be constructed for these transverse photonic bands, via the TETB methods proposed in **Chapter 3**. This approach involves the introduction of auxiliary longitudinal modes $\mathbf{v}^L$, which can regularize the Γ-point obstruction, such that $\mathbf{v}^{T+L} = \mathbf{v}^T + \mathbf{v}^L$ is regular. By exploiting a formal mapping between the Schrödinger and electromagnetic wave equations, which relates energies and frequencies quadratically ($\lambda \sim \omega^2$), a TETB model is developed enforcing the lowest set of longitudinal bands at $\omega^2 \leq 0$, resulting in the $\mathbf{v}^T = \mathbf{v}^{T+L} - \mathbf{v}^L$ transverse vector capturing all the symmetry, topology and energetic features of the active bands in the PhC. For the specific $\mathbf{v}^T$ of **Equation 4.9**, this can be achieved via

$$\mathbf{v}^{T+L} = A_{2u}@4b + A_{2u}@4c. \tag{4.10}$$

with $\mathbf{v}^L = A_1@2a$, where the decomposition is done in terms of Elementary Band Representations (EBRs), which constitute the trivial atomic limits induced by localized or-

Parameters	Value
α_1	0.306159
α_2	0.123753
a_1	0.157927
a_2	-0.064197
r_2	0.068848
s_2	-0.100771
w_2	0.022712
a_3	0.035449
r_3	-0.041474

Table 4.2: Parameters of the TB Hamiltonian for SG $Pn\bar{3}m$ (No. 224).

bitals at a specific Wyckoff position, as in the notation of BCS. This results in a 8-band model, from A_{2u} photonic pseudo-orbitals at Wyckoff position $4c$: $(1/2, 1/2, 1/2)$ and $4b$: $(0, 0, 0)$, both with site-symmetry group $\bar{3}m$. This gives rise to a TB Hamiltonian, which can be expressed as a 8×8 matrix $H(\mathbf{k})$, where the symmetry of the crystal constrains the functional dependence on $\mathbf{k}$. The analytical expression of the $H(\mathbf{k})$ Hamiltonian, obtained including interactions up to third-nearest neighbors, is shown in **Equation D.5** of **Appendix B**. The resulting Hamiltonian $H(\mathbf{k})$ can be written in terms of nine free, real parameters: α_1 and α_2 are on-site energies, while the six remaining parameters are first (a_1), second (a_2, r_2, s_2, w_2) and third (a_3, r_3) nearest neighbor hoppings. The free parameters in the Hamiltonian are fitted to the band structure of the crystal, shown in **Figure 4.20**, while forcing the auxiliary nonphysical longitudinal bands to have negative eigenvalues. The result is given in **Table 4.2**. We perform the fitting using a least-square minimization routine at all HSPs. The cost function is a multiobjective, multivariable function, which measures the distances between the square of the frequencies computed numerically in MPB for the PhC and the eigenvalues of the TETB for each irrep. The objective vector contains the multiple distances, while the variables are the TB coefficients. Specifically, we use the least-squares function of the *scipy.optimize* package in Python [251]. The eigenvalues of the TB model are shown in **Figure 4.20**. The longitudinal bands are in the green-shaded region and represent the negative eigenvalues, detached from the physical, transverse ones. Finally, we take the square root of the eigenvalues ($\lambda = \omega^2$) and discard the longitudinal bands, obtaining the physical band-structure shown in **Figure 4.20**. One can see that the TETB model reproduces the MPB band structure of the crystal accurately for the six lowest energy bands, both in their dispersion and symmetry content.

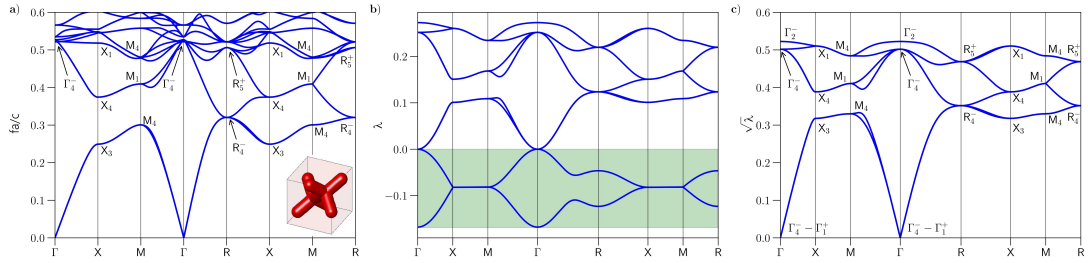

Figure 4.21: TETB for the magnetic case. **a**: Photonic bands and associated dielectric structure of the 3D PhC with SG $Pn\bar{3}m$ (No. 224). Irreps are labeled at HSP according to BCS notation. **b**: Band structure of the TB model built from the photonic pseudo-orbitals. The bands enclosed by the green-shaded region belong to the additional modes included to regularize the symmetry content at Γ. **c**: TETB obtained after applying the spectral mapping and imposing the transversality constraint.

4.2.2.1 Gyrotropy

The introduction of a z-directed gyromagnetic bias gives rise to a topological charge-1 Weyl dipole oriented along the k_z axis. In the TETB, gyrotropy can be modeled via non-minimal coupling to an external magnetic field **H**:

$$H(\mathbf{k}, \mathbf{H}) = H(\mathbf{k}) + f(\mathbf{k}, \mathbf{H}), \tag{4.11}$$

where the function $f(\mathbf{k}, \mathbf{H})$ should respect the symmetries of the crystal, **H** transforming as a pseudovector. Non-minimal coupling is adopted, due to the uncharged nature of photons, which prevents the use of Peierls substitution. The $\mathbf{H} = (0, 0, H_z)$ field is tuned in order for a Weyl dipole to form along the k_z line, with a separation of $|\mathbf{Q}| = |\mathbf{q}_+ - \mathbf{q}_-| = 2\pi/N$ and $N \in N$ and $N \geq 2$, as shown in **Figure 4.18(a)**. To model this phenomenon via the TETB, we will use a first-order perturbation in **H**, with the magnetic field directed along the z axis. As a result of the constraints (3.53) and (3.54), the linear coupling to the magnetic field depends on five free, real parameters: δ_1 for first-nearest neighbor hopping terms, and δ_2, β_2, κ_2 and ϵ_2 for second-nearest neighbor hoppings. Due to symmetry constraints, first-order linear perturbation does not affect the third nearest neighbor hoppings. The corresponding magnetic TETB perturbation $f_M(\mathbf{k}, \mathbf{H})$ is given in **Equation D.9** of **Appendix B**. Now, the new parameters need to be adjusted to fit the MPB band structure of the crystal affected by the static magnetic field (shown **Figure 4.21**).

As in the previous section, we apply the same minimization routine over the new parameters, keeping the last TETB parameters (**Table 4.2**) unchanged. We obtain the values shown in **Table 4.3** for the perturbation. **Figure 4.21** displays the eigenvalues of the perturbed TETB model with a magnetic field along z. Again, the longitu-

Parameters	Value
δ_1	0
δ_2	0.001
β_2	−0.001
κ_2	0.001
ϵ_2	−0.001

Table 4.3: Parameters of the linear function $f_L(\mathbf{k}, \mathbf{H})$.

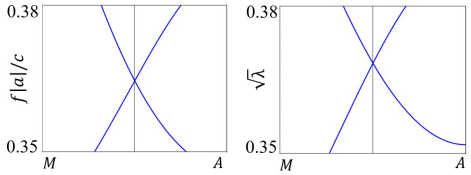

Figure 4.22: Position of the Weyl point obtained from MPB and TB model for a crystal with SG $Pn\bar{3}m$ (No. 224) in perfect agreement with Ref. [50]. **a:** Weyl point at exactly half the MA line for the MPB computations. **b:** Weyl point situated at exactly half the MA line for the TB model.

dinal auxiliary bands are kept in the green-shaded region, showing that they continue to be negative even in the presence of the magnetic field. Finally, using $\lambda = \omega^2$, the longitudinal modes are discarded, obtaining the physical band-structure shown in **Figure 4.21** that closely matches the one obtained through the electromagnetic numerical simulations of the PhC **Figure 4.21**. Note that in the MPB simulations, the applied magnetic field generates a pair of Weyl points [50], one of them halfway along the MA high symmetry line. As shown in **Figure 4.21**, the TETB model exactly replicates this behavior.

4.2.2.2 Supercell modulation

Starting from the $H(\mathbf{k}, \mathbf{H})$ magnetic Hamiltonian, we consider an additional perturbation aimed at capturing the effect of a SM of the dielectric elements. The SM is introduced in the TETB via a simple onsite supercell-modulated potential, that mimics the local electromagnetic energy redistribution in the modulated dielectric rods:

$$H_\Delta(\mathbf{r}, \mathbf{H}) = H(\mathbf{r}, \mathbf{H}) + \sum_i V_i \cos\left(\frac{2\pi z_i}{N|a|} + \phi\right) c_i^\dagger(\mathbf{r}) c_i(\mathbf{r}), \tag{4.12}$$

where $H(\mathbf{r}, \mathbf{H})$ is the real-space TETB Hamiltonian for the magnetic system before modulation, $|a|$ is the lattice parameter of the crystal before modulation, and V_i and ϕ parameterize the amplitude and the phase of the modulation, respectively. Note that the sum in **Equation 4.12** runs over all the basis pseudo-orbitals used in the TETB model, i.e., the pseudo-orbitals placed at Wyckoff positions 4*c* and 4*b*. Since these po-

sitions are related by symmetry, the amplitude of the modulation in the positions inside a Wyckoff position should be equal. We will call them V_{4c} and V_{4b}, respectively. However, since the maximal Wyckoff position $4b$ and $4c$ cannot be adiabatically deformed into each other without breaking the symmetry of the model, we have the additional freedom of choosing the relative sign of their modulation amplitude, V_{4b} and V_{4c}. Justified by the fact that the Wyckoff positions $4c$ fall inside the dielectric elements, while the Wyckoff positions $4b$ are in the air region, we decide to adopt the convention where the on-site potentials on $4b$ and $4c$ are opposite in sign, i.e. $V_{4c} = -V_{4b} > 0$, consistent with regions of higher and lower electromagnetic energy concentration. As shown in **Figure 4.18(c)**, the effect of the SM is correctly captured by the transverse modes of the TETB after the introduction of the on-site potential, which results in the opening of a $C_z = 1$ gap. As we will demonstrate now, the supercell-modulated pseudo-orbitals of the TETB induce all the irreps of the supercell-modulated PhC band-structure, representing an exact representation for the $\tilde{\mathbf{v}}^T_\phi$ electromagnetic modes bellow the gap, $\tilde{}$ standing for the symmetry vector after modulation. We express the symmetry vector in the notation of MSG #2.4 ($P\bar{1}$), which is the symmetry of the crystal after the introduction of the H_z magnetic bias, the $\mathcal{I}$-symmetric SM, and the off-axis $h_{x,y}$ perturbation. For the geometry-modulated PhCs, we find:

$$\tilde{\mathbf{v}}^T_{\phi=0} = [(\blacksquare)^{2T} + 2\Gamma_1^+ + 2\Gamma_1^-, 2R_1^+ + 4R_1^-, 3T_1^+ + 3T_1^-, 3U_1^+ + 3U_1^-, 2V_1^+ + 4V_1^-, \\ 3X_1^+ + 3X_1^-, 3Y_1^+ + 3Y_1^-, 3Z_1^+ + 3Z_1^-] \tag{4.13}$$

and

$$\tilde{\mathbf{v}}^T_{\phi=\pi} = [(\blacksquare)^{2T} + 2\Gamma_1^+ + 2\Gamma_1^-, 2R_1^+ + 4R_1^-, 3T_1^+ + 3T_1^-, 3U_1^+ + 3U_1^-, 4V_1^+ + 2V_1^-, \\ 3X_1^+ + 3X_1^-, 3Y_1^+ + 3Y_1^-, 3Z_1^+ + 3Z_1^-] \tag{4.14}$$

On the other hand, for the onsite-modulated TETB, we obtain:

$$\tilde{\mathbf{v}}^{T+L}_{\phi=0} = [4\Gamma_1^+ + 8\Gamma_1^-, 5R_1^+ + 7R_1^-, 6T_1^+ + 6T_1^-, 6U_1^+ + 6U_1^-, 5V_1^+ + 7V_1^-, \\ 6X_1^+ + 6X_1^-, 6Y_1^+ + 6Y_1^-, 6Z_1^+ + 6Z_1^-] \tag{4.15}$$

and

$$\tilde{\mathbf{v}}^{T+L}_{\phi=\pi} = [4\Gamma_1^+ + 8\Gamma_1^-, 5R_1^+ + 7R_1^-, 6T_1^+ + 6T_1^-, 6U_1^+ + 6U_1^-, 7V_1^+ + 5V_1^-, \\ 6X_1^+ + 6X_1^-, 6Y_1^+ + 6Y_1^-, 6Z_1^+ + 6Z_1^-] \tag{4.16}$$

The TETB therefore captures a double band inversion occurring at the $V = (\pi, \pi, 0)$ point, between the system with $\phi = 0$ and $\phi = \pi$. After having identified the irregular irrep content at Γ, as $(\blacksquare)^{2T} = -\Gamma_1^+ + 3\Gamma_1^-$, consistent with symmetry-constrained decomposition for point group $\bar{1}$ as in Refs. [23,250], we can split the TETB as follows: $\tilde{\mathbf{v}}_\phi^{T+L} = \tilde{\mathbf{v}}_\phi^T + \tilde{\mathbf{v}}_\phi^L$, where:

$$\begin{aligned}\tilde{\mathbf{v}}^L_{\phi=0,\pi} = [&3\Gamma_1^+ + 3\Gamma_1^-, 3R_1^+ + 3R_1^-, 3T_1^+ + 3T_1^-, 3U_1^+ + 3U_1^-, 3V_1^+ + 3V_1^-, \\ &3X_1^+ + 3X_1^-, 3Y_1^+ + 3Y_1^-, 3Z_1^+ + 3Z_1^-]\end{aligned} \tag{4.17}$$

represents the longitudinal auxiliary modes with $\omega^2 < 0$, and has the same expression for both $\phi = 0, \pi$. This shows that the symmetry vector of the TETB represents an accurate representation of the electromagnetic modes below the gap of the rAXI. Specifically, the TETB symmetry vector with an onsite supercell-modulation can be decomposed as a longitudinal component $\tilde{\mathbf{v}}_\phi^L$ which has same expression for both $\phi = 0, \pi$ phases and a transverse part $\tilde{\mathbf{v}}_\phi^T$, which coincides with symmetry vector of the transverse modes of the PhC.

4.2.2.3 Magnetic symmetry-indicators

In order to highlight the role of $\mathcal{I}$-symmetry in protecting the rAXI topology, we compute the magnetic symmetry-indicators (SI) $\nu_\phi^T = \{\bar{z}_{2,x}, \bar{z}_{2,y}, \bar{z}_{2,z} | \bar{z}_4\}$ [45, 67, 195–198] for the tranverse-electromagnetic modes of the PhC (the $\bar{}$ overbar stands for magnetic and the $()^T$ superscript indicates transverse bands). In particular, we focus our interest on the $\bar{z}_4$ strong index, which is associated to axion topology [66, 198, 222]. We consider the structures with $\phi = 0$ and $\phi = \pi$, in the presence of both H_z and a small in-plane $h_{x,y}$ which reduce the symmetry to MSG 2.4 (in the BNS notation of Refs. [153,252]). For the effective photonic TETB, which is regular and does not present any obstruction at Γ, the calculation of the SI follows directly from the well-known closed-formula expression that relates the $\mathcal{I}$-eigenvalues to the $\{\bar{z}_{2,x}, \bar{z}_{2,y}, \bar{z}_{2,z} | \bar{z}_4\}$ magnetic SI [45, 67, 195–197], i.e.:

$$\bar{z}_{2,i} = \frac{1}{2} \sum_{\substack{\mathbf{k}_h \in \{IIMS\} \\ \mathbf{k}_h \cdot \mathbf{R}_i = \pi}} (n_h^+ - n_h^-) \mod 2 \tag{4.18}$$

$$\bar{z}_4 = \frac{1}{2} \sum_{\mathbf{k}_h \in \{IIMS\}} (n_h^+ - n_h^-) \mod 4 \tag{4.19}$$

where n_h^+ (n_h^-) are the multiplicities of the positive (negative) parity eigenvalues at the high-symmetry point $\mathbf{k}_h$, and $\mathbf{R}_i$ are the primitive lattice vectors. This returns, depending on the phase ϕ:

$$\nu_{\phi=0}^{T+L} = \{0, 0, 1|0\} \tag{4.20}$$

and

$$\nu_{\phi=\pi}^{T+L} = \{0, 0, 1|2\}. \tag{4.21}$$

To obtain the corresponding ν_ϕ^T transverse SI for the electromagnetic modes, we can exploit the linearity of the SI with respect to the symmetry vector [23, 203], i.e.:

$$\nu_i^T = \nu_i^{L+T} - \nu_i^L. \tag{4.22}$$

Since the SI of the longitudinal modes of **Equation 4.17** are trivial, it follows that the SI of the TETB and the MPB calculations coincide, $\nu_i^T = \nu_i^{L+T}$. This confirms that the $\phi = 0$ and the $\phi = \pi$ systems are obstructed with respect to each other, with a $\delta\bar{z}_4 = 2$ discontinuity of the *even* $\bar{z}_4$ signaling a *relative* axionic obstruction. On the other hand, the invariance of the $\bar{z}_{2,z}$ term is related to an odd C_z Chern invariant, which, as confirmed via photonic Wilson loop [1, 33, 50] calculations, is $C_z = 1$ identically for both structures. Note that although we have computed $\nu_{\phi=0}^T$ and $\nu_{\phi=\pi}^T$ using the TETB model , the difference

$$\nu_{\phi=\pi}^T - \nu_{\phi=0}^T = \{0, 0, 0|2\} \tag{4.23}$$

depends only on the sign of the modulation-induced band gap.

4.2.3 Topological characterization

To verify the quantization of the *relative* axion angle between $\phi = 0, \pi$, we compute the layer Chern number G_z of a z-slab with its normal along the magnetization axis. The θ angle can be extracted from the layer Chern number G_z of a z-slab with its normal along the AXI magnetization axis. More specifically, the θ angle manifests as an offset in G_z, according to the relation [59, 235]:

$$G_z = C_z n_z + \theta/\pi, \tag{4.24}$$

where n_z counts the layers of the slab and where C_z is the bulk Chern number of a single layer. This calculation can be approached in two steps:

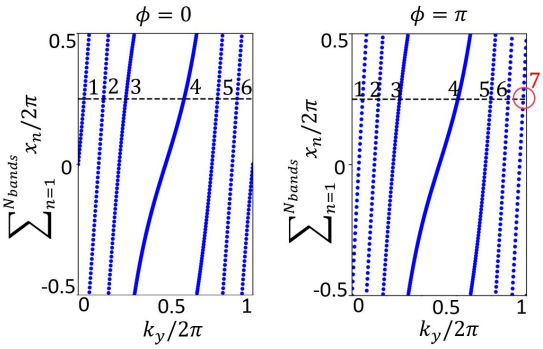

Figure 4.23: The layer Chern number for the two phases of an AXI insulator. The slab Wilson loop winds in respectively n_z and $n_z + 1$ times, with the +1 extra winding shown in the green circle. This confirms that the two phases present a difference in axion angle of $\delta\theta = \pi$.

1. Compute the *bulk* Chern number C_z for the 3D periodic structure.

2. Compute the *layer* Chern number G_z for the 2D slab confined in z of $n_z >> 1$ layers. Importantly, the slab should respect the symmetry protecting the AXI, in our case, inversion.

Step 1 can be implemented via the use of the section Chern number introduced in **Section 4.1.3.3**. Since Step 2 is can computationally intensive in MPB, we evaluate it using the effective model for the 3D PhC. We describe the construction of this model in**Appendix B**. In **Figure 4.23** we evaluate the layer Chern number for the two phases of an AXI insulator (the AXI PhC described in detail in **Section 4.2**). Both phases (panel **a** and **b**) have a bulk Chern number $C_z = 1$. An $\mathcal{I}$-symmetric slab of $n_z = 6$ layers is considered. The x-directed slab Wilson loop winds in respectively n_z and $n_z + 1$ times along k_y, with a +1 extra winding. This confirms that the two phases present a difference in axion angle of $\delta\theta = \pi$.

4.2.4 Relative AXI domain walls

In this section, our goal is to render physically manifest the *relative* axion topology demonstrated just now. To accomplish this, we create a domain wall in x between the photonic 3D insulator with $\phi = 0$ and its obstructed counterpart with $\phi = \pi$, i.e. imposing a *relative* axion phase difference of $\delta\theta \equiv \delta\phi = \pi$, as shown in **Figure 4.24(a)**. We expect this domain wall configuration to be formally equivalent to the critical point between an AXI with $\theta = \pi$ and a trivial insulator [222,238,239,239,253] and therefore gapped. To ensure a surface gap, we apply a tilt to the magnetic field

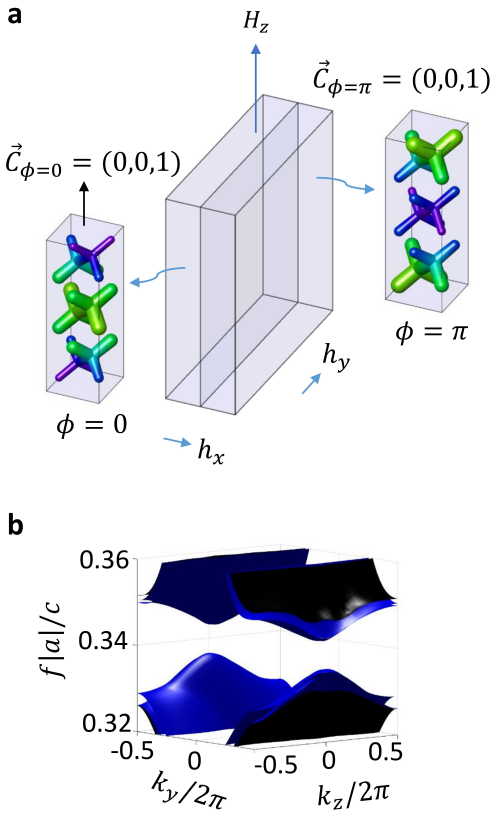

Figure 4.24: Axionic surface gap for an $\mathcal{I}$-symmetric domain wall with $\delta\theta \equiv \delta\phi = \pi$. In panel **a**, PhC geometry of the phase-obstructed domain wall configuration. In panel **b**, domain wall band structure on the $x = 0$ plane, with projected bulk bands in black, and surface-localized states in blue.

directed towards the z-axis, represented as with

$$\mathbf{H} = (|h|\cos(\sigma), |h|\sin(\sigma), H_z) \tag{4.25}$$

and $|h| \ll |H_z|$. As shown in**Appendix D**, the component of the magnetic perturbation normal to the interface plane ensures the existence of a surface gap, which is essential for the observation of the higher-order topology of the rAXI. The tilted external field couples to the PhC, inducing an in-plane gyrotropic perturbation $\eta_{x,y} = \eta_{x,y}(h_{x,y})$ in the permittivity tensor. As a result, the PhC domain wall bands are gapped, as shown in **Figure 4.24(b)**. The size of the surface gap can be controlled via the $h_{x,y}$ bias, by gradually deviating from the gapless condition which results from the boundary condition choice, as demonstrated in**Appendix D**. In what follows, we select a boundary condition in which the size of the surface gap disappears in the absence of any magnetization orthogonal to the interface plane: this boundary configuration is reached by maintaining the rod geometry continuously connected across the interface for the PhC. In the TETB, this corresponds to a surface potential that linearly interpolates between the two modulations. Importantly, the $\phi = 0$ and $\phi = \pi$ structures differ only in their $\bar{z}_4$ index but have an identical Chern vector. It is critical to maintain the condition of equal Chern vectors across the interface in order to prevent anomalous Hall surface states from populating the surface gap, consistently with vectorial bulk-boundary correspondence [42].

4.2.5 Chiral hinge states

Next, to generate and manipulate a chiral hinge channel of light, we will be investigating the higher-order topology of the PhC. For this purpose, we construct an $\mathcal{I}$-symmetric z-wire configuration. We embed a $N_x \times N_y$ core of $\phi = 0$ PhC inside a $2N_x \times 2N_y$ region of PhC showing $\phi = \pi$. The corresponding dielectric structure, which is fully connected, is shown in **Figure 4.26(a)**, with the central rod extruded upwards, for better visualization. To keep the simulations affordable, we compute the boundary modes for this rod geometry via the use of the TETB model. As shown in **Figure 4.25(c)**, chiral gapless modes emerge as in-gap states in the projected domain wall bands, consistent with the bulk–hinge correspondence of the photonic rAXI. These HOTI states are consistent with the existence of a single unidirectional mode wrapping around a central phase-obstructed core. Moreover, their group velocity can be easily switched by flipping of the external magnetic bias H_z. Displayed for a cross-

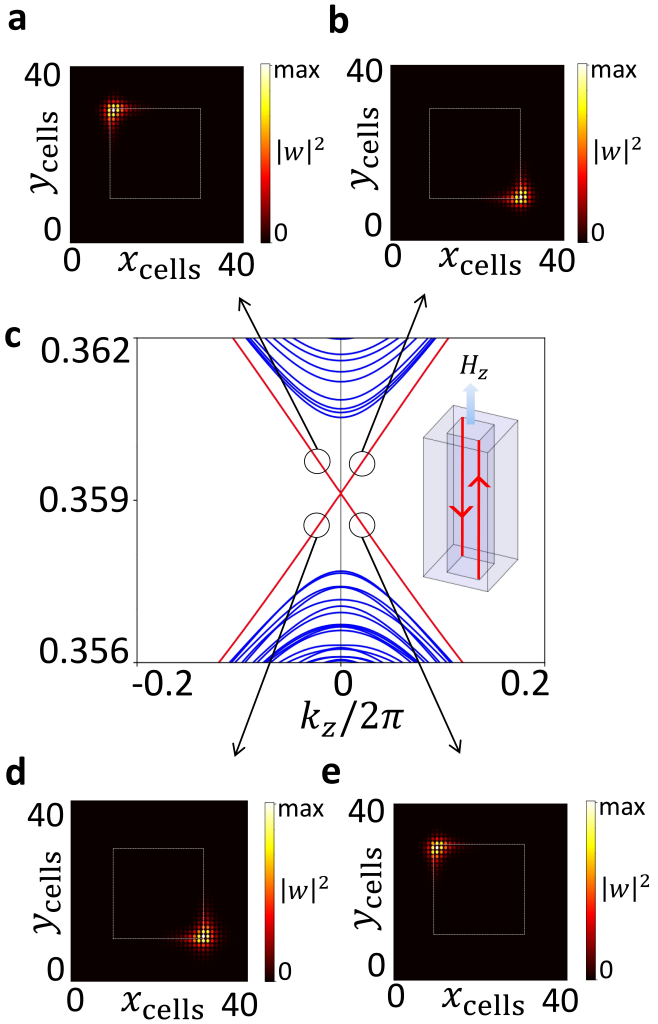

Figure 4.25: Gapless AXI hinge states evaluated a z-wire configuration, with $2N_x \times 2N_y = 40 \times 40$ cells. The crystal structure is fully connected but presents an axion phase discontinuity of $\delta\theta \equiv \delta\phi = \pi$. Projected surface bands in blue, hinge bands in red, in panel **c**. The chiral modes are localized on $\mathcal{I}$-related hinges: a xy-cross section of the z-wire geometry is shown in panels **a,b,d,e**. The flipping of the external H_z field results in an overall exchange of the group velocity signs. These HOTI states are consistent with the existence of a single unidirectional mode wrapping around a central phase-obstructed core.

section of the connected structure in **Figure 4.25(a-e)**, the 1D channels localize on $\mathcal{I}$-related hinges parallel to the z direction. It is noteworthy that not all of the four $\mathcal{I}$-related hinges support chiral modes at once. Instead, the localization on either a pair of $\mathcal{I}$-related hinges or the other can be chosen by rotation of the small $h_{x,y}$ bias in the xy plane, leading to 4 possible realizations of the hinges, α, β (with occupancy of the hinges passing through the corners on the $1\bar{1}0$ diagonal) and γ, δ (with occupancy of the hinges passing through the corners on the 110 diagonal), as shown in **Figure 4.26(b-e)**. These different hinge-state configurations are plotted in **Figure 4.26** at the Γ point for the upwards-moving state. As shown in**Appendix D**, they can be regarded as distinct boundary-obstructed phases [254, 255], since a surface gap (but not a bulk gap) must close in passing from one configuration to another. The α,β,γ,δ gyrotropic-bias-field induced transitions offer a promising and physically accessible way to manipulate the photonic 1D modes, via rotation of the PhC gyrotropic axis through magnetic control by external field. Therefore, the present platform can provide an effective photonic topological switch between different 1D photonic fiber configurations. Remarkably, the observed hinge modes are embedded within a fully connected 3D dielectric structure, making them highly suitable for guided-light communication applications, as they are protected from radiation through the electromagnetic continuum [248]. By proposing the first tunable HOTI chiral hinge states in PhCs [19], we provide a PhC realization and a distinct manifestation of the axionic hinge states predicted in supercell-modulated Weyl semimetals [222, 237–239, 253]. More specifically, the hinge modes of **Figure 4.25(b-e)** are consistent with the presence of a single, unidirectional axionic mode wrapping around a central phase-obstructed core [256].

4.2.6 Discussion and outlook

In this section, we proposed a mechanism inducing axionic band topology in a gyrotropic PhC and demonstrated the potential use for magnetically tunable photonic switch devices. This approach provides a realistic and physically accessible platform for generating and manipulating the higher-order topology of the AXI PhC, enabling effective topological switching between different configurations for axionic hinges of light. In addition to its fundamental theoretical significance, related to the possibility of coupling between photonic axionic excitations and dark-matter axions, the realization of AXI PhC has the potential to open up the field of axion-based topology, enabling more efficient and versatile control of light propagation in PhCs, and thus advancing the state-of-the-art in photonic communication and optical technologies. Our next

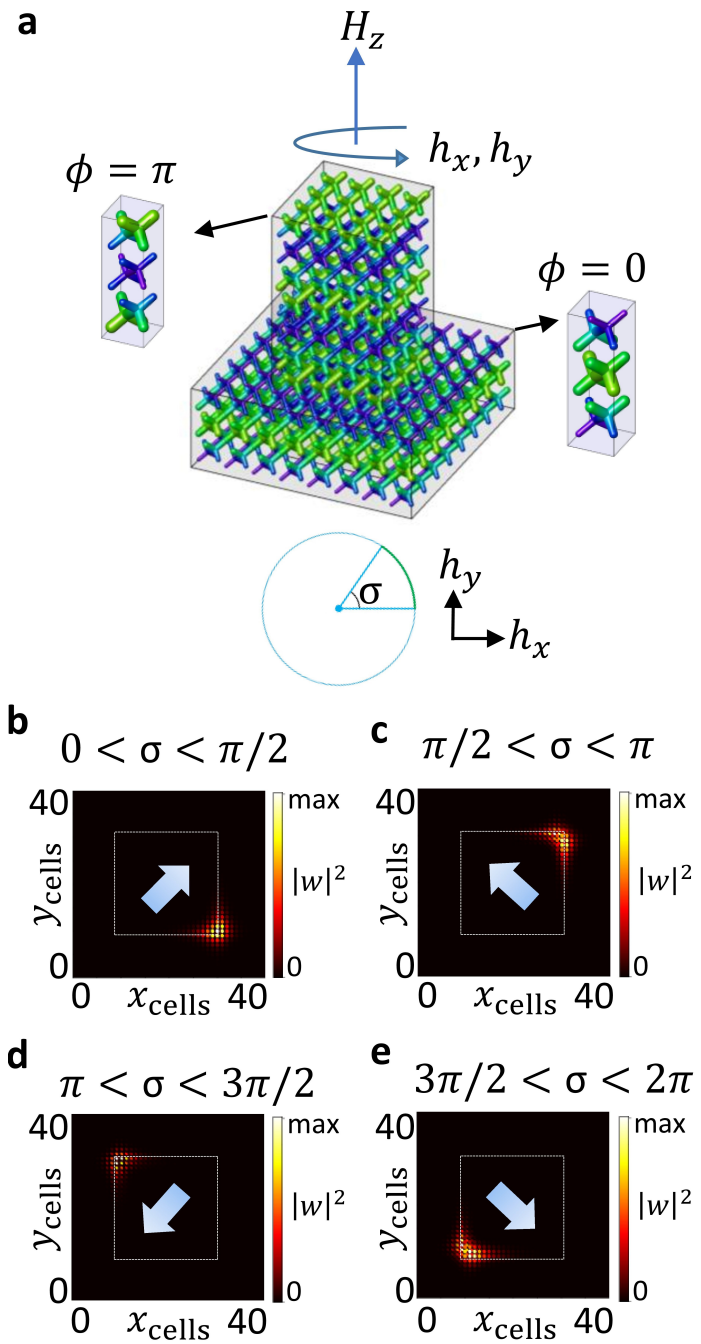

Figure 4.26: Tunable AXI hinge states at Γ, for different magnetic bias configurations, computed via the TETB. Panel **a** displays the corresponding PhC dielectric structure. For visual purposes, the central $\phi = 0$ core is extruded vertically with respect to the phase-obstructed embedding with $\phi = \pi$. Panels **b-e** correspond to $\alpha, \gamma, \beta, \delta$ configurations. A single eigenvector is plotted here, upwards moving. The activation of the 90°-rotated hinges is made possible via a $h_{x,y}$ in-plane small bias component

step would be to make the axionic response dynamic, introducing a time dependence in the PhC setup. Traditional axion haloscopes exploit conversion into massive photons inside cavity plasma or dielectric haloscopes [243, 244]. More recent topological approaches have proposed to exploit the conversion from dark-matter axions into dynamic condensed-matter axionic excitations [240, 245]. Obtaining a dynamic axion in a PhC could help bridge this different approach for dark-matter detection, and help for a better understanding of the axion-photon coupling.

4.3 Unpaired Photonic Weyl Semimetal

4.3.1 Introduction

Since the development of topological photonics, a large variety of photonic Weyl points have been demonstrated in PhCs [12, 50, 223, 257–263]. Weyl photons, with unit topological charge and linear dispersion, have been proposed in Refs. [12,50,223,257,258]. Weyl photons of higher topological charge have been observed in Refs [259, 263]. However, all these photonic Weyl points have in common that they appear as dipolar systems with zero net charge, according to the *Nielsen-Ninomiya* theorem which binds left- and right-handed Weyl points to come in pairs [264, 265]. Photonic Weyl crystals have mostly been searched because of their topologically protected FAs, which appear on surfaces that connect the projections of the Weyl points with opposite charge [259–262]. Photonic FAs, such as helicoid surface states and large surface arcs, have been for example exploited for achieving unidirectional light propagation [259], spatial frequency filtering of surface modes [262] and diffractionless propagation of light waves [260]. However, more recently, photonic Weyl points have started to attract interest in the context of coupled quantum emitters (QE), due to the possibility of engineering the QE interactions, by manipulating the Weyl environment. Quantum emitters are nano-sized or quantum-confined systems capable of emitting individual photons [266–269]. Recent studies have demonstrated that Weyl PhC environments can mediate tunable long-range coherent interactions for QEs, to be employed for realizing entanglement protocols and for quantum simulator implementations [270, 271]. However, existing setups often involve dipolar-Weyl systems, that lead to momentum-space interference effects. In these implementations, the QE interaction mediated via a specific Weyl point usually competes with the presence of at least another Weyl point partner in the BZ, both of them with finite momentum: the resulting power-law decay interaction between QEs is thus naturally affected by an interference term related to the

separation of the opposite charge Weyl points [270]. An ideal scenario could be represented by an unpaired photonic Weyl point at the center of the BZ, in a highly symmetric environment. Going back to the theoretical aspects of non-dipolar Weyl systems, in condensed matter large efforts have been dedicated to eluding the *Nielsen-Ninomiya* theorem and obtaining isolated Weyl points either via artificial dimensions (on the 3+1D boundary of a 4+1D bulk [272, 273]), via dynamical driving or non-Hermitian systems [274–277] as well as in presence of long-range non-local interactions [278]. However, very recently it has been demonstrated that the *Nielsen-Ninomiya* can be simply circumvented by stabilizing an absorbing Weyl Nodal Wall (WNW) on the BZ boundary, via non-symmorphic symmetries [279–282], a situation that could be potentially realized in conventional all-dielectric 3D PhCs of the silicon-type. Specific symmetry conditions for achieving this, either in spinless or spinful systems have been explicitly derived in Refs. [280, 282]. Motivated by the above considerations, in this section we show how to obtain an unpaired photon Weyl point (UPhW) in a realistic PhC. This configuration requires simultaneously the presence of a point-group symmetry to fix the Weyl point at the Gamma point (Γ) and a way to circumvent the no-go theorem, stabilizing an absorbing nodal Weyl wall (WNW) on the BZ boundary. First, we create a stable photonic nodal wall, acting as a topological sink absorbing the Berry flux. Since we are dealing with a bosonic system, a combination of even time-reversal symmetry ($\mathcal{T}^2 = 1$) with a two-fold screw-rotation, can ensure Kramers degeneracy on the plane orthogonal to the screw axis [282]. In order to have a closed nodal wall spreading on the entire BZ boundary, we proceed by looking for candidate PhCs in SGs containing twofold screw-rotation symmetries for all three cartesian directions. Moreover, in order to have the Weyl point at Γ, we consider non-symmorphic chiral structures with additional crystal symmetries able to pin the Weyl point at the BZ center, for example in point group D_4 and O [283–285]. Finally, in order to prevent the presence of nodal lines, we ensure to deal with chiral structures.

4.3.2 Design strategy: triply periodic structures

Guided by these reasonings, we model dielectric PhCs from symmetry-constrained triply periodic surfaces (TPS) [229, 286–296] and characterize their properties. A TPS represents an isolevel surface, $Ref(\mathbf{r}) = f_0$ ($f_0 \in \mathbb{R}$), obtained from Fourier expansion of the lattice:

$$f(\mathbf{r}) = \sum_{\mathbf{G}} c_{\mathbf{G}} e^{i\mathbf{G}\cdot\mathbf{r}}, \tag{4.26}$$

where $\mathbf{G}$ are the reciprocal lattice vectors. By definition, a TPS is 3D periodic $f(\mathbf{r}) = f(\mathbf{r}+\mathbf{R})$ in the direct basis $\mathbf{R}$. A PhC can be defined from a TPS via its permittivity profile:

$$\varepsilon(\mathbf{r}) = \begin{cases} \varepsilon_{die} & \text{for} \quad Ref(\mathbf{r}) < f_0 \\ \varepsilon_{air} & \text{for} \quad Ref(\mathbf{r}) > f_0 \end{cases} , \tag{4.27}$$

i.e. filling the spatial regions defined by the TPS by either a simple dielectric ($\varepsilon_{die} = 12$) or by air ($\varepsilon_{air} = 1$). TPS-based structures can be found in a large variety of natural templates such as butterfly wings and soap films, giving rise to their structural colors [287–290]. Recently, micro- and nano-manufacturing techniques have been developed to synthesize TPS-based PhCs and metamaterials, over a broad range of length scales [229, 291, 293, 294], such as templating and coating techniques [295], as well as via sol-gel assembly [296]. In order for the TPS-based PhC to satisfy the desired symmetry properties for obtaining a UPhW, we constrain the spatial profile of the TPS by imposing $gf(\mathbf{r}) = f(g^{-1}\mathbf{r}) = f(\mathbf{r})$, for each operation $g = \{\mathbf{R}|\mathbf{t}\}$ in the SG of interest. This condition enforces constraints on the coefficients $c_{\mathbf{G}}$, specifically:

$$c_{\mathbf{G}} e^{i\mathbf{G}\cdot\mathbf{t}} = c_{g\mathbf{G}}, \tag{4.28}$$

that can be solved as a set of coupled equations via the method suggested by *Thomas Christensen* in Ref. [23]. Note that, the use of non-gyrotropic and non-magnetoelectric materials, of the silicon-type:

$$\varepsilon_{TRS} = \begin{pmatrix} \varepsilon(\mathbf{r}) & 0 & 0 \\ 0 & \varepsilon(\mathbf{r}) & 0 \\ 0 & 0 & \varepsilon(\mathbf{r}) \end{pmatrix} \tag{4.29}$$

with $\varepsilon \in \mathbb{R}$ guarantees us to have $\mathcal{T}^2 = 1$, in virtue of the bosonic nature of the system. We study two different types of chiral photonic lattices, both modeled via of simple isotropic dielectric: a tetragonal crystal in SG 92 and a cubic crystal in SG 213. Both SGs present twofold screw-rotation symmetries for all *three* cartesian directions, therefore being compatible with the formation of a closed nodal wall on the BZ boundary.

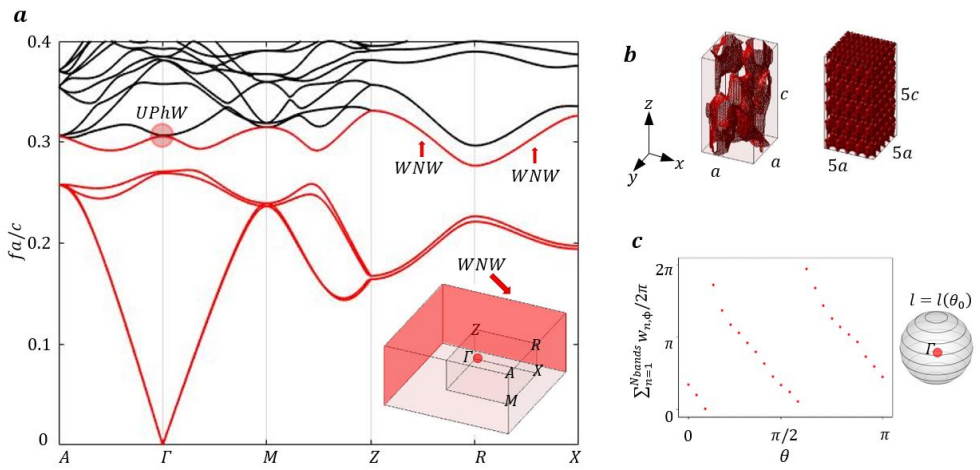

Figure 4.27: Unpaired photonic Weyl point with topological charge -2 between photonic bands $5, 6$ located at Γ, in a chiral tetragonal PhC (SG 92). **a**: Photonic bandstructure. The lines ZR and RX lie on the BZ boundary and are fully degenerate, hosting a Weyl nodal wall. The nodal wall is visualized via the darker faces of the BZ cube. **b**: The tetragonal unit cell with the isolevel of TPS. In the numerical simulations, these are filled by a simple dielectric. **c**: Photonic Wilson loop is computed on parallel circles of a small sphere surrounding the unpaired Weyl point.

4.3.3 Nodal wall and unpaired photonic Weyl

We obtain a UPhW with a charge of 4 in the cubic photonic lattice and with a charge of 2 in the tetragonal one. In both cases, the UPhW is located at Γ. We characterize the type of dispersion of the photonic spectra, along different BZ directions and show a practical way to switch the chirality of the Weyl point. Finally, we verify the presence of an absorbing nodal wall at the BZ boundary. We compute the dispersion of the PhCs via MPB [168]. To check for the presence of a UPhW at Γ we analyze the high-symmetry lines, checking for the bands to be gapped only on the lines connected to Γ and two-fold degenerate on the BZ boundary. To extract the spatial profile of the nodal wall, we numerically evaluate the zeroes of the frequency difference between the degenerate bands on a dense k-mesh of 60^3 grid points. The crystal unit cell, the photonic spectra, and the Wilson loops are displayed in **Figures 4.27** and **4.28**. As shown, the bands are two-fold degenerate at Γ, become fully gapped along each high symmetry line originating from Γ, and then become gapless again on the BZ boundary. For both the chiral structures, we verify that the sign of the UPhW charge can be changed by switching the chirality of the TPS, $f(\mathbf{r}) \rightarrow f(-\mathbf{r})$. In the chiral cubic lattice (**Figure** 2) we find a UPhW with maximal chiral charge (-4) between photonic bands $3, 4$, located at Γ. In the tetragonal lattice (**Figure** 1) we observe a UPhW with topological charge -2 between photonic bands $5, 6$, located at Γ. As we will detail in the next section, to obtain the topological charge of the UPhW, we employ

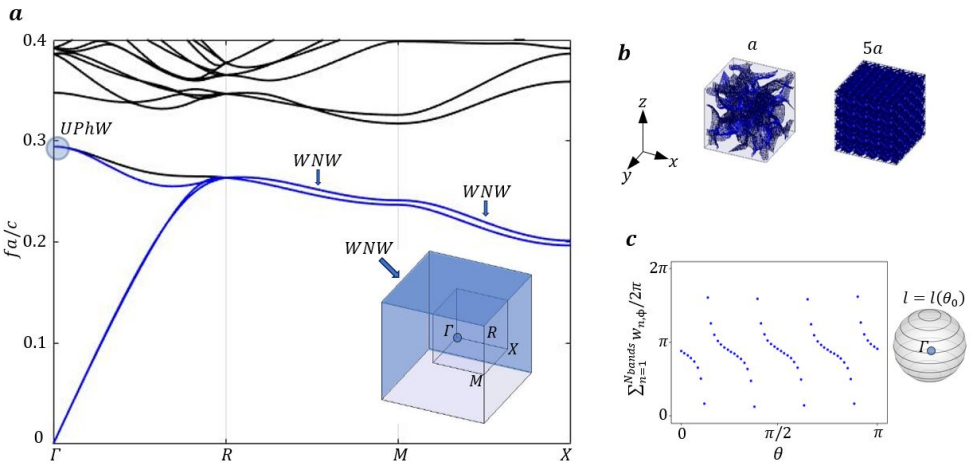

Figure 4.28: UPhW with topological charge -4, in a chiral cubic PhC (SG 213). Photonic band structure, showing a crossing between bands 3, 4 located at Γ. These transverse bands are directly connected with the $\omega = 0$ modes. **a**: Photonic bandstructure. The lines RM and MX lie on the BZ boundary and are fully degenerate, hosting a Weyl nodal wall. The nodal wall is visualized via the darker faces of the BZ cube. **b**: The cubic unit cell with the isolevel of TPS. In the numerical simulations, these are filled by a simple dielectric. **c**: Photonic Wilson loop is computed on parallel circles of a small sphere surrounding the unpaired Weyl point.

the photonic Wilson loop method, implemented for 3D electromagnetic fields [1, 50]: specifically, since we are dealing with a system that is nowhere gapped, we evaluate Wilson loops on the surface of a small sphere surrounding the UPhW, according to the methods developed in **Section 3.2**

4.3.4 Topological characterization

In this section, we show how to evaluate the topological charge of the UPhW (q_{UPhW}) for the system shown in **Figure 4.28**. The UPhW in **Figure 4.28** occurs between a pair of bands (3rd and 4th band) of which the lower one is directly connected to the transversal modes connected to zero energy. The system is complicated by the fact that the entire boundary of the BZ (the surface of the BZ cube) constitutes a topological WNW, absorbing the topological charge of the Weyl point ($q_{WNW} = -q_{UPhW}$). This means that the system is nowhere gapped on any planar cross-section taken in the BZ. Therefore, the section Chern number method cannot be applied. In order to determine q_{UPhW}, we evaluate the WL on the surface of a small sphere surrounding the UPhW at Γ, excluding the $\mathbf{k} = 0$ eigenstates, as in **Figure 3.3**. We consider a small sphere with radius $|k_r|$ surrounding the Γ point, and we compute the WL along the "lines of latitude" of the sphere, on the circles parallel to the equator. These circles are

parametrized by the azimuthal angle $\varphi \in [0, 2\pi)$ for a fixed polar angle θ_0:

$$k_x = |k_r| \sin(\theta_0) \cos(\varphi)$$
$$k_y = |k_r| \sin(\theta_0) \sin(\varphi)$$
$$k_z = |k_r| \cos(\theta_0).$$

Since the lines of latitudes are closed, they provide valid paths on which to evaluate the WL:

$$\mathcal{W}_l = \mathcal{W}_l(\theta_0). \tag{4.30}$$

The UPhW's charge can be determined by tracking the evolution of the eigenvalues of $\mathcal{W}_l$ with respect to θ_0. Since the lines of latitudes cover the entire sphere as the θ_0 angle varies in $[0, \pi)$, the result is a closed 2D manifold, for which a Chern number can be defined. In the example of **Figure 4.28**, the WLs winds -4 times, confirming that the topological charge of the UPhW located at Γ is $q_{UPhW} = -4$. Since there are no other gap closings in the BZ beyond the UPhW and the WNW, the nodal wall charge is $q_{NW} = +4$. The value of the topological charge is independent of the radius $|k_r|$, as long as the sphere includes only the node of interest. Note that in the calculation we considered all 3 three low-energy transverse bands connected at $\omega = 0$ are considered, but none of the eigenstates with $\mathbf{k} = 0$ has been included.

4.3.5 Discussion and outlook

In this section, we unveil a new type of maximally-charged UPhW in a PhC modeled from all-dielectric TPS. Interestingly, these Weyl photons seem to elude a no-go theorem in topology, acting as an isolated source of Berry curvature but lacking an opposite topological charge partner. We show that the UPhWs are stabilized by the combination of the point group symmetries of the PhC together with the spinless TRS of the all-dielectric material. The proposed UPhWs have either maximal (-4) or high (-2) topological charge and appear at the center of the 3D Brillouin zone, surrounded by an absorbing closed nodal wall. In virtue of the UPhW isolation in the BZ and their topological properties, the present design can be used as a starting platform for coupling QEs. The cubic symmetry of the nodal configuration and the centrality of the Weyl point in the BZ make the PhC environment highly symmetric. While this work is still under development, we plan to leverage this symmetry property, combined with the PhC's topology, to benefit the manipulation of quantum emitters interactions,

minimizing limitations present in conventional Weyl-dipolar systems [270, 271]. As a next step, we intend to investigate the bulk-boundary correspondence within these structures. A notable observation emerged during our initial analysis: the presence of nodal walls effectively negates any gapped BZ slice, essential for the topological argument of surface Fermi surfaces. Because of this, the PhC with UPhWs challenges the *Nielsen-Ninomiya* theorem, presenting a unique topological anomaly: this suggests an intriguing scenario where topological FA surface states might be absent [279], even in the presence of a Weyl point. The construction of a TETB model of the PhCs using methods from **Chapter 3** could help delve deeper into this aspect.

Chapter 5

Conclusions

Chapter Outline

This thesis provides a comprehensive study of topological phenomena in PhCs, focusing on the three-dimensional context. The primary aim of this research is to deepen the theoretical understanding of 3D topological phases of light within PhCs. To this end, we have formulated detailed designs of these 3D topological phases, underscoring their potential applications and theoretical significance. Addressing the unique challenges posed by light's vectorial nature required the development of specialized characterization techniques and methodologies. In the subsequent sections, we will delineate the primary contributions of this thesis. These contributions encompass the development of innovative tools for modeling and characterizing 3D PhCs, the proposal of novel topological phases, and the exploration of open questions that pave the way for future investigations in the field.

5.1 Modeling and Characterization of 3D PhCs

After an initial introduction **Chapter1** and covering the fundamental theoretical framework of the thesis **Chapter2**, in **Chapter3** we developed dimension-specific characterization techniques suited for approaching topology in 3D PhCs: the vectorial electromagnetic Wilson loops and the transversality-enforced tight-binding models. Through these methodologies, we were able to circumvent the theoretical intricacies associated with light's transversal and vectorial nature, enabling us to model and characterize the topological properties of 3D PhC. We presented the electromagnetic Wilson loop as a robust tool for computing a number of 3D topological invariants, focusing on the ad-

justments needed for these methods, particularly in the face of vectorial waves and the Γ-point challenge. We supplemented this with a hands-on tutorial for practical computations, emphasizing its versatility and broad applicability in different 3D topological phases. Using hybrid Wannier energy centers, we showed how to compute the magnetoelectric angle of a photonic axion insulator, the topological charge of a nodal-wall semimetal, and the Chern vector of a PhC insulator. These methods can be readily adapted for other applications. For instance, they can be used to assess the braiding of multigap photonic 3D nodal links [189], given its potential as a robust platform for topological quantum computation. Additionally, they can be employed to evaluate fragile topology within the fundamental photonic bandgap, a phase in 3D PhCs that remains elusive and conceptually challenging [190]. Furthermore, we unveiled a method for constructing reliable tight-binding representations of 3D PhCs, even when faced with an irregular symmetry content at zero frequency and the non-existence of maximally localized Wannier functions for such systems. This method, named as the TETB, not only captures and regularizes electromagnetic obstructions but also reproduces the symmetry, topology, and energetic dispersion of transverse bands in the PhC all across the BZ. By introducing a magnetic version of our model, we showcased its potential in modeling gyrotropy, emphasizing the method's computational efficiency compared to exact solvers. Recent applications of this method, such as simulating the higher-order response of photonic axion insulators' hinges, underline its significance and potential in the field of topological photonics. This method can facilitate the study of boundary responses of future photonic topological phases, particularly in the case of 3D PhCs. Beyond its computational efficiency, the ability to have a simplified mathematical expression for a PhC's effective model can enhance analytical insights into understanding the PhC environment, such as in studying the dynamics between coupled quantum emitters and PhCs.

5.2 Design and Applications of 3D Topological PhCs

In **Chapter 4**, we proposed the design of three distinct PhCS displaying different novel topological phases: the 3D Chern photonic insulator, the photonic axion insulator, and the nodal-wall Weyl semimetal. The modeling and topological characterization were made possible via the tools developed in the previous **Chapter 3**, allowing to circumvent the challenges arising from vectorial and transversal properties of light in 3D. In our exploration of the 3D Chern photonic insulator, we have unveiled a method to tai-

lor the Chern vector, via cubic and multi-fold supercell modulations and inducing the annihilation of Weyl points. Key features of this phase encompass high Chern numbers, the capability for reduced magnetic constraints, and the potential for orientable Chern vectors. As a significant hallmark of this phase, we observed the emergence of anomalous surface states. Characterized by their non-reciprocal properties, these states are further distinguished by the formation of distinct equifrequency loop structures, which arise from a topological transition from the Weyl semimetal phase to the 3D Chern insulating phase. The same design revealed the ability to achieve large Chern numbers, leading to multi-modal propagation of topological surface states. This innovation has the potential to extend its applications to the realm of topological surface lasers. Our method, is adaptable to reducing the TRS breaking parameters by leveraging larger supercells, emphasizing its adaptability to weakly-magnetic media. These findings also underscore the exploration of vectorial aspects of bulk-boundary correspondence in 3D CIs, a substantial shift from the traditional scalar analogy prevalent in 2D systems. The orientation of Chern vectors has been shown to play a pivotal role in the accurate prediction and understanding of photonic surface modes. Looking ahead, our work offers some unexplored theoretical aspects. While our study predominantly focuses on the surface response, other boundary configurations could be explored. An especially intriguing avenue is the prospect of a 3D CI arranged around a trivial core with inward-pointing Chern vectors, a magnetoelectric configuration proposed in the electronic context, and which awaits an equivalent in photonics. As a second design, we proposed a way to induce axionic band topology in a gyrotropic PhC, emphasizing its transformative potential as a magnetically tunable photonic switch device. We showed that the crystal gyrotropy offers a tangible and efficient strategy for generating and controlling the higher-order topology of the AXI PhC, allowing for topological switching among different axionic hinge configurations. Beyond its core theoretical implications, especially concerning the potential coupling of photonic axionic excitations with dark-matter axions, the axion PhC lays the ground for the development of the field of axion-based photonics and broader applications in controlled light manipulation. Our next objective is to incorporate a dynamic time dependence into the axionic response of PhC design, to explore the possibilities discussed in relation to the dark-photon conversion. Whereas classical axion haloscopes utilize conversion into massive photons within specific media, more recent topological methods suggest conversion from dark-matter axions to dynamic axions in condensed-matter systems. Implementing such a dynamic axion in a PhC might bridge these approaches, enrich-

ing our understanding of axion-photon coupling. As a last design, in the design of the nodal-wall PhC, we identified a novel type of Weyl point within an all-dielectric photonic crystal. These Weyl points, with high-topological charge, apparently challenge conventional fermion-doubling theories by existing as isolated Berry curvature sources without an inverse topological charge counterpart. Positioned centrally in the 3D Brillouin zone, these nodes are encapsulated by a BZ boundary acting as a closed nodal wall, which absorbs their topological charge. As we discussed, the topology and momentum-space symmetry of this PhC configuration offer promising avenues for the manipulation of quantum emitter interactions, in particular, to overcome the limitations of conventional dipolar-Weyl PhC environments. Via the formation of Weyl-bound states, these systems may represent a valuable starting point for future research in photonic quantum implementations of long-range interactions via quantum emitters in a PhC environment.

5.3 3D Phases of Light Beyond This Thesis

The 3D PhC phases examined in this thesis primarily derive their topology from the breaking of TRS and the inclusion of crystalline symmetries. Another area worth exploring is the role of duality symmetry in the topological protection of 3D PhCs. Achieving electromagnetic duality in materials that macroscopically violate it (with $\varepsilon > 1$ and $\mu = 1$) has typically been approached by leveraging the local response of small dielectric objects and their induced electric and magnetic dipoles within specific frequency ranges of interest [38, 297]. In the context of topological PhCs, certain studies suggest the feasibility of inducing Dirac-like band crossings in 3D PhCs by enforcing duality through fine-tuned dielectric meta-atom geometries, artificially instantiated at discrete points in the BZ [38]. A pivotal question arises: can one induce emergent electromagnetic duality throughout entire the BZ for a specific band in a PhC with an inherently dual-broken symmetry? One potential approach could be to use inverse design, seeking for TM/TE degeneracy on a flat band, in 2D PhCs that exhibit macroscopic dual-broken symmetry. This approach is inspired by observations that, in our simulations, there exists a correlation between macroscopic duality and band flatness. We propose this line of inquiry as a promising direction for subsequent research. Furthermore, all the proposed phases here displayed topological features in the first fundamental gap, thereby requiring the use of modeling and characterization methods suited to transversal waves. To circumvent the singularities arising from the transver-

sality constraint of Maxwell equations in periodic dielectric media, we employed the use of auxiliary longitudinal modes able to regularize this obstruction. An open question remains concerning the possibility of being able to symmetry-identify other types of topologies in the first fundamental gap. A possible alternative approach could be realized by defining Real Space Invariants (RSIs) [298, 299] in the electromagnetic context. These, with an enforced transversality constraint, may offer an approach to identify, for example, obstructed atomic limits or fragile topology, below the first fundamental gap. RSIs assess whether two configurations of occupied orbitals can be smoothly deformed while preserving system symmetries, aiding in distinguishing certain topological obstructed phases. Even though fragile bands exhibit integer-valued RSIs, akin to topologically trivial bands, they can be diagnosed through inequalities or modular equations involving RSIs [298, 300]. A related question concerns the interplay between fragile topology and the Γ singularity. Can the topological vortex at the Γ point be modified by realizing non-trivial fragile topology below the fundamental gap [301, 302]? Or again, is it possible to induce a transition from trivial to fragile topology that creates a gap between the auxiliary longitudinal and transverse bands? We raise these questions as a starting stimulus for future investigation.

Finally, another interesting avenue involves the quest for achieving flatbands in 3D PhC. The advantages of slow light, which offers capabilities like high spatial energy enhancement, have been demonstrated in 2D setups [303–305], yet their realization in 3D remains a challenge. Our numerical observations suggest that the challenge in achieving 3D flatbands might stem from the interplay between even and odd polarizations: as even modes flatten, the dispersion of odd modes tends to increase. Photonic flat bands are fundamentally very different from electronic ones. Unlike electronic systems where distant atomic sites lead to trivial flatbands, as exemplified by the spaghetti bands in certain layered systems, photons in the limit of far-separated dielectric objects disperse linearly within the light cone: photonic flatbands necessary require lattice wavefunction interference. In the electronic context, 2D flatbands resulting from wavefunction interference often exhibit topological (e.g. fragile) characteristics, as seen in systems like twisted bilayer graphene or Kagome/Lieb lattices [306, 307]. Topologically derived flatbands in 3D PhCs could present transformative opportunities for slow light applications.

In summary, this thesis examines topological phenomena in PhCs, providing insights and methodologies tailored for 3D. Through the development of characterization techniques, we have addressed the challenges presented by light's vectorial and

transversal nature. We proposed realistic designs to implement 3D topological phases of light in PhCs, establishing a clear connection between theoretical formulations and potential applications. This work wants to address some open questions and areas yet to be explored. The pursuit of 3D flatbands, the interplay of fragile topologies with the Γ singularity, and the implications of electromagnetic duality for 3D topological protection are notable areas for further investigation. We hope this thesis can provide a deeper understanding of 3D electromagnetism and offer the tools leading to further advancements in the exploration of 3D topological phases in PhCs.

Appendix A

Method of Invariants for coupled Weyl points

In this appendix, we establish two symmetry-adapted models to study the topological Weyl-Chern transition detailed in **Section 4.1.2**. We begin by modeling the formation of Weyl points, which originate from the splitting of the threefold degeneracy at **R** upon the application of an external magnetic field, **H**. This model enables us to identify the only possible perturbations that can couple the Weyl points, leading to the opening of a topological gap. The analytical models are based on the standard group theoretical *method of invariants* [308], here adapted for electromagnetic waves in 3D. This method allows us to find an expansion in powers of the wave vector **k** of the photonic energy bands ω, able to replicate the photonic modes dispersion in the vicinity of a point in momentum space. Here, we proceed by constructing an effective energy dispersion operator $H(\mathbf{k})$, expressed in terms of the space group irreducible representations, able to capture symmetry properties of the photonic modes. In the photonic context, $H(\mathbf{k})$ can be viewed as a perturbative expansion of the Maxwell-Bloch operator acting on the electromagnetic fields in the first-order formulation of Maxwell's equations [104]. For related applications of the $\mathbf{k}\cdot\mathbf{p}$ approach to 2D photonic systems, see e.g. Refs. [9, 309]. In what follows, we adopt the notation convention taken in the BCS [310], unless otherwise stated, and express reciprocal lattice vectors in reduced units $2\pi/|a| = 1$.

A.1 Weyl Dipole Formation

We start by modeling the Weyl points formation from the splitting of the threefold degeneracy at $\mathbf{R} = (1/2, 1/2, 1/2)$ (see **Figure A.1(a)**). From the analysis of the transfor-

mations of the electromagnetic field under spatial symmetries, obtained via numerical computations, we know that this degeneracy is related to the three-dimensional small representation R_4^- of the little group of **R**, given the transformation properties of these modes under the elements of the space group $Pn\bar{3}m$ (No.224). Following the method of invariants, we first note that the product $R_4^{-*} \times R_4^-$ can be decomposed into small irreducible representations (irreps) at Γ as:

$$R_4^{-*} \times R_4^- = \Gamma_1^+ + \Gamma_3^+ + \Gamma_4^+ + \Gamma_5^+ \tag{A.1}$$

using the character orthogonality relations. A general eigenstate in this three-band space can be expanded in the basis $\{|\phi_i\rangle\}$ of the R_4^- representation as:

$$|\psi_{\mathbf{k}}\rangle = c_i(\mathbf{k})|\phi_{\mathbf{k}}^i\rangle, \tag{A.2}$$

adopting the Einstein summation convention. The energy expectation value is a scalar invariant, which is computed as:

$$\langle H\rangle = \langle\psi_{\mathbf{k}}|H|\psi_{\mathbf{k}}\rangle = c_i^*(\mathbf{k})c_j(\mathbf{k})H(\mathbf{k})_{ij}. \tag{A.3}$$

We seek a combination of bilinears $c_i^* c_j$ transforming as the irreps above and take the Hermitian scalar product with functions of the crystal momentum (**k**) and the external field (**H**) with the same symmetry properties. From each term with $c_i^* c_j$ in this scalar product, it is easy to obtain the matrix elements of $H(\mathbf{k}, \mathbf{H})$. The energy scalar is written in this scalar product form:

$$\langle H\rangle = \sum_{\alpha,i} C_i^\alpha (q_i^\alpha)^* \cdot p_i^\alpha \tag{A.4}$$

where the sum runs over the irreps in the decomposition and $\{q_i\}$ and $\{p_i\}$ are the symmetry-adapted bases of the state coefficients and **k** and **H**, respectively. The coupling constants C_i^α are parameters of the model. To find the bases of bilinears in the wave coefficients transforming as the irreps above, we use the representation $\rho_{R_4^-}$ of the generators (omitting inversion for brevity, as it is represented by the negative identity

matrix):

$$\rho_{R_4^-}(2_{001}) = \begin{pmatrix} -1 & 0 & 0 \\ 0 & -1 & 0 \\ 0 & 0 & 1 \end{pmatrix}, \rho_{R_4^-}(3^+_{111}) = \begin{pmatrix} 0 & 1 & 0 \\ 0 & 0 & 1 \\ 1 & 0 & 0 \end{pmatrix}, \\ \rho_{R_4^-}(2_{110}) = \begin{pmatrix} 0 & 1 & 0 \\ 1 & 0 & 0 \\ 0 & 0 & -1 \end{pmatrix}, \tag{A.5}$$

where, for convenience, we have labeled the matrices by the rotation part of the symmetry element only. Note that these differ from the BCS data by a permutation of the basis, chosen to rearrange H in a more convenient form. Since it is a non-symmorphic space group, some operations have fractional translations. In Seitz notation, these are:

$$\{2_{001}|\frac{1}{2},\frac{1}{2},0\}, \{2_{110}|\frac{1}{2},\frac{1}{2},0\}. \tag{A.6}$$

We then find functions of $\mathbf{k}$ and $\mathbf{H}$ with the same transformation properties, up to the second order in the wave vector. In principle, the magnetic field could be strong. Therefore, the criterion to choose the maximum power of $\mathbf{H}$ that is included for each order in $\mathbf{k}$ is to exhaust all the possibilities in the irrep decomposition. This way, we ensure that all the couplings allowed by symmetry are included for a given order in the wave vector. Finally, we require $H(\mathbf{k},\mathbf{H})$ to be Hermitian. Following this procedure, we find that the most general expression for the energy operator is:

$$H = (a_0 k^2 + \alpha_0 H^2)\mathbb{1}_3 + i\delta_0 \varepsilon_{jkl} H_l + b_0 \begin{pmatrix} k_x^2 & 0 & 0 \\ 0 & k_y^2 & 0 \\ 0 & 0 & k_z^2 \end{pmatrix} + \\ \beta_0 \begin{pmatrix} H_x^2 & 0 & 0 \\ 0 & H_y^2 & 0 \\ 0 & 0 & H_z^2 \end{pmatrix} + c_0 \begin{pmatrix} 0 & k_x k_y & k_x k_z \\ k_x k_y & 0 & k_y k_z \\ k_x k_z & k_y k_z & 0 \end{pmatrix} + \\ \gamma_0 \begin{pmatrix} 0 & H_x H_y & H_x H_z \\ H_x H_y & 0 & H_y H_z \\ H_x H_z & H_y H_z & 0 \end{pmatrix}, \tag{A.7}$$

where $\mathbf{k} = (k_x, k_y, k_z)$ is the wave vector measured from the point $\mathbf{R}$ and we employ real coefficients (Latin when referring to $\mathbf{k}$ and Greek to $\mathbf{H}$). One can check that the

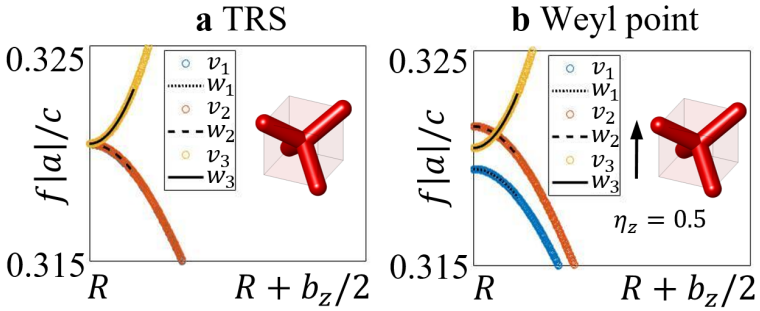

Figure A.1: Extracting the coefficients of the analytical $k \cdot p$ model in the vicinity of **R**. Here, we are considering an extrapolation of the model at a distance of $\delta k = 0.008$ from **R**. The empty circles are for numerically computed bands $v_{1,2,3}$ while the lines for the analytical dispersion $w_{1,2,3}$. **a** In presence of TRS, we conclude that $b_0 = -2.9a_0 > 0$. **b** In a weak field $\eta = 0.5$, we obtain that $\alpha_0 \sim -\beta_0$ since the third band does not move in energy and $\alpha_0 \sim 0$ since the vertical displacement of the two lowest degenerate modes is equal and opposite. Weyl points appear at positions: $k_z^{\pm} = \pm\sqrt{\frac{|\delta_0 H_z|}{b_0}}$, which here is at $k_z^{\pm} = \pm 0.004$. The $\delta_0 H_z > 0$ and $\delta_0 H_z < 0$ cases are equivalent upon reversing the two lowest photonic modes.

energy operator is invariant under the little-group symmetries as it verifies, for every operation $g = \{R|\mathbf{t}\}$:

$$\rho_{R_4^-}(g) H \rho_{R_4^-}(g)^{-1} = H(R\mathbf{k}, R\mathbf{H}). \tag{A.8}$$

We also have imposed that the model be invariant when *both* the system and the external magnetic field **H** are transformed by time reversal Θ. We can express the TR operation as $\Theta = U\kappa$, where U is a unitary matrix and κ is the complex conjugation operator. Then, the TRS condition reads:

$$\Theta H(\mathbf{k}, \mathbf{H})\Theta^{-1} = U H^*(\mathbf{k}, \mathbf{H}) U^{-1} = H(-\mathbf{k}, -\mathbf{H}) \tag{A.9}$$

where the unitary 3×3 matrix part has the simple form $U = \mathbb{1}_3$. Evaluating the model at the point **R**, in the presence of TRS, allows us to fix some of the coefficients by comparing with the numerical simulations, as described in **Figure A.1**. This yields $b_0 \sim 2.9a_0$. When a magnetic field is applied along one of the coordinate axes $\mathbf{H} = H_i \hat{\mathbf{x}}_i$, the energy dispersion of the three photonic modes along the line parallel to the field is:

$$\begin{cases} \omega_1 = (a_0 + b_0)k_i^2 + (\alpha_0 + \beta_0)H_i^2 \\ \omega_2 = a_0 k_i^2 + \alpha_0 H_i^2 - \delta_0 H_i \\ \omega_3 = a_0 k_i^2 + \alpha_0 H_i^2 + \delta_0 H_i \end{cases} . \tag{A.10}$$

This further fixes $\alpha_0 \sim -\beta_0 \sim 0$ and shows that the magnetic field fully lifts the threefold degeneracy. We see in **Figure A.1(b)** that the band curved upwards in energy will cross with one of the remaining two, giving rise to a Weyl point. The strength of the magnetic field tunes where this crossing happens along this line, according to the expression:

$$k_i^{\pm} = \pm\sqrt{\frac{|\delta_0 H_i|}{b_0}}. \tag{A.11}$$

The same happens in the opposite direction along the same line, hence the $\pm$ sign. This shows that a Weyl dipole appears along the line parametrized by k_i and that the position of the nodes can be tuned by the magnetic field strength H_i.

A.2 Coupling of Weyl points

Here we want to identify the possible perturbations able to couple and gap the Weyl nodes. Because the validity of the previous analysis is limited to the neighborhood of the point **R**, we construct another model that expands directly around the Weyl points. In particular, we can fix the magnetic field to $\mathbf{H} = H_z\hat{\boldsymbol{z}}$ and tune the strength H_z to create a pair of Weyl points at along the $\mathbf{T} = (1/2, 1/2, u)$ line, for example at $\mathbf{K}_{1,2} = (1/2, 1/2, \pm 1/4)$. As we will show, the Weyl nodes can then be coupled by a supercell modulation that doubles the real-space unit cell in the $\hat{\boldsymbol{z}}$ direction. This corresponds to the uniaxial $N_W = N = 2$ case in **Section 4.1**, i.e. a $(1, 1, 2)$ supercell. A generalization to cubic (N, N, N) supercells is straightforward since each Cartesian component of the modulation can be turned on independently. The compatibility relations from **R** into the **T** line yield:

$$R_4^-(3) \to T_1(1) + T_5(2), \tag{A.12}$$

where the dimensions of the small irreps are in parentheses. The magnetic field splits the states of T_5 and one of them degenerate with the T_1 state at $\mathbf{K}_{1,2}$. Now, we will set up a model that describes these six photonic modes and their coupling by an external perturbation. Therefore, we may divide the 6×6 energy operator matrix into 3×3 blocks. The diagonal blocks are identified with the Weyl points and the off-diagonal ones with any perturbation that couples the states at both nodes, possibly looking for those that gap them. To do so, we build the representation that acts on the six photonic states, from the space group representation induced from the direct sum $T_1 + T_5$. We

	$\mathbf{\Gamma}$	$\mathbf{X}_3$
$D_1^* \times D_1$	$\Gamma_1^+ + \Gamma_3^+ + \Gamma_4^-$	X_1
$D_1^* \times D_5$	$\Gamma_4^+ + \Gamma_4^- + \Gamma_5^+ + \Gamma_5^-$	$X_3 + X_4$
$D_5^* \times D_1$	$\Gamma_4^+ + \Gamma_4^- + \Gamma_5^+ + \Gamma_5^-$	$X_3 + X_4$
$D_5^* \times D_5$	$\Gamma_1^+ + \Gamma_1^- + \Gamma_2^+ + \Gamma_2^-$ $+2\Gamma_3^+ + 2\Gamma_3^- + \Gamma_4^+$ $+\Gamma_4^- + \Gamma_5^+ + \Gamma_5^-$	$2X_1 + 2X_2$

Table A.1: Decomposition of the product $D^* \times D$. Each row labels the decomposition of the term-wise product, considering that $D = D_1 + D_5$ is derived from a space group irrep induced from the sum of small irreps $T_1 + T_5$, which is then restricted to the arms $\mathbf{K}_{1,2}$. The terms in the reduction are small irreps of the little groups at $\mathbf{\Gamma}$ and $\mathbf{X}_3 = (0, 0, 1/2)$. The labels for the X irreps are those from the point $\mathbf{X} \equiv \mathbf{X}_2 = \frac{\mathbf{b}_y}{2} = (0, 1/2, 0)$, since $\mathbf{X}_3$ is in the star of $\mathbf{X}$. Note that the label for the $\mathbf{X}$ point differs from that in **Section 4.1** (where it is called $\mathbf{X}_2$) and was chosen for consistency with the BCS notation.

then restrict this representation only to the $\mathbf{K}_{1,2}$ arms and consider the elements that either leave $\mathbf{K}_i$ invariant or relate one to the other. Both $\mathbf{K}_1$ and $\mathbf{K}_2$ belong to the same star and are related by inversion. The subspace of these two arms is invariant under all these elements, which form a group that we denote by G_W. Let us call D the representation of G_W so obtained. D is divided into blocks arising from the T_1 and T_5 irreps, hence we write $D = D_1 + D_5$. The direct product of the full space group irrep can be used to find the reduction of the product $D^* \times D$ into small irreps of the little groups at $\mathbf{\Gamma}$ and $\mathbf{X}_3 = \frac{\mathbf{b}_z}{2} = (0, 0, 1/2)$. The result of this product is shown in **Table A.1**. From **Table A.1**, we can determine the elements of the diagonal blocks using the Γ irreps, and those of the off-diagonal blocks using the X_m irreps ($m = 1, 2, 3, 4$). The X_m irreps are consistent with lattice translations that have a non-trivial representation, indicating that they couple points in the BZ that are not equivalent. Following the same procedure as in the previous section, we obtain the matrix representation of the energy operator. The matrices of D that are needed to find the symmetry-adapted bases are the following (again, we omit the representation matrix of inversion for brevity):

$$\rho_{D_1}(2_{001}) = \begin{pmatrix} 1 & 0 \\ 0 & 1 \end{pmatrix}, \rho_{D_1}(m_{010}) = \begin{pmatrix} e^{-i\pi/4} & 0 \\ 0 & e^{i\pi/4} \end{pmatrix}, \\ \rho_{D_1}(4^+_{001}) = \begin{pmatrix} e^{i\frac{\pi}{4}} & 0 \\ 0 & e^{-i\frac{\pi}{4}} \end{pmatrix} \tag{A.13}$$

and

$$\rho_{D_5}(2_{001}) = \begin{pmatrix} -1_2 & 0 \\ 0 & -1_2 \end{pmatrix},$$
$$\rho_{D_5}(m_{010}) = \begin{pmatrix} 0 & e^{-i3\pi/4} & 0 & 0 \\ e^{i\pi/4} & 0 & 0 & 0 \\ 0 & 0 & 0 & e^{-i\pi/4} \\ 0 & 0 & e^{i3\pi/4} & 0 \end{pmatrix}, \tag{A.14}$$
$$\rho_{D_5}(4^+_{001}) = \begin{pmatrix} 0 & e^{-i3\pi/4} & 0 & 0 \\ e^{-i3\pi/4} & 0 & 0 & 0 \\ 0 & 0 & 0 & e^{-i\pi/4} \\ 0 & 0 & e^{-i\pi/4} & 0 \end{pmatrix}.$$

We obtain: **Equation A.18**:

$$X = \begin{pmatrix} C_1(p_1 - iq_1) & ip_3 + q_4 & -iq_3 + p_4 \\ -ip_3 - q_4 & C_2p_1 - iC_3q_1 & ip_2 + q_2 \\ -iq_3 + p_4 & -ip_2 - q_2 & -iC_2q_1 + C_3p_1 \end{pmatrix}, \tag{A.15}$$

where (p_m, q_m) are real and belong to the 2D irreps X_m and $C_{1,2,3}$ are real coupling constants, associated to the X_1 modulation. As a last step, we impose TRS. The unitary part of the TR operation $\Theta = U\kappa$ is in this case

$$U = \begin{pmatrix} 0 & 1 \\ 1 & 0 \end{pmatrix} \otimes \begin{pmatrix} 1 & 0 & 0 \\ 0 & -1 & 0 \\ 0 & 0 & 1 \end{pmatrix}. \tag{A.16}$$

We are interested in modulations implemented by physically altering the dielectric structure of the crystal. Therefore, the modulation itself is considered to transform trivially under Θ. TRS forbids one of the couplings for each one of the X_2, X_3, and X_4 modulations. Furthermore, analyzing the effect of these three by numerically diagonalizing the H matrix shows that none of them is able to open a gap, but they simply move the Weyl points. **Figure A.2** shows examples of these modulations that do not open a gap.

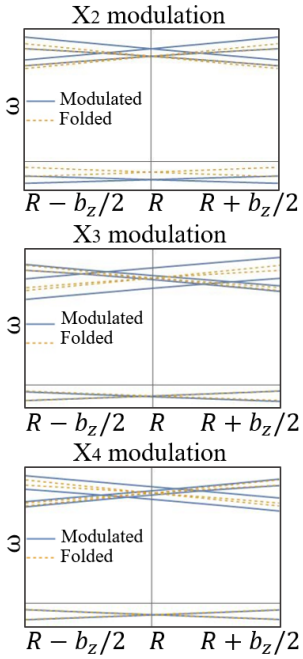

Figure A.2: Examples of perturbations that do not open a gap. **a,b,c** modulations belonging to irreps X_2, X_3 and X_4 respectively.

A.2.1 Gap opening by supercell modulations

It turns out that only modulations transforming in the X_1 representation can gap out the Weyl points. We now want to obtain a representation for X_1 to check which type of geometrical perturbation it can be associated to. The representation matrices used to obtain the X_1 modulation terms are the following:

$$\rho_{X_1}(2_{001}) = \begin{pmatrix} 1 & 0 \\ 0 & 1 \end{pmatrix}, \rho_{X_1}(m_{010}) = \begin{pmatrix} 0 & -1 \\ 1 & 0 \end{pmatrix}, \\ \rho_{X_1}(4^+_{001}) = \begin{pmatrix} 0 & -1 \\ 1 & 0 \end{pmatrix}. \tag{A.17}$$

Herewith we present the final expression of the energy operator along the **T** line of $H(k_z, H_z)$ with only the X_1 couplings included:

$$H(k_z, H_z) = \begin{pmatrix} W_+ & X_1 \\ X_1^\dagger & W_- \end{pmatrix}, \tag{A.18}$$

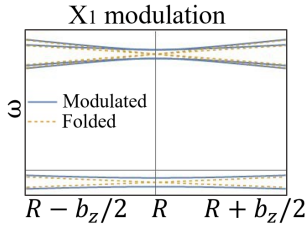

Figure A.3: Effect of the X_1 modulation and Weyl points coupling. From the analytical model, a four-fold degeneracy point is achieved at the folding condition $H_z = \frac{\delta}{\alpha-\beta}$, as shown in dashed lines. When a X_1 modulation is introduced, the Weyl dipole couples and a bandgap is opened, as shown by solid lines. Parameters: $a = -7$,$b = -30$,$\alpha = 1$,$c = 1$, $d = 30$, $\gamma = 1$, $\beta = 0.45$, $\delta = 7.5$, $C_{1,2,3} = 1$, $p_1 = 7$, $q_1 = 0$.

$$W_{\pm} = \begin{pmatrix} ak_z^2 \pm bk_z + \alpha H_z^2 & 0 & 0 \\ 0 & ck_z^2 \pm dk_z + \beta H_z^2 & H_z\delta \pm \gamma k_z H_z \\ 0 & H_z\delta \pm \gamma k_z H_z & ck_z^2 \pm dk_z + \beta H_z^2 \end{pmatrix}, \tag{A.19}$$

$$X_1(p_1, q_1) = \begin{pmatrix} C_1(p_1 - iq_1) & 0 & 0 \\ 0 & C_2 p_1 - iC_3 q_1 & 0 \\ 0 & 0 & -iC_2 q_1 + C_3 p_1 \end{pmatrix}, \tag{A.20}$$

where the coordinates (p_1, q_1) transform as X_1 and parametrize the modulation strength, and $C_{1,2,3}$ are real coupling constants, while the rest of the parameters are also real. The k_z component is taken from the point where the Weyl points merge after the cell folding. The effect of this modulation is visualized in **Figure A.3**. The bandgap opened via supercell modulation in the TRS broken system is shown to be a Chern gap in **Section 4.1**. From the analytical model, we also observe that, to exactly superimpose the Weyl points, we need to tune the magnetic field to the folding condition:

$$H_z = \frac{\delta}{\alpha - \beta}, \tag{A.21}$$

as can be seen by diagonalizing the matrix $H(0, H_z)$. We use the projectors onto the i-th basis element in the space of the irrep X_1:

$$P_{ii} \propto \sum_{g \in G} X_1^*(g)_{ii} g \tag{A.22}$$

where g runs over the little co-group at $\mathbf{X}_3 = (0, 0, 1/2)$ and we disregard any normalization factors. Applying these to an arbitrary function $f(z)$, we find:

$$X_1 : \begin{cases} P_{11} f \propto f(z) + f(-z) \\ P_{22} f \propto f(z) - f(-z) \end{cases} \qquad (A.23)$$
$$X_2, X_3, X_4 : \; P_{ii} f = 0, \quad i = 1, 2.$$

Therefore, given functions of z that under lattice translations obey $\mathbf{T} f = e^{i\mathbf{X}_3 \cdot \mathbf{T}} f$, those that provide a basis for this irrep are one even and one odd, respectively. This proves that modulation of the radius of the rods $\Delta r = r(z) - r_0 = r_m \cos(2\pi z/N|a|)$ with $N = 2$ belongs to X_1. In particular, it is parametrized by $(p, q) = (p, 0)$ in the model given in the previous section. We also note that when the modulation is cubic, i.e. $\Delta r = r(x, y, z) - r_0 = r_m[\cos(\pi x/|a|) + \cos(\pi y/|a|) + \cos(\pi z/|a|)]$, it is only the z dependent part that is responsible for gapping the Weyl points generated in a H_z field.

A.2.2 Case $N = N_W > 2$

As stated before, this model addresses the case where $N = N_W = 2$. When $N_W = 2$ is fixed but $N = 2n$ with n integer (see **Figure 4.5**), the modulation belongs to point $(0, 0, 1/N)$ and must enter at order n in H. Therefore, unless $N_W = N = 2$, the modulation will belong to the high-symmetry line $\mathbf{\Delta}$. The little group of its wave vector is smaller than in the $N = 2$ case. The expression for the diagonal blocks in **Equation A.18** is identical since the Weyl points still lie on the $\mathbf{T}$ line, but the reduced symmetry of the modulation modifies the off-diagonal blocks. The most general expression for TR-even modulations in this case is the following:

$$\Delta = \begin{pmatrix} A_1 r_3 & -r_5 & i s_5 \\ r_5 & r_1 + A_2 r_3 & i r_4 \\ i s_5 & -i r_4 & -r_1 + A_2 r_3 \end{pmatrix}, \qquad (A.24)$$

where r_l and s_l belong to the Δ_l ($l = 1, 3, 4, 5$) irreps and all of them are complex. Note that (r_5, s_5) is the basis for the 2D irrep Δ_5 and $A_{1,2}$ are real coupling constants for the Δ_3 modulation.

Appendix B

Transversality Enforced Tight Binding Model

In this Appendix, we demonstrate the process for extracting optimal pseudo-orbitals that are integral to constructing the minimal TETB for the PhC. Initially, we address the method for isolating a transverse bundle appropriate for a TETB description. Subsequently, we present a minimization procedure that yields a set of efficient pseudo-orbitals, minimizing the number of additional longitudinal modes. Lastly, we examine the constraints of physicality and detail the methodology to enforce them.

B.1 Transverse Symmetry Vector

The bundle size used to compile the transverse symmetry vector depends on the number of bands one wants to include in the TB description of the PhC. In general, this is a nontrivial decision, as TB models can not be constructed for arbitrary sets of bands. Specifically, the bands described by a TB model must fulfill the following conditions:

- **Condition 1**: They must satisfy compatibility conditions.
- **Condition 2**: All the topological symmetry indicators must be trivial.

Condition 1 is automatically satisfied by any isolated set of bands, i.e., by a collection of bands separated by gaps from the rest. This happens, for instance, when the lowest frequency bands are separated from the rest by a global gap, which in the case of PhCs is known as the *fundamental gap*. Looking at **Figure 4.20**, no global gap that one could use to easily define a suitable set of bands for the TB model is appreciated. Consequently, we must artificially detach a set of lower frequency bands from

the rest, up to the point we want the TETB to describe the properties of the bands. **Condition 2** is satisfied for electronic bands or 1D and 2D PhCs bands if the irreps at the HSP can be written as a sum of EBRs. However, for 3D PhCs, the second condition is harder to check owing to the irregular irrep contents for the zero-frequency modes at Γ. This is a highly nontrivial problem pointed out for the first time in Ref. [23], leading to the definition of "transverse" symmetry indicators. All possible *transverse connectivities* for the 230 space groups have been computed in Ref. [23], with and without TRS, together with their topological symmetry indicators. These connectivities can be used to identify, in the photonic bands of interest, a bundle satisfying **Condition 1-2**.

B.1.1 Transverse bundling: Example in SG No. 224

In the case of SG No. 224 with TRS, Ref. [23] gives $\mu_1^T = 4$, with 4 possible transverse symmetry vectors, and $\mu_2^T = 6$ with 22 different transverse symmetry vectors. This means that we can build TB models with four or six transverse bands but not with 1, 2, 3, or 5. There are, of course, other possibilities with more bands corresponding to μ_n^T for $n > 2$ that will not be considered here. The irreps labeled in **Figure 4.20** don't correspond to any of the four minimal solutions. Still, one of the 22 second minimal solutions precisely matches the irreps for the six lower frequency bands. By analyzing the symmetry properties of the electromagnetic modes at the HSP, we compute the symmetry vector for the lowest six active bands of the PhC, which returns:

$$\mathbf{v}^T = [(\blacksquare)^{2T} + \Gamma_2^- + \Gamma_4^-, R_4^- + R_5^+, M_1 + 2M_4, X_1 + X_3 + X_4]. \tag{B.1}$$

The second condition is also satisfied, as all the symmetry indicators for $SG224$ with TRS are trivial [130]. This means that building a TB model that faithfully replicates the properties of the six lower frequency bands in the spectrum should be possible.

B.2 Non-Minimal Pseudo-Orbital Choice

As we showed in **Section 3.2.2.2**, the Diophantine problem has, in principle, infinite solutions. The easiest way to solve **Equation 3.42** is to set $\mathbf{z} = 0$ in **Equation 3.44**. This provides a valid solution but is not guaranteed to be of minimal norm.

B.2.1 Non-minimal orbital choice: example in SG No. 224

For the example with symmetry vector of **Equation B.1**, setting $\mathbf{z} = 0$ in **Equation 3.44**, returns the following vector with $N_{EBR} = 25$ components:

$$\mathbf{n} = (1,0,0,0,2,-1,0,0,0,0,0,-1,0,0,0,0,0,0,0,0,0,0,0,0,0)^T \tag{B.2}$$

which, in the notation of BCS, corresponds to the following combination of EBRs:

$$\mathbf{v}^T_{\mathbf{z}=0} = A_1@2a + 2T_2@2a - A_{1g}@4b - A_{1g}@4c. \tag{B.3}$$

This vector solution has norm $\mu = 22$. As we will show now, this is not the minimal norm solution. To verify whether a solution with a shorter length can be found, we propose a minimization strategy.

B.3 Minimizing the Number of Longitudinal Modes

The minimization strategy starts with the following observation. **Equation 3.42** has in principle infinite solutions.. The PhC system under study fixes the number of transverse physical bands. However, the number of longitudinal, additional bands remains arbitrary. We would prefer the minimal number of additional bands necessary to describe the band structure since the resulting TB model will be easier to implement. For this reason, we aim to impose an upper limit on the number of longitudinal bands. This can be achieved by splitting the problem defined in **Equation 3.42** into three problems:

- **Step 1**: Search for all possible longitudinal solutions having a fixed number of bands (d_L). This returns a finite set of possible candidate longitudinal modes, $\mathbf{n}^L$.

- **Step 2**: Employ the longitudinal modes obtained in the previous step, to look for solutions to the EBR decomposition problem. This problem can still have multiple solutions, but these are no longer infinite.

- **Step 3**: Verify whether the transversality constraint is respected, i.e. the Γ singularity is correctly reproduced by the solution.

The smallest value of $d_L > 0$ for which the three problems are simultaneously satisfied returns the optimal transversality-enforced pseudo-orbitals basis for the TB model.

The first step is implemented as follows. Given a fixed number of bands d_L, we look for longitudinal vectors $\mathbf{n}^L$, that satisfy:

$$\mathbf{g} \cdot \mathbf{n}^L = d_L, \tag{B.4}$$

where $\mathbf{g} = [g_1, .., g_i, ..., g_{N_{EBR}}]$ is a vector containing the g_i dimensions of all EBRs of the SG and $\cdot$ is the dot product. We want to keep d_L as small as possible since we aim to minimize the number of longitudinal bands. Obviously, d_L must be strictly positive ($d_L > 0$) since at least one longitudinal mode is needed to regularize the Γ obstruction. In practice though, d_L can never be smaller than $d_L = d_L^{\min}$, where $d_L^{\min}$ is the dimension of the smallest EBR in the SG ($d_L^{\min} = \min[g_i]$). With this starting choice for d_L, we move to the next step. If no solution is found for the smallest choice of d_L, we increase its value, until a valid solution is found to both problems.

Before proceeding to the description of steps 2 and 3, we introduce two new auxiliary transverse symmetry vectors, allowing us to simplify the problem.

B.3.1 Γ-reduction

To help the practical numerical implementation of Step 2 and Step 3, we define two auxiliary Γ-reduced symmetry vectors, starting from the $\mathbf{v}^T$. Both vectors are agnostic of the irregular symmetry content at $\omega = 0$, making our method totally agnostic of the extrapolated $\omega = 0$ irreps. These two Γ-reduced vectors are defined as follows:

- A Γ-agnostic symmetry vector, $\mathbf{v}^T_{(BZ-\Gamma)}$. This vector is directly obtained from $\mathbf{v}^T$ by eliminating the entire symmetry content at $\mathbf{k} = 0$, both for $\omega > 0$ and $\omega = 0$. This reduced vector has size $(N_{irr} - N_{irr}[\Gamma])$, being $N_{irr}[\Gamma]$ the number of irreps at Γ. This vector is used to define a reduced Diophantine problem:

$$\mathbf{v}^T_{(BZ-\Gamma)} = \mathbf{A}_{\mathrm{RD}}\mathbf{n}, \tag{B.5}$$

  where the reduced matrix $\mathbf{A}_{\mathrm{RD}}$, of size $(N_{irr} - N_{irr}[\Gamma]) \times N_{EBR}$, is obtained by eliminating the irreps at the Γ point from the EBR matrix $\mathbf{A}$.

- A Γ-defective vector $\mathbf{v}^T_{\omega>0}$. This vector is full-sized, with N_{irr} components. At Γ it contains the $\omega > 0$ irreps obtained from MPB, but leaves the $\omega = 0$ symmetry-content ill-defined. Technically, this is no longer a symmetry vector, because this subtraction makes it defective, i.e. we have 2 missing entries in the total

multiplicity of the irreps at Γ as compared to the other HSPs

$$2 + \sum_{j}^{N_{irr}[\Gamma])} n_j = \sum_{j}^{N_{irr}[\mathbf{k}_{\mathrm{HSP}} \neq \Gamma]} n_j. \tag{B.6}$$

Step 2 of is implemented using the Γ-agnostic symmetry vector, $\mathbf{v}^T_{(BZ-\Gamma)}$. Step 3 requires the use of the Γ-defective vector $\mathbf{v}^T_{\omega>0}$, to perform the transversality check.

B.3.2 Multiple solutions

Step 2 involves solving the reduced Diophantine problem **Equation B.5**, via:

$$\mathbf{n} = \mathbf{n}^{T+L} - \mathbf{n}^L \tag{B.7}$$

where $\mathbf{n}^L$ are the longitudinal modes obtained in the previous step (Step 1) through **Equation B.4**. For a fixed d_L, this problem can have multiple, but no longer infinite solutions. These are therefore accessible to any computational constraint solver [311].

B.3.3 Physicality constraint

In Step 3, we verify that the physicality constraint is respected, i.e. that the Γ singularity is correctly reproduced by the solution. As we have already mentioned, due to the transversality constraint at Γ, the symmetry content at $\omega = 0$ is irregular. In other words, it contains negative multiplicities in the irreps decomposition. This negative multiplicity can be formally canceled by the irreps of the $\omega > 0$ transverse modes or by the auxiliary longitudinal bands. If a transverse mode at $\omega > 0$ is sacrificed to cancel the negative multiplicities at $\omega = 0$, our model will not enforce transversality, making it unphysical. Therefore, for a solution to be transversal, it must satisfy either of the two equivalent conditions:

1. All negative irreps arising from the singularity at Γ must be present in auxiliary longitudinal bands so they can be canceled.

2. All the $\omega > 0$ transverse irreps in $\mathbf{v}^T$ should also be contained in the transverse bands of the EBR decomposition.

Note that $d_L > 0$ is a necessary but not sufficient condition for a solution to be transverse. An example of an unphysical pseudo-orbital choice with $d_L > 0$ is given in **Section B.3.4**.

B.3.4 Unphysical orbital choice: example in SG No. 224

Here we present an example of an unphysical pseudo-orbital choice that can arise if transversality is not enforced (i.e. skipping Step 3). We are in SG224 and we consider the following:

$$\mathbf{v}^T = [(\blacksquare)^{2T} + \Gamma_1^+ + \Gamma_1^- + 2\Gamma_2^+ + \Gamma_3^-, R_1^- + R_2^- + R_3^+ + R_4^+, M_1 + 2M_2 + M_4, X_1 + 2X_2 + X_3] \tag{B.8}$$

which is a valid transverse symmetry vector [23]. The associated Γ-defective vector $\mathbf{v}^T_{\omega>0}$ is:

$$\mathbf{v}^T_{\omega>0} = [\Gamma_1^+ + \Gamma_1^- + 2\Gamma_2^+ + \Gamma_3^-, R_1^- + R_2^- + R_3^+ + R_4^+, M_1 + 2M_2 + M_4, X_1 + 2X_2 + X_3] \tag{B.9}$$

If we apply Step 2 and look for all possible solutions to the reduced Diophantine problem, we obtain two possible EBR decompositions ($\mathbf{v}_1^T$ and $\mathbf{v}_2^T$). As we will see, the first one is unphysical:

$$\mathbf{v}_1^T = A_1@2a + 2 * A_2@2a + E_g@4b - A_{1g}@4b - A_2@2a \qquad \text{(unphysical)} \tag{B.10}$$

$$\mathbf{v}_2^T = A_1@2a + 2 * A_2@2a + E_u@4c - A_{1g}@4b - A_2@2a \qquad \text{(physical).} \tag{B.11}$$

Both $\mathbf{v}^T_{1,2}$ EBR decompositions are associated to the following longitudinal mode:

$$\mathbf{v}^L = A_{1g}@4b + A_2@2a \tag{B.12}$$

and their extrapolated Γ content is the following:

$$(\blacksquare)_1 = -\Gamma_1^+ + \Gamma_2^- - \Gamma_2^+ - \Gamma_3^+ + \Gamma_3^+ + \Gamma_4^+ \tag{B.13}$$

$$(\blacksquare)_2 = -\Gamma_1^+ + \Gamma_2^- - \Gamma_2^+ + \Gamma_4^- + \Gamma_5^- - \Gamma_5^+. \tag{B.14}$$

The unphysicality of the first EBR decomposition arises from the annihilation of a Γ_3^+ irrep which belonged to the positive frequency modes in $\mathbf{v}^T_{\omega>0}$. More specifically, a transversal $\omega > 0$ mode is sacrificed to regularize the singularity. While this cancellation is mathematically valid, it is unphysical, since we are breaking transversality forcing another transversal mode to go to $\omega = 0$ to cancel that irrep.

B.3.5 Minimal orbital choice: example in SG No. 224

Let us now see how the minimal decomposition works for the SG No. 224 example with symmetry vector $\mathbf{v}^T$ as in **Equation B.1**. The first possibility to try is to take $d_L = d_L^{\min} = 2$ since the lowest dimension of any EBR in this SG is $\min[g_i] = 2$. Applying the steps described in **Section B.3**, we obtain the following solution:

$$\mathbf{v}^{T+L} = A_{2u}@4b + A_{2u}@4c, \tag{B.15}$$

$$\mathbf{v}^{L} = A_{1}@2a. \tag{B.16}$$

Since we can‘t go lower than $d_L = 2$, this needs to be the solution with the minimal number of bands. As well, physicality is satisfied. Therefore this represents an optimal pseudo-orbital choice for building a TETB of the six transverse modes in **Equation B.1**.

Appendix C

Photonic 3D CIs: Generalizations

This appendix provides complementary information on the "Photonic 3D CI" detailed in **Section 4.1**. It discusses the robustness and limitations of the topological phase and proposes generalizations. **Section C.1** explores the stability of the topological gap, noting that Weyl points can be annihilated without perfect band folding. The discussion then shifts to strategies for minimizing magnetic bias and increasing Chern numbers, detailing on the effects on the bandgap size. Differences between uniaxial, cubic and other more general commensurate supercell modulations are outlined, and the orientation of the Weyl dipole is discussed in relation to these.

Section C.2 examines the symmetries of FLs and highlights how their shape can change based on geometrical symmetries. The section also considers diagonal Chern vector's orientations and its implications for topological protection on oblique surface cuts.

C.1 Bulk Topological Properties

C.1.1 Robustness of the topological gap

Fine-tuning and perfect band folding are not strict requirements for achieving the annihilation of Weyl points, endowing our system with a certain level of robustness and tolerance over reciprocal lattice vector mismatches. As shown in **Figure C.1**, the annihilation of Weyl points, in the modulated system, occurs even under a bias field which is different from finely tuned value allowing perfect band folding, i.e. when N_W is an integer. The bandgap is maximized at fine-tuning and then gradually decreases when deviating from it. This indicates that the 3D CI phase can be achieved under a certain

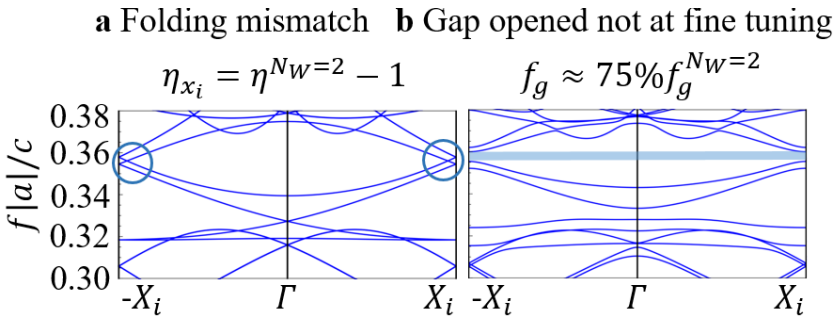

Figure C.1: Weyl point annihilation occurs with tolerance over folding lattice vector and Weyl point location mismatch. **a** Supercell of size $(2, 2, 2)$ with no modulation: the gyro-electric parameter ($\eta^{N_W=2} = 15$) deviates from the finely tuned one ($\eta^{N_W=2} = 16$) required to merge Weyl points exactly at zone boundary. **b** After modulation, Weyl points annihilate, resulting in a topological bandgap f_g which is $\sim 75\%$ the maximum value $f_g^{N_W=2}$ obtained at fine-tuning.

continuum interval of TRS-breaking conditions centered around discrete values (N_W) of the Weyl dipole splitting.

C.1.2 Minimizing the magnetic bias

In **Section 4.2**, we developed a strategy allowing us to generate the 3D photonic CI phase under more accessible magnetization conditions. The method is based on the use of multi-fold supercells at small Weyl splitting: a 3D CI phase can be achieved under smaller splitting of the Weyl dipole as compared to the $N = N_W = 2$ system, by a proper choice of the modulation with $N = N_W > 2$. The detailed steps of this procedure are visualized in **Figure C.2**, for an uniaxial supercell with $N = N_W = 3$. The resulting bandgap displays the same Chern number as the $N = N_W = 2$ system but it is achieved at less than half the gyro-electric bias ($\eta_z^{N_W=3} = 7.8$, $\eta_z^{N_W=2} = 16$). To decrease further the magnetic strength factor, in **Figure C.3** we provide some examples with larger $N = N_W$, in which we increased and optimized the modulation intensity to partially compensate for the bandgap decrease. The example case where $\eta/\epsilon = 1.6/16$ at $N = N_W = 7$, constitutes a significant reduction in the magnetic bias. However, we cannot indefinitely iterate this process down to zero magnetic field. Indeed, as $N = N_W$ grows, the bandgap suffers an unavoidable reduction: a decrease in the magnetic field necessarily leads to a compromise on the resulting gap.

To visualize this, we display a table of decreasing bandgaps for the uniaxial supercell where modulation intensity is chosen to maximize the bandgap at growing N, in **Table C.1**. As it can be seen, the bandgap diminishes as $N = N_W$ grows. Clearly, in the limit of very large N, there is no splitting of Weyl points, and thus no

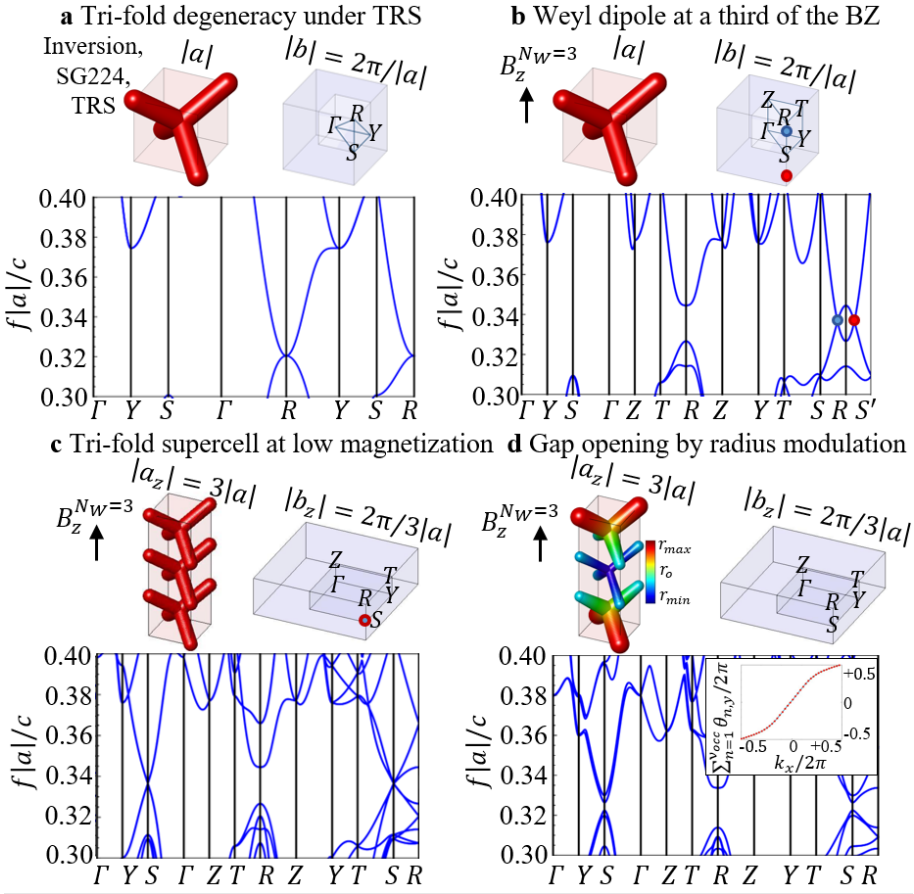

Figure C.2: Usual 3D CI design strategy, but in a reduced magnetization environment, with $N = N_W = 3$. **a**: PhC in the presence of TRS, where $|a_z| = 3|a|$ is the lattice parameter along z axis direction. **b**: Limited TRS breaking implemented via a gyro-electric response to an applied $\mathbf{H} = H_z\hat{\mathbf{z}}$ field inducing a bias parameter $\eta_z^{N_W=3} = 7.8$: the bias field is adjusted to split the Weyl points of approximately a third the BZ, i.e. at $k_z^{\pm} = \pm\frac{2\pi}{3|a|}$, along the **SRS′** line where $\mathbf{S}' = \mathbf{S} - \mathbf{b}_z$. **c**: Artificial folding of the bands on a $N = 3$ uniaxial supercell: Weyl points superimpose at **S** in the new BZ. **d**: Coupling and annihilation of Weyl points through a $N = 3$ uniaxial supercell modulation with modulation parameter $r_m = r_0/20$, resulting in a topological direct gap at **S** with gap-to-midgap (f_g/f_m) ratio of 1.2%. The section Chern C_z number is constant everywhere in the BZ and displays unit value (inset), establishing the system to be in the same topological insulating phase as the $N_W = N = 2$ system, but with a large reduction of the required magnetic bias.

$N = N_W$	5	6	7
η	3.0	2.1	1.6
$f_g/f_m(\%)$	1.5	1.4	1.0
$f_g(f\|a\|/c)$	0.005	0.004	0.003

Table C.1: Reduction of the magnetic bias η and associated gap-to-midgap ratio $f_g/f_m(\%)$. Values are optimized by adjusting the magnitude of the modulation (r_m), yet the bandgap reduction is unavoidable.

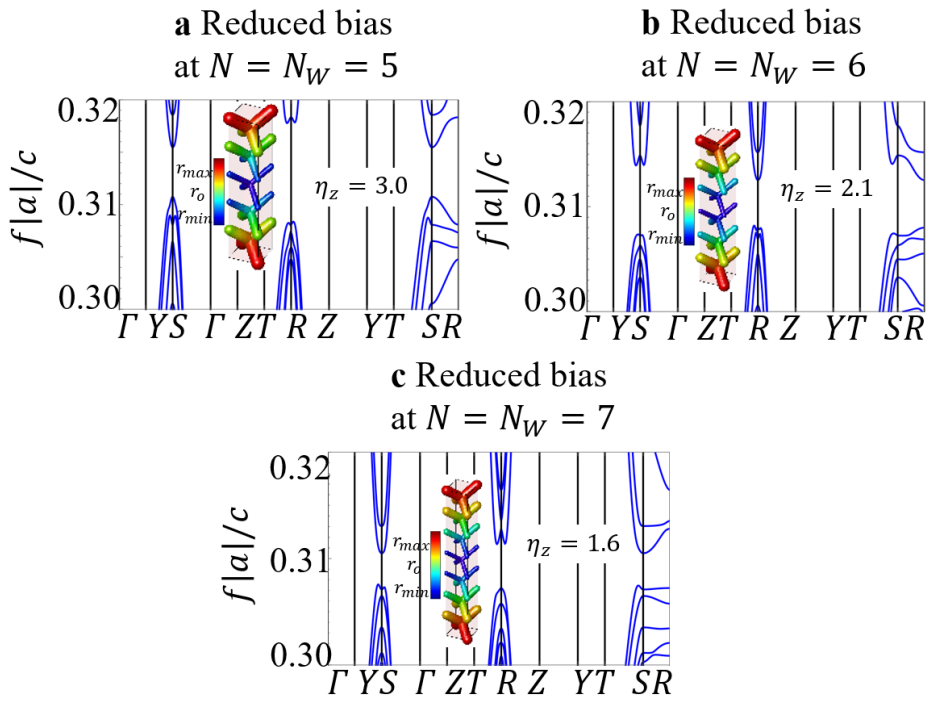

Figure C.3: Bandgap reduction with decreasing Weyl point separation, at increasing $N = N_W$. Partial compensation of the bandgap reduction is achieved by strengthening the modulation intensity (r_m).

TRS broken gap can be opened, $\lim_{N\to\infty} f_g = 0$.

C.1.3 Higher Chern numbers on multi-fold supercells N>2

In **Section 4.1**, we proved that arbitrarily large Chern numbers can be obtained by folding over multi-fold supercells with $N = 2n > 2$ and at $N_W = 2$. **Figure C.4** displays the band-structure associated to the WLs shown in **Figure 4.5** of **Section 4.1**, for uniaxial supercells with N up to eight. As it can be noticed, the bandgap opens up at $\mathbf{R} - \mathbf{Z} = \mathbf{S}$ if n is even and at $\mathbf{R}$ is n is odd. As the supercell modulation approaches a longer wavelength limit, the size of the gap gradually diminishes.

C.1.4 Uniaxial vs cubic supercell modulation

In this section, we explain how to activate different modulation components and better clarify the concept of multifold supercell modulation. In the PhC studied here radius of the cylinders is locally varied, by locally changing the radius of the spheres in the covering approximation. The local change from the original r_0 radius to the new local

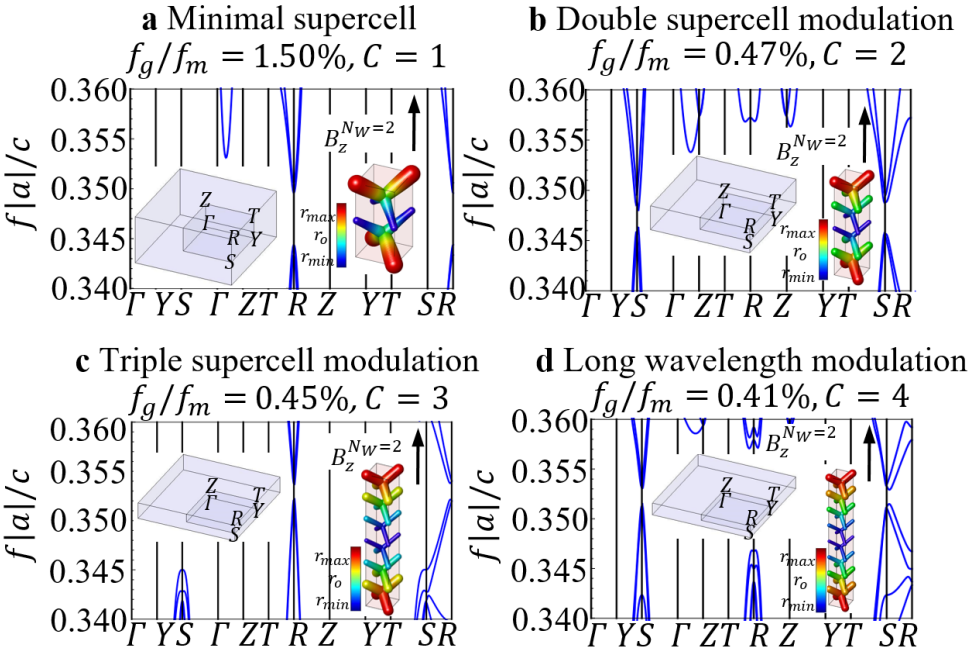

Figure C.4: Band-structure for systems with increasing Chern number. Uniaxial $(1, 1, N)$ supercells with **a**: $N = 2$, **b**: $N = 4$, **c**: $N = 6$ and **d**: $N = 8$ and with modulation parameter $r_m = r_0/20$. The corresponding WLs are shown in **Figure 4.5** in the **Section 4.1**.

one $r(x, y, z)$ is performed according to the relation:

$$\Delta r(x, y, z) = r_m[\delta_x \cos(2\pi x/N|a|) + \delta_y \cos(2\pi y/N|a|) + \delta_z \cos(2\pi z/N|a|)] \quad \text{(C.1)}$$

where we introduced a vector of model parameters $\delta = (\delta_z, \delta_y, \delta_z)$ that differentiates between different types of modulations. The cubic case is represented by $\delta = (1, 1, 1)$ and the z-directed uniaxial case by $\delta = (0, 0, 1)$. This means that, for an uniaxial supercell the modulation is performed along a single Cartesian axis while for a cubic one, the structure is modulated along all the Cartesian components. **Figure C.5** compare cubic and uniaxial supercells, on a (222) lattice so that one could better follow the 3D periodicity. Here the modulation parameter has been largely amplified $r_m \sim r_0/5$. Graphically, the supercell modulation is visualized by employing a scale of colors for the dielectric structure plots and a color bar is associated with the local radius of the cylinders. Note that in the cases considered in the **Section 4.1**, the modulation applied is a perturbation ($r_m << r_0$), which may result in a very subtle graphical difference between the original lattice and the modulated one.

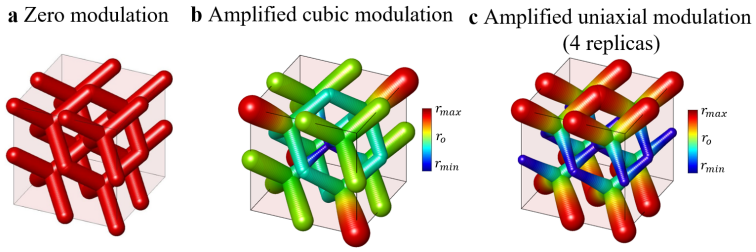

Figure C.5: Visualizing the supercell modulation when the model parameters are largely amplified $r_m \sim r_0/5$. Cubic (**b**) and uniaxial case (**c**). For the uniaxial case, we replicate laterally 4 unit cells, to compare with the 3D periodic structure with the cubic modulations.

C.1.5 Weyl dipole tilted from the Cartesian directions

The strategy we developed in **Section 4.1.3.1** to obtain 3D CIs also applies when the magnetic field deviates from the crystal high symmetry lines, as long as the Weyl dipole is oriented along an integer linear combination of the lattice vectors. In such cases, it is possible to find a proper supercell commensurate with the Weyl dipole separation. For a (110) Weyl dipole orientation, as in **Figure C.6**, the proper auxiliary supercell should have the following structure (N_x, N_y, N_z) with $N_x = N_y = N = N_W$ chosen to be commensurate with the Weyl dipole separation. For example, assume splitting the Weyl points at $N_W = 4$ along (110): by simple folding arguments, a bandgap can be opened via folding and modulating along (110) on a commensurate $N_x = N_y = N = 4$ supercell (either cubic with $N_z = N$ or anisotropic with $N_z \neq N$). This way one can achieve a Chern vector whose direction is not strictly a Cartesian direction provided being an integer linear combination of them. For the example discussed previously, we can expect the resulting system to have a non-zero Chern vector along (110). In general, the Chern vector should display the same orientation as the Weyl dipole, as long as one chooses a commensurate supercell that annihilates them.

C.2 Surface Topological Properties

C.2.1 Winding and symmetries of the Fermi Loops

In **Section 4.1.5**, we displayed FLs which have reflection symmetry with respect to a line in the surface momentum space. Differently from their winding, the symmetry of the FLs in $\mathbf{k}$ is not a universal property and depends on the geometry of the crystal, as we show here with a clarifying example. **Figure C.7** displays the FLs of the C_z/C_x configuration explored in **Section 4.1.5.4** (panel **a**), compared with the FLs of

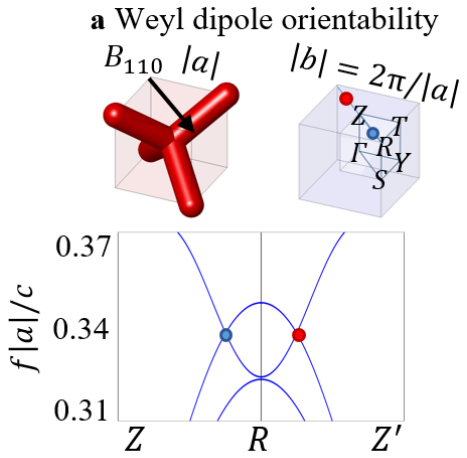

Figure C.6: Orienting the Weyl dipole along an integer linear combination of the Cartesian components. Splitting occurs along the **ZRZ′** line where $\mathbf{Z}' = \mathbf{Z} - \mathbf{b}_y - \mathbf{b}_x$

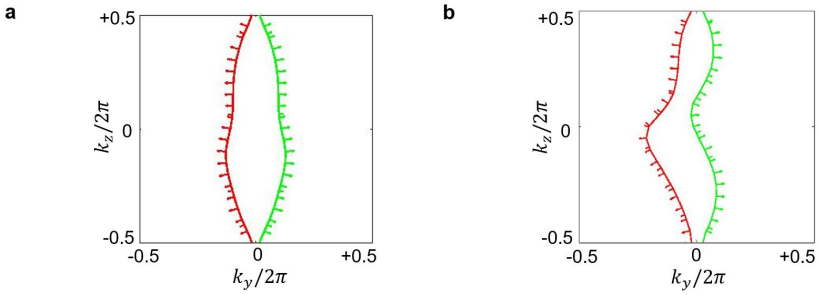

Figure C.7: FLs with the same winding but different symmetries.

a topologically equivalent system, but on which y-mirror symmetry is geometrically broken (panel **a**). Specifically, the crystals in panel **a** are supercell modulated along y via a *sin*-like modulation, in contrast to the *cos*-like modulation employed in the system sustaining the FLs of panel **a**. As it can be observed comparing both panels, in the system with a *sin*-like modulation y the y direction, the y-mirror symmetry of the original FLs is broken but the connectivity, the winding, and the topology of the FLs are unaffected. Therefore, although the winding of the FLs is not affected by the real space geometrical symmetries, their shape can be altered by them. Nevertheless, the BBC relations are not modified by an asymmetry of the FLs.

C.2.2 Diagonal Chern vector orientation

In this section, we discuss how to apply vBBC in the case of oblique orientation of the surface cut of a 3D cube with respect to the Chern vector, i.e. when the Chern vector is neither parallel nor perpendicular to the boundary. Specifically, we ask which diagonal

cuts do not break topological protection and how to apply vBBC in that case. This question is relevant since the topological invariants of a 3D CI are only defined on its lower-dimensional surfaces and some constraints exist on the planes which can support unidirectional boundary states [45,46,180–185,212]. In this sense, 3D CIs have some similarities with weak 3D quantum spin Hall systems [52,312,313], which are a "weak" topological phase and rely on translation along some preferential direction. However, 3D CIs are more robust than this, since no local perturbation on an edge can gap their surface states. Indeed, as we show now, for a 3D CI it is possible to find some diagonal cuts, where the topological protection of surface modes is preserved. In such a case, vBBC can be easily applied provided moving to a new reference frame. We show this with a clarifying example.

Consider a cut with a normal vector given by (m, n, ℓ) and a Chern vector given by $(0, 0, 1)$ for simplicity. Since the surface normal is an integer number of lattice vectors, we can go to a new coordinate system $e_1 = (m, n, \ell), e_2 = (-n, m, 0), e_3 = (-\ell m, \ell n, m^2 + n^2)$, such that the boundary normal vector is $(1, 0, 0)$. In this new coordinate system (i.e. the new reciprocal lattice vectors), the Chern vector is given by $(\ell, 0, m^2+n^2)$. Therefore, we know there will be surface states since the Chern number change has a component perpendicular to the boundary, according to **Equation 4.5** of the **section 4.1.5**. This means that it is possible to find some oblique planes, an integer linear combination of reciprocal lattice vectors, where the topological protection of unidirectional surface states is not lost. Moreover, it shows that also for an oblique cut, vBBC can be easily applied, by simply moving to the new coordinate frame. This important point is related to the fact that a 3D Chern insulating phase is defined by weak indices in the CAZ classification table [25], therefore imposing some constraints on the surfaces that can support unidirectional surface states.

Appendix D

Magnetic Properties of the Photonic Axion Insulator

This appendix aims to characterize and model the gyrotropic response of the "Photonic Axion Insulator" presented in **Section 4.2**. The appendix starts by providing the magnetic Hamiltonian and the magnetic space group analysis of the PhC structure, explaining the impact of the rotation of the external magnetic field on the topological and symmetry properties of the *r*AXI. Connecting bulk results with the domain wall surface gap, the relation between the magnetically induced surface gap and the different hinge configurations is investigated.

D.1 Bulk Symmetry Properties

D.1.1 TETB Hamiltonian for the magnetic Weyl phase

Here we provide the analytical expression of the $H(\mathbf{k})$ Hamiltonian for the gyrotropic PhCs obtained including interactions up to third-nearest neighbors, comparing the magnetic and nonmagnetic cases. The nonmagnetic Hamiltonian for the 3D PhC of **Figure 4.20** is given by **Equation D.5**). It is a 8×8 matrix $H(\mathbf{k})$, built by placing pseudo-orbitals that transform as A_{2u} in Wyckoff positions $4c : (1/2, 1/2, 1/2)$ and $4b : (0, 0, 0)$ and including interactions up to third-nearest neighbors. The Hamiltonian involves nine free, real parameters: α_1 and α_2 are on-site energies, while the six remaining parameters are first (a_1), second (a_2, r_2, s_2, w_2) and third (a_3, r_3) nearest

neighbor hoppings. It is compactly expressed in terms of the following functions:

$$h_1(x_1, x_2) = a_2 \cos\left(\pi[x_1 + x_2]\right) + r_2 \cos\left(\pi[x_1 - x_2]\right), \tag{D.1}$$

$$\begin{aligned} h_2(x_1, x_2, x_3) = a_3 \cos\left(\pi[x_1 + x_2 + x_3]\right) + r_3 \cos\left(\pi[x_1 - x_2 - x_3]\right) \\ +2r_3 \cos\left(\pi x_1\right) \cos\left(\pi[x_2 - x_3]\right) \end{aligned}, \tag{D.2}$$

$$h_3(x_1) = a_1 \cos\left(\pi x_1\right) \tag{D.3}$$

$$h_4(x_1, x_2) = s_2 \cos\left(\pi[x_1 + x_2]\right) + w_2 \cos\left(\pi[x_1 - x_2]\right). \tag{D.4}$$

The linear coupling to the external magnetic field $f_M(\mathbf{k}, \mathbf{H})$ is written in **Equation D.9** for the PhC in **Figure 4.21**. It depends on five free, real parameters: δ_1 for first-nearest neighbor hopping terms, and δ_2, β_2, κ_2 and ϵ_2 for second-nearest neighbor hoppings. Due to symmetry constraints, first-order linear perturbation does not affect the third nearest neighbor hopping. It can be compactly expressed in terms of the following functions:

$$f_{M1}(x_1, x_2, H_1, H_2) = i(H_1 - H_2)\left\{\beta_2 \cos\left(\pi[x_1 - x_2]\right) + \delta_2 \cos\left(\pi[x_1 + x_2]\right)\right\} \tag{D.6}$$

$$f_{M2}(x_1, H_1, H_2) = i\delta_1(H_1 - H_2) \cos\left(\pi x_1\right) \tag{D.7}$$

$$f_{M3}(x_1, x_2, H_1, H_2) = i(H_1 - H_2)\left\{\kappa_2 \cos\left(\pi[x_1 - x_2]\right) + \epsilon_2 \cos\left(\pi[x_1 + x_2]\right)\right\} \tag{D.8}$$

.

D.1.2 Magnetic space group analysis

In this section, we analyze the Magnetic Space Group (MSG) for the gyrotropic PhCs. The MSG assignation is conducted on the dielectric structure, via the use of the functionalities of *FINDSYM* [314]. We perform this analysis for the case of a Supercell Modulation (SM) of a $N = 3$ period, with phase $\phi = 0, \pi$ and in the presence of an external magnetic field :

$$\mathbf{H} = (|h|\cos(\sigma), |h|\sin(\sigma), H_z) \tag{D.10}$$

with $|h| << |H_z|$. We evaluate the symmetry content of the electromagnetic fields, via the study of the transformation properties of the **D** electric and **B** magnetic modes supported by the PhC, using the MPB solver [168], as explained in the **Chapter 3**.

$$
H(\mathbf{k}) = \begin{pmatrix}
a_1 & h_1(k_x,k_y) & h_1(k_x,k_z) & h_1(k_y,k_z) & h_2(k_x,k_y,k_z) & h_3(k_z) & h_3(k_y) & h_3(k_x) \\
h_1(k_x,k_y) & a_1 & h_1(k_y,-k_z) & h_1(k_x,-k_z) & h_3(k_z) & h_2(k_y,k_x,-k_z) & h_3(k_x) & h_3(k_y) \\
h_1(k_x,k_z) & h_1(k_y,-k_z) & a_1 & h_1(k_x,-k_y) & h_3(k_y) & h_3(k_x) & h_2(k_z,k_y,-k_x) & h_3(k_z) \\
h_1(k_y,k_z) & h_1(k_x,-k_z) & h_1(k_x,-k_y) & a_1 & h_3(k_x) & h_3(k_y) & h_3(k_z) & h_2(-k_y,k_x,-k_z) \\
h_2(k_x,k_y,k_z) & h_3(k_z) & h_3(k_y) & h_3(k_x) & a_2 & h_4(k_x,k_y) & h_4(k_x,k_z) & h_4(k_y,k_z) \\
h_3(k_z) & h_2(k_y,k_x,-k_z) & h_3(k_x) & h_3(k_y) & h_4(k_x,k_y) & a_2 & h_4(k_y,-k_z) & h_4(k_x,-k_z) \\
h_3(k_y) & h_3(k_x) & h_2(k_z,k_y,-k_x) & h_3(k_z) & h_4(k_x,k_z) & h_4(k_y,-k_z) & a_2 & h_4(k_x,-k_y) \\
h_3(k_x) & h_3(k_y) & h_3(k_z) & h_2(-k_y,k_x,-k_z) & h_4(k_y,k_z) & h_4(k_x,-k_z) & h_4(k_x,-k_y) & a_2
\end{pmatrix}
\tag{D.5}
$$

$$
f_{\mathcal{M}}(\mathbf{k},\mathbf{H}) = \begin{pmatrix}
0 & f_{\mathcal{M}1}(k_x,k_y,H_x,H_y) & f_{\mathcal{M}1}(k_z,k_x,H_z,H_x) & f_{\mathcal{M}1}(k_y,k_z,H_y,H_z) & f_{\mathcal{M}2}(k_z,H_x,H_y) & f_{\mathcal{M}2}(k_x,H_y,H_z) & f_{\mathcal{M}3}(k_x,k_y,H_x,H_y) & f_{\mathcal{M}3}(k_z,k_x,H_z,H_x) & f_{\mathcal{M}3}(k_y,k_z,H_y,H_z) \\
f^*_{\mathcal{M}1}(k_x,k_y,H_x,H_y) & 0 & f_{\mathcal{M}1}(k_y,k_z,H_y,H_z) & f_{\mathcal{M}1}(k_z,k_x,H_z,H_x) & f_{\mathcal{M}2}(k_y,H_z,H_x) & f_{\mathcal{M}2}(k_z,H_x,H_y) & f_{\mathcal{M}3}(k_y,k_z,H_y,H_z) & f_{\mathcal{M}3}(k_x,k_y,H_x,H_y) & f_{\mathcal{M}3}(k_z,k_x,H_z,H_x) \\
f^*_{\mathcal{M}1}(k_z,k_x,H_z,H_x) & f^*_{\mathcal{M}1}(k_y,k_z,H_y,H_z) & 0 & f_{\mathcal{M}1}(k_x,k_y,H_x,H_y) & f_{\mathcal{M}2}(k_z,H_x,H_y) & f_{\mathcal{M}2}(k_x,H_y,H_z) & f_{\mathcal{M}3}(k_z,k_x,H_z,H_x) & f_{\mathcal{M}3}(k_y,k_z,H_y,H_z) & f_{\mathcal{M}3}(k_x,k_y,H_x,H_y) \\
f^*_{\mathcal{M}1}(k_y,k_z,H_y,H_z) & f^*_{\mathcal{M}1}(k_z,k_x,H_z,H_x) & f^*_{\mathcal{M}1}(k_x,k_y,H_x,H_y) & 0 & f_{\mathcal{M}2}(k_y,H_z,H_x) & f_{\mathcal{M}2}(k_z,H_x,H_y) & f_{\mathcal{M}3}(k_y,k_z,H_y,H_z) & f_{\mathcal{M}3}(k_x,k_y,H_x,H_y) & f_{\mathcal{M}3}(k_z,k_x,H_z,H_x) \\
f^*_{\mathcal{M}2}(k_z,H_x,H_y) & f^*_{\mathcal{M}2}(k_y,H_z,H_x) & f^*_{\mathcal{M}2}(k_z,H_x,H_y) & f^*_{\mathcal{M}2}(k_y,H_z,H_x) & 0 & f_{\mathcal{M}3}(k_x,k_y,H_x,H_y) & f^*_{\mathcal{M}3}(k_x,k_y,H_x,H_y) & f^*_{\mathcal{M}3}(k_y,k_z,H_y,H_z) & f^*_{\mathcal{M}3}(k_z,k_x,H_z,H_x) \\
f^*_{\mathcal{M}2}(k_x,H_y,H_z) & f^*_{\mathcal{M}2}(k_z,H_x,H_y) & f^*_{\mathcal{M}2}(k_x,H_y,H_z) & f^*_{\mathcal{M}2}(k_z,H_x,H_y) & f^*_{\mathcal{M}3}(k_x,k_y,H_x,H_y) & 0 & f^*_{\mathcal{M}3}(k_y,k_z,H_y,H_z) & f^*_{\mathcal{M}3}(k_z,k_x,H_z,H_x) & f^*_{\mathcal{M}3}(k_x,k_y,H_x,H_y) \\
f^*_{\mathcal{M}2}(k_y,H_z,H_x) & f^*_{\mathcal{M}2}(k_x,H_y,H_z) & f^*_{\mathcal{M}2}(k_y,H_z,H_x) & f^*_{\mathcal{M}2}(k_x,H_y,H_z) & f^*_{\mathcal{M}3}(k_z,k_x,H_z,H_x) & f^*_{\mathcal{M}3}(k_y,k_z,H_y,H_z) & 0 & f_{\mathcal{M}3}(k_x,k_y,H_x,H_y) & f_{\mathcal{M}3}(k_y,k_z,H_y,H_z) \\
f^*_{\mathcal{M}3}(k_y,k_z,H_y,H_z) & f^*_{\mathcal{M}3}(k_z,k_x,H_z,H_x) & f^*_{\mathcal{M}3}(k_x,k_y,H_x,H_y) & f^*_{\mathcal{M}3}(k_y,k_z,H_y,H_z) & f^*_{\mathcal{M}3}(k_x,k_y,H_x,H_y) & f^*_{\mathcal{M}3}(k_z,k_x,H_z,H_x) & f_{\mathcal{M}3}(k_x,k_y,H_x,H_y) & 0 & f_{\mathcal{M}3}(k_z,k_x,H_z,H_x) \\
f^*_{\mathcal{M}3}(k_x,k_y,H_x,H_y) & f^*_{\mathcal{M}3}(k_y,k_z,H_y,H_z) & f^*_{\mathcal{M}3}(k_z,k_x,H_z,H_x) & f^*_{\mathcal{M}3}(k_x,k_y,H_x,H_y) & f^*_{\mathcal{M}3}(k_y,k_z,H_y,H_z) & f^*_{\mathcal{M}3}(k_z,k_x,H_z,H_x) & f_{\mathcal{M}3}(k_y,k_z,H_y,H_z) & f_{\mathcal{M}3}(k_z,k_x,H_z,H_x) & 0
\end{pmatrix}
\tag{D.9}
$$

We label the irreps at the HSPs according to the notation of BCS [154, 202]. We compute the symmetry vector $\tilde{\mathbf{v}}$, which contains the multiplicity of each irrep in the little group of each HSP. From these, we finally extract the corresponding Symmetry Indicators (SI) [45, 67, 195–198]. Please note that all operations and coordinates are expressed with respect to the following primitive lattice vectors:

$$\mathbf{e}_1 = \hat{\mathbf{x}}, \quad \mathbf{e}_2 = \hat{\mathbf{y}}, \quad \mathbf{e}_3 = 3\hat{\mathbf{z}}. \tag{D.11}$$

These lattice vectors are those of the BCS parent Space Group (SG) #224. We will stick to this cartesian system even for the lower symmetry phases.

D.1.2.1 Case with $|h| = 0$

When the gyrotropic axis is along z, i.e. in the presence of an external $\mathbf{H} = (0, 0, H_z)$ magnetic field, the PhCs are in MSG 67.505. Please note that there is a $\pi/4$ rotation in the OXY plane between SG 224 and MSG 67.505.

To label the irreps at the HSP, we consider the maximal unitary subgroup of MSG #67.505 (Cm'm'a), i.e. Space Group (SG) #13 ($P2/m$), whose generators are:

$$\{C_{2z}|\frac{1}{2},\frac{1}{2},0\}, \quad \{m_z|\frac{1}{2},\frac{1}{2},0\}, \quad \{\bar{1}|0,0,0\}, \tag{D.12}$$

expressed in the basis of **Equation D.11**. The anti-unitary generators of MSG #67.505 are:

$$\begin{aligned} &\{C'_{2_{110}}|\frac{1}{2},\frac{1}{2},0\}, \quad \{m'_{110}|\frac{1}{2},\frac{1}{2},0\}, \\ &\{C'_{2_{1\bar{1}0}}|0,0,0\}, \quad \{m'_{1\bar{1}0}|0,0,0\}, \end{aligned} \tag{D.13}$$

which are also expressed in the basis of **Equation D.11** and where the prime indicates the time-reversal operation. Please note that there is a $\pi/2$ rotation in the OYZ plane between MSG 67.505 and SG 13.

The symmetry vectors, computed for the lowest six transverse bands of the PhC are:

$$\begin{aligned} \tilde{\mathbf{v}}^T_{\phi=0} = [&3A_1, 3B_1, C_1^- + 2C_2^+ + 3C_2^-, 3D_1, 3E_1, (\blacksquare)^{2T} \\ &+2\Gamma_2^+ + 2\Gamma_2^-, Y_1^- + 2Y_2^+ + 3Y_2^-, 3Z_2^+ + 3Z_2^-] \end{aligned} \tag{D.14}$$

and

$$\begin{aligned} \tilde{\mathbf{v}}^T_{\phi=\pi} = [&3A_1, 3B_1, C_1^- + 2C_2^+ + 3C_2^-, 3D_1, 3E_1, (\blacksquare)^{2T} \\ &+2\Gamma_2^+ + 2\Gamma_2^-, Y_1^+ + 3Y_2^+ + 2Y_2^-, 3Z_2^+ + 3Z_2^-] \end{aligned} \tag{D.15}$$

where $(\blacksquare)^{2T}$ indicates the irregular symmetry content at Γ and $\omega = 0$ arising from

transversality of the electromagnetic waves [23, 250], where $()^T$ labels the transverse bands and where˜superscript indicates that the analysis is done after the introduction of the SM. Note that HSPs labeled as Y, Z, C correspond to the following reduced coordinates in the BZ, whose little group has solely 1-dimensional irreps:

$$Y = (\pi, \pi, 0), \quad Z = (0, 0, \pi), \quad C = (\pi, \pi, \pi). \tag{D.16}$$

The HSPs A, B, D, E, whose little group has a single 2-dimensional irrep, correspond to the following:

(D.17)

On the other hand, for the lowest modes of the Transversality-Enforced Tight-Binding (TETB) model, we obtain:

$$\begin{aligned}\tilde{\mathbf{v}}^{T+L}_{\phi=0} =&[6A_1, 6B_1, 3C_1^+ + 4C_1^- + 2C_2^+ + 3C_2^-, 6D_1,\\ &6E_1, 2\Gamma_1^+ + 4\Gamma_1^- + 2\Gamma_2^+ + 4\Gamma_2^-, 3Y_1^+ + 4Y_1^-\\ &+ 2Y_2^+ + 3Y_2^-, 3Z_1^+ + 3Z_1^- + 3Z_2^+ + 3Z_2^-]\end{aligned} \tag{D.18}$$

and

$$\begin{aligned}\tilde{\mathbf{v}}^{T+L}_{\phi=\pi} =&[6A_1, 6B_1, 3C_1^+ + 4C_1^- + 2C_2^+ + 3C_2^-, 6D_1,\\ &6E_1, 2\Gamma_1^+ + 4\Gamma_1^- + 2\Gamma_2^+ + 4\Gamma_2^-, 4Y_1^+ + 3Y_1^-\\ &+ 3Y_2^+ + 2Y_2^-, 3Z_1^+ + 3Z_1^- + 3Z_2^+ + 3Z_2^-].\end{aligned} \tag{D.19}$$

These equations are in correspondence with **Equations 4.15** and **4.16** where we take into account solely inversion symmetry. After having identified the irregular irrep content at Γ, as $(\blacksquare)^{2T} = -\Gamma_1^+ + \Gamma_1^- + 2\Gamma_2^-$, consistent with symmetry-constrained decomposition for point group $2/m$ as in Refs. [23, 250], we can split the TETB symmetry vector as follows: $\tilde{\mathbf{v}}^{T+L}_{\phi} = \tilde{\mathbf{v}}^{T}_{\phi} + \tilde{\mathbf{v}}^{L}_{\phi}$. Since $\tilde{\mathbf{v}}^{L}_{\phi}$ have trivial SI, we can extract the transverse SI for the photonic bands obtaining:

$$\begin{aligned}\nu^{T+L}_{\phi=0} &= \{1, 0\}\\ \nu^{T+L}_{\phi=\pi} &= \{1, 1\}\end{aligned} \tag{D.20}$$

corresponding to the $\mathbb{Z}_2 \times \mathbb{Z}_2$ magnetic SI group, see Table 5 in Ref. [195].

D.1.2.2 Case with $0 < |h| << |H_z|$

When we apply a small off-z tilt to the external magnetic field, as described by **Equation D.10**, the PhC undergoes subduction to MSG #2.4 ($P\bar{1}$). As long as the $|h|$ perturbation is weak enough as compared to $|H_z|$, the transition occurs without closing the bulk Chern gap, leaving the Chern numbers unaffected, with

$$(C_x, C_y, C_z) = (0, 0, 1). \tag{D.21}$$

More precisely, the $|h|$ component introduces a small deviation from the Weyl folding commensurate condition, which results in a graduaopeninking of the bulk 3D Chern gap as $|h|$ is increased. However, as long as the bulk 3D Chern gap remains opens and **Equation D.21** condition is satisfied, the SI analysis done for $|h| = 0$ uniquely determines the SIs for the $|h| \neq 0$ case. The reason for this is that the SI group for MSG #2.4, which is $\mathbb{Z}_2^3 \times \mathbb{Z}_4$, is a supergroup of $\mathbb{Z}_2^2$ in MSG #67.505. Applying the compatibility relations in MSG #67.505 to the well-known expression for the inversion SI [45, 67, 195–198], returns that $\{\bar{z}_{2,x}, \bar{z}_{2,y}, \bar{z}_{2,z}|\bar{z}_4\}$ can only takes value in:

$$\{0,0,0|0\}, \quad \{0,0,0|2\}, \quad \{0,0,1|0\}, \quad \{0,0,1|2\}, \tag{D.22}$$

thus forming $\mathbb{Z}_2^2$. The transverse SI for the photonic bands in the presence of $0 < |h| << |H_z|$, computed in the MSG 2.4 setting, are:

$$\begin{aligned} \nu_{\phi=0}^{T+L} &= \{0,0,1|0\} \\ \nu_{\phi=\pi}^{T+L} &= \{0,0,1|2\} \end{aligned} \tag{D.23}$$

which is in agreement with **Equations D.20**, which were obtained in SG 13 setting. In SG 13, the $\mathcal{I}$-SI $\{\bar{z}_{2,x}, \bar{z}_{2,y}, \bar{z}_{2,z}|\bar{z}_4\}$ are reduced to

$$\bar{z}_{2,x} = \bar{z}_{2,y} = 0 \mod 2 \tag{D.24}$$

$$\bar{z}_{2,z} = n(\Gamma_1^-) + n(\Gamma_2^-) + n(Y_1^-) + n(Y_2^-) \mod 2 \tag{D.25}$$

$$\bar{z}_4 = 2n(\Gamma_2^-) + 2n(Y_2^-) + 2n(C_1^-) + 2n(Z_1^-) \mod 4 \tag{D.26}$$

where $n(irrep)$ counts the irrep multiplicity at the corresponding HSP. These relations directly follow from applying compatibility constraints. Importantly, note that $\bar{z}_4 \in \{0, 2\}$. This shows that the *relative* Axion Insulators (rAXI) with $\phi = 0, \pi$ display an obstruction of their $\bar{z}_4$ symmetry indicators, irrespective of the presence of a small $|h|$

magnetic perturbation.

D.2 Domain-Wall and Rod Configurations

In the **Section 4.2**, we constructed phase-obstructed domain walls of PhCs, with the $\phi(x)$ SM phase changing from $\phi(x) = 0$ for $x < 0$, to $\phi(x) = \pi$ for $x > 0$. Even in the presence of the domain wall, the AXI PhC is a continuous and fully connected structure, with the rods connected all across the interface. The electromagnetic modes supported by the PhC can be numerically simulated by solving Maxwell's equations on a dense real-space grid, where discontinuities in the dielectric constant are treated via a simple linear interpolation on a dense mesh. Specifically, we use the MIT Photonic-Bands package (MPB) [168] in this case. Conversely, TB models are typically constructed using discrete orbitals localized at specific Wyckoff positions. To accurately capture the continuous nature of PhC geometry in the TETB model, we employ a specific boundary condition choice:

- We keep the hopping terms constant across the interface;
- We use linear interpolation to transition between the onsite energies of the subsystems with SM $\phi = 0$ and $\phi = \pi$.

This prevents the emergence of surface effects in the TETB which deviate from the surface electromagnetic response of a fully connected 3D photonic structure. Specifically, for the model considered here, this boundary choice ensures that the SM mass term which couples the Weyl points [236]:

$$m = \Delta e^{i\phi}, \tag{D.27}$$

crosses zero across a domain wall where $m(x \to -\infty) = m$ and $m(x \to \infty) = -m$, where (Δ, ϕ) are amplitude and phase of the SM. This ensures the domain wall bands are gapless at criticality, as shown in **Figure D.1(a)**.

D.2.1 Gapless Dirac cone on the $x = 0$ plane

As shown in **Figure D.1(a)**, the $\delta\theta = \pi$ domain wall bands display a massless 2D Dirac cone, located at $(k_y, k_z) = (\pi, \pi)$ in the surface BZ. This gapless state arises as a projection of the folded bulk Weyl points $V = (\pi, \pi, 0)$, when $\delta\theta = \pi$, and when the

external magnetic field complies with the commensuration folding condition and does not present any component orthogonal to the interface plane. More specifically, since:

$$m(x = 0) = 0, \tag{D.28}$$

the nested Weyl points reappear as a projection of the bulk Weyl points on the $x = 0$ plane, due to the local cancellation of the effects of the SM. At $x = 0$, the rAXI irreps are exchanged through the phase-obstructed domain wall as a result of the double band inversion occurring in the bulk at V, which is the point where folding of the Weyl points occurs. Importantly, this Dirac cone is not robust to perturbations at the boundary. In particular, the gapless condition for the surface modes on the $x = 0$ plane is only maintained as long as the magnetic field does not present any component orthogonal to the interface, i.e., for an x-domain wall, when $h_x = |h|\cos(\sigma) = 0$.

D.2.2 Magnetic control of the surface gap

To impart a mass to the Dirac cone, we introduce a small magnetic perturbation in the xy plane with $|h| << |H_z|$, resulting in the gapped domain wall bands displayed in **Figure D.1(b)**. As shown in **Figure D.2**, by tuning the value of $|h|$ it is possible to control the size of this surface gap. For example, for a fixed value of $\sigma = \pi/4$, the optimum gap is reached at $|h| \sim 1$. Note that $|h|$ has to be treated as a perturbation as compared to H_z: for values of $|h| \sim |H_z|$, the gap tends to close again, due to deviation from the Weyl folding condition, and correspondent shrinking of the bulk gap.

D.2.3 Topological transition between hinge states

In the **Section 4.2**, we verified that it is possible to induce topological transitions across different hinge-state configurations by tuning the σ angle and rotating magnetic perturbation in the xy plane. This results in four distinct hinge-state configurations α,β,γ,δ, with localization of the upwards-moving state on either of the four different hinges. Since these transitions occur across these topologically distinct boundary configurations, we expect them to be accompanied by a gap-closing point. Indeed, as shown in **Figure D.3**, for a x domain wall, the gap closes when the magnetic perturbation is along $\pm y$. We checked that the same happens for a y domain wall, with a gap closing when the magnetic perturbation is along 10, i.e. $\pm x$. These four values of the in-plane

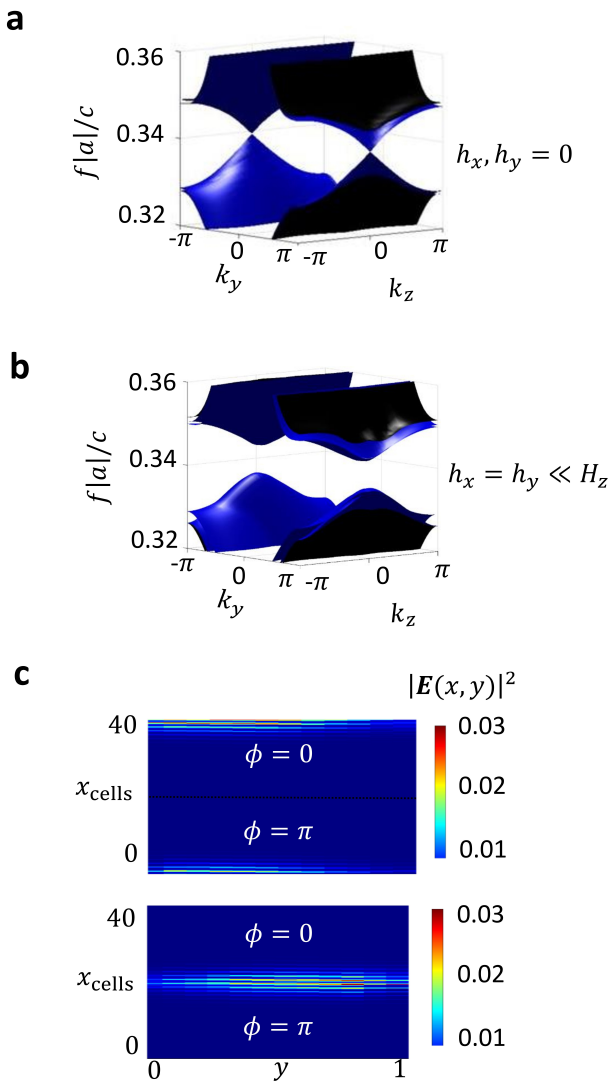

Figure D.1: Surface bands for a x domain wall with $\delta\phi = \delta\theta = \pi$. **a**: Gapless configuration. Projected bulk bands in black, surface bands in blue. **b**: gapped configuration in the presence of a small magnetic perturbation $|h|$ in the xy plane. **c**: Localization of the surface modes at the interface.

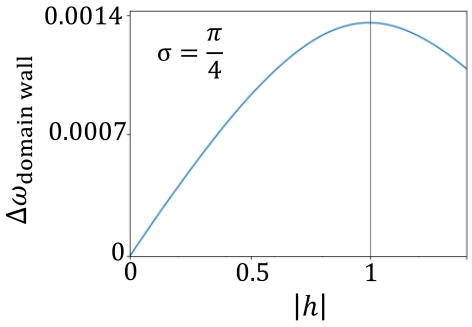

Figure D.2: Dependence of the surface gap with respect to the amplitude of the magnetic perturbation $|h|$, for an x domain wall and for a fixed angle $\sigma = \pi/4$, as computed for the TETB model.

angle:

$$\sigma = 0, \frac{\pi}{2}, \pi, \frac{3\pi}{2} \tag{D.29}$$

corresponds to magnetic orientations that do not break any symmetry among the four inversion-symmetric hinge configurations.

D.2.4 Relative phase difference

As already observed, an x domain wall across phase-obstructed 3D Chern photonic insulators, behaves as the critical point between AXI and a trivial insulator, as long as the SM phase satisfies $\delta\phi = \delta\theta = \pi$. **Figure D.4** shows the surface bands while deviating from this condition, setting

$$-\pi < \delta\theta < \pi. \tag{D.30}$$

As depicted, the surface bands gradually disappear as the phase difference is tuned to 0, recovering the projected 3D Chern gap. The surface modes then reappear as the sign of the phase difference is reversed, reaching criticality again when $\delta\theta = -\pi = \pi$ (mod2π).

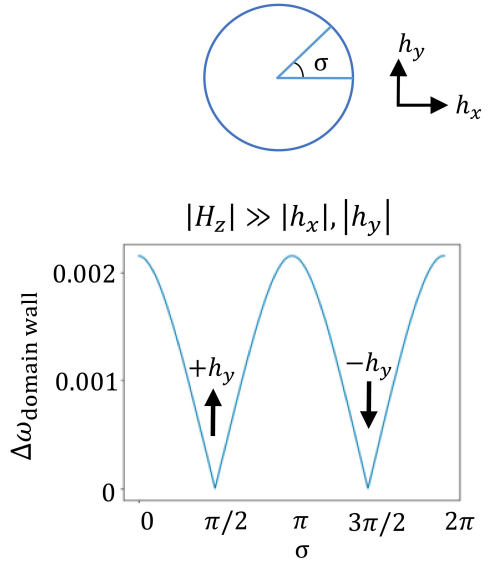

Figure D.3: Dependence of the surface gap with respect to the σ in-plane angle of the magnetic perturbation, for an x domain wall and for a fixed amplitude $|h| = 1$, as computed for the TETB model.

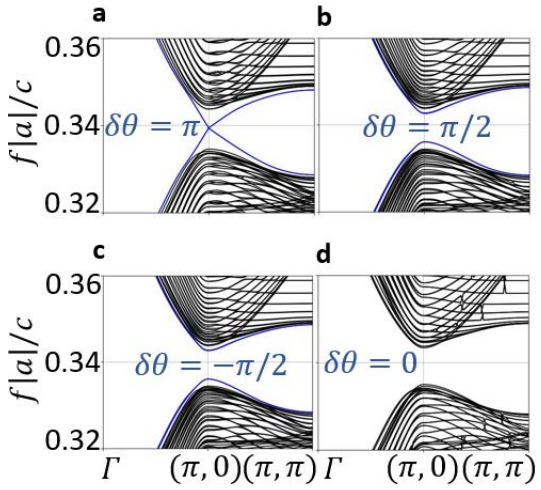

Figure D.4: Dependence of the surface gap for an x domain wall with respect to the value of the $\delta\phi = \delta\theta$ phase difference across the interface. Projected bulk bands in black, surface bands in blue.

Bibliography

[1] Maria Blanco de Paz, Chiara Devescovi, Geza Giedke, Juan José Saenz, Maia G Vergniory, Barry Bradlyn, Dario Bercioux, and Aitzol García-Etxarri. Tutorial: computing topological invariants in 2d photonic crystals. *Advanced Quantum Technologies*, 3(2):1900117, 2020.

[2] Sajeev John. Strong localization of photons in certain disordered dielectric superlattices. *Physical review letters*, 58(23):2486, 1987.

[3] Eli Yablonovitch. Inhibited spontaneous emission in solid-state physics and electronics. *Physical review letters*, 58(20):2059, 1987.

[4] Yoshihiro Akahane, Takashi Asano, Bong-Shik Song, and Susumu Noda. High-q photonic nanocavity in a two-dimensional photonic crystal. *nature*, 425(6961):944–947, 2003.

[5] B Wang and MA Cappelli. A plasma photonic crystal bandgap device. *Applied Physics Letters*, 108(16), 2016.

[6] K v Klitzing, Gerhard Dorda, and Michael Pepper. New method for high-accuracy determination of the fine-structure constant based on quantized hall resistance. *Physical review letters*, 45(6):494, 1980.

[7] David J Thouless, Mahito Kohmoto, M Peter Nightingale, and Marcel den Nijs. Quantized hall conductance in a two-dimensional periodic potential. *Physical review letters*, 49(6):405, 1982.

[8] Mahito Kohmoto. Topological invariant and the quantization of the hall conductance. *Annals of Physics*, 160(2):343–354, 1985.

[9] Srinivas Raghu and Frederick Duncan Michael Haldane. Analogs of quantum-hall-effect edge states in photonic crystals. *Physical Review A*, 78(3):033834, 2008.

[10] FDM Haldane and S Raghu. Possible realization of directional optical waveguides in photonic crystals with broken time-reversal symmetry. *Physical review letters*, 100(1):013904, 2008.

[11] Zheng Wang, Yidong Chong, John D Joannopoulos, and Marin Soljačić. Observation of unidirectional backscattering-immune topological electromagnetic states. *Nature*, 461(7265):772–775, 2009.

[12] Ling Lu, Zhiyu Wang, Dexin Ye, Lixin Ran, Liang Fu, John D Joannopoulos, and Marin Soljačić. Experimental observation of weyl points. *Science*, 349(6248):622–624, 2015.

[13] Ling Lu, Liang Fu, John D Joannopoulos, and Marin Soljačić. Weyl points and line nodes in gyroid photonic crystals. *Nature photonics*, 7(4):294–299, 2013.

[14] Hermann Weyl. Gravitation and the electron. *Proceedings of the National Academy of Sciences*, 15(4):323–334, 1929.

[15] Shuichi Murakami. Phase transition between the quantum spin hall and insulator phases in 3d: emergence of a topological gapless phase. *New Journal of Physics*, 9(9):356, 2007.

[16] Kazuaki Sakoda and K Sakoda. *Optical properties of photonic crystals*, volume 2. Springer, 2005.

[17] John D. Joannopoulos, Steven G. Johnson, Joshua N. Winn, and Robert D. Meade. *Photonic Crystals: Molding the Flow of Light (Second Edition)*. Princeton University Press, 2 edition, 2008.

[18] Ling Lu, John D Joannopoulos, and Marin Soljačić. Topological photonics. *Nature photonics*, 8(11):821–829, 2014.

[19] Minkyung Kim, Zubin Jacob, and Junsuk Rho. Recent advances in 2d, 3d and higher-order topological photonics. *Light: Science & Applications*, 9(1):1–30, 2020.

[20] Hongfei Wang, Samit Kumar Gupta, Biye Xie, and Minghui Lu. Topological photonic crystals: a review. *Frontiers of Optoelectronics*, 13:50–72, 2020.

[21] Guo-Jing Tang, Xin-Tao He, Fu-Long Shi, Jian-Wei Liu, Xiao-Dong Chen, and Jian-Wen Dong. Topological photonic crystals: physics, designs, and applications. *Laser & Photonics Reviews*, 16(4):2100300, 2022.

[22] Kurt Busch, Sergei F Mingaleev, Antonio Garcia-Martin, Matthias Schillinger, and Daniel Hermann. The Wannier function approach to photonic crystal circuits. *Journal of Physics: Condensed Matter*, 15(30):R1233, 2003.

[23] Thomas Christensen, Hoi Chun Po, John D Joannopoulos, and Marin Soljačić. Location and topology of the fundamental gap in photonic crystals. *Physical Review X*, 12(2):021066, 2022.

[24] Ching-Kai Chiu, Jeffrey CY Teo, Andreas P Schnyder, and Shinsei Ryu. Classification of topological quantum matter with symmetries. *Reviews of Modern Physics*, 88(3):035005, 2016.

[25] Alexander Altland and Martin R Zirnbauer. Nonstandard symmetry classes in mesoscopic normal-superconducting hybrid structures. *Physical Review B*, 55(2):1142, 1997.

[26] David E Fernandes and Mário G Silveirinha. Topological origin of electromagnetic energy sinks. *Physical Review Applied*, 12(1):014021, 2019.

[27] Xavier Zambrana-Puyalto, Xavier Vidal, Mathieu L Juan, and Gabriel Molina-Terriza. Dual and anti-dual modes in dielectric spheres. *Optics express*, 21(15):17520–17530, 2013.

[28] Giuseppe De Nittis and Max Lein. On the role of symmetries in the theory of photonic crystals. *Annals of Physics*, 350:568–587, 2014.

[29] Giuseppe De Nittis and Max Lein. Symmetry classification of topological photonic crystals. *arXiv preprint arXiv:1710.08104*, 2017.

[30] Long-Hua Wu and Xiao Hu. Scheme for achieving a topological photonic crystal by using dielectric material. *Physical review letters*, 114(22):223901, 2015.

[31] Jian-Wei Liu, Fu-Long Shi, Xin-Tao He, Guo-Jing Tang, Wen-Jie Chen, Xiao-Dong Chen, and Jian-Wen Dong. Valley photonic crystals. *Advances in Physics: X*, 6(1):1905546, 2021.

[32] Alexander B Khanikaev and Gennady Shvets. Two-dimensional topological photonics. *Nature photonics*, 11(12):763–773, 2017.

[33] Mariá Blanco De Paz, Maia G Vergniory, Dario Bercioux, Aitzol García-Etxarri, and Barry Bradlyn. Engineering fragile topology in photonic crystals: Topological quantum chemistry of light. *Physical Review Research*, 1(3):032005, 2019.

[34] Jian-Wen Dong, Xiao-Dong Chen, Hanyu Zhu, Yuan Wang, and Xiang Zhang. Valley photonic crystals for control of spin and topology. *Nature materials*, 16(3):298–302, 2017.

[35] Dawn TH Tan. Topological silicon photonics. *Advanced Photonics Research*, 2(9):2100010, 2021.

[36] Chiara Devescovi, Antonio Morales-Pérez, Yoonseok Hwang, Mikel García-Díez, Iñigo Robredo, Juan Luis Mañes, Barry Bradlyn, Aitzol García-Etxarri, and Maia G. Vergniory. Axion topology in photonic crystal domain walls, 2023.

[37] Shinsei Ryu, Andreas P Schnyder, Akira Furusaki, and Andreas WW Ludwig. Topological insulators and superconductors: tenfold way and dimensional hierarchy. *New Journal of Physics*, 12(6):065010, 2010.

[38] Alexey Slobozhanyuk, S Hossein Mousavi, Xiang Ni, Daria Smirnova, Yuri S Kivshar, and Alexander B Khanikaev. Three-dimensional all-dielectric photonic topological insulator. *Nature Photonics*, 11(2):130–136, 2017.

[39] Giuseppe De Nittis and Kiyonori Gomi. Classification of "real" bloch-bundles: topological quantum systems of type ai. *Journal of Geometry and Physics*, 86:303–338, 2014.

[40] Wen-Jie Chen, Shao-Ji Jiang, Xiao-Dong Chen, Baocheng Zhu, Lei Zhou, Jian-Wen Dong, and Che Ting Chan. Experimental realization of photonic topological insulator in a uniaxial metacrystal waveguide. *Nature communications*, 5(1):5782, 2014.

[41] Gui-Geng Liu, Zhen Gao, Qiang Wang, Xiang Xi, Yuan-Hang Hu, Maoren Wang, Chengqi Liu, Xiao Lin, Longjiang Deng, Shengyuan A Yang, et al. Topological chern vectors in three-dimensional photonic crystals. *Nature*, 609(7929):925–930, 2022.

[42] Chiara Devescovi, Mikel Garcia-Diez, Barry Bradlyn, Juan Luis Mañes, Maia G Vergniory, and Aitzol Garcia-Etxarri. Vectorial bulk-boundary correspondence for 3d photonic chern insulators. *arXiv preprint arXiv:2206.04147*, 2022.

[43] Chen Fang, Yige Chen, Hae-Young Kee, and Liang Fu. Topological nodal line semimetals with and without spin-orbital coupling. *Physical Review B*, 92(8):081201, 2015.

[44] Yinming Shao, Zhiyuan Sun, Ying Wang, Chenchao Xu, Raman Sankar, Alexander J Breindel, Chao Cao, Michael M Fogler, Andrew J Millis, Fangcheng Chou, et al. Optical signatures of dirac nodal lines in nbas2. *Proceedings of the National Academy of Sciences*, 116(4):1168–1173, 2019.

[45] Yuanfeng Xu, Luis Elcoro, Zhi-Da Song, Benjamin J Wieder, MG Vergniory, Nicolas Regnault, Yulin Chen, Claudia Felser, and B Andrei Bernevig. High-throughput calculations of magnetic topological materials. *Nature*, 586(7831):702–707, 2020.

[46] David Vanderbilt. *Berry Phases in Electronic Structure Theory: Electric Polarization, Orbital Magnetization and Topological Insulators*. Cambridge University Press, 2018.

[47] Bertrand I Halperin. Possible states for a three-dimensional electron gas in a strong magnetic field. *Japanese Journal of Applied Physics*, 26(S3-3):1913, 1987.

[48] Taylor L Hughes, Emil Prodan, and B Andrei Bernevig. Inversion-symmetric topological insulators. *Physical Review B*, 83(24):245132, 2011.

[49] FDM Haldane. Berry curvature on the fermi surface: Anomalous hall effect as a topological fermi-liquid property. *Physical review letters*, 93(20):206602, 2004.

[50] Chiara Devescovi, Mikel García-Díez, Iñigo Robredo, María Blanco de Paz, Jon Lasa-Alonso, Barry Bradlyn, Juan L Mañes, Maia G Vergniory, and Aitzol García-Etxarri. Cubic 3d chern photonic insulators with orientable large chern vectors. *Nature communications*, 12(1):1–12, 2021.

[51] Frank Wilczek. Two applications of axion electrodynamics. *Physical review letters*, 58(18):1799, 1987.

[52] Liang Fu, Charles L Kane, and Eugene J Mele. Topological insulators in three dimensions. *Physical review letters*, 98(10):106803, 2007.

[53] Ari M Turner, Yi Zhang, Roger SK Mong, and Ashvin Vishwanath. Quantized response and topology of magnetic insulators with inversion symmetry. *Physical Review B*, 85(16):165120, 2012.

[54] Chen Fang, Matthew J Gilbert, and B Andrei Bernevig. Bulk topological invariants in noninteracting point group symmetric insulators. *Physical Review B*, 86(11):115112, 2012.

[55] Benjamin J Wieder and B Andrei Bernevig. The axion insulator as a pump of fragile topology. *arXiv preprint arXiv:1810.02373*, 2018.

[56] Xiao-Liang Qi, Rundong Li, Jiadong Zang, and Shou-Cheng Zhang. Inducing a magnetic monopole with topological surface states. *science*, 323(5918):1184–1187, 2009.

[57] Akihiko Sekine and Kentaro Nomura. Axion electrodynamics in topological materials. *Journal of Applied Physics*, 129(14):141101, 2021.

[58] Liang Wu, M Salehi, N Koirala, J Moon, S Oh, and NP Armitage. Quantized faraday and kerr rotation and axion electrodynamics of a 3d topological insulator. *Science*, 354(6316):1124–1127, 2016.

[59] Nicodemos Varnava and David Vanderbilt. Surfaces of axion insulators. *Physical Review B*, 98(24):245117, 2018.

[60] Rafael González-Hernández, Carlos Pinilla, and Bernardo Uribe. Axion insulators protected by c 2 t symmetry, their k-theory invariants, and material realizations. *Physical Review B*, 106(19):195144, 2022.

[61] Fan Zhang, Charles L Kane, and Eugene J Mele. Surface state magnetization and chiral edge states on topological insulators. *Physical Review Letters*, 110(4):046404, 2013.

[62] Changming Yue, Yuanfeng Xu, Zhida Song, Yuan-Ming Lu, Hongming Weng, Chen Fang, and Xi Dai. Symmetry enforced chiral hinge states and surface quantum anomalous hall effect in magnetic axion insulator. *arXiv preprint arXiv:1807.01414*, 2018.

[63] Eslam Khalaf. Higher-order topological insulators and superconductors protected by inversion symmetry. *Physical Review B*, 97(20):205136, 2018.

[64] Yuanfeng Xu, Zhida Song, Zhijun Wang, Hongming Weng, and Xi Dai. Higher-order topology of the axion insulator euin 2 as 2. *Physical review letters*, 122(25):256402, 2019.

[65] Thomas Olsen, Tomáš Rauch, David Vanderbilt, and Ivo Souza. Gapless hinge states from adiabatic pumping of axion coupling. *Physical Review B*, 102(3):035166, 2020.

[66] Yutaro Tanaka, Ryo Takahashi, Tiantian Zhang, and Shuichi Murakami. Theory of inversion-z 4 protected topological chiral hinge states and its applications to layered antiferromagnets. *Physical Review Research*, 2(4):043274, 2020.

[67] Ryo Takahashi, Yutaro Tanaka, and Shuichi Murakami. Bulk-edge and bulk-hinge correspondence in inversion-symmetric insulators. *Physical Review Research*, 2(1):013300, 2020.

[68] Ming Gong, Haiwen Liu, Hua Jiang, Chui-Zhen Chen, and XC Xie. Half-quantized helical hinge currents in axion insulators. *arXiv preprint arXiv:2203.12982*, 2022.

[69] M Sh Birman and Mikhail Zakharovich Solomyak. L2-theory of the maxwell operator in arbitrary domains. *Russian Mathematical Surveys*, 42(6):75, 1987.

[70] Peter Kuchment. The mathematics of photonic crystals. In *Mathematical modeling in optical science*, pages 207–272. SIAM, 2001.

[71] John David Jackson. Classical electrodynamics, 1999.

[72] Paul N Butcher and David Cotter. *The elements of nonlinear optics*. Cambridge university press, 1990.

[73] Jean G Van Bladel. *Electromagnetic fields*, volume 19. John Wiley & Sons, 2007.

[74] Anatoly Serdyukov, Igor Semchenko, Sergei Tretyakov, and Ari Sihvola. Electromagnetics of bi-anisotropic materials: Theory and applications. 2001.

[75] Ismo Lindell, Ari Sihvola, Sergei Tretyakov, and Ari J Viitanen. *Electromagnetic waves in chiral and bi-isotropic media*. Artech House, 1994.

[76] Alexander Cerjan and Terry A Loring. An operator-based approach to topological photonics. *Nanophotonics*, 11(21):4765–4780, 2022.

[77] Giuseppe De Nittis and Max Lein. Effective light dynamics in perturbed photonic crystals. *Communications in Mathematical Physics*, 332:221–260, 2014.

[78] Sylvain Lannebère and Mário G Silveirinha. Photonic analogues of the haldane and kane-mele models. *Nanophotonics*, 8(8):1387–1397, 2019.

[79] Mário G Silveirinha. Chern invariants for continuous media. *Physical Review B*, 92(12):125153, 2015.

[80] Mário G Silveirinha. Quantized angular momentum in topological optical systems. *Nature Communications*, 10(1):349, 2019.

[81] Mário G Silveirinha. Topological classification of chern-type insulators by means of the photonic green function. *Physical Review B*, 97(11):115146, 2018.

[82] Daria A Smirnova, Lev A Smirnov, Daniel Leykam, and Yuri S Kivshar. Topological edge states and gap solitons in the nonlinear dirac model. *Laser & Photonics Reviews*, 13(12):1900223, 2019.

[83] Logan W Clark, Nathan Schine, Claire Baum, Ningyuan Jia, and Jonathan Simon. Observation of laughlin states made of light. *Nature*, 582(7810):41–45, 2020.

[84] Vittorio Peano, Martin Houde, Florian Marquardt, and Aashish A Clerk. Topological quantum fluctuations and traveling wave amplifiers. *Physical Review X*, 6(4):041026, 2016.

[85] Filipa R Prudêncio and Mário G Silveirinha. Ill-defined topological phases in local dispersive photonic crystals. *Physical Review Letters*, 129(13):133903, 2022.

[86] Janet Zhong, Kai Wang, Yubin Park, Viktar Asadchy, Charles C Wojcik, Avik Dutt, and Shanhui Fan. Nontrivial point-gap topology and non-hermitian skin effect in photonic crystals. *Physical Review B*, 104(12):125416, 2021.

[87] Sebastian Weidemann, Mark Kremer, Tobias Helbig, Tobias Hofmann, Alexander Stegmaier, Martin Greiter, Ronny Thomale, and Alexander Szameit. Topological funneling of light. *Science*, 368(6488):311–314, 2020.

[88] Babak Bahari, Abdoulaye Ndao, Felipe Vallini, Abdelkrim El Amili, Yeshaiahu Fainman, and Boubacar Kanté. Nonreciprocal lasing in topological cavities of arbitrary geometries. *Science*, 358(6363):636–640, 2017.

[89] Zhongsheng Chen, Bin Guo, Yongmin Yang, and Congcong Cheng. Metamaterials-based enhanced energy harvesting: A review. *Physica B: Condensed Matter*, 438:1–8, 2014.

[90] Willie J Padilla, Dimitri N Basov, and David R Smith. Negative refractive index metamaterials. *Materials today*, 9(7-8):28–35, 2006.

[91] John Franklin, John Biddle, and Bohdan Balko. Double negative materials (dnm) phenomena and applications. *Institute of Defense Analysis central research Program*, 2009.

[92] Nathaniel Kinsey, Clayton DeVault, Alexandra Boltasseva, and Vladimir M Shalaev. Near-zero-index materials for photonics. *Nature Reviews Materials*, 4(12):742–760, 2019.

[93] Iñigo Liberal and Nader Engheta. The rise of near-zero-index technologies. *Science*, 358(6370):1540–1541, 2017.

[94] Tomoya Hayata. A new route to negative refractive index from topological metals. *Progress of Theoretical and Experimental Physics*, 2018(8):083I01, 2018.

[95] Tun Cao and Shuai Wang. Topological insulator metamaterials with tunable negative refractive index in the optical region. *Nanoscale research letters*, 8:1–8, 2013.

[96] Yuting Yang, Yun Fei Xu, Tao Xu, Hai-Xiao Wang, Jian-Hua Jiang, Xiao Hu, and Zhi Hong Hang. Visualization of a unidirectional electromagnetic waveguide using topological photonic crystals made of dielectric materials. *Physical review letters*, 120(21):217401, 2018.

[97] Bi-Ye Xie, Guang-Xu Su, Hong-Fei Wang, Hai Su, Xiao-Peng Shen, Peng Zhan, Ming-Hui Lu, Zhen-Lin Wang, and Yan-Feng Chen. Visualization of higher-order topological insulating phases in two-dimensional dielectric photonic crystals. *Physical Review Letters*, 122(23):233903, 2019.

[98] Scott A Skirlo, Ling Lu, Yuichi Igarashi, Qinghui Yan, John Joannopoulos, and Marin Soljačić. Experimental observation of large chern numbers in photonic crystals. *Physical review letters*, 115(25):253901, 2015.

[99] Takuto Yamaguchi, Yasutomo Ota, Ryota Katsumi, Katsuyuki Watanabe, Satomi Ishida, Alto Osada, Yasuhiko Arakawa, and Satoshi Iwamoto. Gaas valley photonic crystal waveguide with light-emitting inas quantum dots. *Applied Physics Express*, 12(6):062005, 2019.

[100] Xin-Tao He, En-Tao Liang, Jia-Jun Yuan, Hao-Yang Qiu, Xiao-Dong Chen, Fu-Li Zhao, and Jian-Wen Dong. A silicon-on-insulator slab for topological valley transport. *Nature communications*, 10(1):872, 2019.

[101] Mikhail I Shalaev, Wiktor Walasik, Alexander Tsukernik, Yun Xu, and Natalia M Litchinitser. Robust topologically protected transport in photonic crystals at telecommunication wavelengths. *Nature nanotechnology*, 14(1):31–34, 2019.

[102] Min Wu, Yibiao Yang, Hongming Fei, Han Lin, Xiaodan Zhao, Lijuan Kang, and Liantuan Xiao. On-chip ultra-compact hexagonal boron nitride topological ring-resonator in visible region. *Journal of Lightwave Technology*, 40(23):7610–7618, 2022.

[103] Wenjing Liu, Minsoo Hwang, Zhurun Ji, Yuhui Wang, Gaurav Modi, and Ritesh Agarwal. Z2 photonic topological insulators in the visible wavelength range for robust nanoscale photonics. *Nano Letters*, 20(2):1329–1335, 2020.

[104] Giuseppe De Nittis and Max Lein. The schrödinger formalism of electromagnetism and other classical waves—how to make quantum-wave analogies rigorous. *Annals of Physics*, 396:579–617, 2018.

[105] Giuseppe De Nittis and Max Lein. The perturbed maxwell operator as pseudodifferential operator. *arXiv preprint arXiv:1302.1956*, 2013.

[106] Giuseppe De Nittis and Max Lein. Derivation of ray optics equations in photonic crystals via a semiclassical limit. In *Annales Henri Poincaré*, volume 18, pages 1789–1831. Springer, 2017.

[107] Daniel M Lipkin. Existence of a new conservation law in electromagnetic theory. *Journal of Mathematical Physics*, 5(5):696–700, 1964.

[108] Yousef Saad. *Numerical methods for large eigenvalue problems: revised edition*. SIAM, 2011.

[109] Marc-Antoine Parseval. Mémoire sur les séries et sur l'intégration complète d'une équation aux différences partielles linéaires du second ordre, à coefficients constants. *Mém. prés. par divers savants, Acad. des Sciences, Paris,(1)*, 1:638–648, 1806.

[110] Philippe Francesco, Pierre Mathieu, and David Sénéchal. *Conformal field theory*. Springer Science & Business Media, 2012.

[111] AJ Ward and John B Pendry. Refraction and geometry in maxwell's equations. *Journal of modern optics*, 43(4):773–793, 1996.

[112] Mário G Silveirinha. Proof of the bulk-edge correspondence through a link between topological photonics and fluctuation-electrodynamics. *Physical Review X*, 9(1):011037, 2019.

[113] Roger Temam. *Navier-Stokes equations: theory and numerical analysis*, volume 343. American Mathematical Soc., 2001.

[114] Alexander Figotin and Abel Klein. Localization of classical waves ii: Electromagnetic waves. *Communications in mathematical physics*, 184(2):411–441, 1997.

[115] Giuseppe Grosso and Giuseppe Pastori Parravicini. *Solid state physics*. Academic press, 2013.

[116] Neil W Ashcroft and N David Mermin. *Solid state physics*. Cengage Learning, 2022.

[117] Daniel Sjöberg, Christian Engström, Gerhard Kristensson, David JN Wall, and Niklas Wellander. A floquet–bloch decomposition of maxwell's equations applied to homogenization. *Multiscale Modeling & Simulation*, 4(1):149–171, 2005.

[118] Hai-Xiao Wang, Guang-Yu Guo, and Jian-Hua Jiang. Band topology in classical waves: Wilson-loop approach to topological numbers and fragile topology. *New Journal of Physics*, 21(9):093029, 2019.

[119] Masaru Onoda, Shuichi Murakami, and Naoto Nagaosa. Geometrical aspects in optical wave-packet dynamics. *Physical Review E*, 74(6):066610, 2006.

[120] Giuseppe De Nittis and Max Lein. Equivalence of electric, magnetic, and electromagnetic chern numbers for topological photonic crystals. *Journal of Mathematical Physics*, 61(2):022901, 2020.

[121] Christian Wolff, Patrick Mack, and Kurt Busch. Generation of Wannier functions for photonic crystals. *Physical Review B*, 88(7):075201, 2013.

[122] Haruki Watanabe and Ling Lu. Space group theory of photonic bands. *Physical review letters*, 121(26):263903, 2018.

[123] Antonio Morales-Pérez, Chiara Devescovi, Yoonseok Hwang, Mikel García-Díez, Barry Bradlyn, Juan Luis Mañes, Maia G Vergniory, and Aitzol García-Etxarri. Transversality-enforced tight-binding model for 3d photonic crystals aided by topological quantum chemistry. *arXiv preprint arXiv:2305.18257*, 2023.

[124] Sreela Datta, Che Ting Chan, KM Ho, and Costas M Soukoulis. Effective dielectric constant of periodic composite structures. *Physical Review B*, 48(20):14936, 1993.

[125] AA Krokhin, P Halevi, and J Arriaga. Long-wavelength limit (homogenization) for two-dimensional photonic crystals. *Physical Review B*, 65(11):115208, 2002.

[126] John Milnor. Analytic proofs of the "hairy ball theorem" and the brouwer fixed point theorem. *The American Mathematical Monthly*, 85(7):521–524, 1978.

[127] Murray Eisenberg and Robert Guy. A proof of the hairy ball theorem. *The American Mathematical Monthly*, 86(7):571–574, 1979.

[128] Barry Bradlyn, Luis Elcoro, Jennifer Cano, Maia G Vergniory, Zhijun Wang, Claudia Felser, Mois I Aroyo, and B Andrei Bernevig. Topological quantum chemistry. *Nature*, 547(7663):298–305, 2017.

[129] Jorrit Kruthoff, Jan De Boer, Jasper Van Wezel, Charles L Kane, and Robert-Jan Slager. Topological classification of crystalline insulators through band structure combinatorics. *Physical Review X*, 7(4):041069, 2017.

[130] Hoi Chun Po, Ashvin Vishwanath, and Haruki Watanabe. Symmetry-based indicators of band topology in the 230 space groups. *Nature communications*, 8(1):50, 2017.

[131] Vaibhav Gupta and Barry Bradlyn. Wannier-function methods for topological modes in one-dimensional photonic crystals. *Physical Review A*, 105(5):053521, 2022.

[132] Maria C Romano, Arianne Vellasco-Gomes, and Alexys Bruno-Alfonso. Wannier functions and the calculation of localized modes in one-dimensional photonic crystals. *JOSA B*, 35(4):826–834, 2018.

[133] JP Albert, C Jouanin, D Cassagne, and D Bertho. Generalized Wannier function method for photonic crystals. *Physical Review B*, 61(7):4381, 2000.

[134] M Blanco de Paz, MAJ Herrera, P Arroyo Huidobro, H Alaeian, MG Vergniory, Barry Bradlyn, G Giedke, Aitzol García-Etxarri, and Dario Bercioux. Energy density as a probe of band representations in photonic crystals. *Journal of Physics: Condensed Matter*, 34(31):314002, 2022.

[135] Ali Ghorashi, Sachin Vaidya, Mikael Rechtsman, Wladimir Benalcazar, Marin Soljačić, and Thomas Christensen. Prevalence of two-dimensional photonic topology. *arXiv preprint arXiv:2307.15701*, 2023.

[136] L He, HY Ji, YJ Wang, and XD Zhang. Topologically protected beam splitters and logic gates based on two-dimensional silicon photonic crystal slabs. *Optics Express*, 28(23):34015–34023, 2020.

[137] Siying Peng, Nick J Schilder, Xiang Ni, Jorik Van De Groep, Mark L Brongersma, Andrea Alù, Alexander B Khanikaev, Harry A Atwater, Albert Polman, et al. Probing the band structure of topological silicon photonic lattices in the visible spectrum. *Physical review letters*, 122(11):117401, 2019.

[138] Nikhil Parappurath, Filippo Alpeggiani, L Kuipers, and Ewold Verhagen. Direct observation of topological edge states in silicon photonic crystals: Spin, dispersion, and chiral routing. *Science advances*, 6(10):eaaw4137, 2020.

[139] Zheng Wang, YD Chong, John D Joannopoulos, and Marin Soljačić. Reflection-free one-way edge modes in a gyromagnetic photonic crystal. *Physical review letters*, 100(1):013905, 2008.

[140] Scott A. Skirlo, Ling Lu, Yuichi Igarashi, Qinghui Yan, John Joannopoulos, and Marin Soljačić. Experimental observation of large chern numbers in photonic crystals. *Phys. Rev. Lett.*, 115:253901, Dec 2015.

[141] Charles L Kane and Eugene J Mele. Quantum spin hall effect in graphene. *Physical review letters*, 95(22):226801, 2005.

[142] Hendrik Antoon Kramers. Théorie générale de la rotation paramagnétique dans les cristaux. *Proc. Acad. Amst*, 33(6), 1930.

[143] Konstantin Y Bliokh, Daria Smirnova, and Franco Nori. Quantum spin hall effect of light. *Science*, 348(6242):1448–1451, 2015.

[144] Alexander B Khanikaev, S Hossein Mousavi, Wang-Kong Tse, Mehdi Kargarian, Allan H MacDonald, and Gennady Shvets. Photonic topological insulators. *Nature materials*, 12(3):233–239, 2013.

[145] Ivan Fernandez-Corbaton, Xavier Zambrana-Puyalto, Nora Tischler, Xavier Vidal, Mathieu L Juan, and Gabriel Molina-Terriza. Electromagnetic duality symmetry and helicity conservation for the macroscopic maxwell's equations. *Physical review letters*, 111(6):060401, 2013.

[146] Jon Lasa-Alonso, Diego Romero Abujetas, Álvaro Nodar, Jennifer A Dionne, Juan José Sáenz, Gabriel Molina-Terriza, Javier Aizpurua, and Aitzol García-Etxarri. Surface-enhanced circular dichroism spectroscopy on periodic dual nanostructures. *ACS Photonics*, 7(11):2978–2986, 2020.

[147] Lisa V Poulikakos, Jennifer A Dionne, and Aitzol García-Etxarri. Optical helicity and optical chirality in free space and in the presence of matter. *Symmetry*, 11(9):1113, 2019.

[148] Hai-Xiao Wang and Jian-Hua Jiang. A short review of all-dielectric topological photonic crystals. *Frontiers in Physics*, 10:866552, 2022.

[149] Mário G Silveirinha. P· t· d symmetry-protected scattering anomaly in optics. *Physical Review B*, 95(3):035153, 2017.

[150] Yoichi Ando and Liang Fu. Topological crystalline insulators and topological superconductors: From concepts to materials. *Annu. Rev. Condens. Matter Phys.*, 6(1):361–381, 2015.

[151] Liang Fu. Topological crystalline insulators. *Physical review letters*, 106(10):106802, 2011.

[152] Willard Miller. *Symmetry groups and their applications*. Academic Press, 1973.

[153] Christopher Bradley and Arthur Cracknell. *The mathematical theory of symmetry in solids: representation theory for point groups and space groups*. Oxford University Press, 2010.

[154] Mois I Aroyo, Juan Manuel Perez-Mato, Danel Orobengoa, EMRE Tasci, Gemma de la Flor, and Asel Kirov. Crystallography online: Bilbao crystallographic server. *Bulg. Chem. Commun*, 43(2):183–197, 2011.

[155] L Michel and J Zak. Elementary energy bands in crystals are connected. *Physics Reports*, 341(1-6):377–395, 2001.

[156] H Bacry, L Michel, and J Zak. Symmetry and classification of energy bands in crystals. In *Group Theoretical Methods in Physics: Proceedings of the XVI International Colloquium Held at Varna, Bullgaria, June 15–20, 1987*, pages 289–308. Springer, 1988.

[157] Frank Wilczek and Anthony Zee. Appearance of gauge structure in simple dynamical systems. *Physical Review Letters*, 52(24):2111, 1984.

[158] J Zak. Band center—a conserved quantity in solids. *Physical Review Letters*, 48(5):359, 1982.

[159] Raphaël Leone. The geometry of (non)-abelian adiabatic pumping. *Journal of Physics A: Mathematical and Theoretical*, 44(29):295301, 2011.

[160] Jaume Gomis and Filippo Passerini. Holographic wilson loops. *Journal of High Energy Physics*, 2006(08):074, 2006.

[161] Aris Alexandradinata, Xi Dai, and B Andrei Bernevig. Wilson-loop characterization of inversion-symmetric topological insulators. *Physical Review B*, 89(15):155114, 2014.

[162] Dominik Gresch, Gabriel Autes, Oleg V Yazyev, Matthias Troyer, David Vanderbilt, B Andrei Bernevig, and Alexey A Soluyanov. Z2pack: Numerical implementation of hybrid wannier centers for identifying topological materials. *Physical Review B*, 95(7):075146, 2017.

[163] Rui Yu, Xiao Liang Qi, Andrei Bernevig, Zhong Fang, and Xi Dai. Equivalent expression of z 2 topological invariant for band insulators using the non-abelian berry connection. *Physical Review B*, 84(7):075119, 2011.

[164] Nicola Marzari, Arash A Mostofi, Jonathan R Yates, Ivo Souza, and David Vanderbilt. Maximally localized wannier functions: Theory and applications. *Reviews of Modern Physics*, 84(4):1419, 2012.

[165] Claudia Sgiarovello, Maria Peressi, and Raffaele Resta. Electron localization in the insulating state: Application to crystalline semiconductors. *Physical Review B*, 64(11):115202, 2001.

[166] Mário G Silveirinha. Z 2 topological index for continuous photonic materials. *Physical Review B*, 93(7):075110, 2016.

[167] Motohiko Ezawa. Topological kirchhoff law and bulk-edge correspondence for valley chern and spin-valley chern numbers. *Physical Review B*, 88(16):161406, 2013.

[168] Steven G Johnson and John D Joannopoulos. Block-iterative frequency-domain methods for maxwell's equations in a planewave basis. *Optics express*, 8(3):173–190, 2001.

[169] Georg W Winkler, Alexey A Soluyanov, and Matthias Troyer. Smooth gauge and wannier functions for topological band structures in arbitrary dimensions. *Physical Review B*, 93(3):035453, 2016.

[170] Doru Sticlet, Frederic Piéchon, Jean-Noël Fuchs, Pavel Kalugin, and Pascal Simon. Geometrical engineering of a two-band chern insulator in two dimensions with arbitrary topological index. *Physical Review B*, 85(16):165456, 2012.

[171] Hiromu Araki, Takahiro Fukui, and Yasuhiro Hatsugai. Entanglement chern number for three-dimensional topological insulators: Characterization by weyl points of entanglement hamiltonians. *Physical review B*, 96(16):165139, 2017.

[172] Shuhei Oono, Toshikaze Kariyado, and Yasuhiro Hatsugai. Section chern number for a three-dimensional photonic crystal and the bulk-edge correspondence. *Physical Review B*, 94(12):125125, 2016.

[173] Ming-Li Chang, Meng Xiao, Wen-Jie Chen, and Che Ting Chan. Multiple weyl points and the sign change of their topological charges in woodpile photonic crystals. *Physical Review B*, 95(12):125136, 2017.

[174] Xiangang Wan, Ari M Turner, Ashvin Vishwanath, and Sergey Y Savrasov. Topological semimetal and fermi-arc surface states in the electronic structure of pyrochlore iridates. *Physical Review B*, 83(20):205101, 2011.

[175] AA Zyuzin and AA Burkov. Topological response in weyl semimetals and the chiral anomaly. *Physical Review B*, 86(11):115133, 2012.

[176] AA Burkov and Leon Balents. Weyl semimetal in a topological insulator multilayer. *Physical review letters*, 107(12):127205, 2011.

[177] NP Armitage, EJ Mele, and Ashvin Vishwanath. Weyl and dirac semimetals in three-dimensional solids. *Reviews of Modern Physics*, 90(1):015001, 2018.

[178] Di-Fei Xu, Yong-Ping Du, Zhen Wang, Yu-Peng Li, Xiao-Hai Niu, Qi Yao, Dudin Pavel, Zhu-An Xu, Xian-Gang Wan, and Dong-Lai Feng. Observation of fermi arcs in non-centrosymmetric weyl semi-metal candidate nbp. *Chinese Physics Letters*, 32(10):107101, 2015.

[179] Gang Xu, Hongming Weng, Zhijun Wang, Xi Dai, and Zhong Fang. Chern semimetal and the quantized anomalous hall effect in hgcr 2 se 4. *Physical review letters*, 107(18):186806, 2011.

[180] Gang Xu, Jing Wang, Claudia Felser, Xiao-Liang Qi, and Shou-Cheng Zhang. Quantum anomalous hall effect in magnetic insulator heterostructure. *Nano letters*, 15(3):2019–2023, 2015.

[181] Shang Liu, Tomi Ohtsuki, and Ryuichi Shindou. Effect of disorder in a three-dimensional layered chern insulator. *Physical review letters*, 116(6):066401, 2016.

[182] YJ Jin, R Wang, BW Xia, BB Zheng, and H Xu. Three-dimensional quantum anomalous hall effect in ferromagnetic insulators. *Physical Review B*, 98(8):081101, 2018.

[183] Sang Wook Kim, Kangjun Seo, and Bruno Uchoa. Three-dimensional quantum anomalous hall effect in hyperhoneycomb lattices. *Physical Review B*, 97(20):201101, 2018.

[184] Fangdong Tang, Yafei Ren, Peipei Wang, Ruidan Zhong, John Schneeloch, Shengyuan A Yang, Kun Yang, Patrick A Lee, Genda Gu, Zhenhua Qiao, et al. Three-dimensional quantum hall effect and metal–insulator transition in zrte 5. *Nature*, 569(7757):537–541, 2019.

[185] Luis Elcoro, Benjamin J Wieder, Zhida Song, Yuanfeng Xu, Barry Bradlyn, and B Andrei Bernevig. Magnetic topological quantum chemistry. *arXiv preprint arXiv:2010.00598*, 2020.

[186] Andrew M Essin, Joel E Moore, and David Vanderbilt. Magnetoelectric polarizability and axion electrodynamics in crystalline insulators. *Physical review letters*, 102(14):146805, 2009.

[187] Thomas Olsen, Maryam Taherinejad, David Vanderbilt, and Ivo Souza. Surface theorem for the chern-simons axion coupling. *Physical Review B*, 95(7):075137, 2017.

[188] Kuan-Sen Lin, Giandomenico Palumbo, Zhaopeng Guo, Jeremy Blackburn, Daniel P Shoemaker, Fahad Mahmood, Zhijun Wang, Gregory A Fiete, Benjamin J Wieder, and Barry Bradlyn. Spin-resolved topology and partial axion angles in three-dimensional insulators. *arXiv preprint arXiv:2207.10099*, 2022.

[189] Adrien Bouhon and Robert-Jan Slager. Multi-gap topological conversion of euler class via band-node braiding: minimal models, *pt*-linked nodal rings, and chiral heirs. *arXiv preprint arXiv:2203.16741*, 2022.

[190] A Alexandradinata, J Höller, Chong Wang, Hengbin Cheng, and Ling Lu. Crystallographic splitting theorem for band representations and fragile topological photonic crystals. *Physical Review B*, 102(11):115117, 2020.

[191] Nicholas Rivera and Ido Kaminer. Light–matter interactions with photonic quasiparticles. *Nature Reviews Physics*, 2(10):538–561, 2020.

[192] CM Goringe, DR Bowler, and E Hernandez. Tight-binding modelling of materials. *Reports on Progress in Physics*, 60(12):1447, 1997.

[193] DA Papaconstantopoulos and MJ Mehl. The slater–koster tight-binding method: a computationally efficient and accurate approach. *Journal of Physics: Condensed Matter*, 15(10):R413, 2003.

[194] W Matthew C Foulkes and Roger Haydock. Tight-binding models and density-functional theory. *Physical review B*, 39(17):12520, 1989.

[195] Haruki Watanabe, Hoi Chun Po, and Ashvin Vishwanath. Structure and topology of band structures in the 1651 magnetic space groups. *Science advances*, 4(8):eaat8685, 2018.

[196] Heejae Kim, Ken Shiozaki, and Shuichi Murakami. Glide-symmetric magnetic topological crystalline insulators with inversion symmetry. *Physical Review B*, 100(16):165202, 2019.

[197] Luis Elcoro, Benjamin J Wieder, Zhida Song, Yuanfeng Xu, Barry Bradlyn, and B Andrei Bernevig. Magnetic topological quantum chemistry. *Nature communications*, 12(1):1–10, 2021.

[198] Hoi Chun Po. Symmetry indicators of band topology. *Journal of Physics: Condensed Matter*, 32(26):263001, 2020.

[199] Juan L. Mañes. Fragile phonon topology on the honeycomb lattice with time-reversal symmetry. *Phys. Rev. B*, 102:024307, Jul 2020.

[200] Martin Gutierrez-Amigo, Maia G. Vergniory, Ion Errea, and J. L. Mañes. Topological phonon analysis of the two-dimensional buckled honeycomb lattice: An application to real materials. *Phys. Rev. B*, 107:144307, Apr 2023.

[201] Yuanfeng Xu, M. G. Vergniory, Da-Shuai Ma, Juan L. Mañes, Zhi-Da Song, B. Andrei Bernevig, Nicolas Regnault, and Luis Elcoro. Catalogue of topological phonon materials, 2022.

[202] Luis Elcoro, Barry Bradlyn, Zhijun Wang, Maia G Vergniory, Jennifer Cano, Claudia Felser, B Andrei Bernevig, Danel Orobengoa, G Flor, and Mois I Aroyo. Double crystallographic groups and their representations on the bilbao crystallographic server. *Journal of Applied Crystallography*, 50(5):1457–1477, 2017.

[203] Jennifer Cano and Barry Bradlyn. Band representations and topological quantum chemistry. *Annual Review of Condensed Matter Physics*, 12:225–246, 2021.

[204] Hoi Chun Po, Haruki Watanabe, and Ashvin Vishwanath. Fragile topology and wannier obstructions. *Physical review letters*, 121(12):126402, 2018.

[205] Giuseppe De Nittis and Max Lein. The schrodinger formalism of electromagnetism and other classical waves—how to make quantum-wave analogies rigorous. *Annals of Physics*, 396:579–617, 2018.

[206] Andreas P Schnyder, Shinsei Ryu, Akira Furusaki, and Andreas WW Ludwig. Classification of topological insulators and superconductors in three spatial dimensions. *Physical Review B*, 78(19):195125, 2008.

[207] Rudolph Peierls. Zur theorie des diamagnetismus von leitungselektronen. *Zeitschrift für Physik*, 80(11-12):763–791, 1933.

[208] JM Luttinger. The effect of a magnetic field on electrons in a periodic potential. *Physical Review*, 84(4):814, 1951.

[209] F Duncan M Haldane. Model for a quantum hall effect without landau levels: Condensed-matter realization of the" parity anomaly". *Physical review letters*, 61(18):2015, 1988.

[210] Holger Bech Nielsen and Masao Ninomiya. The adler-bell-jackiw anomaly and weyl fermions in a crystal. *Physics Letters B*, 130(6):389–396, 1983.

[211] Mikael C Rechtsman. High chern numbers in photonic crystals. *Physics*, 8:122, 2015.

[212] BI Halperin. Japan j. of appl. phys. 26. *Suppl*, 1913:26–3, 1987.

[213] B Andrei Bernevig, Taylor L Hughes, Srinivas Raghu, and Daniel P Arovas. Theory of the three-dimensional quantum hall effect in graphite. *Physical review letters*, 99(14):146804, 2007.

[214] Bohm-Jung Yang, Mohammad Saeed Bahramy, and Naoto Nagaosa. Topological protection of bound states against the hybridization. *Nature communications*, 4(1):1–9, 2013.

[215] Sora Cho, Leon Balents, and Matthew PA Fisher. Transport of surface states in the bulk quantum hall effect. *Physical Review B*, 56(24):15814, 1997.

[216] Yigal Meir. Quantum hall effect in three-dimensional layered systems. *Physical Review B*, 58(4):R1762, 1998.

[217] Marcus Metzler. Spectral properties of three-dimensional layered quantum hall systems. *Journal of the Physical Society of Japan*, 67(12):4006–4009, 1998.

[218] Chao Zheng, Kun Yang, and Xin Wan. Thouless conductances of a three-dimensional quantum hall system. *Physical Review B*, 102(6):064208, 2020.

[219] DP Druist, PJ Turley, EG Gwinn, K Maranowski, and AC Gossard. 2d transport at the surface of a 3d quantum hall system. *Physica B: Condensed Matter*, 249:70–74, 1998.

[220] Leon Balents and Matthew PA Fisher. Chiral surface states in the bulk quantum hall effect. *Physical review letters*, 76(15):2782, 1996.

[221] Ling Lu, Haozhe Gao, and Zhong Wang. Topological one-way fiber of second chern number. *Nature communications*, 9(1):1–7, 2018.

[222] Benjamin J Wieder, Kuan-Sen Lin, and Barry Bradlyn. Axionic band topology in inversion-symmetric weyl-charge-density waves. *Physical Review Research*, 2(4):042010, 2020.

[223] Zhaoju Yang, Meng Xiao, Fei Gao, Ling Lu, Yidong Chong, and Baile Zhang. Weyl points in a magnetic tetrahedral photonic crystal. *Optics express*, 25(14):15772–15777, 2017.

[224] Jin Gyun Lee, Allan M Brooks, William A Shelton, Kyle JM Bishop, and Bhuvnesh Bharti. Directed propulsion of spherical particles along three dimensional helical trajectories. *Nature communications*, 10(1):1–8, 2019.

[225] Dominik Gresch, Gabriel Autès, Oleg V. Yazyev, Matthias Troyer, David Vanderbilt, B. Andrei Bernevig, and Alexey A. Soluyanov. Z2pack: Numerical implementation of hybrid wannier centers for identifying topological materials. *Phys. Rev. B*, 95:075146, Feb 2017.

[226] Alexey A. Soluyanov and David Vanderbilt. Computing topological invariants without inversion symmetry. *Phys. Rev. B*, 83:235401, Jun 2011.

[227] Alexey A Soluyanov and David Vanderbilt. Wannier representation of z 2 topological insulators. *Physical Review B*, 83(3):035108, 2011.

[228] Gui-Geng Liu, Zhen Gao, Peiheng Zhou, Qiang Wang, Yuan-Hang Hu, Maoren Wang, Chengqi Liu, Xiao Lin, Shengyuan A Yang, Yihao Yang, et al. Observation of weyl point pair annihilation in a gyromagnetic photonic crystal. *arXiv preprint arXiv:2106.02461*, 2021.

[229] L Martin-Moreno, FJ Garcia-Vidal, and AM Somoza. Self-assembled triply periodic minimal surfaces as molds for photonic band gap materials. *Physical review letters*, 83(1):73, 1999.

[230] Shuang Jia, Su-Yang Xu, and M Zahid Hasan. Weyl semimetals, fermi arcs and chiral anomalies. *Nature materials*, 15(11):1140–1144, 2016.

[231] Said M Mikki and Ahmed A Kishk. Electromagnetic wave propagation in non-local media: Negative group velocity and beyond. *Progress In Electromagnetics Research*, 14:149–174, 2009.

[232] Babak Bahari, Liyi Hsu, Si Hui Pan, Daryl Preece, Abdoulaye Ndao, Abdelkrim El Amili, Yeshaiahu Fainman, and Boubacar Kanté. Photonic quantum hall effect and multiplexed light sources of large orbital angular momenta. *Nature Physics*, pages 1–4, 2021.

[233] Frank Schindler, Zhijun Wang, Maia G Vergniory, Ashley M Cook, Anil Murani, Shamashis Sengupta, Alik Yu Kasumov, Richard Deblock, Sangjun Jeon, Ilya Drozdov, et al. Higher-order topology in bismuth. *Nature physics*, 14(9):918–924, 2018.

[234] Frank Schindler, Ashley M Cook, Maia G Vergniory, Zhijun Wang, Stuart SP Parkin, B Andrei Bernevig, and Titus Neupert. Higher-order topological insulators. *Science advances*, 4(6):eaat0346, 2018.

[235] Nicodemos Varnava, Ivo Souza, and David Vanderbilt. Axion coupling in the hybrid wannier representation. *Physical Review B*, 101(15):155130, 2020.

[236] Dan Sehayek, Manisha Thakurathi, and AA Burkov. Charge density waves in weyl semimetals. *Physical Review B*, 102(11):115159, 2020.

[237] Yizhi You, Gil Young Cho, and Taylor L Hughes. Response properties of axion insulators and weyl semimetals driven by screw dislocations and dynamical axion strings. *Physical Review B*, 94(8):085102, 2016.

[238] Johannes Gooth, Barry Bradlyn, Shashank Honnali, Clemens Schindler, Nitesh Kumar, Jonathan Noky, Yangpeng Qi, Chandra Shekhar, Yan Sun, Zhijun Wang, et al. Axionic charge-density wave in the weyl semimetal (tase4) 2i. *Nature*, 575(7782):315–319, 2019.

[239] Zhong Wang and Shou-Cheng Zhang. Chiral anomaly, charge density waves, and axion strings from weyl semimetals. *Physical Review B*, 87(16):161107, 2013.

[240] So Chigusa, Takeo Moroi, and Kazunori Nakayama. Axion/hidden-photon dark matter conversion into condensed matter axion. *Journal of High Energy Physics*, 2021(8):1–33, 2021.

[241] David JE Marsh, Kin Chung Fong, Erik W Lentz, Libor Šmejkal, and Mazhar N Ali. Proposal to detect dark matter using axionic topological antiferromagnets. *Physical Review Letters*, 123(12):121601, 2019.

[242] Rundong Li, Jing Wang, Xiao-Liang Qi, and Shou-Cheng Zhang. Dynamical axion field in topological magnetic insulators. *Nature Physics*, 6(4):284–288, 2010.

[243] Alexander J Millar, Georg G Raffelt, Javier Redondo, and Frank D Steffen. Dielectric haloscopes to search for axion dark matter: theoretical foundations. *Journal of Cosmology and Astroparticle Physics*, 2017(01):061, 2017.

[244] Matthew Lawson, Alexander J Millar, Matteo Pancaldi, Edoardo Vitagliano, and Frank Wilczek. Tunable axion plasma haloscopes. *Physical review letters*, 123(14):141802, 2019.

[245] Naoto Yokoi and Eiji Saitoh. Stimulated emission of dark matter axion from condensed matter excitations. *Journal of High Energy Physics*, 2018(1):1–21, 2018.

[246] Wujun Shi, Benjamin J Wieder, Holger L Meyerheim, Yan Sun, Yang Zhang, Yiwei Li, Lei Shen, Yanpeng Qi, Lexian Yang, Jagannath Jena, et al. A charge-density-wave topological semimetal. *Nature Physics*, 17(3):381–387, 2021.

[247] Hidetoshi Fukuyama and Patrick A Lee. Dynamics of the charge-density wave. i. impurity pinning in a single chain. *Physical Review B*, 17(2):535, 1978.

[248] John D Joannopoulos, Steven G Johnson, Joshua N Winn, and Robert D Meade. Molding the flow of light. *Princet. Univ. Press. Princeton, NJ [ua]*, 2008.

[249] Xiang Xi, Bei Yan, Linyun Yang, Yan Meng, Zhen-Xiao Zhu, Jing-Ming Chen, Ziyao Wang, Peiheng Zhou, Perry Ping Shum, Yihao Yang, et al. Topological

antichiral surface states in a magnetic weyl photonic crystal. *Nature Communications*, 14(1):1991, 2023.

[250] Antonio Morales Perez, Chiara Devescovi, Yoonseok Hwang, Mikel Garcia Diez, Barry Bradlyn, Juan Luis Manes, Maia Garcia Vergniory, and Aitzol Garcia Etxarri. Transversality-enforced tight-binding model for 3d photonic crystals aided by topological quantum chemistry. *arXiv:2305.18257*.

[251] "Least_squares" package in "scipy.optimize".

[252] NV Belov. Neronova, nn and smirnova t. *S., Shubnikov groups. Sov. Phys./Crystallography*, 2:311–322, 1957.

[253] Jeffrey CY Teo and Charles L Kane. Topological defects and gapless modes in insulators and superconductors. *Physical Review B*, 82(11):115120, 2010.

[254] Eslam Khalaf, Wladimir A Benalcazar, Taylor L Hughes, and Raquel Queiroz. Boundary-obstructed topological phases. *Physical Review Research*, 3(1):013239, 2021.

[255] Ka Ho Wong, Mark R Hirsbrunner, Jacopo Gliozzi, Arbaz Malik, Barry Bradlyn, Taylor L Hughes, and Dirk K Morr. Higher order topological superconductivity in magnet-superconductor hybrid systems. *arXiv preprint arXiv:2210.15582*, 2022.

[256] Eslam Khalaf, Hoi Chun Po, Ashvin Vishwanath, and Haruki Watanabe. Symmetry indicators and anomalous surface states of topological crystalline insulators. *Physical Review X*, 8(3):031070, 2018.

[257] Jorge Bravo-Abad, Ling Lu, Liang Fu, Hrvoje Buljan, and Marin Soljačić. Weyl points in photonic-crystal superlattices. *2D Materials*, 2(3):034013, 2015.

[258] Luyang Wang, Shao-Kai Jian, and Hong Yao. Topological photonic crystal with equifrequency weyl points. *Physical Review A*, 93(6):061801, 2016.

[259] Wen-Jie Chen, Meng Xiao, and Che Ting Chan. Photonic crystals possessing multiple weyl points and the experimental observation of robust surface states. *Nature communications*, 7(1):1–10, 2016.

[260] Biao Yang, Qinghua Guo, Ben Tremain, Lauren E Barr, Wenlong Gao, Hongchao Liu, Benjamin Béri, Yuanjiang Xiang, Dianyuan Fan, Alastair P Hibbins, et al. Direct observation of topological surface-state arcs in photonic metamaterials. *Nature communications*, 8(1):1–7, 2017.

[261] Jiho Noh, Sheng Huang, Daniel Leykam, Yi Dong Chong, Kevin P Chen, and Mikael C Rechtsman. Experimental observation of optical weyl points and fermi arc-like surface states. *Nature Physics*, 13(6):611–617, 2017.

[262] Biao Yang, Qinghua Guo, Ben Tremain, Rongjuan Liu, Lauren E Barr, Qinghui Yan, Wenlong Gao, Hongchao Liu, Yuanjiang Xiang, Jing Chen, et al. Ideal weyl points and helicoid surface states in artificial photonic crystal structures. *Science*, 359(6379):1013–1016, 2018.

[263] Christina Jörg, Sachin Vaidya, Jiho Noh, Alexander Cerjan, Shyam Augustine, Georg von Freymann, and Mikael C Rechtsman. Observation of quadratic (charge-2) weyl point splitting in near-infrared photonic crystals. *Laser & Photonics Reviews*, 16(1):2100452, 2022.

[264] Holger Bech Nielsen and Masao Ninomiya. Absence of neutrinos on a lattice:(ii). intuitive topological proof. *Nuclear Physics B*, 193(1):173–194, 1981.

[265] Holger Bech Nielsen and Masao Ninomiya. Absence of neutrinos on a lattice:(i). proof by homotopy theory. *Nuclear Physics B*, 185(1):20–40, 1981.

[266] Miguel Bello, Gloria Platero, Juan Ignacio Cirac, and Alejandro González-Tudela. Unconventional quantum optics in topological waveguide qed. *Science advances*, 5(7):eaaw0297, 2019.

[267] Alejandro González-Tudela and Fernando Galve. Anisotropic quantum emitter interactions in two-dimensional photonic-crystal baths. *ACS Photonics*, 6(1):221–229, 2018.

[268] Lei Ying, Ming Zhou, Michael Mattei, Boyuan Liu, Paul Campagnola, Randall H Goldsmith, and Zongfu Yu. Extended range of dipole-dipole interactions in periodically structured photonic media. *Physical Review Letters*, 123(17):173901, 2019.

[269] Daniele De Bernardis, Ze-Pei Cian, Iacopo Carusotto, Mohammad Hafezi, and Peter Rabl. Light-matter interactions in synthetic magnetic fields: Landau-photon polaritons. *Physical Review Letters*, 126(10):103603, 2021.

[270] Iñaki García-Elcano, Jorge Bravo-Abad, and Alejandro González-Tudela. Light-matter interactions near photonic weyl points. *Physical Review A*, 103(3):033511, 2021.

[271] Iñaki García-Elcano, Alejandro González-Tudela, and Jorge Bravo-Abad. Tunable and robust long-range coherent interactions between quantum emitters mediated by weyl bound states. *Physical Review Letters*, 125(16):163602, 2020.

[272] Roman Jackiw and Cláudio Rebbi. Solitons with fermion number $1/2$. *Physical Review D*, 13(12):3398, 1976.

[273] David B Kaplan. A method for simulating chiral fermions on the lattice. *Physics Letters B*, 288(3-4):342–347, 1992.

[274] Takumi Bessho and Masatoshi Sato. Nielsen-ninomiya theorem with bulk topology: Duality in floquet and non-hermitian systems. *Physical Review Letters*, 127(19):196404, 2021.

[275] Charles C Wojcik, Xiao-Qi Sun, Tomáš Bzdušek, and Shanhui Fan. Homotopy characterization of non-hermitian hamiltonians. *Physical Review B*, 101(20):205417, 2020.

[276] Xiao-Qi Sun, Meng Xiao, Tomáš Bzdušek, Shou-Cheng Zhang, and Shanhui Fan. Three-dimensional chiral lattice fermion in floquet systems. *Physical review letters*, 121(19):196401, 2018.

[277] Sho Higashikawa, Masaya Nakagawa, and Masahito Ueda. Floquet chiral magnetic effect. *Physical review letters*, 123(6):066403, 2019.

[278] Tobias Meng and Jan Carl Budich. Unpaired weyl nodes from long-ranged interactions: Fate of quantum anomalies. *Physical Review Letters*, 122(4):046402, 2019.

[279] J-Z Ma, Q-S Wu, M Song, S-N Zhang, EB Guedes, SA Ekahana, M Krivenkov, MY Yao, S-Y Gao, W-H Fan, et al. Observation of a singular weyl point surrounded by charged nodal walls in ptga. *Nature communications*, 12(1):1–8, 2021.

[280] Zhi-Ming Yu, Weikang Wu, YX Zhao, and Shengyuan A Yang. Circumventing the no-go theorem: A single weyl point without surface fermi arcs. *Physical Review B*, 100(4):041118, 2019.

[281] Weikang Wu, Ying Liu, Si Li, Chengyong Zhong, Zhi-Ming Yu, Xian-Lei Sheng, YX Zhao, and Shengyuan A Yang. Nodal surface semimetals: Theory and material realization. *Physical Review B*, 97(11):115125, 2018.

[282] Qi-Feng Liang, Jian Zhou, Rui Yu, Zhi Wang, and Hongming Weng. Node-surface and node-line fermions from nonsymmorphic lattice symmetries. *Physical Review B*, 93(8):085427, 2016.

[283] Moritz M Hirschmann, Andreas Leonhardt, Berkay Kilic, Douglas H Fabini, and Andreas P Schnyder. Symmetry-enforced band crossings in tetragonal materials: Dirac and weyl degeneracies on points, lines, and planes. *Physical Review Materials*, 5(5):054202, 2021.

[284] Tiantian Zhang, Ryo Takahashi, Chen Fang, and Shuichi Murakami. Twofold quadruple weyl nodes in chiral cubic crystals. *Physical Review B*, 102(12):125148, 2020.

[285] Chaoxi Cui, Xiao-Ping Li, Da-Shuai Ma, Zhi-Ming Yu, and Yugui Yao. Charge-four weyl point: Minimum lattice model and chirality-dependent properties. *Physical Review B*, 104(7):075115, 2021.

[286] Kristel Michielsen and JS Kole. Photonic band gaps in materials with triply periodic surfaces and related tubular structures. *Physical Review B*, 68(11):115107, 2003.

[287] Lu Han and Shunai Che. An overview of materials with triply periodic minimal surfaces and related geometry: from biological structures to self-assembled systems. *Advanced Materials*, 30(17):1705708, 2018.

[288] Kristel Michielsen and Doekele G Stavenga. Gyroid cuticular structures in butterfly wing scales: biological photonic crystals. *Journal of The Royal Society Interface*, 5(18):85–94, 2008.

[289] Caroline Pouya, Johannes TB Overvelde, Mathias Kolle, Joanna Aizenberg, Katia Bertoldi, James C Weaver, and Pete Vukusic. Characterization of a mechanically tunable gyroid photonic crystal inspired by the butterfly parides sesostris. *Advanced Optical Materials*, 4(1):99–105, 2016.

[290] Alan H Schoen. Infinite periodic minimal surfaces without self-intersections. Technical report, 1970.

[291] Oraib Al-Ketan and Rashid K Abu Al-Rub. Multifunctional mechanical metamaterials based on triply periodic minimal surface lattices. *Advanced Engineering Materials*, 21(10):1900524, 2019.

[292] Mark D Turner, Matthias Saba, Qiming Zhang, Benjamin P Cumming, Gerd E Schröder-Turk, and Min Gu. Miniature chiral beamsplitter based on gyroid photonic crystals. *Nature Photonics*, 7(10):801–805, 2013.

[293] Yuka Kobayashi, Ryosuke Ohnuki, and Shinya Yoshioka. Discovery of i-wp minimal-surface-based photonic crystal in the scale of a longhorn beetle. *Journal of the Royal Society Interface*, 18(184):20210505, 2021.

[294] James A Dolan, Matthias Saba, Raphael Dehmel, Ilja Gunkel, Yibei Gu, Ullrich Wiesner, Ortwin Hess, Timothy D Wilkinson, Jeremy J Baumberg, Ullrich Steiner, et al. Gyroid optical metamaterials: Calculating the effective permittivity of multidomain samples. *ACS photonics*, 3(10):1888–1896, 2016.

[295] Siying Peng, Runyu Zhang, Valerian H Chen, Emil T Khabiboulline, Paul Braun, and Harry A Atwater. Three-dimensional single gyroid photonic crystals with a mid-infrared bandgap. *ACS Photonics*, 3(6):1131–1137, 2016.

[296] Liping Wu, Wanlin Wang, Wang Zhang, Huilan Su, Jiajun Gu, Qinglei Liu, Di Zhang, Dejan Pantelić, and Branislav Jelenković. Optical performance study of gyroid-structured tio2 photonic crystals replicated from natural templates using a sol-gel method. *Advanced Optical Materials*, 6(21):1800064, 2018.

[297] Xavier Zambrana-Puyalto, I Fernandez-Corbaton, ML Juan, Xavier Vidal, and Gabriel Molina-Terriza. Duality symmetry and kerker conditions. *Optics letters*, 38(11):1857–1859, 2013.

[298] Zhi-Da Song, Luis Elcoro, and B Andrei Bernevig. Twisted bulk-boundary correspondence of fragile topology. *Science*, 367(6479):794–797, 2020.

[299] Yuanfeng Xu, Luis Elcoro, Zhi-Da Song, MG Vergniory, Claudia Felser, Stuart SP Parkin, Nicolas Regnault, Juan L Mañes, and B Andrei Bernevig. Filling-enforced obstructed atomic insulators. *arXiv preprint arXiv:2106.10276*, 2021.

[300] Yoonseok Hwang, Junyeong Ahn, and Bohm-Jung Yang. Fragile topology protected by inversion symmetry: Diagnosis, bulk-boundary correspondence, and Wilson loop. *Physical Review B*, 100(20):205126, 2019.

[301] Heinz Hopf. Vektorfelder in n-dimensionalen mannigfaltigkeiten. *Mathematische Annalen*, 96:225–249, 1927.

[302] Adrien Bouhon, Tomáš Bzdušek, and Robert-Jan Slager. Geometric approach to fragile topology beyond symmetry indicators. *Physical Review B*, 102(11):115135, 2020.

[303] Toshihiko Baba. Slow light in photonic crystals. *Nature photonics*, 2(8):465–473, 2008.

[304] Juntao Li, Thomas P White, Liam O'Faolain, Alvaro Gomez-Iglesias, and Thomas F Krauss. Systematic design of flat band slow light in photonic crystal waveguides. *Optics express*, 16(9):6227–6232, 2008.

[305] Yi Yang, Charles Roques-Carmes, Steven E Kooi, Haoning Tang, Justin Beroz, Eric Mazur, Ido Kaminer, John D Joannopoulos, and Marin Soljačić. Photonic flatband resonances for free-electron radiation. *Nature*, 613(7942):42–47, 2023.

[306] Nicolas Regnault, Yuanfeng Xu, Ming-Rui Li, Da-Shuai Ma, Milena Jovanovic, Ali Yazdani, Stuart SP Parkin, Claudia Felser, Leslie M Schoop, N Phuan Ong, et al. Catalogue of flat-band stoichiometric materials. *Nature*, 603(7903):824–828, 2022.

[307] Dumitru Călugăru, Aaron Chew, Luis Elcoro, Yuanfeng Xu, Nicolas Regnault, Zhi-Da Song, and B Andrei Bernevig. General construction and topological classification of crystalline flat bands. *Nature Physics*, 18(2):185–189, 2022.

[308] Lok C. Lew Yan Voon and Morten Willatzen. *Method of Invariants*, pages 79–151. Springer Berlin Heidelberg, Berlin, Heidelberg, 2009.

[309] NF Johnson, PM Hui, and KH Luk. Theory of photonic band structures: a vector-wave k· p approach. *Solid state communications*, 90(4):229–232, 1994.

[310] Luis Elcoro, Barry Bradlyn, Zhijun Wang, Maia G. Vergniory, Jennifer Cano, Claudia Felser, B. Andrei Bernevig, Danel Orobengoa, Gemma de la Flor, and Mois I. Aroyo. Double crystallographic groups and their representations on the Bilbao Crystallographic Server. *Journal of Applied Crystallography*, 50(5):1457–1477, Oct 2017.

[311] Francesca Rossi, Peter Van Beek, and Toby Walsh. *Handbook of constraint programming*. Elsevier, 2006.

[312] Joel E Moore and Leon Balents. Topological invariants of time-reversal-invariant band structures. *Physical Review B*, 75(12):121306, 2007.

[313] Rahul Roy. Three dimensional topological invariants for time reversal invariant hamiltonians and the three dimensional quantum spin hall effect. *arXiv preprint cond-mat/0607531*, 2006.

[314] Harold T Stokes and Dorian M Hatch. Findsym: program for identifying the space-group symmetry of a crystal. *Journal of Applied Crystallography*, 38(1):237–238, 2005.